Kinetochore-microtubule coupling and its regulation during mitosis

Jerry F. Tien

A dissertation

submitted in partial fulfillment of the

requirements for the degree of

Doctor of Philosophy

University of Washington

2014

Reading Committee:

Trisha N. Davis, Chair

Charles L. Asbury

James B. Hurley

Program Authorized to Offer Degree:

Biochemistry

University of Washington

Abstract

Kinetochore-microtubule coupling and its regulation during mitosis

Jerry F. Tien

Chair of the Supervisory Committee:

Trisha N. Davis, Professor and Chair

Department of Biochemistry

The coupling of kinetochores to dynamic spindle microtubules is crucial for chromosome positioning and segregation, error correction, and cell cycle progression. This linkage depends on the Ndc80 complex, a conserved and essential microtubule-binding component of the kinetochore. As a member of the complex, the Ndc80 protein forms microtubule attachments through a calponin homology domain, which has been the focus of biochemical and structural characterization. However, the function of the remainder of Ndc80 is poorly understood. We coupled high-throughput sequencing to a saturating linker-scanning mutagenesis screen in *Saccharomyces cerevisiae* and identified essential domains in previously uncharacterized regions of Ndc80. By analyzing mutants from the screen, we found that one domain within the Ndc80 coiled-coil is involved in assembling, but not maintaining, metaphase spindles. This process likely depends on a conformational change in the complex. Furthermore, we found that a helical hairpin adjacent to the calponin homology domain influences microtubule binding by the

complex *in vitro*, and a C-terminal segment of Ndc80 is required for tetramerization of the complex *in vivo*.

In *S. cerevisiae*, the Ndc80 complex recruits the microtubule-binding Dam1 complex to kinetochores. The Ndc80 and Dam1 complexes are not redundant, but their distinct contributions are unknown. We show that the Dam1 complex is a processivity factor for the Ndc80 complex, enhancing the ability of the Ndc80 complex to couple to microtubule tips *in vitro*. Moreover, the interaction between the Ndc80 and Dam1 complexes is abolished when the Dam1 complex is phosphorylated by Aurora B. This provides evidence for a mechanism by which Aurora B resets aberrant kinetochore-microtubule attachments in *S. cerevisiae*. In higher eukaryotes, recent findings suggest that Aurora B also influences microtubule dynamics as part of its error correction mechanism. We show that the human Ndc80 complex directly stabilizes the tips of disassembling microtubules and promotes rescue (the transition from microtubule shortening to growth). Human Ndc80 complex with Aurora B phosphomimetic mutations is defective at promoting microtubule rescue, even while robustly coupled to disassembling microtubule tips. Together, these results suggest that in addition to regulating attachment stability, Aurora B controls microtubule dynamics through phosphorylation of the human Ndc80 complex.

TABLE OF CONTENTS

LIST OF FIGURES

LIST OF TABLES

ACKNOWLEDGEMENTS

First and foremost, I thank Trisha Davis for her support and guidance throughout my graduate career. I especially thank her for providing me with the opportunities to develop as a scientist. I also thank Chip Asbury, who welcomed me into his lab and has been a great mentor throughout graduate school. I thank Trisha Davis, Chip Asbury, Jim Hurley, Sue Biggins, Peter Brzovic, and Brian Kennedy for serving on my supervisory committee, and Trisha Davis, Chip Asbury, and Jim Hurley for providing feedback on my dissertation. I am grateful to all members of the Davis lab, past and present. I especially wish to acknowledge Neil Umbreit, Dan Gestaut, Kim Fong, and Alex Zelter for working with me on the projects presented in this thesis. I also thank Eric Muller, Michelle Shimogawa, Megan Wargacki, Beth Graczyk, and Emily Mazanka for helpful advice and assistance. The work presented here would not be possible without my collaborators. In particular, I thank Chip Asbury, Andrew Franck, Andy Powers, Krishna Sarangapani, Maitreya Dunham, Celia Payen, Linda Wordeman, Mike Wagenbach, Justin Decarreau, Jeremy Cooper, Sue Biggins, Matthew Miller, Tamir Gonen, Breanna Vollmar, Bryan Fonslow, Jay Shendure, and Charlie Lee. Finally, I thank Erin Kirschner and the Department of Biochemistry for their assistance and support.

Chapter 1
Introduction

The mitotic spindle

Mitosis is the process by which somatic cells physically organize and segregate their replicated chromosomes. As a fundamental phase of the cell cycle, mitosis is essential for the development and survival of organisms. Through multiple rounds of cell division, a single human zygote can develop into a fully-grown adult, estimated to contain ~4 x 10^{13} cells (BIANCONI *et al.* 2013). It is therefore critically important that mitosis proceed with high fidelity, such that each daughter cell receives a full complement of genetic material. Errors during mitosis can lead to chromosome missegregation and aneuploidy, a state in which a cell possesses an abnormal number of chromosomes. Mitotic defects can also contribute to genome instability by inducing chromosome breaks and DNA damage (CRASTA *et al.* 2012; GANEM and PELLMAN 2012). These defects in mitosis have been linked to cell death, tumorigenesis (GORDON *et al.* 2012; WEAVER *et al.* 2007), birth defects, and numerous other disorders (discussed in CIMINI and DEGRASSI 2005).

To ensure the proper transmission of replicated chromosomes during cell division, most eukaryotic cells utilize a microtubule-based molecule machine called the mitotic spindle (Figure 1.1A). The mitotic spindle contains two poles that act as microtubule organizing centers (called centrosomes in metazoans and spindle pole bodies in yeast). Each pole nucleates microtubules, which are hollow tubes comprised of repeating units of α- and β-tubulin heterodimers. The tubulin heterodimers assemble to form long protofilaments, and thirteen protofilaments arrange cylindrically in a 25-nm diameter microtubule (EVANS *et al.* 1985;

LEDBETTER and PORTER 1963). Each microtubule has an inherent polarity, with the "minus" end anchored at the pole where it is nucleated, and the "plus" end extending outwards from the pole. There are three main types of spindle microtubules: (1) astral microtubules contact the cell cortex and are responsible for positioning the spindle, (2) interpolar microtubules interdigitate with one another to stabilize the bipolar spindle, and (3) kinetochore microtubules attach to chromosomes through protein assemblies called kinetochores. In most organisms, the plus-end of the microtubule is dynamic, frequently switching between periods of growth and shortening in a stochastic manner. This behavior was termed "dynamic instability" (MITCHISON and KIRSCHNER 1984), and has been the basis for models describing how microtubules mediate chromosome positioning and segregation.

At the start of mitosis, each duplicated chromosome has two kinetochores, one assembled onto the centromeric region of each sister chromatid (Figure 1.1B). During prometaphase, one sister kinetochore first attaches laterally to the side of a kinetochore microtubule. Because microtubules exhibit dynamic instability, it was hypothesized that the initial capture of kinetochores is likely stochastic, as described by the "search-and-capture" model (KIRSCHNER and MITCHISON 1986). Once captured, kinetochores are moved along the side of microtubules towards the pole and the lateral attachments are transitioned to an end-on arrangement with the plus-ends of kinetochore-microtubules (RIEDER and ALEXANDER 1990). The molecular mechanisms underlying this process remain poorly understood, but it is known to involve minus-end directed motors (dynein in metazoans, Kar3 in budding yeast) (KING *et al.* 2000; TANAKA *et al.* 2005). Based on recent experiments in *Caenorhabditis elegans*, it was proposed that lateral binding of kinetochores to microtubules is achieved indirectly through dynein, and that kinetochores only attach directly to microtubules in the "end-on" orientation (CHEERAMBATHUR

et al. 2013). In budding yeast, forming end-on attachments also require an additional contribution from the Dam1 kinetochore complex (SHIMOGAWA *et al.* 2006; TANAKA *et al.* 2007). Once at the plus-end, chromosomes harness microtubule dynamics to produce force and movement. When sister kinetochores are attached to the plus-ends of microtubules emanating from opposite poles, the chromosome is properly bioriented. Here, tension is established across sister kinetochores, which directly stabilizes kinetochore-microtubule attachments (AKIYOSHI *et al.* 2010; NICKLAS and WARD 1994). At metaphase, every chromosome is bioriented and aligned at the metaphase plate. During anaphase, cohesion holding sister chromatids together is lost, and sister chromatids are pulled to opposite ends of the cell, coupled to the shortening of kinetochore microtubules. Proper progression through mitosis ultimately depends on the correct positioning and movement of chromosomes. Keys to this process include regulatory events that ensure the formation of correct kinetochore-microtubule attachments and modulation of microtubule plus-end dynamics.

The kinetochore-microtubule interface

The kinetochore is a large structure that physically couples DNA to the dynamic plus-ends of spindle microtubules. Depending on the organism, kinetochores vary drastically in size and can assemble onto point centromeres, regional centromeres, or holocentromeres (reviewed in PERPELESCU and FUKAGAWA 2011). Despite this diversity, the core components of the kinetochore are well conserved in all eukaryotes (MERALDI *et al.* 2006). The budding yeast *Saccharomyces cerevisiae* has one of the simplest kinetochores; kinetochores assemble onto 125-bp point centromeres, and each kinetochore attaches to just one spindle microtubule (FITZGERALD-HAYES *et al.* 1982; HIETER *et al.* 1985; PETERSON and RIS 1976; WINEY *et al.* 1995). By contrast, vertebrate kinetochores assemble onto regional centromeres spanning

megabase-pairs of DNA, and each kinetochore binds a "K-fiber" composed of a bundle of 10-45 microtubules (HENIKOFF *et al.* 2001; RIEDER 1982).

Early observations of mammalian kinetochores using electron microscopy revealed a tri-laminar structure (JOKELAINEN 1967). More recently, the spatial organization of individual kinetochore components *in vivo* was determined (JOGLEKAR *et al.* 2009; WAN *et al.* 2009). Kinetochore components can be generally grouped into one of three sections: (1) the inner kinetochore contains components that assemble onto centromeric DNA, (2) the outer kinetochore features the microtubule-binding elements, and (3) the middle kinetochore components bridge the inner and outer kinetochores. In the current model of kinetochore assembly, inner kinetochore components first bind to centromeric DNA, and recruit middle and outer kinetochore components in a hierarchical manner (DE WULF *et al.* 2003).

The core kinetochore in budding yeast consists of more than 40 distinct proteins, many of which can assemble into stable subcomplexes (reviewed in BIGGINS 2013). The Ndc80 complex is an outer kinetochore component that directly binds microtubules *in vitro* (CIFERRI *et al.* 2008; WEI *et al.* 2007). Along with the Spc105 and Mtw1 complexes, it forms the conserved microtubule-binding core of the kinetochore, termed the "KMN network" (CHEESEMAN *et al.* 2006). Budding yeast also have the fungal-specific Dam1 complex, which binds microtubules *in vitro* (MIRANDA *et al.* 2005; WESTERMANN *et al.* 2006). In addition to core kinetochore components, other proteins localize to the outer kinetochore and/or microtubule plus-ends, including Stu1, Stu2, Bik1, and Slk19 (HE *et al.* 2001; ORTIZ *et al.* 2009; SHIMOGAWA *et al.* 2006; SHIMOGAWA *et al.* 2010; ZENG *et al.* 1999). It is still unclear how individual components at the kinetochore-microtubule interface give rise to the behaviors kinetochores exhibit *in vivo*. In general, four key properties have been observed. First, kinetochores can attach persistently to

the dynamic plus-ends of spindle microtubules during repeated rounds of microtubule growth and shortening (MADDOX *et al.* 2003; SKIBBENS *et al.* 1995; SKIBBENS *et al.* 1993). Second, these attachments are strong enough to withstand the forces exerted by the spindle. This is particularly important during biorientation, when tension is applied across sister kinetochores. Third, microtubule plus-end dynamics can be modulated for chromosome movement and positioning. Lastly, kinetochore-microtubule attachments can be targeted by regulatory systems to prevent errors in mitosis. Studying kinetochore components individually and in combination will be required to dissect their distinct roles in kinetochore-microtubule coupling.

The spindle assembly checkpoint

During mitosis, a conserved surveillance mechanism monitors kinetochore-microtubule attachments to ensure that chromosomes are equally segregated to daughter cells. The first part of this mechanism is a signaling cascade, termed the "spindle assembly checkpoint," which functions to delay anaphase until all kinetochores are attached to spindle microtubules (reviewed in HAUF 2013) (Figure 1.1B and C). The second component of this surveillance mechanism is an error correction system that detects and detaches aberrant kinetochore-microtubule attachments (discussed below). The resulting unattached kinetochores fail to satisfy the spindle assembly checkpoint, ensuring that anaphase does not proceed until all chromosomes are properly bioriented.

A single unattached kinetochore is sufficient to prevent satisfaction of the spindle assembly checkpoint (LI and NICKLAS 1995; RIEDER *et al.* 1995). There is also evidence that lack of tension across sister kinetochores prevents satisfaction of the checkpoint (BIGGINS and MURRAY 2001; STERN and MURRAY 2001). It is still not known whether inter-kinetochore tension defects and unattached kinetochores generate independent signals to keep the checkpoint

active, or if tension defects indirectly prevent satisfaction of the checkpoint by destabilizing kinetochore-microtubule attachments. Furthermore, intra-kinetochore tension has also been implicated in checkpoint response (MARESCA and SALMON 2009; UCHIDA *et al.* 2009). Therefore, defining the structural changes within the kinetochore upon biorientation will be one key aspect to understanding how the checkpoint is satisfied.

The core components of the spindle assembly checkpoint include Mad1, Mad2, Mad3 (BubR1), Bub1, Bub3, and Mps1 (HOYT *et al.* 1991; LI and MURRAY 1991; WEISS and WINEY 1996). In the current model, the checkpoint signal for unattached kinetochores is initiated by kinetochore-localized Mps1, which is possibly recruited by Ndc80 (HARDWICK *et al.* 1996; HE *et al.* 1998; KEMMLER *et al.* 2009; MARTIN-LLUESMA *et al.* 2002). Mps1 has many kinetochore targets, but phosphorylation of the Spc105 protein has been shown to recruit Bub1 and Bub3 to the kinetochore (LONDON *et al.* 2012; SHEPPERD *et al.* 2012). Here, Mps1 phosphorylates Bub1, which in turn recruits the Mad1-Mad2 complex (LONDON and BIGGINS 2014). Mad1 at the kinetochore converts Mad2 into an active conformation (DE ANTONI *et al.* 2005), and active Mad2 assembles with Mad3, Bub3, and Cdc20 into the mitotic checkpoint complex (MCC) (SUDAKIN *et al.* 2001). Formation of the MCC effectively sequesters Cdc20, an activator of the anaphase promoting complex (APC). The APC is an E3 ubiquitin ligase that induces anaphase onset by targeting key mitotic regulators for degradation (reviewed in PINES 2011). When all kinetochores are properly attached to spindle microtubules, the checkpoint "wait" signal is silenced and Cdc20 is free to activate the APC, which leads to degradation of cyclin B1 and securin. Degradation of securin relieves the inhibition on separase, such that it can cleave the cohesin holding sister chromatids together, allowing cells to proceed into anaphase.

Correction of aberrant kinetochore-microtubule attachments by Aurora B

In addition to monitoring for detached kinetochores, cells must also correct erroneous kinetochore-microtubule attachments (Figure 1.1C). In budding yeast, errors can occur in the form of syntelic attachments, where both sister kinetochores are attached to microtubules emanating from the same pole. In organisms where kinetochores attach to a K-fiber containing multiple microtubules, merotelic attachments can also occur. Here, a single kinetochore is attached to microtubules emanating from both poles. The conserved Aurora B kinase plays a crucial role in the resolution of aberrant kinetochore-microtubule attachments (reviewed in LIU and LAMPSON 2009). Aurora B localizes to the inner centromere, where it phosphorylates many targets at the kinetochore (CALDAS *et al.* 2013; CHEESEMAN *et al.* 2002; DELUCA *et al.* 2006; PINSKY *et al.* 2003; SHANG *et al.* 2003; WELBURN *et al.* 2010). It is generally thought that phosphorylation of these targets destabilizes erroneous kinetochore-microtubule attachments, such that another attempt at proper attachments can be made (BIGGINS and MURRAY 2001; CIMINI *et al.* 2006; HAUF *et al.* 2003; PINSKY *et al.* 2006; TANAKA *et al.* 2002). Consistent with this hypothesis, Aurora B phosphorylation of several purified kinetochore components results in decreased microtubule-binding activity (CHEESEMAN *et al.* 2006; CIFERRI *et al.* 2008; GESTAUT *et al.* 2008; WANG *et al.* 2008). However, the mechanism by which Aurora B promotes detachment *in vivo* remains unclear.

The current prevailing model suggests that Aurora B corrects syntelic attachments by destabilizing linkages that are not under tension (Figure 1.1C) (BIGGINS and MURRAY 2001; CANE *et al.* 2013; NICKLAS and KOCH 1969; TANAKA *et al.* 2002). In mutants that are defective in kinetochore tension, Aurora B can generate unattached kinetochores and prevent satisfaction of the spindle assembly checkpoint (PINSKY *et al.* 2006). Two models have been proposed to

explain how Aurora B senses the lack of tension. In the "spatial separation model," tension exerted by biorientation pulls kinetochore targets away from Aurora B localized to the inner centromere (LIU *et al.* 2009; TANAKA *et al.* 2002). This permits dephosphorylation of these targets by PP1 phosphatase, which in turn stabilizes microtubule attachments. The spatial separation model is dependent on inter-kinetochore stretching, an increased separation between sister kinetochores connected by elastic centromeric chromatin (LIU *et al.* 2009; WELBURN *et al.* 2010). Recent findings suggest, however, that cells can still discriminate between correct and incorrect attachments if Aurora B is ectopically targeted to microtubules instead of the inner centromere (CAMPBELL and DESAI 2013). In the second model, Aurora B is activated at kinetochores that do not generate sufficient tension. Here, Aurora B activity could be dependent on conformational changes within the kinetochore, and thus sensitive to intra-kinetochore stretching. This model is consistent with results from super-resolution microscopy experiments that demonstrate structural differences between kinetochores with and without tension (JOGLEKAR *et al.* 2009; MARESCA and SALMON 2009; WAN *et al.* 2009). The two Aurora B tension sensor models make different predictions on the positioning of active Aurora B relative to its kinetochore targets. Therefore, defining the effects of Aurora B on its various kinetochore substrates will be essential in understanding its ability to recognize aberrant microtubule attachments.

The role of Aurora B in error correction features additional layers of complexity in higher eukaryotes, where kinetochores attach to a bundle of microtubules (a K-fiber). While the tension-dependent models can explain how syntelic attachments are detected, it is still unclear how the cell senses merotelic attachments, which can generate nearly normal levels of tension (Figure 1.1C) (reviewed in GREGAN *et al.* 2011). Merotelic attachments are prevalent early in

mitosis, and the correction of these attachments depends in part on Aurora B (CIMINI *et al.* 2003; CIMINI *et al.* 2006; KNOWLTON *et al.* 2006). Although several models have been proposed, the mechanisms by which Aurora B detects and resolves merotelic attachments are still poorly understood. One model posits that merotelic attachments can be resolved by tuning the plus-end dynamics of the attached K-fiber microtubules (BAKHOUM *et al.* 2009). Evidence suggests that modulating microtubule dynamics may also be important in Aurora B-mediated correction of syntelic attachments in higher eukaryotes (LAMPSON *et al.* 2004). The extent to which this mechanism functions *in vivo* is unclear, since the strength of kinetochore-microtubule attachments also depends on microtubule tip dynamics (AKIYOSHI *et al.* 2010). Understanding the link between Aurora B and microtubule dynamics will require isolating the kinetochore and non-kinetochore components involved, and dissecting their response to regulation by Aurora B and/or tension.

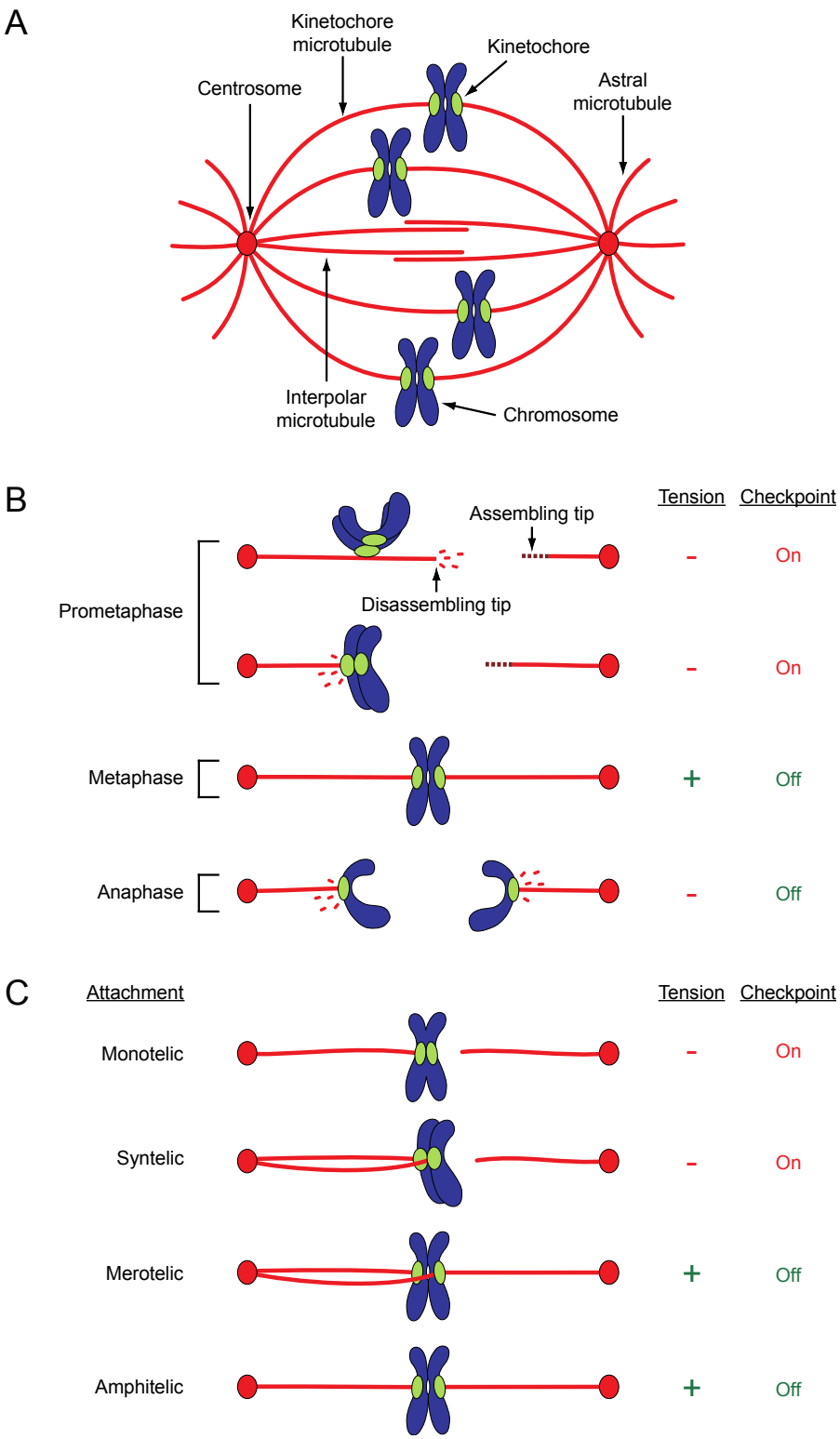

Figure 1.1 Kinetochore-microtubule attachments underlie chromosome movements during mitosis and are monitored by an error-correction system and the spindle assembly checkpoint
(*A*) Components of the mitotic spindle. (*B*) Kinetochore-microtubule attachments during various stages of mitosis. (*C*) Types of kinetochore-microtubule attachment errors. Figure adapted from ASBURY *et al.* (2011).

Chapter 2

Linker-scanning mutagenesis of the Ndc80 kinetochore protein

Introduction

Accurate chromosome segregation depends on the attachment between kinetochores and the dynamic plus-ends of spindle microtubules. This attachment requires the Ndc80 complex, an essential and conserved microtubule-binding component of the kinetochore. *In vivo*, inactivation or depletion of Ndc80 complex components leads to detached kinetochores and severe chromosome segregation defects (reviewed in KLINE-SMITH *et al.* 2005). Mirroring kinetochore-microtubule linkages *in vivo*, recent experiments show that attachments between purified Ndc80 complexes and microtubule tips can persist throughout rounds of microtubule growth and shortening, can withstand tensile forces, can modulate microtubule dynamics, and can respond to regulation by mitotic kinases (DELUCA *et al.* 2011; GUIMARAES *et al.* 2008; MILLER *et al.* 2008; POWERS *et al.* 2009; SCHMIDT *et al.* 2012; UMBREIT *et al.* 2012).

The Ndc80 complex (Figure 2.1) is a rod-shaped heterotetramer of Ndc80, Nuf2, Spc24, and Spc25 (JANKE *et al.* 2001; OSBORNE *et al.* 1994; WEI *et al.* 2005; WIGGE and KILMARTIN 2001). The two ends of the complex have globular domains, formed by Ndc80/Nuf2 and Spc24/Spc25, respectively. All four components of the complex are predicted to participate in coiled-coil interactions that link these two globular ends. Structural studies of the complex at atomic resolution have been limited to the two globular domains, revealing a microtubule-binding calponin homology domain in Ndc80 (CIFERRI *et al.* 2008; WEI *et al.* 2007; WEI *et al.* 2006).

These structural studies on the globular ends of the Ndc80 complex have provided high-resolution views of key protein-protein interfaces (ALUSHIN *et al.* 2010; MALVEZZI *et al.* 2013;

NISHINO *et al.* 2013). Together, they help explain how the Ndc80 complex plays a central role in kinetochore function by physically linking spindle microtubules to centromere-proximal kinetochore components. However, genetic and biochemical studies have suggested additional roles for the Ndc80 complex during mitosis. For example, mutations in *NDC80* result in mislocalization of kinetochore- and microtubule-associated proteins, such as the Dam1 complex and Stu2 in yeast (HE *et al.* 2001; JANKE *et al.* 2002). It is still unknown how the Ndc80 complex interacts with many of its proposed binding partners, and much of the complex is composed of long coiled-coil elements that have not been amenable to structural characterization. To identify the functionally important regions within Ndc80, we employed an unbiased linker-scanning mutagenesis screen. This screen utilizes short insertions at random positions within a protein to determine putative functional domains. Previous applications of linker-scanning mutagenesis have been successful in generating mutants to examine cohesin complex formation and Cre recombinase activity, and to map the Rab8A interaction interface on JFC1 (MILUTINOVICH *et al.* 2007; PAJUNEN *et al.* 2007; PETYUK *et al.* 2004). Here, we comprehensively covered *NDC80* with 15-bp insertions at random positions, and the resulting mutant library was screened for viability in a red/white plasmid shuffle assay. High-throughput Illumina sequencing showed that lethal mutations fell into clusters, revealing several regions of Ndc80 that are essential for its function. These include the microtubule-binding domain, the helical hairpin, the tetramerization domain, and previously uncharacterized segments. Our approach, which couples unbiased mutagenesis to high-throughput sequencing, can be generally applied to reveal new functional domains of proteins in *S. cerevisiae*.

Materials and methods

Media

The compositions of YPD (yeast peptone dextrose-rich) and SD (synthetic dextrose minimal) media were previously described (BURKE *et al.* 2000). YPD-NAT medium is YPD with 25 μg/ml clonNAT (Werner BioAgents). SD-lys medium was described previously (NGUYEN *et al.* 1998). SD-ura low ade is SD medium containing 100 μg/ml tryptophan, 0.1% casamino acids, and 5 μg/ml adenine.

Plasmids

All plasmids used in this study are listed in Table 2.1. QuikChange Lightning site-directed mutagenesis (Stratagene) was used to construct plasmids containing mutations in *NDC80*.

Strains

All yeast strains used in this study were derived from W303 and are listed in Table 2.2. To make the strain used in the linker-scanning mutagenesis screen, JTY5-5C, the endogenous copy of *NDC80* was deleted by PCR amplifying a *NatMX* cassette from pKG9 using primers with homology to the flanking DNA of *NDC80.* The deletion cassette was then transformed into the diploid strain JTY1 and selected for on YPD-NAT to generate JTY4. The deletion was checked by PCR to ensure replacement of *NDC80* with the cassette. JTY4 was transformed with the '*ADE3* plasmid' (pJT12) containing *ADE3 LYS2 NDC80*, and selected for on SD-lys. The transformants were sporulated and dissected to obtain JTY5-5C.

Linker-scanning mutagenesis

A 'target plasmid' (pJT36) was constructed containing the wild-type *NDC80* gene (including 245 upstream and 299 downstream base pairs), the ampicillin resistance gene, and the *URA3* gene for selection. Importantly, this plasmid did not contain a *Not*I recognition sequence. Using the MuA transposase, an artificial transposon was inserted at a random location within the target plasmid (Finnzymes). Transposition efficiency was kept low so that, on average, each plasmid would only contain one transposon insertion. The transposon contains a kanamycin resistance gene flanked by the 8 bp *Not*I recognition sequence. Plasmids that contained a transposon were isolated by selection on kanamycin. These plasmids were then cut with *Not*I to remove the kanamycin cassette and then re-ligated. The resulting 'transposition library' contained plasmids that each have 15 bp inserted at a random location. Each 15-bp insertion contained 5 bp of duplicated target sequence and the *Not*I recognition sequence.

Red/white plasmid shuffle screen

To identify lethal insertions in *NDC80*, the transposition library was screened in *S. cerevisiae* using a red/white plasmid shuffle system (DAVIS 1992; MULLER 1996). This screen was carried out in the strain JTY5-5C (*ade2-1oc ade3*Δ*-100 ura3-1 ndc80*Δ*::NatMX*), transformed with pJT12 (*NDC80 ADE3* in a 2 μm vector). In an *ade2-1oc ade3*Δ*-100* background, yeast containing this *ADE3* plasmid produce a red pigment when grown on low adenine plates (BENDER and PRINGLE 1991). The transposition library was transformed into this strain and selected for growth on SD–ura low ade plates at 37˚C. Insertions that abolish the function of *NDC80* are lethal and render cells dependent on the *ADE3* plasmid with the wild-type copy of *NDC80* for survival. Therefore, lethal mutations can be identified as those that yield solid red colonies. Insertions that do not disrupt the function of *NDC80* have no effect on

cell viability, making the *ADE3* plasmid extraneous. These colonies have a sectored appearance — red in the center and white around the edges where the *ADE3* plasmid was lost. Non-sectored red colonies, containing lethal mutations, were isolated and their plasmid DNA was extracted for Illumina sequencing.

We determined that the false positive rate of the red/white plasmid shuffle screen is less than 0.3%. This was accomplished by transforming JTY5-5C [pJT12] with a plasmid containing wild-type *NDC80* (pJT36) and counting the number of non-sectoring colonies. These false positives therefore represent colonies that were solid red despite the presence of a second wild-type copy of the gene. The representative lethal insertions selected for characterization (see below) were also re-tested in the red/white plasmid shuffle assay. JTY5-5C [pJT12] cells transformed with plasmids containing these insertions were confirmed to not sector.

To obtain temperature-sensitive mutants, all 959 non-sectored red colonies (assayed at 37˚C) were spotted onto SD–ura low ade plates and grown at 25˚C. Colonies that sectored well (compared to a wild-type *NDC80* control) were isolated, and their plasmid DNA was extracted for traditional sequencing. Temperature-sensitive mutants with insertions that clustered around the 1400 bp region of *NDC80* were selected for further analysis (Table 2.4). Mutations were cloned into an integrating plasmid (pRS306) and integrated at the endogenous *NDC80* locus. To perform a spontaneous suppressor screen, cultures of *ndc80-121* (JTY8, ~5 x 10^8 cfu total) were plated on YPD at 36˚C. Colonies that grew were isolated and sequenced for *NDC80* and *NUF2*.

Illumina sequencing

Illumina sequencing was used to determine the coverage of insertions in the transposition library, and to identify the location of each lethal insertion obtained from the solid red colonies. Using the Expand Long Template PCR System (Roche), *NDC80* was amplified both from the

transposition library and the pooled lethal mutants. In this PCR, primers were designed to specifically amplify the mutant alleles from the transposition library plasmids and not *NDC80* from the *ADE3* plasmid (Appendix A, Table S3). Single-end Illumina libraries were prepared from PCR products that were sheared to an average size of 500 bp by sonication. The sheared DNA ends were repaired using the End-It DNA Repair kit (Epicentre), and A-tailed for ligation of adaptors (Appendix A, Table S3). The products were size-selected (250-350 bp) and enriched by PCR using the primers presented in Appendix A, Table S3. Unique 6-bp indices on the PCR primers permitted multiplexed Illumina sequencing to distinguish between products from the transposition library and the pooled lethal mutants. One sequencing run of the transposition library and both sequencing runs of the lethal insertion subsets were alternatively prepared using the TruSeq DNA Sample Preparation v2 Kit. Briefly, PCR products were sheared to an average size of 500 bp using a Covaris S213. The sheared DNA ends were repaired and adenylated using the TruSeq protocol. Adapters AD002, AD018, and AD019 (Appendix A, Table S3) were ligated onto the transposition library sample and the two lethal insertion subset samples, respectively. The products were size-selected (400-500 bp) and enriched by PCR using the TruSeq PCR Master Mix. All sequencing was performed on an Illumina Genome Analyzer II, to obtain 36-bp single reads. Sequencing results are provided in Appendix A, Table S4.

Custom programs (Alex Zelter) were used to analyze the FASTQ files for each Illumina sequencing run. The 36-bp reads were queried for the *Not*I recognition sequence; for each hit, the position of the *Not*I sequence within the read was recorded. The sequences flanking each *Not*I insertion were then aligned to the *NDC80* gene using mrsFAST (HACH *et al.* 2010) to determine the position of the insertion in *NDC80*. Read coverage was obtained by aligning all reads (with and without *Not*I) to *NDC80* using mrsFAST. Each 15-bp insertion was also

translated to determine the protein sequence of the five inserted amino acids. See Table 2.3 for examples of insertion positions, resulting sequences, and the translated insertion residues.

We selected representative mutations from each lethal insertion cluster for further analysis. Each mutation represents the insertion with one of the highest number of *Not*I reads in the cluster. For further characterization, we required that each insertion was lethal at both the screening temperature of 37˚C and additionally 24˚C. Based on these criteria, we selected ins506, ins656, ins839, ins940, ins1148, ins1687, and ins1957 (Table 2.3) for further analysis.

Coiled-coil prediction and sequence alignment of Ndc80

The probabilities of coiled-coil formation for wild-type and mutant Ndc80 were predicted using Paircoil2 (MCDONNELL *et al.* 2006). To perform sequence alignments, *NDC80* from *S. cerevisiae* and its orthologs in *Saccharomyces bayanus*, *Saccharomyces kudriavzevii*, *Saccharomyces mikatae* (SCANNELL *et al.* 2011) and *Lachancea (Kluyveromyces) thermotolerans*, *Kluyveromyces lactis* and *Debaryomyces hansenii* (http://genolevures.org) were translated using Transeq (RICE *et al.* 2000) and then aligned using Clustal-O (BLACKSHIELDS *et al.* 2010). The similarity score was plotted for each position using Plotcon (RICE *et al.* 2000) with a window size of 21 bp.

Protein expression and purification

Recombinant *S. cerevisiae* Ndc80 and Dam1 complexes were expressed and purified as previously described (ASBURY *et al.* 2006; MIRANDA *et al.* 2005; POWERS *et al.* 2009; WEI *et al.* 2005).

Immunoprecipitation

JTY29-1C (*NUF2-TAP*) and JTY47-2B (*SPC24-TAP*) were transformed with plasmids encoding wild-type or mutant *GFP-NDC80* (Table 2.1) and selected for growth on SD-ura at 24˚C. Controls for the immunoprecipitation include JTY29-1C and JTY47-2B transformed with pRS316, as well as JTY29-1B (*NUF2*) and JTY47-2A (*SPC24*) transformed with a wild-type *GFP-NDC80* plasmid. Cells were grown to ~100 Klett units in 50 ml SD-ura at 24˚C, washed with dH_2O, and the pellets were frozen in liquid nitrogen. Pellets were resuspended in 500 µl lysis buffer (20 mM HEPES, pH 7.4, 300 mM NaCl, 100 µM GTP, 1 mM $MgCl_2$, 1 mM dithiothreitol, 4 µg/ml pepstatin, 4 µg/ml leupeptin, 4 µg/ml aprotinin, 4 µg/ml chymostatin, 1 mM phenylmethanesulfonyl fluoride, 1 mM sodium pyrophosphate, 1 mM sodium fluoride, 1 mM β-glycerophosphate, 5% glycerol) and vortexed with ice-cold glass beads in 1 min intervals until >60% of cells were lysed. Triton X-100 was added to 0.5% and lysates were cleared by centrifugation at 18,000 x *g* for 20 min at 4˚C. An aliquot (50 µl) of 60 mg/ml Dynabeads (Invitrogen) conjugated with rabbit IgG (MP Biomedicals) was added to the clarified lysate and incubated for 30 min at 4˚C. Beads were then washed with 150 µl of wash buffer (20 mM HEPES, pH 7.4, 200 mM NaCl, 100 µM GTP, 1 mM $MgCl_2$, 5% glycerol) three times and resuspended in 50 µl of SDS-PAGE sample buffer.

For immunoprecipitation of Nuf2-TAP from *ndc80-121* cultures, 2 L of JTY30-1A (*ndc80-121 NUF2-TAP*) cells were grown to ~100 Klett units in YPD at 25˚C. JTY30-4A (*NDC80 NUF2-TAP*) cells served as a wild-type control. Cultures were shifted to 37˚C for 100 min and harvested by centrifugation. Pellets were cryogenically ground into cell dust using a PM100 (Retsch) and stored at -80˚C, as per the protocol from the Rout laboratory (http://lab.rockefeller.edu/rout/assets/file/protocols). For each condition, 4 g of cell dust were

resuspended in lysis buffer (as above, with 0.5% Triton X-100), homogenized, and cleared by centrifugation at 2000 x *g* for 10 min at 4˚C. An aliquot (250 µl) of 60 mg/ml Dynabeads (Invitrogen) conjugated with rabbit IgG (MP Biomedicals) was added to the clarified lysate and incubated for 30 min at 4˚C. Beads were then washed three times with 150 µl of wash buffer (20 mM HEPES, pH 7.4, 200 mM NaCl, 100 µM GTP, 1 mM $MgCl_2$, 1 mM dithiothreitol, 4 µg/ml pepstatin, 4 µg/ml leupeptin, 4 µg/ml aprotinin, 4 µg/ml chymostatin, 1 mM phenylmethanesulfonyl fluoride, 1 mM sodium pyrophosphate, 1 mM sodium fluoride, 1 mM β-glycerophosphate, 5% glycerol), washed once with 150 µl of TEV buffer (40 mM HEPES, pH 7.4, 200 mM NaCl, 2 mM $MgCl_2$, 1 mM EDTA, 1 mM dithiothreitol, 1 mM GTP, 5% glycerol), and resuspended in 100 µl TEV buffer. TEV was added to 67 nM and the reaction was incubated for 2 hr at 4˚C. Trichloroacetic acid protein precipitation was performed on 60 µl of eluate after TEV cleavage. Immunoprecipitated proteins were identified by mass spectrometry and MudPIT analysis (performed by Bryan Fonslow, Yates laboratory, Scripps Research Institute).

Fluorescence microscopy

For live-cell imaging, JTY12-25A (*NUF2-mCherry NDC80*) was transformed with plasmids encoding wild-type or mutant *GFP-NDC80* (Table 2.1) and selected for growth on SD-ura at 24˚C. Cells were mounted for microscopy as previously described (MULLER *et al.* 2005). Images of cells were taken at a single focal plane, binned 1x1, using a DeltaVision system (Applied Precision) equipped with an IX70 inverted microscope (Olympus), an U Plan Apo 100x objective (1.35 NA), and a CoolSnap HQ digital camera (Photometrics). Exposures were 0.4 s for both GFP and mCherry. Images were processed as previously described (SHIMOGAWA *et al.*

2010) using custom Matlab programs to isolate and quantify the fluorescence intensities of GFP and mCherry spots.

To assay for chromosome biorientation, *CEN3* was visualized using LacI-GFP bound to a LacO-array adjacent to the centromere (Table 2.2). LacI-GFP is under control of the *pCUP1* promoter and imaged using uninduced conditions. For G1 synchronization, MAT**a** cells were grown to ~60 Klett units at 25˚C and arrested for 1.5 generations with α-factor. To release from the arrest, cells were collected by filtration, washed with 3 volumes of YPD, sonicated, and shifted to 37˚C medium. At 100 min after the release, ~100 µl of cells were centrifuged and resuspended in media made with yeast nitrogen base without copper (ForMedium). Cells were mounted for microscopy as previously described (MULLER *et al.* 2005), except that agarose pads were made with yeast nitrogen base without copper (ForMedium). Images were taken with 7 z-sections spanning 4.2 µm, binned 1x1, using the DeltaVision system (as above) equipped with a U Plan Apo 100x objective (1.35 NA). Exposures were 0.4 s for GFP and 0.3 s for mCherry.

For time-lapse imaging of synchronized cells, the CellAsic ONIX microfluidics system (Millipore) was used. For G1 synchronization, MAT**a** cells (Table 2.2) were grown to ~60 Klett units at 25˚C and arrested for a total of 1.5 generations with α-factor. One generation into the arrest, cells were briefly sonicated and 50 µl were loaded onto an Y04C CellAsic ONIX plate. The arrest was completed on the plate before releasing into media lacking α-factor. For metaphase arrests, cells with an auxin-inducible Cdc20 degron (Table 2.2) were grown to ~50 Klett units at 25˚C, arrested with 500 µM 3-indoleacetic acid (Sigma Aldrich) for 3 hours, and loaded onto an Y04C plate. All flow rates were at ~12 µl/hr. After completing the arrests, plate and objective heaters were raised to 37˚C (t = 0) and cells were imaged. Time-lapse images of cells were taken at 7.5 min intervals, with 3 z-sections spanning 2.4 µm, binned 1x1, using the

DeltaVision system (as above) equipped with a Plan Apo 60x objective (1.40 NA). Exposures were 0.1 s for GFP and 0.15 s for mCherry.

Total internal reflection fluorescence (TIRF) microscopy was performed with a custom illumination system constructed by modification of a commercial inverted microscope (Nikon Ti-U). Total internal reflection of 488 nm (Sapphire 488-100 CW, Coherent Inc.) and 561 nm (Sapphire 561-100 CW, Coherent Inc.) wavelength lasers was achieved using a through-the-objective arrangement with a 100x oil immersion 1.49 NA lens (Nikon CFI APO 100x Oil TIRF NA 1.49 WD 0.12 mm). Simultaneous imaging of GFP and Alexa Fluor 568 was captured by two cooled EM CCD cameras (iXon+ DU897, Andor Technology). Flow cell channels were constructed using double-sided sticky tape (Scotch), sandwiched between a glass slide (Gold Seal) and silanized coverslip (Corning). To bind taxol-stabilized microtubules, a modified "rigor" kinesin (RICE *et al.* 1999) was flowed into the channel and bound non-specifically to the coverslip. The flow cell channel was washed with 50 µl BB80 (80 mM Pipes, 120 mM K^+, 1 mM MgCl2, 1 mM EGTA, 8 mg/ml BSA, pH 6.9) and 50 µl BB80T (BB80 with 10 µM taxol). Alexa Fluor 568-labeled microtubules diluted in BB80T were flowed in and allowed to bind for 5 min. The channel was washed once more with 50 µl BB80T. Proteins were then introduced, diluted in BB80T containing 0.1 mg/ml κ-casein, 200 µg/ml glucose oxidase, 35 µg/ml catalase, 25 mM glucose, and 5 mM dithiothreitol. GFP-tagged Ndc80 complex was assayed at 50 pM to resolve single molecules, and untagged Dam1 complex was added at 2.5 nM. Flow cell channels were sealed with nail polish and immediately imaged for 1,500 frames at 10 frames per second. Software analysis of TIRF microscopy data was performed using custom software in Labview (National Instruments) and Igor Pro (WaveMetrics).

Cross-linking of recombinant Ndc80 complex

Cross-linking experiments were performed by Alex Zelter, as previously described (ZELTER *et al.* 2010). Briefly, recombinant Ndc80 complex was cross-linked for 2 min with disuccinimidyl suberate (Rockfold) and quenched with NH_4HCO_3. Cross-linked proteins were reduced with dithiothreitol, alkylated with iodoacetamide, and digested with trypsin. Cross-link peptides were identified by mass spectrometry.

Table 2.1 Plasmids used in this study

Plasmid	Relevant markers	Reference
pRS316	*CEN6 ARSH4 URA3 Amp^r* f1 origin	(SIKORSKI and HIETER 1989)
pRS306	*URA3 Amp^r* f1 origin	(SIKORSKI and HIETER 1989)
pKG9	*NatMX*	(GREENLAND *et al.* 2010)
pJT12	*NDC80 ADE3 LYS2* in 2 μm vector	This study
pJT36	*NDC80* in pRS316	This study
pJT153	*GFP-NDC80* in pRS316	This study
pJT185	*ins506 GFP-ndc80* in pRS316	This study
pJT187	*ins656 GFP-ndc80* in pRS316	This study
pJT188	*ins839 GFP-ndc80* in pRS316	This study
pJT189	*ins940 GFP-ndc80* in pRS316	This study
pJT190	*ins1148 GFP-ndc80* in pRS316	This study
pJT154	*ins1687 GFP-ndc80* in pRS316	This study
pJT155	*ins1957 GFP-ndc80* in pRS316	This study
His_6-Spc24/Spc25 expression plasmid	*His_6-SPC24/SPC25* dicistron, *Kan^r*	(WEI *et al.* 2005)
Ndc80/Nuf2-GFP expression plasmid	*NDC80/NUF2-GFP* dicistron, *Amp^r*	(POWERS *et al.* 2009)
Ndc80/Nuf2 expression plasmid	*NDC80/NUF2* dicistron, *Amp^r*	(POWERS *et al.* 2009)
pJT138	*ins506 ndc80/NUF2-GFP* dicistron, *Amp^r*	This study
pJT139	*ins511 ndc80/NUF2-GFP* dicistron, *Amp^r*	This study
pJT140	*ins656 ndc80/NUF2-GFP* dicistron, *Amp^r*	This study
pJT141	*ins839 ndc80/NUF2-GFP* dicistron, *Amp^r*	This study
pJT142	*ins940 ndc80/NUF2-GFP* dicistron, *Amp^r*	This study
pJT143	*ins1148 ndc80/NUF2-GFP* dicistron, *Amp^r*	This study
pJT145	*ins1687 ndc80/NUF2-GFP* dicistron, *Amp^r*	This study
pJT146	*ins1957 ndc80/NUF2-GFP* dicistron, *Amp^r*	This study
pJT106	*ndc80-121/NUF2* dicistron, *Amp^r*	This study
pJT113	*ndc80(Y465C)* in pRS306	This study
pJT114	*ndc80(I469Q)* in pRS306	This study
pJT112	*ndc80(S467A S468A)* in pRS306	This study
pJT116	*ndc80(S467D S468D)* in pRS306	This study
pJT115	*ndc80(D466G)* in pRS306	This study
pJT105	*ndc80-121* in pRS306	This study

Table 2.2 Yeast strains used in this study

Strain	Genotype	Reference
W303	*ade2-1oc can1-100 his3-11,15 leu2-3,112 trp1-1 ura3-1*	
CRY1	MAT**a** *ade2-1oc can1-100 his3-11,15 leu2-3,112 trp1-1 ura3-1*	
JTY1	MAT**a**/α *ade2-1oc/ade2-1oc ade3Δ-100/ade3Δ-100 can1-100/can1-100 his3-11,15/his3-11,15 leu2-3,112/leu2-3,112 lys2Δ::HIS3/lys2Δ::HIS3 trp1-1/trp1-1 ura3-1/ura3-1*	This study
JTY4	MAT**a**/α *ade2-1oc/ade2-1oc ade3Δ-100/ade3Δ-100 can1-100/can1-100 his3-11,15/his3-11,15 leu2-3,112/leu2-3,112 lys2Δ::HIS3/lys2Δ::HIS3 trp1-1/trp1-1 ura3-1/ura3-1 NDC80/ndc80Δ::NatMX*	This study
JTY5-5C	MAT**a** *ade2-1oc ade3Δ-100 can1-100 his3-11,15 leu2-3,112 lys2Δ::HIS3 trp1-1 ura3-1 ndc80Δ::NatMX* [pJT12]	This study
JTY12-25A	MAT**a** *ade2-1oc ade3Δ-100 can1-100 his3-11,15 leu2-3,112 trp1-1 ura3-1 NDC80 NUF2-mCherry::hphMX*	This study
JTY29-1B	MATα *ade2-1oc ade3Δ-100 can1-100 his3-11,15 leu2-3,112 trp1-1 ura3-1 NUF2*	This study
JTY29-1C	MATα *ade2-1oc ade3Δ-100 can1-100 his3-11,15 leu2-3,112 trp1-1 ura3-1 NUF2-TAP::KanMX*	This study
JTY47-2A	MATα *ade2-1oc ade3Δ-100 can1-100 his3-11,15 leu2-3,112 trp1-1 ura3-1 SPC24*	This study
JTY47-2B	MAT**a** *ade2-1oc ade3Δ-100 can1-100 his3-11,15 leu2-3,112 trp1-1 ura3-1 SPC24-TAP::KanMX*	This study
JTY14	MAT**a** *ade2-1oc ade3Δ-100 can1-100 his3-11,15 leu2-3,112 lys2Δ::HIS3 trp1-1 ura3-1 ndc80(Y465C)*	This study
JTY23	MAT**a** *ade2-1oc ade3Δ-100 can1-100 his3-11,15 leu2-3,112 lys2Δ::HIS3 trp1-1 ura3-1 ndc80(I469Q)*	This study
JTY13	MAT**a** *ade2-1oc ade3Δ-100 can1-100 his3-11,15 leu2-3,112 lys2Δ::HIS3 trp1-1 ura3-1 ndc80(S467A S468A)*	This study
JTY17	MAT**a** *ade2-1oc ade3Δ-100 can1-100 his3-11,15 leu2-3,112 lys2Δ::HIS3 trp1-1 ura3-1 ndc80(S467D S468D)*	This study
JTY18	MAT**a** *ade2-1oc ade3Δ-100 can1-100 his3-11,15 leu2-3,112 lys2Δ::HIS3 trp1-1 ura3-1 ndc80(D466G)*	This study
JTY8	MAT**a** *ade2-1oc ade3Δ-100 can1-100 his3-11,15 leu2-3,112 lys2Δ::HIS3 trp1-1 ura3-1 ndc80-121*	This study
JTY83	MAT**a** *ade2-1oc ade3Δ-100 can1-100 his3-11,15 leu2-3,112 lys2Δ::HIS3 trp1-1 ura3-1 ndc80-125*	This study
JTY84	MAT**a** *ade2-1oc ade3Δ-100 can1-100 his3-11,15 leu2-3,112 lys2Δ::HIS3 trp1-1 ura3-1 ndc80-121 NUF2-101*	This study
JTY30-4A	MAT**a** *ade2-1oc ade3Δ-100 can1-100 his3-11,15 leu2-3,112 trp1-1 ura3-1 NUF2-TAP::KanMX NDC80*	This study
JTY30-1A	MAT**a** *ade2-1oc ade3Δ-100 can1-100 his3-11,15 leu2-3,112 trp1-1 ura3-1 NUF2-TAP::KanMX ndc80-121*	This study

Continued on next page

Strain	Genotype	Reference
MSY141-16D	MAT**a** *ade2-1oc ade3Δ-100 can1-100 his3-11,15 leu2-3,112 trp1-1 ura3-1 mad1Δ::URA3 NDC80*	(SHIMOGAWA *et al.* 2006)
JTY26-11C	MAT**a** *ade2-1oc ade3Δ-100 can1-100 his3-11,15 leu2-3,112 trp1-1 ura3-1 SPC110-mCherry::hphMX mad1Δ::URA3 ndc80-121*	This study
JTY9-4A	MAT**a** *ade2-1oc ade3Δ-100 can1-100 his3-11,15 leu2-3,112 trp1-1 ura3-1 URA3::TUB1-GFP SPC110-mCherry::hphMX NDC80*	This study
JTY9-10D	MAT**a** *ade2-1oc ade3Δ-100 can1-100 his3-11,15 leu2-3,112 lys2Δ::HIS3 trp1-1 ura3-1 URA3::TUB1-GFP SPC110-mCherry::hphMX ndc80-121*	This study
JTY10-11C	MAT**a** *ade2-1oc ade3Δ-100 can1-100 his3-11,15 leu2-3,112 lys2Δ::HIS3 trp1-1 ura3-1 MTW1-GFP::HIS3 SPC110-mCherry::hphMX NDC80*	This study
JTY10-3C	MAT**a** *ade2-1oc ade3Δ-100 can1-100 his3-11,15 leu2-3,112 lys2Δ::HIS3 trp1-1 ura3-1 MTW1-GFP::HIS3 SPC110-mCherry::hphMX ndc80-121*	This study
JTY11-5A	MAT**a** *ade2-1oc ade3Δ-100 can1-100 his3-11,15 leu2-3,112 trp1-1 ura3-1 NUF2-GFP::HIS3 SPC110-mCherry::hphMX NDC80*	This study
JTY11-16A	MAT**a** *ade2-1oc ade3Δ-100 can1-100 his3-11,15 leu2-3,112 trp1-1 ura3-1 NUF2-GFP::HIS3 SPC110-mCherry::hphMX ndc80-121*	This study
JTY58-5D	MAT**a** *ade2-1oc ade3Δ-100 can1-100 his3-11,15 leu2-3,112 trp1-1 ura3-1 NDC10-GFP::KanMX SPC110-mCherry::hphMX NDC80*	This study
JTY58-1C	MAT**a** *ade2-1oc ade3Δ-100 can1-100 his3-11,15 leu2-3,112 trp1-1 ura3-1 NDC10-GFP::KanMX SPC110-mCherry::hphMX ndc80-121*	This study
JTY59-12D	MAT**a** *ade2-1oc ade3Δ-100 can1-100 his3-11,15 leu2-3,112 lys2Δ::HIS3 trp1-1 ura3-1 STU2-GFP::NatMX SPC110-mCherry::hphMX NDC80*	This study
JTY59-7A	MAT**a** *ade2-1oc ade3Δ-100 can1-100 his3-11,15 leu2-3,112 lys2Δ::HIS3 trp1-1 ura3-1 STU2-GFP::NatMX SPC110-mCherry::hphMX ndc80-121*	This study
JTY73-17C	MAT**a** *ade2-1oc ade3Δ-100 can1-100 his3-11,15 leu2-3,112 lys2Δ::HIS3 trp1-1 ura3-1 STU2-GFP::NatMX SPC110-mCherry::hphMX CDC20-AID::KanMX ura3::pADH1-OsTIR1-9myc::URA3 NDC80*	This study
JTY73-2A	MATα *ade2-1oc ADE3 can1-100 his3-11,15 leu2-3,112 trp1-1 ura3-1 STU2-GFP::NatMX SPC110-mCherry::hphMX CDC20-AID::KanMX ura3::pADH1-OsTIR1-9myc::URA3 ndc80-121*	This study
JTY78-12A	MATα *ade2-1oc ade3Δ-100 can1-100 his3-11,15 leu2-3,112 lys2Δ::HIS3 trp1-1 ura3-1 NUF2-GFP::HIS3 SPC110-mCherry::hphMX CDC20-AID::KanMX ura3::pADH1-OsTIR1-9myc::URA3 NDC80*	This study
JTY78-13D	MAT**a** *ade2-1oc ADE3 can1-100 his3-11,15 leu2-3,112 trp1-1 ura3-1 NUF2-GFP::HIS3 SPC110-mCherry::hphMX CDC20-AID::KanMX ura3::pADH1-OsTIR1-9myc::URA3 ndc80-121*	This study
MMWY61#2	MAT**a** *ade2-1oc ade3Δ-100 can1-100 his3-11,15 leu2-3,112 trp1-1 ura3-1 pCUP1-GFP 12LacI12::HIS3 CEN3-LacO33array::KanMX SPC110-mCherry::hphMX NDC80*	(WARGACKI *et al.* 2010)
JTY65-16B	MAT**a** *ade2-1oc ade3Δ-100 can1-100 his3-11,15 leu2-3,112 trp1-1 ura3-1 pCUP1-GFP 12LacI12::HIS3 CEN3-LacO33array::KanMX SPC110-mCherry::hphMX ndc80-121*	This study

Results

Construction of the linker-scanning transposition library

To discover new functional domains in the Ndc80 kinetochore protein (Figure 2.1), I performed a saturating screen that combined linker-scanning mutagenesis with a plasmid shuffle colorimetric assay and high-throughput sequencing. I first constructed a transposition library using an artificial transposition system (Figure 2.2A; Materials and methods). This library contains a collection of plasmids, each with a single 15-bp insertion at a random location, corresponding to a five-amino acid insertion in the translated protein product. The *NDC80* transposition library was generated from ~11,000 transposition events on a 7.4-kb plasmid, which includes the 2.1-kb *NDC80* gene. Each 15-bp insertion contained the 8-bp *Not*I recognition sequence, which was used to identify the position of the insertion within the gene.

Insertion coverage of the *NDC80* gene was determined by Illumina sequencing (Figure 2.3A-D and Appendix A, Figure S1). From three independent sequencing runs, I determined that transpositions targeted 1074 unique positions on *NDC80*, corresponding to 52% coverage of the 2076-bp gene (see Appendix A, Table S4 for a summary of the sequencing study). Furthermore, insertions were spread evenly across *NDC80*, with an average of 10.8 insertions per 21-bp window across the entire gene (Figure 2.3D, right plot). From the 1074 insertion positions identified in the library, the translated protein sequences were determined. The frame of each insertion and its surrounding wild-type *NDC80* sequence ultimately dictates the identity of the amino acids inserted into the protein (Appendix A, Figure S2A). By experimental design, the insertions did not introduce stop codons and were always 15 bp long to prevent frame shifts in the resulting coding sequence (Appendix A, Figure S2A). The transposition library contained insertions at 444 unique codons, resulting in 64% coverage of the

691-amino acid Ndc80 protein. Of these insertions, 30% were in frame 1, 26% were in frame 2, and 44% were in frame 3 (Appendix A, Figure S2B). The transposition library was then screened in *S. cerevisiae* to identify mutations that disrupt the function of Ndc80.

Linker-scanning mutagenesis screen of Ndc80

A red/white plasmid shuffle system (DAVIS 1992; MULLER 1996) was used to screen the transposition library for insertions detrimental to the function of *NDC80* in *S. cerevisiae* (Figure 2.2B). In this screen, colonies containing library plasmids with lethal mutations in *NDC80* do not sector and are solid red (see Materials and methods). I screened 25,439 total colonies and isolated 959 red colonies (4%). These red colonies were pooled and the positions of the insertions were determined by Illumina sequencing (Appendix A, Table S4). Illumina sequencing was performed in collaboration with Maitreya Dunham's and Jay Shendure's laboratories (Department of Genome Sciences), with assistance from Celia Payen, Kimberly Fong, and Charlie Lee. Data analysis included use of custom programs by Alex Zelter. Lethal insertions were found at 336 unique positions in 162 unique codons of *NDC80*, corresponding to 16% coverage of the gene and 23% of the protein. Unlike the transposition library, in which insertions were found evenly spread throughout the *NDC80* gene, plasmids isolated from the red colonies contained insertions that mapped to distinct clusters (Appendix A, Figure S1). This was most evident on a coverage density map, showing the number of lethal insertions in 21-bp windows across *NDC80* (Figure 2.3D). A stretch of lethal insertions was defined as a cluster if four or more insertions per 21-bp window were lethal (Figure 2.3D). In several windows within these clusters, every single insertion present in the transposition library was lethal. Surprisingly, lethal insertions were not enriched in any particular frame relative to the transposition library (Appendix A, Figure S2B). Furthermore, each of the three frames was well represented in all of

the clusters identified (Appendix A, Figure S2C). These results suggest that the position of the insertion, rather than the identity of the residues, was most important in disrupting the function of Ndc80.

To verify that the clusters identified in the screen are not a result of random sampling, I divided the non-sectoring red colonies into two random pools. When sequenced independently (Appendix A, Table S4), both subsets had the same lethal insertion clusters as the original pool (Appendix A, Figure S3), indicating that the starting transposition library was comprehensively screened. Overall, this screen demonstrates that five-amino acid insertions are tolerated throughout most of Ndc80 without disrupting its function. I did not identify lethal insertions in the putative "loop" (Figure 2.3A, blue bar), nor in a segment of Ndc80 that is disordered based on the human Ndc80 globular domain crystal structure (Figure 2.3A, black bar) (CIFERRI *et al.* 2008). No lethal insertion clusters were found in the 113-amino acid N-terminal tail of Ndc80, which is dispensable in *S. cerevisiae* (AKIYOSHI *et al.* 2009; KEMMLER *et al.* 2009). Likewise, there were no lethal insertion clusters in the last ~30 amino acid residues of Ndc80, consistent with the viability of the *ndc80-1* temperature-sensitive allele, which contains a frame-shift mutation that alters the last 18 amino acids of the protein (WIGGE *et al.* 1998).

From the lethal insertion clusters identified in the linker-scanning mutagenesis screen, I selected representative mutations for further analysis. These lethal insertions will be referred to as, for example, "ins506" to indicate that the first position of the insertion is nucleotide 506 of the mutant allele. A representative insertion from each cluster was independently verified to be lethal (see Materials and methods). Insertions from the cluster around nucleotide 1400 of *NDC80* were found to be temperature sensitive; six insertions from this cluster, ranging from nucleotide 1380 to 1406, were lethal at 37˚C but not 24˚C. This cluster will be described

separately below. Here, I selected a total of seven representative mutations from the remaining lethal insertion clusters for analysis (Table 2.3). I first tested if these mutations perturb protein expression or assembly of Ndc80 into a heterotetrameric complex. *In vivo*, all seven lethal insertion mutant alleles were expressed (Figure 2.3E). In these cells, the endogenous wild-type copy of *NDC80* was maintained for viability. A GFP tag on the mutant Ndc80 was used to distinguish it from the wild-type protein. Working with Neil Umbreit, we found that in a recombinant system, six of the seven mutant Ndc80 proteins co-purified as heterotetrameric complexes with Nuf2, Spc24, and Spc25 (Figure 2.3F). These results suggest that most of the insertions identified in this screen specifically disrupt the function of Ndc80 independent from protein production and folding.

Lethal insertions in the Ndc80 microtubule-binding domain

Two of the seven clusters of lethal insertions (represented by ins506 and ins656) are in the conserved microtubule-binding calponin homology (CH) domain (Figure 2.3A-D and Figure 2.4A). Based on homology to the human Ndc80 CH domain crystal structure (CIFERRI *et al.* 2008), these lethal insertion clusters map to helices αC and αG, respectively. Even though these helices are adjacent in the crystal structure, the two mutations had drastically different effects. Ndc80 containing the ins506 mutation was expressed *in vivo* (Figure 2.3E), but failed to assemble into a recombinant complex. Consistent with the conclusion that the position of the insertion is likely most important in disrupting the function of Ndc80, we found that the ins511 mutation, which overlaps ins506 by 10 bp but is in a different frame, also impairs assembly of Ndc80 into a recombinant complex. By contrast, we successfully purified ins656 Ndc80 complex, and further demonstrated that this complex binds microtubules *in vitro* (Figure 2.3F and Appendix A, Figure S4). Two additional clusters of lethal insertions (represented by ins839

and ins940) were found in a region of Ndc80 that folds into a helical hairpin (α H and α I) in the human crystal structure. The hairpin forms C-terminal to the Ndc80 CH domain and, together, they "sandwich" the globular domain of Nuf2 (CIFERRI *et al.* 2008). Both of these mutant complexes bound to microtubules *in vitro* (Appendix A, Figure S4). Furthermore, working in Charles Asbury's laboratory (Department of Physiology and Biophysics), I found that the ins839 mutation altered the behavior of single molecules of the Ndc80 complex on microtubules, increasing their residence time and slowing their diffusion as compared to the wild-type complex (Figure 2.4B and C). This observation suggests that although the hairpin is not part of the microtubule-binding interface, it indirectly affects the attachment between the Ndc80 complex and microtubules.

The ins1957 mutation in Ndc80 disrupts tetramerization of the Ndc80 complex

Localization of Ndc80 to the kinetochore depends on its assembly into an intact complex with Nuf2, Spc24, and Spc25. This complex is anchored to the kinetochore via interactions between Spc24/Spc25 and other components, such as the Mtw1 complex (DE WULF *et al.* 2003; HORNUNG *et al.* 2011; MASKELL *et al.* 2010; PETROVIC *et al.* 2010). From cross-linking and limited proteolysis experiments, it was proposed that the C-termini of Ndc80/Nuf2 contact Spc24/Spc25 to assemble the Ndc80 complex (CIFERRI *et al.* 2005; MAIOLICA *et al.* 2007; WEI *et al.* 2005). However, the proteins and residues involved in this putative tetramerization domain and the structural basis for assembly of the complex remain poorly understood.

My linker-scanning mutagenesis screen identified three lethal insertion clusters in previously uncharacterized regions of Ndc80 (represented by ins1148, ins1687, and ins1957). These regions are C-terminal to the CH domain, and all three representative mutant Ndc80 complexes bound microtubules similar to the wild-type complex (Appendix A, Figure S4). The

ins1687 and ins1957 mutations represent broad, neighboring clusters of lethal insertions that cover an area including the putative tetramerization domain. I screened these and the other representative mutations for defective kinetochore localization of Ndc80. Using fluorescence microscopy, I measured the amount of GFP-tagged mutant Ndc80 that co-localized with Nuf2-mCherry at kinetochores (Figure 2.5A and B). The ins656, ins839, ins940, ins1148, and ins1687 mutant GFP-Ndc80 proteins co-localized with Nuf2-mCherry, indicating that these insertions do not disrupt formation of the Ndc80 complex or its association with the kinetochore *in vivo*. By contrast, ins1957 GFP-Ndc80 was absent from kinetochores. Given its position at the C-terminus of Ndc80, I hypothesized that the ins1957 mutation disrupts tetramerization of the complex. However, the ins1957 mutant co-purifies with Nuf2, Spc24, and Spc25 in a recombinant Ndc80 complex (Figure 2.3F), suggesting that the mutation does not completely abolish complex formation. To address this question *in vivo*, I performed immunoprecipitation experiments with TAP tags fused to the endogenous Nuf2 or Spc24 (Figure 2.5C). I found that ins1957 GFP-Ndc80 co-immunoprecipitated with Nuf2-TAP, but not Spc24-TAP. As a control, wild-type and ins1687 GFP-Ndc80 co-immunoprecipitated with both Nuf2-TAP and Spc24-TAP. Consistent with its inability to form a recombinant complex, ins506 GFP-Ndc80 did not interact with Nuf2-TAP or Spc24-TAP in the co-immunoprecipitation assay and was absent from kinetochores (Figure 2.5B and C). These results show that ins506 GFP-Ndc80 cannot pair with Nuf2 and consequently fails to assemble into an intact complex. By contrast, ins1957 GFP-Ndc80 can pair with Nuf2 *in vivo*, but is unable to compete with endogenous Ndc80 for association with Spc24/Spc25 at kinetochores. Therefore, the lethal insertion cluster represented by ins1957 is likely the tetramerization domain, which mediates the association of Ndc80/Nuf2 with Spc24/Spc25 into intact complexes at kinetochores.

Isolation of a new ndc80 temperature-sensitive mutant

The linker-scanning mutagenesis screen also generated temperature-sensitive mutants. I tested the non-sectoring colonies isolated from the screen for their ability to sector at a lower temperature. Of the 959 colonies that did not sector at 37˚C, 33 sectored well at 25˚C. These 33 colonies contained insertions at 18 unique sites in *NDC80* (Table 2.4). Notably, five of these temperature-sensitive insertions were in the insertion cluster around nucleotide 1400 of *NDC80* (from the screen above, Figure 2.3D, green arrow). These five insertions affected consecutive residues in Ndc80 from Y465 to I469; insertions closer to the N-terminus had a more severe temperature-sensitive phenotype (Table 2.4). Furthermore, unlike the transposition library or the lethal insertions from the screen, these temperature-sensitive mutations were enriched for insertions in frame 1 (4 out of 5 insertions). In narrowing down the mutations responsible for the temperature-sensitive phenotype, I found that the two mutations in combination (Y465C and I469Q) were sufficient to confer temperature sensitivity (Table 2.4). This allele was named *ndc80-121*.

Uncovering new functions for the Ndc80 complex in assembly of metaphase spindles

To determine the cause of temperature-sensitivity in *ndc80-121* cells, I first examined the integrity of the Ndc80 complex. When expressed and purified recombinantly, the *ndc80-121* mutations allow assembly of an intact heterotetrameric complex (Figure 2.6A). *In vivo*, all four components of the Ndc80 complex were co-immunoprecipitated with Nuf2-TAP from asynchronous *ndc80-121* cells shifted to the non-permissive temperature of 37˚C (Table 2.5). The *ndc80-121* mutations are positioned within the predicted coiled-coil domain, and the I469Q mutation is predicted to disrupt the coiled-coil of Ndc80 leading up to the putative “loop”

(Figure 2.6B). However, disruption of the coiled-coil alone does not explain the phenotype, since the I469Q mutation by itself is not temperature sensitive (Table 2.4).

At 25˚C, *ndc80-121* cells had a slightly longer doubling time than wild-type cells (130 minutes compared to 126 minutes). At 37˚C, *ndc80-121* cells arrested as large-budded cells, suggesting a mitotic arrest (Figure 2.6C). This arrest was dependent on the spindle assembly checkpoint, since *ndc80-121 mad1*Δ cells continued to bud at the non-permissive temperature (Figure 2.6D). To further investigate the nature of this arrest, I synchronized cultures at G1, released into 37˚C medium, and tracked individual cells using a microfluidics system (see Materials and methods). As *ndc80-121* cells entered mitosis, spindle pole bodies (marked by Spc110-mCherry) were able to separate as in wild-type cells, but spindle length did not increase monotonically (Figure 2.7A). Instead, spindles repeatedly collapsed throughout the process of pole separation, and cells often arrested with one spindle pole body in the mother cell and the other in the daughter bud. By visualizing microtubules (marked by Tub1-GFP), I observed that *ndc80-121* cells arrest with broken spindles at the non-permissive temperature (Figure 2.7B). To determine if there was a defect in maintaining a metaphase spindle, I arrested *ndc80-121* cells in metaphase and shifted to 37˚C while continuing the arrest. Similar to wild-type cells, *ndc80-121* cells remained in metaphase and spindles did not break (Figure 2.7C). If *ndc80-121* cells were instead released from the metaphase arrest into 37˚C media, they progressed through anaphase normally, but exhibited broken spindles in the subsequent mitosis (Figure 2.7D). Therefore, *ndc80-121* cells are defective in building a metaphase spindle at the non-permissive temperature.

In *ndc80-1* cells, the error-correction kinase Aurora B generates unattached kinetochores and activates the spindle assembly checkpoint at the non-permissive temperature (PINSKY *et al.*

2006). This was indicated by disorganized kinetochores with more than two Mtw1-3GFP foci, some of which lie off the spindle axis (PINSKY *et al.* 2006). To test if kinetochores are properly attached in *ndc80-121* cells at the non-permissive temperature, I visualized Nuf2-GFP, Mtw1-GFP, and Ndc10-GFP as markers for the outer, middle, and inner kinetochores, respectively. In contrast to wild-type and *ndc80-1* cells that have persistent kinetochore foci (PINSKY *et al.* 2006), Nuf2-GFP, Mtw1-GFP, and Ndc10-GFP fluorescence in *ndc80-121* cells gradually disappeared after shifting to 37˚C following a G1 arrest (Figure 2.8A). This effect was not caused by the degradation of Ndc80 protein (Figure 2.8B). Furthermore, *ndc80-121* cells arrested at metaphase and shifted to 37˚C also lost Nuf2-GFP fluorescence, despite maintaining a metaphase spindle (Figure 2.7C). To obtain a separate readout for kinetochore-microtubule attachments, I synchronized cells in G1 and utilized a LacO/LacI system to visualize individual centromeres by fluorescence (see Materials and methods). Consistent with the broken spindle phenotype, 64% of *ndc80-121* cells did not have separated *CEN3-GFP* spots after 100 minutes at 37˚C (compared to 7% of wild-type cells) (Figure 2.8C). These results indicate that *ndc80-121* cells have a biorientation defect and are unable to segregate their chromosomes. However, *CEN3-GFP* spots that did not separate were often localized to one of the spindle pole bodies, suggesting that some kinetochore-microtubule attachments are still intact. Thus, the gradual disappearance of kinetochore fluorescence is likely due to unclustering of kinetochores. Loss of kinetochore clustering alone does not break kinetochore-microtubule attachments, since spindles do not collapse if metaphase has already been established. Ndc80 is essential for proper kinetochore-microtubule attachments (KLINE-SMITH *et al.* 2005), but has no reported role in spindle integrity. Previous experiments demonstrated that unattached kinetochores or loss of tension alone do not generate broken spindles (BIGGINS and MURRAY 2001; PINSKY *et al.* 2006; SHIMOGAWA *et al.*

2009). Thus, the *ndc80-121* mutant phenotype suggests a novel function of Ndc80 in assembly of the metaphase spindle and biorientation, possibly independent from its role in microtubule attachment.

Evidence for a folded conformation of the Ndc80 complex

To determine the mechanistic cause of the *ndc80-121* phenotype, I performed a spontaneous suppressor screen (Table 2.6). I identified one revertant mutation (C465Y) and two intragenic suppressor mutations in Ndc80: C465F and N564I. The C465F mutation is similar to the revertant mutation, as it mimics the wild-type aromatic residue. A Q469I revertant mutation was not isolated in this screen, likely because two base pair mutations are required for the reversion. The N564I mutation is located towards the C-terminus of Ndc80 and is separated from the *ndc80-121* mutations by the putative "loop". Additionally, I isolated one extragenic suppressor mutation, L344S in Nuf2, which is dominant over the *ndc80-121* mutation (Table 2.6). Based on cross-linking of recombinant Ndc80 complexes (see below), $Ndc80^{N564}$ and $Nuf2^{L344}$ are predicted to be in close proximity within the complex. Together, these results demonstrate a genetic interaction between two domains of the Ndc80 complex that are physically separated by ~100 amino acid residues.

Ndc80 is hypothesized to contain a flexible "loop," based on a break in the predicted coiled-coil character (Figure 2.3A, blue bar). Deletion of the entire predicted loop (residues 488 to 517) is lethal, but a smaller deletion (residues 490 to 510) results in a temperature-sensitive phenotype (MAURE *et al.* 2011). This loop is thought to act as a hinge, conferring the flexibility observed for recombinant Ndc80 complexes on negative-stain electron micrographs (WANG *et al.* 2008). To test if this flexibility can explain the genetic interactions we observed *in vivo*, Alex Zelter cross-linked recombinant Ndc80 complexes and identified cross-linked peptides by mass

spectrometry (see Materials and methods). This technique reveals pairs of lysines within ~20 Å of one another. We reasoned that cross-linking can also capture transient conformations of the Ndc80 complex. In total, we identified 51 unique cross-links between Ndc80 and Nuf2 (Figure 2.9). Using these cross-links, we aligned the coiled-coil regions of Ndc80/Nuf2 between the CH domains and the loop. From the loop to the C-terminus of Ndc80/Nuf2, the alignment was further offset by ~50 residues, consistent with a break in the coiled-coil caused by the loop. However, the loop is predicted to be ~30 residues, suggesting that additional residues of Ndc80 could contribute to the break.

Several cross-links suggest regions of flexibility within the Ndc80 complex. Four such cross-links ($Ndc80^{K380}$-$Ndc80^{K598}$, $Ndc80^{K409}$-$Nuf2^{K388}$, $Ndc80^{K448}$-$Nuf2^{K366}$, and $Nuf2^{K270}$-$Nuf2^{K366}$, Figure 2.9, dotted blue lines) physically connect regions of the complex before and after the loop, consistent with a bend in the Ndc80 complex. This folded conformation also places the *ndc80-121* mutations in close proximity to the suppressor mutations (Figure 2.9, green lines). The $Ndc80^{K409}$-$Nuf2^{K388}$ cross-link was also identified in the recombinant mutant complex, suggesting that the *ndc80-121* mutations do not block the ability of the complex to fold. Thus, the defects of *ndc80-121* cells likely stem from specific interactions between $Ndc80^{Y465/I469}$ and $Ndc80^{N564}$/$Nuf2^{L344}$ while the complex is folded. Taken together, our results suggest that a folded conformational of the Ndc80 complex is important for kinetochore clustering, spindle integrity, and assembling a metaphase spindle.

Discussion

Linker-scanning mutagenesis specifically identifies regions essential for function

Here, we describe an approach to uncover new functional domains of essential proteins in *S. cerevisiae*. We accomplished this by combining linker-scanning mutagenesis, a plasmid shuffle assay, and high-throughput sequencing together in a comprehensive screen. We applied this screen to the conserved Ndc80 kinetochore protein, which contains a microtubule-binding globular domain and is predicted to contain long coiled-coil domains. While the short insertions resulting from transposon mutagenesis were generally well tolerated, several clusters of insertions were detrimental to Ndc80 function *in vivo*. These clusters of lethal insertions highlight important regions of the protein, many of which are not readily apparent by inspecting sequence conservation (Figure 2.3C and D).

New functions for the N-terminus of Ndc80

Binding of Ndc80 to microtubules is accomplished by its N-terminus, which contains an unstructured tail domain and a conserved CH domain that is commonly found on actin- and microtubule-binding proteins (CIFERRI *et al.* 2008; GIMONA *et al.* 2002; HAYASHI and IKURA 2003; KORENBAUM and RIVERO 2002; WEI *et al.* 2007). In the linker-scanning mutagenesis screen, insertions were generally tolerated throughout the entire N-terminus of Ndc80, with just two clusters of lethal insertions in the CH domain. A representative mutation from the first cluster (ins506) is expressed *in vivo*, but is absent from kinetochores and does not co-immunoprecipitate with Nuf2-TAP. This mutant impairs the formation of the Ndc80 complex, likely by disrupting the interaction between the Ndc80 and Nuf2 CH domains. This suggests that the CH domain plays a critical role in the dimerization of Ndc80 and Nuf2. The second cluster lies in an interior helix of the CH domain adjacent to the first cluster. A representative mutation

from this cluster (ins656) surprisingly did not abolish microtubule binding by the recombinant complex or disrupt kinetochore localization *in vivo*. It is unlikely that this mutation is lethal because of subtle changes in the microtubule-binding ability of Ndc80, as several mutations that are known to impair microtubule binding by the human complex *in vitro* are tolerated in *S. cerevisiae* (AKIYOSHI *et al.* 2009; CIFERRI *et al.* 2008; KEMMLER *et al.* 2009; LAMPERT *et al.* 2013; UMBREIT *et al.* 2012). We propose that this mutation instead disrupts another essential function of the Ndc80 CH domain that is independent of microtubule binding.

Downstream of the CH domain, we mapped two clusters of lethal insertions to a putative helical hairpin motif. Together with the Ndc80 CH domain, this hairpin packs against the paired CH domain of Nuf2 in a crystal structure of the truncated human Ndc80 complex (CIFERRI *et al.* 2008). One of these lethal insertions, ins839, slows the dissociation and diffusion rates of Ndc80 complexes on microtubules *in vitro*. These effects cannot be due to cooperative interactions between Ndc80 complexes on microtubules, as our experiments were performed at the single-molecule level. Moreover, given its position in the crystal structure, the hairpin is unlikely to contact microtubules directly. Therefore, we propose that the hairpin contributes indirectly to microtubule binding, perhaps through structural stabilization or organization of the microtubule-binding interface.

Identification of novel domains in Ndc80 and defining the tetramerization domain

At the C-terminal end of Ndc80, the lethal insertion cluster represented by ins1957 is in a region predicted to overlap with the N-termini of Spc24/Spc25 by crosslinking experiments (MAIOLICA *et al.* 2007). While this general region is proposed to mediate tetramerization of the complex (CIFERRI *et al.* 2005; MAIOLICA *et al.* 2007; WEI *et al.* 2005), it is not clear which complex components are directly involved and which segments of these components are

required. We found that the ins1957 mutation disrupts formation of the Ndc80 complex *in vivo*, and that the mutant Ndc80 was consequently defective at incorporating into kinetochores. These results suggest that the lethal insertion cluster represented by the ins1957 mutation defines a region in Ndc80 important for tetramerization of the Ndc80 complex.

My linker-scanning mutagenesis screen successfully identified three previously uncharacterized segments of Ndc80 that are essential for its function. These insertion clusters lie in the last ~300 amino acid residues of Ndc80, predicted to form the "rod-shaped" part of the complex as seen by electron microscopy (WANG *et al.* 2008; WEI *et al.* 2005). The first lethal insertion cluster is centered on residue K380 of Ndc80, and coincides with a change in predicted coiled-coil character that may represent a transition point where the coiled-coil begins. Consistent with this prediction, limited proteolysis experiments identified K380 as a cleavage site that is likely not protected by coiled-coil (WEI *et al.* 2005). The representative insertion from this cluster, ins1148, is predicted to abolish the formation of coiled-coil after the insertion (Appendix A, Figure S5). Nevertheless it forms a stable tetramer both *in vivo* and *in vitro,* suggesting the coiled-coil in this region is not driving the interaction between Ndc80 and Nuf2, Spc24 or Spc25. Similarly the lethal insertion cluster represented by ins1687 abolishes the probability of coiled-coil formation after this insertion, but again has no effect on tetramer formation and represents a domain with an, as yet, unknown function. Lastly, the insertion cluster around nucleotide 1400 of *NDC80* also lies in a predicted coiled-coil region, and insertions in this cluster were temperature-sensitive. Two mutations were sufficient to confer temperature-sensitivity: Y465C I469Q. This mutant allele, termed *ndc80-121*, can be used to dissect the function of this previously uncharacterized domain.

A folded conformation of Ndc80 and assembly of a metaphase spindle

The *ndc80-121* mutant arrests at 37˚C with large budded cells, unclustered kinetochores, and broken spindles. This arrest is dependent on the spindle assembly checkpoint, but it remains to be determined if the checkpoint is responding to the loss of tension from spindle collapse or by a population of unattached kinetochores. Broken spindle phenotypes have been previously observed for other kinetochore mutants (*dam1-1*, *mif2-3*), but these defects occurred during anaphase elongation (BROWN *et al.* 1993; CHEESEMAN *et al.* 2001). By contrast, the *ndc80-121* mutant is unable to establish a metaphase spindle. Notably, *ndc80-121* cells are not deficient in maintaining a metaphase spindle, even while kinetochores become unclustered. These observations demonstrate a link between kinetochore clustering and spindle integrity while cells enter metaphase. The mechanism underlying this process depends on a previously uncharacterized region in the predicted coiled-coil of Ndc80. To further investigate the cause of the *ndc80-121* phenotype, I screened for suppressor mutations and identified two within a C-terminal segment of the Ndc80 complex (at N564 of Ndc80 and L344 of Nuf2). This region of Ndc80 is also predicted to be coiled-coil, and is ~100 amino acid residues away from the *ndc80-121* mutations.

Canonical coiled-coils contain a heptad repeat pattern of *HPPHPPP*, where *H* and *P* are hydrophobic and polar residues, respectively (discussed in WOOLFSON 2005). Positions within this heptad repeat are denoted *a* to *g*. The mutations in *ndc80-121* (Y465 and I469) are in positions *d* and *a* of the predicted coiled-coil. Hydrophobic interactions between the *a* and *d* residues of two α-helical strands drive the assembly of dimeric coiled-coils. Notably, the $Ndc80^{N564I}$ and $Nuf2^{L344S}$ suppressor mutations identified are also in the *a* positions of their respective predicted coiled-coils. One explanation for the *ndc80-121* phenotype is that the

Y465C I469Q mutations disrupt the coiled-coil register at the non-permissive temperature, and that the suppressor mutations correct this defect. However, two observations suggest that this is not the case. First, Ndc80$^{Y465/I469}$ and Ndc80^{N564}/Nuf2^{L344} are separated by a predicted disordered loop, so it is unlikely that these residues directly affect the same stretch of coiled-coil. Second, the I469Q mutation is predicted to disrupt coiled-coil formation, but this mutation alone does not confer a growth defect. The Y465C mutation, which has little effect on the predicted coiled-coil, is additionally required for temperature sensitivity. Therefore, we favor a model where Ndc80$^{Y465/I469}$ and Ndc80^{N564}/Nuf2^{L344} physically interact due to folding of the complex.

Previous studies proposed that the Ndc80 complex bends at the disordered loop, affording flexibility to the complex (WANG *et al.* 2008). Our *in vitro* cross-linking results with recombinant Ndc80 complex are consistent with this model. This flexibility was hypothesized to mediate structural changes at the kinetochore in response to tension. Based on super-resolution microscopy experiments, the distance between the N- and C-termini of the Ndc80 complex decreases from ~55 nm to ~34 nm during the metaphase-to-anaphase transition (JOGLEKAR *et al.* 2009). This likely corresponds to an elongated complex while the kinetochore is under tension during metaphase, and a collapsed form of the complex once tension is relieved at anaphase. Here, we provide genetic evidence supporting these observations. Moreover, the *ndc80-121* phenotype suggests that extension of the Ndc80 complex is not a passive result of applied tension, but that this conformational change is functionally important for spindle integrity and establishing metaphase *in vivo*.

To explain the phenotype of *ndc80-121* cells, the goal of future experiments will be to identify interactions disrupted by the mutations. By bending of the Ndc80 complex, Ndc80$^{Y465/I469}$ and Ndc80^{N564}/Nuf2^{L344} could physically interact. Given the positions of these

residues in predicted hydrophobic regions, this interaction could involve higher order coiled-coil structures. An alternative possibility is that Ndc80$^{Y465/I469}$ of one Ndc80 complex interacts with Ndc80^{N564}/Nuf2^{L344} in an adjacent Ndc80 complex at the kinetochore. Disruption of this interaction could explain the unclustering phenotype observed *in vivo*. Lastly, changes in the conformation of the Ndc80 complex could involve binding of a separate regulatory protein that depends on two interfaces within coiled-coil regions of the complex.

Using the linker-scanning mutagenesis screen, we have identified lethal insertions in known structural elements of Ndc80, and additionally defined new functional domains in the protein. Future experiments will examine additional domains with the goal of defining binding interfaces with known partners, searching for novel protein interactions, and uncovering new roles for Ndc80. This approach is generally applicable to other genes in *S. cerevisiae*, and is particularly useful in revealing functional properties and domains in proteins that are not yet amenable to structural characterization.

Table 2.3 Representative lethal insertions in *NDC80*

Insertion position	Sequence[a]	Inserted residues	First mutation	*In vivo* expression[b]	Kinetochore localization[c]
506	TTCAAGTGGT**TGCGGCCGCAGTGGT**TATAT	LRPQW	Y170R	+	-
656	CACAAATTTC**TGCGGCCGCAATTTC**TTGGC	LRPQF	G220R	+	+
839	AAACTGTTAA**TGCGGCCGCAGTTAA**TTGAT	MRPQL	I280M	+	+
940	ATTCGTTCAC**TGCGGCCGCATTCAC**ATAAT	CGRIH	I314C	+	+
1148	AAGATGAAAT**TGCGGCCGCAGAAAT**CCGAG	LRPQK	S383L	+	+
1687	GAAAACTCAA**TGCGGCCGCACTCAA**ATTAA	CGRTQ	I563C	+	+
1957	TATTGATATA**TGCGGCCGCAATATA**ACAAG	CGRNI	T653C	+	-

[a]15-bp insertions are in bold text
[b]Figure 2.3E
[c]Figure 2.5A and B

Table 2.4 Temperature-sensitive mutants generated by linker-scanning mutagenesis

First Mutation	Mutations[a]	Growth		
		25˚C	30°C	37°C
I319C	INTD**CGRTD**IANL	+	-	-
Y465C	TLRQ**CGRRQ**YDSS	++	-	-
D466C	LRQY**CGRKY**DSSI	+++	+	-
S467C	RQYD**CGRND**SSIQ	+++	+	-
S468C	QYDS**CGRNS**SIQN	+++	++	-
I469M	YDSS**MRPQS**IQNL	+++	+++	-
I544C	EKDN**CGRNN**ITLE	+++	-	-
A574C	ELSE**CGRTE**ANSK	+++	-	-
N575C	LSEA**CGRKA**NSKF			
N575M	LSEA**MRPQA**NSKF	+++	+++	-
K582M	FELS**MRPHS**KQEN	+++	++	-
E584V	LSKQ**VRPQQ**ENER	+++	+	-
N585C	SKQE**CGRKE**NERL	+++	+++	-
N585M	SKQE**MRPQE**NERL			
A591R	RLLV**RPQLV**AQRI	+++	+++	-
Q592A	LLVA**AAAVA**QRIE	+++	-	-
Q592H	LLVA**HAAAA**QRIE			
L664A	IQSS**AAASS**LENS	+++	-	-
Wild-type	TLRQYDSSIQNL	+++	+++	+++
D466G	TLRQ**YGRRI**YDSSI	+++	++	-
Y465C	TLRQ**C**DSSIQNL	+++	+++	+++
I469Q	TLRQYDSS**Q**QNL	+++	+++	+++
Y465C[b]	TLRQ**C**DSS**Q**QNL	+++	+++	-
S467A	TLRQYD**AA**IQNL	+++	+++	+++
S467D	TLRQYD**DD**IQNL	+++	+++	+++
D466G	TLRQY**G**SSIQNL	+++	+++	+++

[a]Insertions and mutations are in bold text
[b]*ndc80-121* allele (Y465C I469Q)

Table 2.5 Immunoprecipitation of Ndc80 complex from wild-type and *ndc80-121* cells

Hit Protein	Description	Wild-type[a]			*ndc80-121*[a]		
		Sequence coverage	Spectrum count (SC)	Normalized SC	Sequence coverage	Spectrum count (SC)	Normalized SC
Ndc80	Ndc80 complex	54%	242	2.18	75%	523	1.10
Spc24		85%	268	2.41	81%	394	0.83
Nuf2-TAP		48%	111	1	57%	475	1
Spc25		50%	92	0.83	55%	284	0.60
Dsn1	MIND complex	18%	17	0.15	26%	31	0.07
Nsl1		33%	9	0.08	42%	29	0.06
Nnf1		19%	9	0.08	49%	27	0.06
Mtw1		24%	5	0.05	11%	2	0.004
Spc105	Spc105 complex	9%	8	0.07	22%	29	0.06
Kre28		17%	30	0.27	29%	12	0.03
Mcm21	COMA complex	8%	2	0.02	8%	2	0
Ame1		11%	2	0.02	0%	0	0
Spc19	Dam1 complex	21%	2	0.02	0%	0	0
Cnn1	Kinetochore component	12%	5	0.05	0%	0	0

[a]Asynchronous cultures were shifted to 37˚C for 100 min. Immunoprecipitated proteins, from a Nuf2-TAP pull-down, were identified by mass spectrometry.

Table 2.6 Suppressor mutations of *ndc80-121*

Genotype	Remarks	Growth		
		25˚C	30°C	37°C
NDC80 NUF2	Haploid wild-type	+++	+++	+++
ndc80-121	$Ndc80^{Y465C\ I469Q}$	+++	+++	-
ndc80-125	$Ndc80^{Y465C\ I469Q\ N564I}$	+++	+++	++
ndc80-121 NUF2-101	$Ndc80^{Y465C\ I469Q}$ $Nuf2^{L344S}$	+++	+++	+++
NUF2-101	$Nuf2^{L344S}$	+++	+++	+++
ndc80-125 NUF2-101	$Ndc80^{Y465C\ I469Q\ N564I}$ $Nuf2^{L344S}$	+++	+++	+++
NDC80/NDC80	Diploid wild-type	+++	+++	+++
ndc80-121/ndc80-121	$Ndc80^{Y465C\ I469Q}$/ $Ndc80^{Y465C\ I469Q}$	+++	+++	-
NDC80/ndc80-121	Ndc80/ $Ndc80^{Y465C\ I469Q}$	+++	+++	+++
NDC80/ndc80-125	Ndc80/ $Ndc80^{Y465C\ I469Q\ N564I}$	+++	+++	+++
ndc80-125/ndc80-125	$Ndc80^{Y465C\ I469Q\ N564I}$ / $Ndc80^{Y465C\ I469Q\ N564I}$	+++	+++	+++
ndc80-121/ndc80-125	$Ndc80^{Y465C\ I469Q}$/ $Ndc80^{Y465C\ I469Q\ N564I}$	+++	+++	+
ndc80-121/ndc80-121 NUF2/NUF2-101	$Ndc80^{Y465C\ I469Q}$/ $Ndc80^{Y465C\ I469Q}$, Nuf2/ $Nuf2^{L344S}$	+++	+++	+++

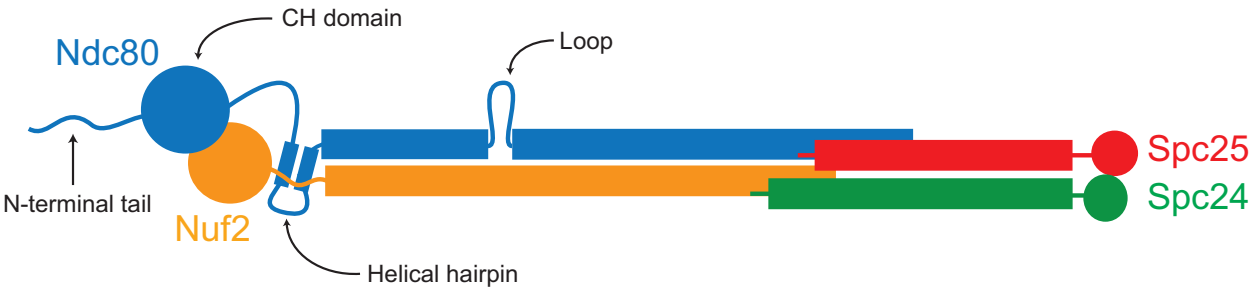

Figure 2.1 The Ndc80 complex contains Ndc80, Nuf2, Spc24, and Spc25

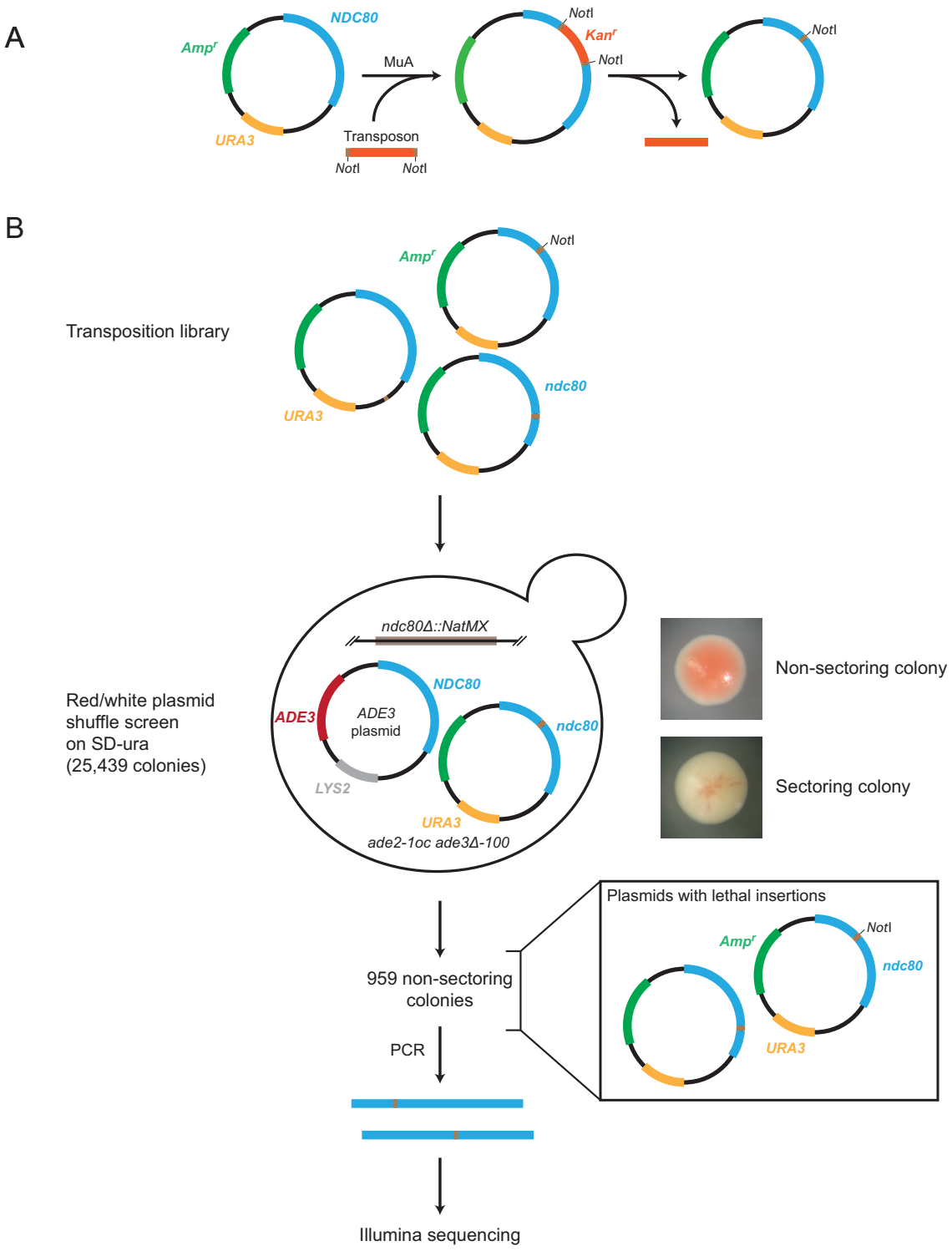

Figure 2.2 Workflow of the linker-scanning mutagenesis screen
(*A*) An Ndc80 transposition library, containing 15-bp insertions at random locations, was created using MuA transposition. (*B*) The transposition library was screened in *S. cerevisiae* using a red/white plasmid shuffle system. Lethal insertions that disrupt the function of Ndc80 appear as non-sectoring red colonies in the screen. From these red colonies, plasmids were isolated and the positions of the lethal insertions were determined by Illumina sequencing.

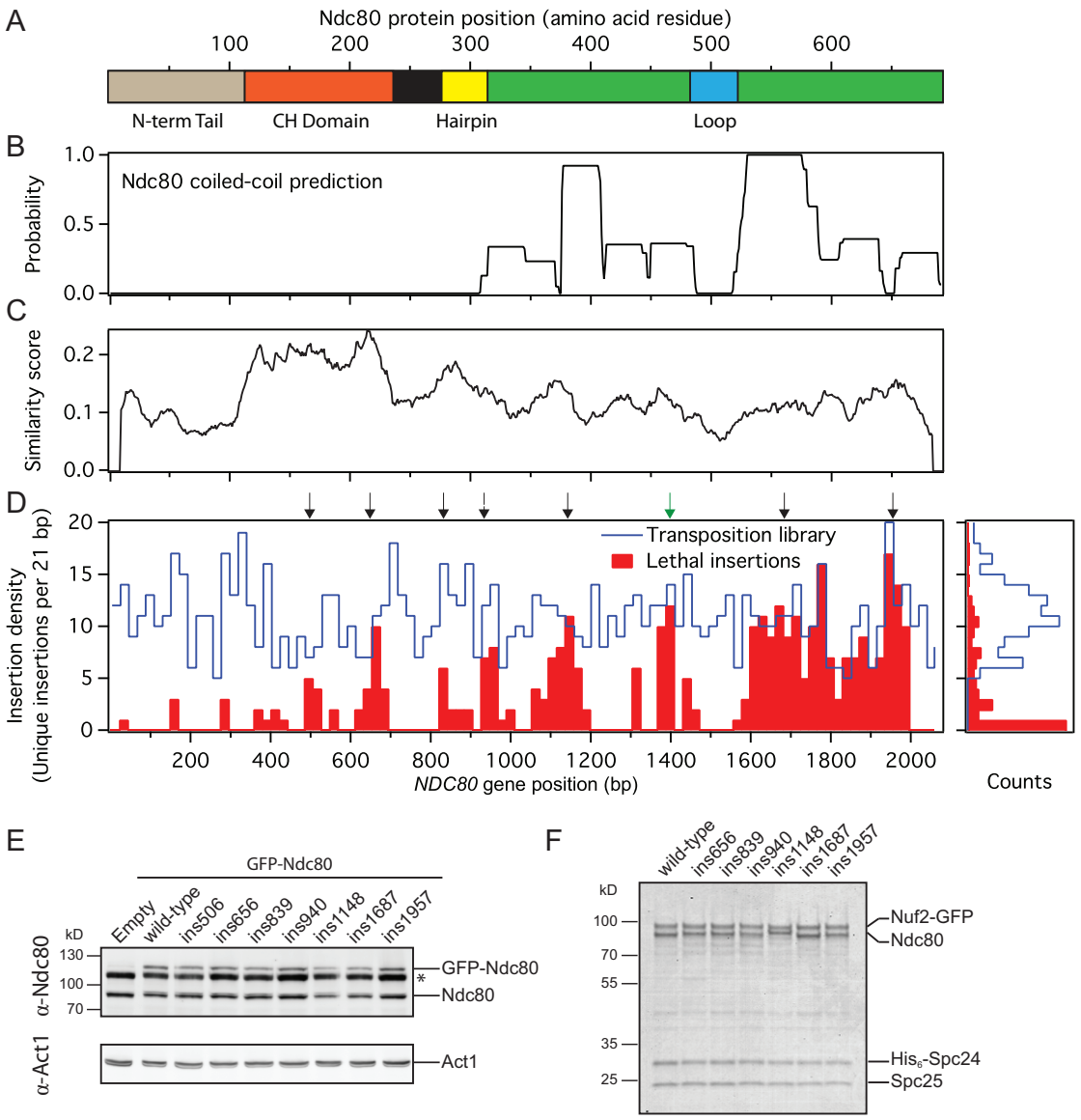

Figure 2.3 Lethal insertions were found in distinct clusters in *NDC80*

(*A*) Bar diagram showing the positions of notable structural features in Ndc80. (*B*) Probability of coiled-coil formation as predicted by Paircoil2 (McDonnell *et al.* 2006). (*C*) Similarity of Ndc80 protein sequences between select fungal species (see Materials and methods). (*D*) Left: the insertion density for the transposition library (blue line) and from the red colonies (red bars) is shown along *NDC80*. Insertion density is plotted as the number of unique insertion sites within a 21-bp window. Black arrows indicate the positions of the representative insertions characterized. Green arrow denotes temperature-sensitive insertion cluster. Right: from the insertion density plot, the distributions of insertion densities for the transposition library (blue line) and from the red colonies (red bars) are shown. (*E*) Immunoblot of cell lysate showing that lethal insertion mutants (GFP-tagged) are expressed *in vivo* over the endogenous Ndc80 (untagged). *Non-specific band from the α-Ndc80 antibody. Act1 serves as a loading control. (*F*) Coomassie-stained gel of recombinant Ndc80 complex containing lethal insertions. Recombinant Ndc80 complexes were purified by affinity chromatography and gel filtration. Mutant Ndc80 complexes migrated similarly to the wild-type complex in the gel filtration column and were collected at the same elution volume. The band for Ndc80 containing the ins1148 mutation reproducibly migrates higher than the wild-type protein.

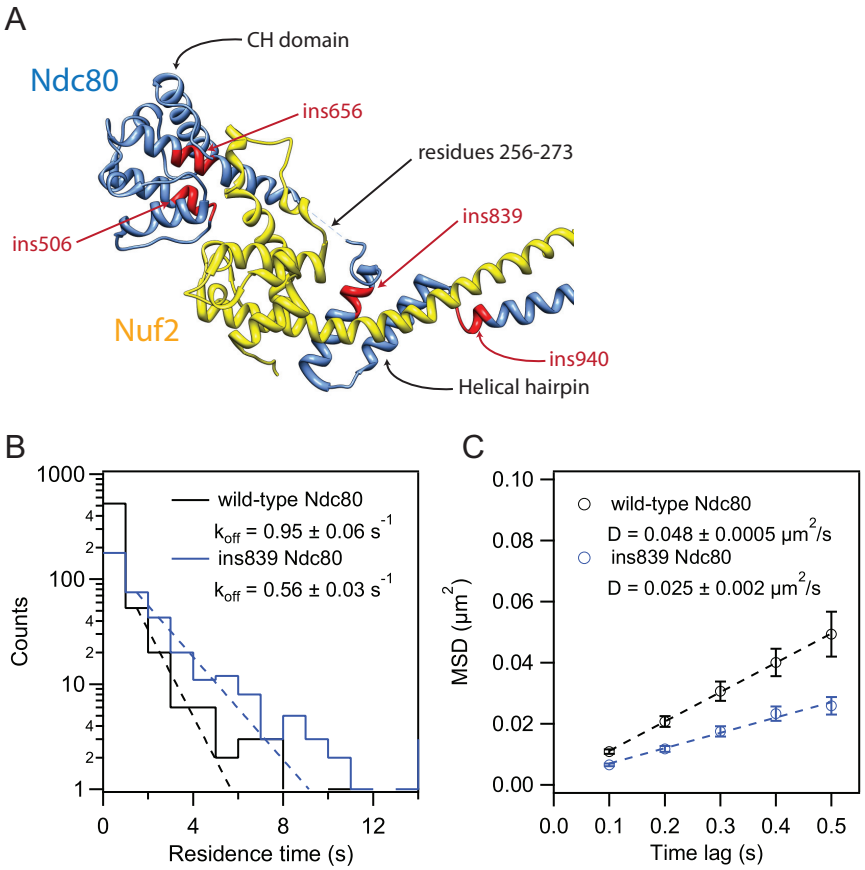

Figure 2.4 A lethal insertion in the helical hairpin of Ndc80 affects binding of the complex to microtubules

(*A*) Four lethal insertion clusters (red) are mapped onto homologous regions of the human Ndc80 (blue) crystal structure (PDB 2VE7; CIFERRI *et al.* 2008). Lethal insertion clusters are labeled based on their representative insertion. The structure is illustrated with the UCSF Chimera package (PETTERSEN *et al.* 2004). (*B*) Residence time distributions of wild-type (black trace, $n = 622$) and ins839 GFP-Ndc80 complex (blue trace, $n = 374$) on microtubules fit with single exponentials (dashed lines) to determine the dissociation rate constants, k_{off}. (*C*) Plots of mean-squared displacement (MSD) ± s.e.m. versus time lag for the binding events in (*B*). Linear fits to the data (dashed lines) were used to determine the diffusion constant, D.

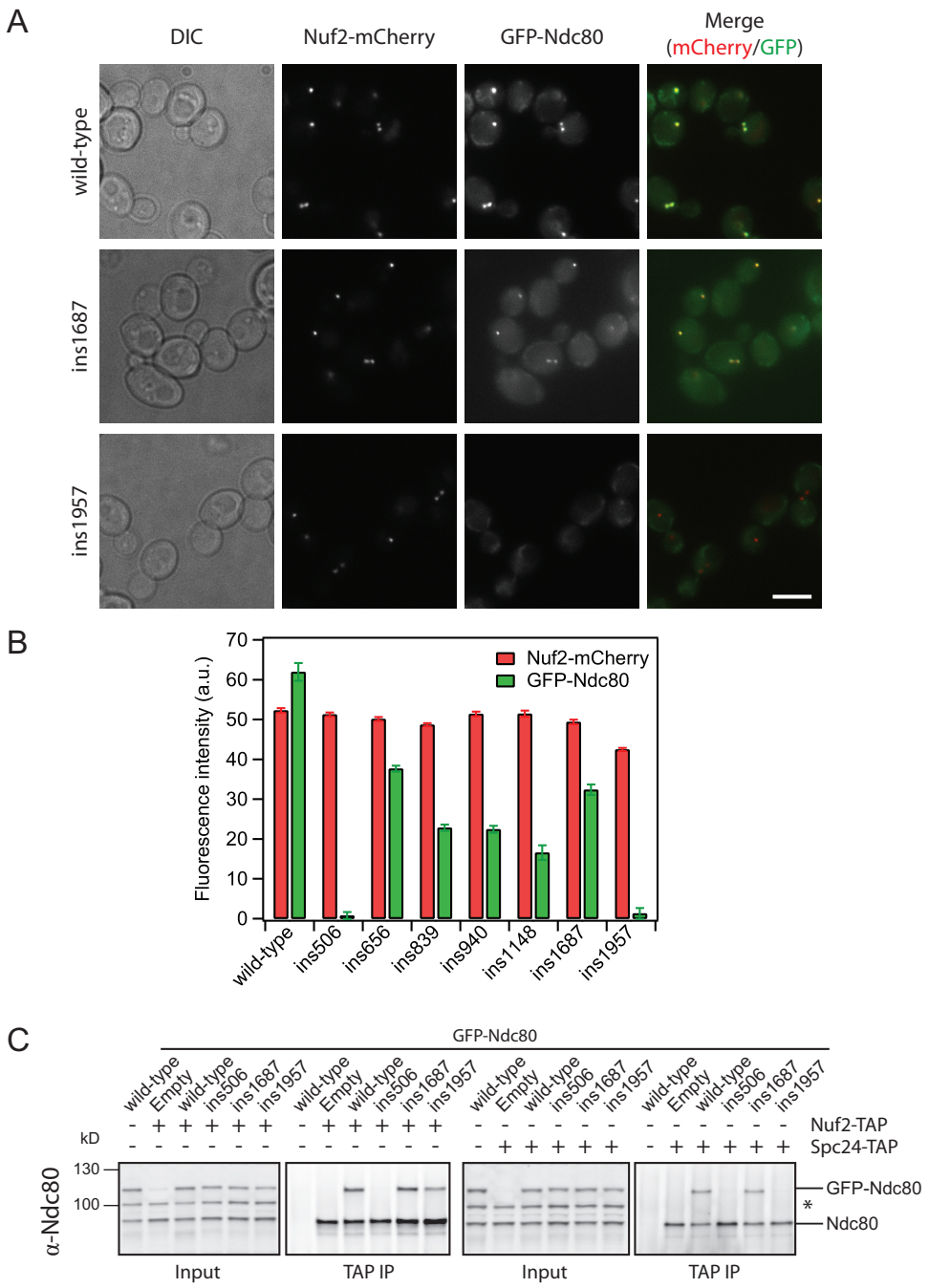

Figure 2.5 A C-terminal segment of Ndc80 controls tetramerization of the Ndc80 complex
(*A*) Sample images of GFP-Ndc80 lethal insertion mutants co-localized with Nuf2-mCherry at kinetochores *in vivo*. Endogenous Ndc80 is untagged. Scale bar is 5 μm. The fluorescence intensity of GFP and mCherry are quantified and shown in (*B*). Intensity is plotted as the mean of fluorescence signal – mean of background signal. Error bars represent s.e.m. The total numbers of mCherry spots quantified are: wild-type (n = 686), ins506 (n = 788), ins656 (n = 760), ins839 (n = 913), ins940 (n = 643), ins1148 (n = 372), ins1687 (n = 576), and ins1957 (n = 389). (*C*) Immunoprecipitation (IP) of GFP-Ndc80 lethal insertion mutants, and untagged endogenous Ndc80, with Nuf2-TAP or Spc24-TAP. *Non-specific band from the α-Ndc80 antibody. On the immunoblots, input is 0.5% of the clarified lysate and TAP IP is 10% of the total volume.

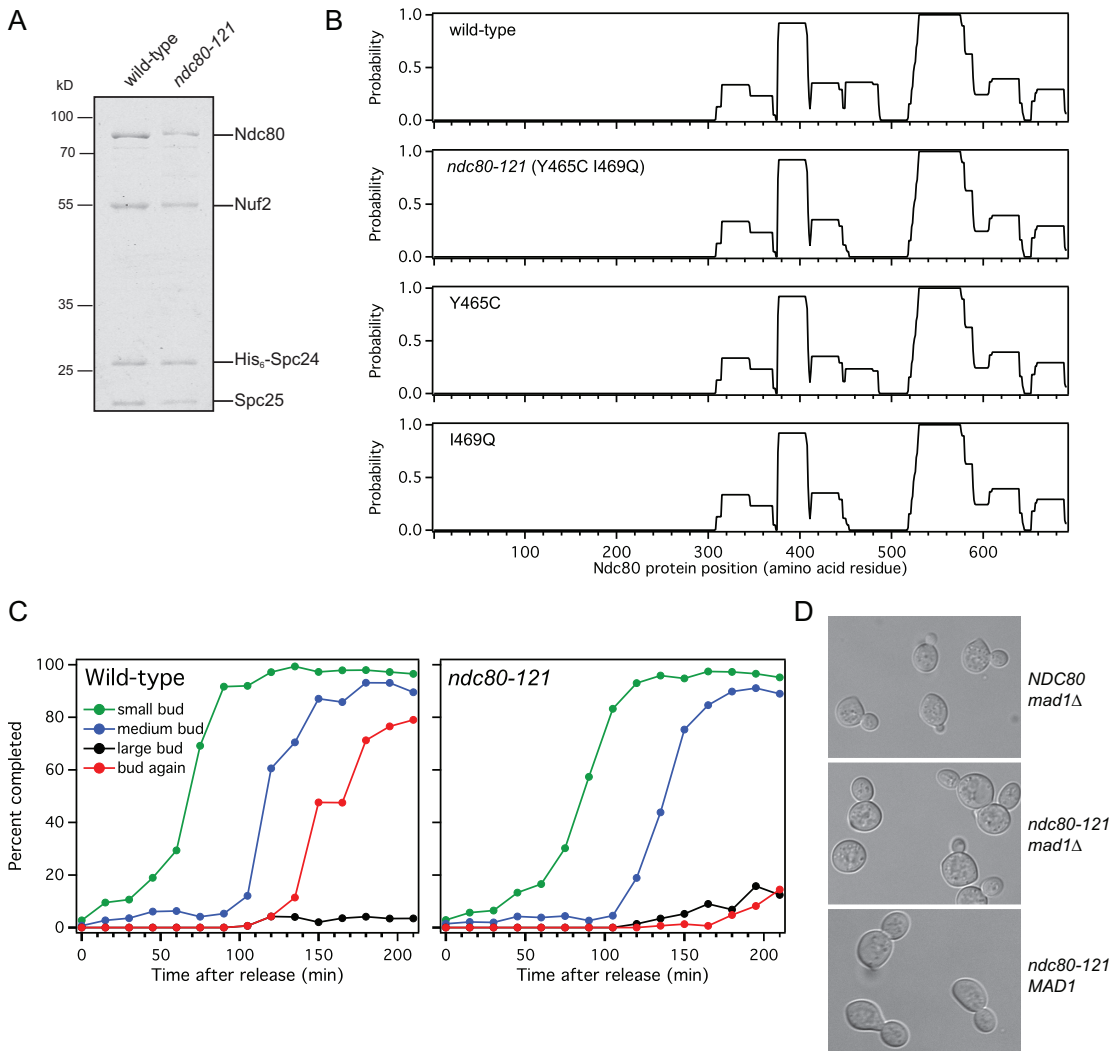

Figure 2.6 Characterization of the *ndc80-121* temperature-sensitive mutation
(*A*) Coomassie-stained gel of an intact recombinant Ndc80 complex containing the *ndc80-121* mutations. Recombinant Ndc80 complexes were purified by affinity chromatography and gel filtration. Ndc80 complex containing the *ndc80-121* mutations migrated similarly to the wild-type complex in the gel filtration column and were collected at the same elution volume. (*B*) Predicted effects of the *ndc80-121* mutations on coiled-coil formation. (*C*) Budding index of wild-type and *ndc80-121* cells after synchronization at G1 and release into 37˚C medium. (*D*) DIC images of wild-type and *ndc80-121* cells after 200 min at 37˚C.

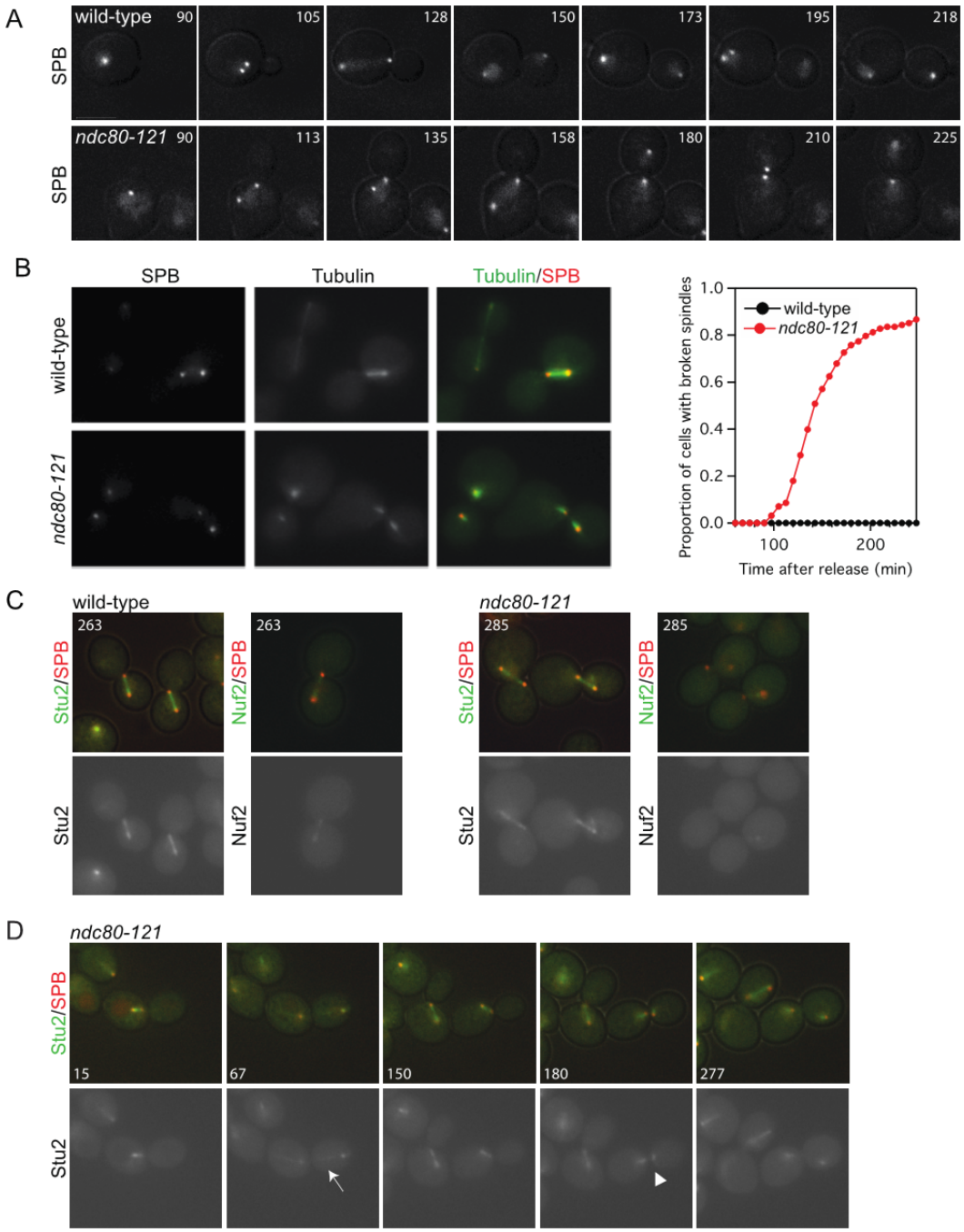

Figure 2.7 *ndc80-121* cells can maintain, but cannot assemble a metaphase spindle
(*A*) Wild-type and *ndc80-121* cells were synchronized at G1 and released into 37˚C medium while visualizing spindle pole bodies (SPBs, Spc110-mCherry). (*B*) Left: Representative images of intact spindles in wild-type cells and broken spindles in *ndc80-121* cells. Tubulin was marked by Tub1-GFP. Right: Accumulation of broken spindles, which were scored based on microtubule morphology as judged by Tub1-GFP or Stu2-GFP fluorescence (n = 119 wild-type cells and n = 128 *ndc80-121* cells). (*C*) Wild-type and *ndc80-121* cells were arrested at metaphase for 3 hr with a Cdc20 degron and shifted to 37˚C without releasing the arrest. Microtubules and Ndc80 complex were marked by Stu2-GFP and Nuf2-GFP, respectively. (*D*) After 3 hr of metaphase arrest, *ndc80-121* cells were released into 37˚C medium. The arrow labels an anaphase spindle, and the arrowhead denotes a broken spindle. For images in (*A*, *C*, and *D*), inset numbers indicate time, in minutes, after temperature shift.

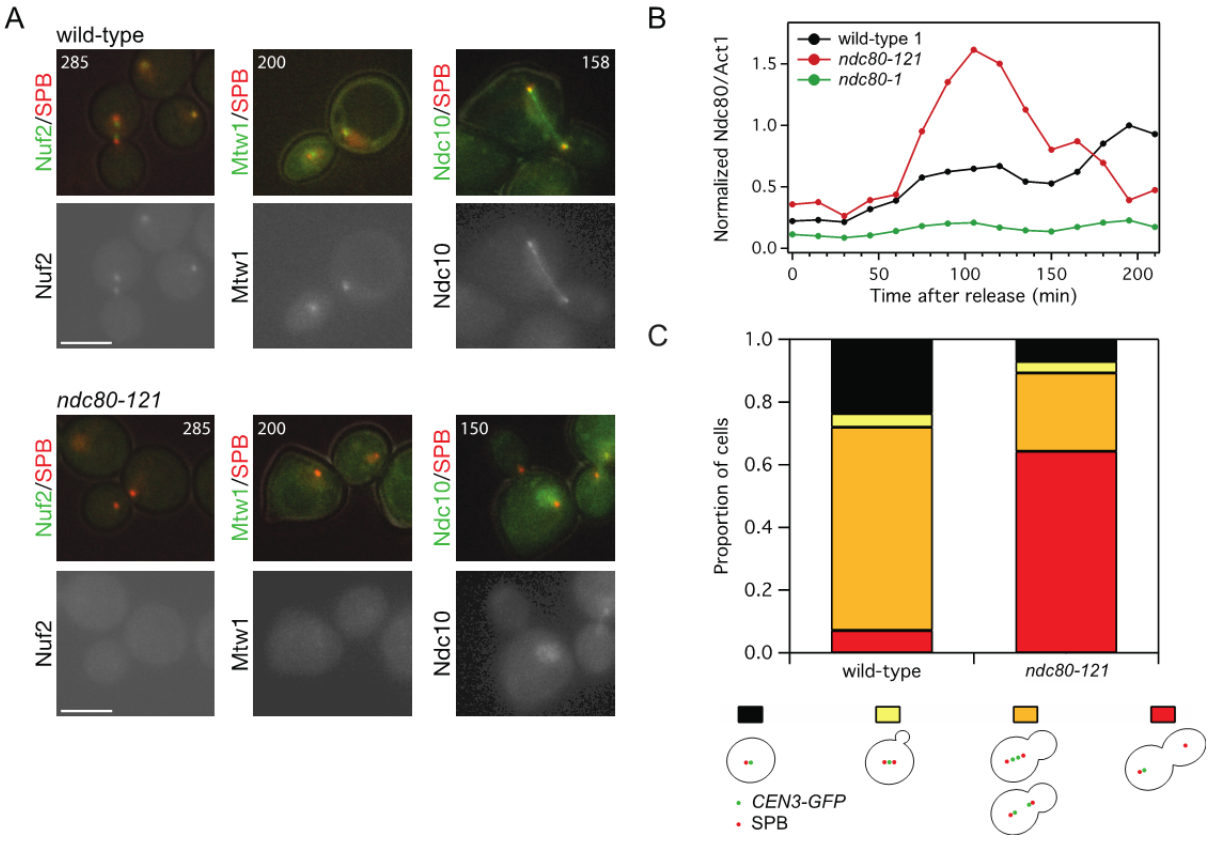

Figure 2.8 Kinetochores in *ndc80-121* cells become unclustered at the non-permissive temperature
(*A*) Wild-type and *ndc80-121* cells were synchronized at G1 and shifted to 37˚C while visualizing outer (Nuf2-GFP), middle (Mtw1-GFP), and inner (Ndc10-GFP) kinetochore components. Positions of spindle pole bodies (SPBs) are marked by Spc110-mCherry. Inset numbers indicate time, in minutes, after temperature shift. Scale bars are 5 µm. (*B*) Quantification of Ndc80 protein levels from immunoblots of cell lysates from wild-type, *ndc80-121*, and *ndc80-1* cultures. Time is in minutes after the release into 37˚C medium. (*C*) Wild-type and *ndc80-121* cells were synchronized at G1 and released into 37˚C medium for 100 min. Biorientation was determined based on the separation of *CEN3-GFP* spots (n = 182 wild-type cells and n = 216 *ndc80-121* cells).

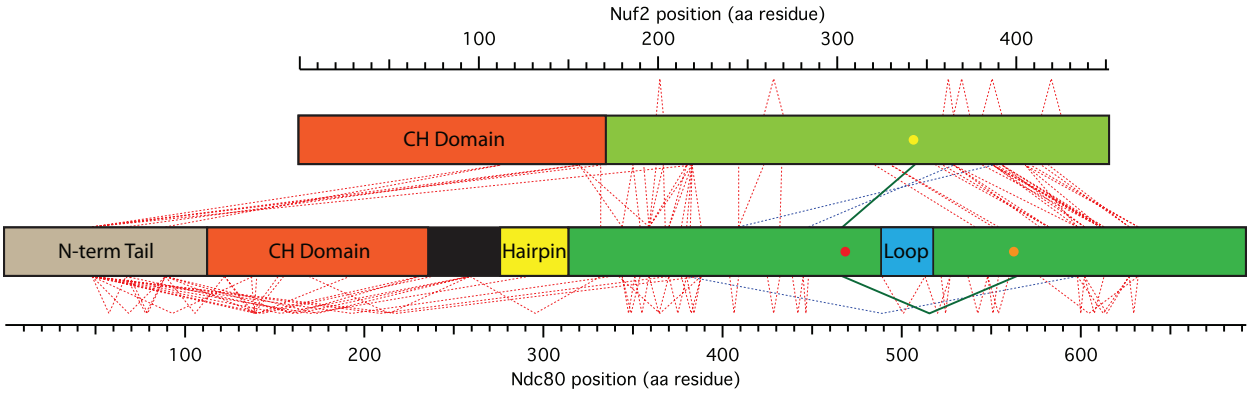

Figure 2.9 Cross-linking of the recombinant budding yeast Ndc80 complex
Cross-links, as identified by mass spectrometry, between Nuf2 (top bar) and Ndc80 (bottom bar) are shown in dotted lines. Red dotted lines are cross-links consistent with known structural features of the Ndc80/Nuf2 dimer. Blue dotted lines denote cross-links that are consistent with a folded conformation of Ndc80/Nuf2. The positions of the *ndc80-121* mutations ($Ndc80^{Y465/I469}$) are labeled by a red dot, and the positions of the suppressor mutations are shown with orange ($Ndc80^{N564}$) and yellow ($Nuf2^{L344}$) dots. Solid green lines show the genetic interactions between the *ndc80-121* and suppressor mutations. Cross-linking experiments were performed by Alex Zelter.

Chapter 3
The Dam1 complex is a processivity factor for the Ndc80 complex in microtubule coupling

Introduction

During mitosis, kinetochores attach to assembling and disassembling microtubule tips while withstanding tensile forces from the mitotic spindle (MADDOX *et al.* 2003; SKIBBENS *et al.* 1995; SKIBBENS *et al.* 1993). Kinetochores are able to harness energy from these disassembling microtubule tips to drive movement of chromosomes (for a review, see INOUE and SALMON 1995). Understanding how the kinetochore establishes microtubule attachments under force requires understanding the organization of the kinetochore components and how they bear and transmit load. The kinetochores of all eukaryotes contain multiple microtubule-binding elements. The conserved KMN network (Spc105, MIND, and Ndc80 complexes) and the Dam1 complex both bind microtubules *in vitro* (CHEESEMAN *et al.* 2006; CIFERRI *et al.* 2008; MIRANDA *et al.* 2005; WEI *et al.* 2007; WESTERMANN *et al.* 2006). Cooperation of the three components of the KMN network was shown by cosedimentation with taxol-stabilized microtubules (CHEESEMAN *et al.* 2006), but how or whether any of the microtubule-binding components cooperate to achieve attachment to dynamic microtubules is unknown. We show for the first time that cooperation between two kinetochore subcomplexes enhances processive, load-bearing coupling to dynamic microtubule tips.

In vitro, both the Ndc80 and Dam1 complexes from budding yeast independently form diffusive attachments to the microtubule lattice and track with disassembling microtubule tips, although the Ndc80 complex requires artificial oligomerization to tip-track (GESTAUT *et al.* 2008; POWERS *et al.* 2009; WESTERMANN *et al.* 2006). When attached to beads, each complex

also forms load-bearing attachments to dynamic microtubule tips (ASBURY *et al.* 2006; FRANCK *et al.* 2007; GRISHCHUK *et al.* 2008a; GRISHCHUK *et al.* 2008b; POWERS *et al.* 2009). Despite these similarities, the Ndc80 and Dam1 complexes are not redundant. The Ndc80 complex is required *in vivo* for attachment to microtubules (KLINE-SMITH *et al.* 2005), and the Dam1 complex is required for attaching to the tips of microtubules and for establishing biorientation (SHIMOGAWA *et al.* 2006; TANAKA *et al.* 2005). Moreover, the Ndc80 complex is required for the assembly of Dam1 complex onto the kinetochore (JANKE *et al.* 2002), and an interaction between the two complexes has been suggested by localization and two-hybrid studies (JOGLEKAR *et al.* 2009; SHANG *et al.* 2003). Studying the combination of Ndc80 and Dam1 complexes *in vitro* will allow us to dissect their distinct roles in kinetochore-microtubule binding.

Here we show that the Dam1 complex is a processivity factor for the Ndc80 complex in kinetochore-microtubule coupling. Using techniques for tracking and manipulating single molecules *in vitro*, we demonstrate directly an interaction between the Ndc80 and Dam1 complexes on microtubules. Through this interaction, the Dam1 complex enhances the ability of the Ndc80 complex to maintain attachment to dynamic microtubule tips even in the presence of external load.

Materials and methods

Protein expression and purification

The *S. cerevisiae* Ndc80 and Dam1 complexes were expressed from polycistronic vectors in *E. coli* as described (GESTAUT *et al.* 2010; GESTAUT *et al.* 2008; POWERS *et al.* 2009; WEI *et al.* 2005). Complexes were purified by affinity chromatography and gel filtration as previously described (ASBURY *et al.* 2006; FRANCK *et al.* 2007; GESTAUT *et al.* 2008; POWERS *et al.* 2009).

TIRF microscopy

A custom TIRF illumination system was constructed for simultaneous excitation of Alexa-647 and GFP (GESTAUT *et al.* 2010; GESTAUT *et al.* 2008; POWERS *et al.* 2009). Total internal reflection of a far-red laser (FTEC-635-0-25-PFQ, Blue Sky Research) and a blue laser (Sapphire 488-75, Coherent) was achieved using a through-the-objective lens arrangement (100 x 1.4 numerical aperture (NA) CFI Plan Apochromat, Nikon). Images from the far-red and green channels were projected side by side onto a cooled EM CCD camera (iXon 887-BI, Andor Technology).

A custom flow cell construction method (GESTAUT *et al.* 2010; GESTAUT *et al.* 2008; POWERS *et al.* 2009) was employed. Glass slides (Gold Seal) were drilled with two holes along the short axis. Double-sided sticky tape (Scotch) was placed on either side of the holes to produce the walls of the flow channel. Silanized coverslips (Corning) were then pressed firmly onto the tape and the ends of the channel were sealed with vacuum grease. To draw fluid through the channel, a peristaltic pump was used via a custom adaptor attached above one of the holes on the glass slide with adhesive transfer tape (3M).

Flow cells were washed with three 100 µl volumes of dH_2O. To bind taxol-stabilized microtubules, we flowed in a modified "rigor" kinesin (G234A) lacking motor activity (RICE *et*

al. 1999) diluted in BRB80 (80 mM Pipes, 120 mM K+, 1 mM $MgCl_2$, 1 mM EGTA, pH 6.9) containing 8 mg·ml^{-1} BSA (BB80). Flow cells were then washed with two 50 µl volumes of BB80, the second of which contained 10 µM taxol (BB80T). Alexa-647 labeled microtubules were diluted in BB80T and incubated in flow cells for 5 min. Flow cells were then washed with two 50 µl volumes of BB80T. Proteins were then introduced, diluted in BB80T containing 0.02 to 0.1 mg·ml^{-1} κ-casein, 200 µg·ml^{-1} glucose oxidase, 35 µg·ml^{-1} catalase, 25 mM glucose and 5 mM DTT. When assayed in combination, Ndc80 and Dam1 complexes were pre-mixed prior to their introduction into flow cells. After flowing in the protein mixture, 2000-frame movies were taken at 10 frames per second with iXon software (Andor Technology). TIRF microscopy experiments with the representative linker-scanning mutagenesis mutations were performed as described in Chapter 2 (Materials and methods).

For disassembling microtubule assays, "rigor" kinesin was bound to flow cells and washed with 50 µl BB80, followed by 50 µl BB80 containing 0.1 mg ml^{-1} κ-casein and 1 mM GTP (GB). Alexa-647 labeled GMPCPP microtubule seeds were then bound and washed with two 50 µl volumes of GB. Microtubules were grown by incubating for ~15 min in GB containing 2 mg·ml^{-1} tubulin (Alexa-647 labeled 1:100), 200 µg·ml^{-1} glucose oxidase, 35 µg ml^{-1} catalase, 25 mM glucose and 5 mM DTT. Microtubule depolymerization was induced by buffer exchange removing free tubulin and simultaneously introducing proteins diluted in BB80 containing 0.1 mg·ml^{-1} κ-casein, 200 µg·ml^{-1} glucose oxidase, 35 µg·ml^{-1} catalase, 25 mM glucose and 5 mM DTT. Movies were started concomitantly with induction of depolymerization and taken at 10 frames per second for 2000 frames.

TIRF microscopy data analysis

Software analysis of TIRF microscopy data was performed using Labview (National Instruments) as previously described (GESTAUT *et al.* 2010; GESTAUT *et al.* 2008; POWERS *et al.* 2009). The software generated the position and brightness of individual GFP-tagged complexes on microtubules over time. Custom Igor Pro (WaveMetrics) programs were used to generate histograms of Ndc80 complex residence times on microtubules. A weighted single exponential fit was applied to determine the mean residence time, τ, and to calculate the dissociation rate constant, $k_{off} = \tau^{-1}$. Association rate constants, k_{on}, were estimated as the number of observed Ndc80 complex binding events per tubulin dimer per second, divided by the free concentration of Ndc80 complex. Standard diffusion plots of mean squared displacement versus time were generated in Igor Pro. A weighted linear fit was used to calculate the one-dimensional diffusion constant, D, of GFP-tagged complexes on microtubules.

To quantify Ndc80 complex tip-tracking, brightness profiles along disassembling tips were created in Labview. Fluorescent signals at the tips were averaged across seven frames (0.7 sec) and we required a minimum intensity threshold of 20% above background to score a tip-tracking event. For each individual frame, the instantaneous depolymerization rate was calculated as the change in tip position over 50 frames (5 sec). A microtubule disassembly event was defined to start at the first appearance of GFP-tagged Ndc80 complex at the tip, and to end when the rate of depolymerization dropped below 0.03 $\mu m \cdot s^{-1}$. Microtubule tips without tracking as defined by this criterion were omitted from further analysis. The total tracking distance for each individual tip was determined and the average tracking distance per depolymerization event was calculated.

To quantify binding to microtubules, we created brightness profiles of 500 pM mCherry-tagged Dam1 complex using our TIRF assay. After 5 min incubation with taxol-stabilized microtubules, an image was recorded (6 or 7 images per condition). For each microtubule in the image, the integrated intensity of mCherry was measured in ImageJ (NIH) and the brightness per unit length was calculated. Brightness per unit length values were averaged across all microtubules within one image, and reported as averages from multiple images.

Electron microscopy

Taxol-stabilized microtubules were made by polymerizing cleared tubulin in a total volume of 40 µl BRB80 containing 1.75 mM GTP, 1 mM $MgCl_2$, and 3.5% DMSO at 37°C for 30 min. Various concentrations of Dam1 complex were mixed with taxol-stabilized microtubules to a final concentration of 36 nM tubulin in BRB80 containing 10 µM taxol, and incubated for 15 min. Samples were prepared for analysis by electron microscopy as follows. Carbon coated copper grids were positively charged in a glow discharge device (EMS) for 2 minutes. A 2 µl drop of sample was applied onto a freshly discharged grid and incubated for 20 seconds. Excess solution was blotted off and the grid washed twice with water and once with 0.075% uranyl formate before staining with uranyl formate. The stain was blotted off and the grid air dried. The preparations were viewed on a transmission electron microscope (Spirit T12, FEI) operating at 120kV and images recorded on a 1k x1k Gatan bottom mount slow-scan charge coupled device camera at a nominal magnification of either 15,000x or 52,000x at the specimen level. For each preparation, the total number of Dam1 complex rings on microtubules were counted and divided by the total length of microtubules to generate an average number of Dam1 complex rings per microtubule micron. In control experiments performed in the presence of

blocking proteins (8 mg·ml^{-1} BSA and 0.02 mg·ml^{-1} κ-casein), rings were still absent at 500 pM Dam1 complex.

Additional Material and methods are described in Appendix B.

Results

The Ndc80 and Dam1 complexes interact on microtubules

Recombinant *S. cerevisiae* Ndc80 and Dam1 complexes were expressed in *E. coli* and purified by affinity chromatography and gel filtration (GESTAUT *et al.* 2008; POWERS *et al.* 2009; WEI *et al.* 2005). By velocity sedimentation analysis, the Ndc80 and Dam1 complexes interacted weakly free in solution (Appendix B, Figure S1). Working with Neil Umbreit, we quantified the interaction of GFP-tagged Ndc80 complexes with microtubules in the presence and absence of Dam1 complex by total internal reflection fluorescence (TIRF) microscopy (Figure 3.1). In the absence of Dam1 complex, individual Ndc80 complexes formed transient and diffusive attachments to microtubules, as reported previously (POWERS *et al.* 2009). We measured a dissociation rate constant (k_{off}) of 0.44 ± 0.03 s^{-1}, an association rate constant (k_{on}) of 0.60 ± 0.02 $\mu M^{-1} \cdot s^{-1}$, and a diffusion constant of 0.067 ± 0.003 $\mu m^2 \cdot s^{-1}$ (Figure 3.1C-E), values comparable to our previous study. We also simultaneously visualized GFP-tagged Ndc80 complexes and mCherry-tagged Dam1 complexes on microtubules. At concentrations affording single molecule resolution of each complex, interaction events were rare. When the two complexes did associate with each other, they appeared to diffuse more slowly (Appendix B, Figure S2). However, interaction events between individual Ndc80 and Dam1 complexes were too infrequent to affect population behavior. To increase the frequency of interactions, we raised the concentration of Dam1 complex while maintaining low concentrations (10 pM) of the Ndc80 complex. Overall, Ndc80 complex transitioned gradually to a more persistent and more slowly diffusing behavior as the concentration of Dam1 complex was increased (Figure 3.1C-E). At 500 pM Dam1 complex, the Ndc80 complex dissociated two-fold more slowly from the microtubule ($k_{off} = 0.23 \pm 0.02$ s^{-1}) and associated 1.6-fold faster onto the microtubule

(k_{on} = 0.99 ± 0.02 $\mu M^{-1} \cdot s^{-1}$) as compared to Ndc80 complex alone. This corresponds to a three-fold decrease in the apparent equilibrium dissociation constant, $K_d = k_{off} \cdot k_{on}^{-1}$ (0.74 ± 0.06 μM to 0.23 ± 0.02 μM). At 500 pM Dam1 complex, the Ndc80 complex also diffused five-fold more slowly (0.013 ± 0.0006 $\mu m^2 \cdot s^{-1}$) as compared to Ndc80 complex alone. The Dam1 complex was unlikely to be acting as a simple barrier to diffusional motility, as the diffusive behavior of the Ndc80 complex was unchanged in the presence of phosphorylated Dam1 complex at the same lattice density (see Chapter 4). The brightness distribution of the GFP signal remained unchanged across concentrations of the Dam1 complex, demonstrating that oligomerization of the Ndc80 complex did not contribute to its modified behavior in the presence of the Dam1 complex (Appendix B, Figure 2). Even at 500 pM Dam1 complex, not all Ndc80 complexes bound persistently and diffused slowly. This indicates that not all Ndc80 complexes were associated with Dam1 complexes, so our calculated values describe a mixed population and likely underestimate Dam1 complex-mediated enhancement of Ndc80 complex-microtubule interactions.

In the presence of the Dam1 complex, diffusion of the Ndc80 complex is slowed far below the reported rate for a single Dam1 complex (GESTAUT *et al.* 2008). Therefore, we hypothesized that at the concentrations required to observe significant changes in the population behavior of the Ndc80 complex, the Dam1 complex forms slowly diffusing oligomers. To test this, we measured the diffusion rate of GFP-tagged Dam1 complex on microtubules (Appendix B, Figure S3A and B). At 2 pM, single GFP-tagged Dam1 complexes diffused rapidly, at 0.060 ± 0.003 $\mu m^2 \cdot s^{-1}$, similar to the rates reported previously (GESTAUT *et al.* 2008; WESTERMANN *et al.* 2006). At 20 and 50 pM Dam1 complex, however, we observed slowly diffusing spots that exhibited fluorescence brighter than individual Dam1 complexes. To

maintain single molecule resolution for quantifying the diffusion of Dam1 complex at higher concentrations, we mixed untagged Dam1 complex with a small amount of GFP-tagged Dam1 complex. At 500 pM, Dam1 complex diffused at least 60-fold more slowly than at 2 pM (Appendix B, Figure S3B). These observations indicate that oligomerization of the Dam1 complex slows its diffusion rate, as reported previously (GRISHCHUK *et al.* 2008a). Moreover, they imply that the enhanced binding of Ndc80 complex to microtubules that we have quantified here (e.g., in Figure 3.1C-E) occurs via interaction with Dam1 complexes that are primarily in an oligomeric state.

In vitro, the Dam1 complex forms rings of 16-25 complexes that encircle microtubules (MIRANDA *et al.* 2007; WANG *et al.* 2007). To investigate whether rings are important for interaction with the Ndc80 complex, we collaborated with Tamir Gonen (Janelia Farm, HHMI) to quantify ring formation on taxol-stabilized microtubules across a range of Dam1 concentrations by negative-stain electron microscopy (Figure 3.2). At 500 pM Dam1 complex, the highest concentration used in our TIRF assays, rings were absent. Instead, we observed small particles scattered around or attached to the filaments. The dimensions of these particles were consistent with Dam1 complex dimers (WANG *et al.* 2007). Rings first appear on microtubules at 1 nM Dam1 complex, substantially increase in density between 5 and 10 nM, and saturate at 100 nM (Table 3.1). These findings are consistent with a strong and cooperative binding of the Dam1 complex to microtubules as reported previously (GESTAUT *et al.* 2008).

While 500 pM Dam1 complex did not assemble into rings on microtubules at 36 nM tubulin, reducing the amount of tubulin could promote ring formation by increasing the density of Dam1 complex bound to microtubules. To explore the magnitude of this effect, we imaged 500 pM Dam1 complex on microtubules at 5-fold lower tubulin (7 nM). Rings were again

absent (n = 8 microtubules, 101 μm total). Further reductions in tubulin concentration were impractical because the microtubules became too sparse on the electron microscopy grids. Since the effective concentration of tubulin polymer in our TIRF assays was lower still (~1 nM), it remains possible that Dam1 complex rings contributed to the observed alterations in behavior of the Ndc80 complex. We note, however, that two observations suggest ring formation is not required for the initial interaction between the Ndc80 and Dam1 complexes. First, the Dam1 and Ndc80 complexes interact during velocity sedimentation, where the Dam1 complex is primarily in dimeric form (see Appendix B, Figure S1). Second, interactions between individual Ndc80 and Dam1 complexes can be observed directly in TIRF assays (albeit rarely; see Appendix B, Figure S2).

The ins839 Ndc80 complex is insensitive to the presence of the Dam1 complex on microtubules

By performing a linker-scanning mutagenesis screen, I identified domains essential for the function of Ndc80 *in vivo* (Chapter 2). To determine if any of these domains interact with the Dam1 complex, I used our established TIRF microscopy assay to test Ndc80 complexes containing the seven representative mutations from the screen. As described above, the Dam1 complex causes wild-type Ndc80 complex to dissociate more slowly from microtubules and to diffuse more slowly on the lattice. The ins839 mutation in the hairpin of Ndc80 (Figure 3.3A) has a similar but less dramatic effect, causing a 2-fold decrease in the diffusion and dissociation rate constants (Figure 3.3B and C, and Appendix A, Figure 4). Therefore, we asked whether the Dam1 complex can further alter the microtubule-binding properties of the Ndc80 complex with the ins839 mutation. Surprisingly, unlike wild-type Ndc80 complex and the other five lethal mutant complexes we purified, the ins839 Ndc80 complex was not influenced by the presence of

the Dam1 complex (Figure 3.3B and C, and Appendix A, Figure S4). Instead, the ins839 mutation makes the Ndc80 complex insensitive to the presence of the Dam1 complex. Whether this is a result of the mutation perturbing the microtubule-binding ability of the Ndc80 complex or disrupting an interaction with the Dam1 complex remains to be determined (see Discussion).

The Dam1 complex enhances attachment of the Ndc80 complex to dynamic microtubule tips

The Ndc80 complex has been shown to track efficiently with disassembling microtubule tips *in vitro*, but only when it is bound to beads or to antibodies (POWERS *et al.* 2009). In contrast, the Dam1 complex tracks robustly with disassembling tips without artificial oligomerization (GESTAUT *et al.* 2008; WESTERMANN *et al.* 2006). We therefore tested whether the Dam1 complex enhances tip-tracking by the Ndc80 complex. We grew microtubules from non-hydrolyzable GMPCPP seeds in the presence of free fluorescent-labeled tubulin and GTP. We visualized the behavior of GFP-tagged Ndc80 complex as microtubules disassembled after the free tubulin was removed. By itself, the Ndc80 complex localized only briefly to microtubule tips during disassembly (Figure 3.4A). Most binding events were transient and diffusive similar to those seen on taxol-stabilized microtubules (and as reported in POWERS *et al.* 2009). In contrast, the addition of Dam1 complex, which accumulates at the disassembling microtubule tip (Appendix B, Figure S3C), substantially increased the tip-tracking behavior of the Ndc80 complex (Figure 3.4A). Ndc80 complexes bound preferentially at the microtubule tip, were more persistently attached, and moved with the disassembling tip.

For quantification, we defined tip-tracking as the colocalization of GFP-tagged Ndc80 complex with disassembling microtubule tips. In the presence of Dam1 complex, Ndc80 complex tracked with 78% (62 of 80) of disassembling microtubule tips over an average distance of 1.2 ± 0.2 μm, compared to only 27% (19 of 71) of tips over an average distance of

0.13 ± 0.09 μm in the absence of Dam1 complex (Figure 3.4B). In the presence of the Dam1 complex, tip-tracking events by the Ndc80 complex often continued until the tips reached the microtubule seeds. Therefore, we likely underestimate the effect of the Dam1 complex to enhance the ability of the Ndc80 complex to track disassembling tips.

To test if the Dam1 complex enhances the tip-tracking ability of Ndc80 complex while under load, Andrew Franck (collaborator in the Asbury laboratory, Department of Physiology and Biophysics) employed an optical trapping-based force clamp assay (ASBURY *et al.* 2006; FRANCK *et al.* 2010; FRANCK *et al.* 2007; POWERS *et al.* 2009). Beads decorated with Ndc80 complex were attached to the tips of assembling microtubules in the presence and absence of free Dam1 complex. A constant tensile force was applied until the attachment broke, the microtubule switched to disassembly or, in a few cases, the event was terminated by other causes (e.g., the bead became stuck to the coverslip). In the absence of Dam1 complex, bead-bound Ndc80 complex formed persistent load-bearing attachments to assembling and disassembling microtubule tips (Appendix B, Figure 5), as reported previously (POWERS *et al.* 2009). While bearing 1.8 ± 0.4 pN of continuous load, travel distances during assembly were broadly distributed with a mean of 350 nm (n = 115). Detachment from assembling tips occurred at a rate of 0.026 ± 0.003 s^{-1}. In the presence of the Dam1 complex, the mean travel distance increased three-fold to 1100 nm (n = 42, $P = 3 \cdot 10^{-8}$, KS test) and the detachment rate decreased five-fold to 0.005 ± 0.0008 s^{-1}. Accordingly, plots of survival probability versus distance show that the couplers remained more persistently attached when Dam1 complex was present (Appendix B, Figure 5C). These observations show that interactions between Dam1 and Ndc80 complexes enhance coupling to both assembling and disassembling microtubule tips under load.

Furthermore, this enhancement occurs under conditions where the entire load is ultimately transmitted to the cargo through the Ndc80 complex.

Discussion

Identifying the interaction interface between the Ndc80 and Dam1 complexes

One key role of Ndc80 *in vivo* is to recruit the Dam1 complex to kinetochores (JANKE *et al.* 2002), but the nature of this interaction remains unclear. Here we show that the Ndc80 complex interacts directly with the Dam1 complex in a microtubule-dependent manner *in vitro*. The addition of Dam1 complex decreases the dissociation and diffusion rates of single Ndc80 complexes on microtubules. The ins839 mutation parallels these effects on the Ndc80 complex, and the addition of Dam1 complex does not further change the behavior of the ins839 Ndc80 complex on microtubules. Notably, while the dissociation and diffusion rates of single ins839 Ndc80 complexes on microtubules are lower than that of the wild-type complex, they are higher than that of the wild-type complex when assayed in the presence of Dam1 complex. This observation raises the interesting possibility that the Dam1 complex does not simply contribute an additional microtubule-binding domain when it interacts with the Ndc80 complex, but changes how the Ndc80 complex binds to the microtubule lattice. The ins839 mutation could partially mimic this effect, which explains why the mutant Ndc80 complex is not further influenced by the Dam1 complex.

An alternative explanation for these observations is that the ins839 mutation disrupts the interaction interface between Ndc80 and the Dam1 complex. Recent studies have proposed that the Dam1 complex binds directly to Ndc80 within the Ndc80 complex, but did not agree on the location of this interaction interface (LAMPERT *et al.* 2013; MAURE *et al.* 2011). One of these proposed regions, a stretch of Ndc80 between the CH domain and the hairpin (residues 256-273; Figure 3.3A), lies in close proximity to the ins839 mutation. When this region was deleted, the Dam1 complex did not enhance the co-sedimentation of the mutant complex with microtubules

in vitro (LAMPERT *et al.* 2013). The authors concluded that residues 256-273 represent an interaction interface between Ndc80 and the Dam1 complex. However, like the ins839 mutation, a deletion of this region alters the microtubule-binding behavior of the Ndc80 complex alone (LAMPERT *et al.* 2013). Therefore, it remains unclear whether these mutations directly disrupt the Dam1 binding interface, or if microtubule attachments made by the mutant complexes are simply unable to be strengthened by the Dam1 complex. Future studies will be aimed at determining whether this region of Ndc80 is in direct contact with the Dam1 complex.

The Dam1 complex acts as a processivity factor for the Ndc80 complex

Many molecular machines require factors that enhance their processivity. For example, the proliferating cell nuclear antigen (PCNA) sliding clamp is required for efficient DNA replication by DNA polymerase ε (KELMAN 1997). Likewise, dynactin is required for long-distance movement of cytoplasmic dynein along microtubules (KING and SCHROER 2000). Kinetochores are processive and form persistent attachments to dynamic microtubule tips over the times and distances required for chromosome biorientation and segregation. However, the contribution of individual components to the processivity of kinetochore-microtubule attachments is poorly understood. Here we show that the Dam1 complex enables the Ndc80 complex to track with disassembling microtubule tips over distances in excess of the length of the entire yeast spindle. *In vivo*, assembly of the Dam1 complex onto the kinetochore requires the Ndc80 complex (JANKE *et al.* 2002). In our optical trap experiments, bead-bound Ndc80 complex was assayed with the Dam1 complex free in solution to mimic this arrangement *in vitro*. The increased ability of bead-bound Ndc80 complexes to bear load in the presence of free Dam1 complex indicates that tensile force can be transmitted through an Ndc80 complex-based linkage in a physiologically relevant arrangement.

We propose that the Dam1 complex acts as a processivity factor for the Ndc80 complex, and that the two complexes cooperate to form load-bearing kinetochore-microtubule attachments. *In vivo*, the budding yeast Ndc80 complex forms lateral attachments to spindle microtubules prior to kinetochore association of Dam1 complex and biorientation (SHIMOGAWA *et al.* 2006; TANAKA *et al.* 2005). Our results are consistent with a model in which the Ndc80 complex initially mediates kinetochore attachment to microtubules. The Dam1 complex is later loaded onto the kinetochore to maintain attachment to dynamic microtubule tips. Association of the Dam1 complex is particularly important for these attachments to withstand the tensile forces required for biorientation. The existence of a distinct and separable processivity factor could also provide a point of regulation for corrective detachment.

Table 3.1 Electron microscopy of ring formation on microtubules at different Dam1 complex concentrations

Dam1 complex concentration	Number of microtubules	Total microtubule length (μm)	Number of rings	Ring density (μm^{-1})[a]
500 pM	27	259	0	0
1 nM	16	280	20	0.1 ± 0.02
2 nM	26	308	76	0.2 ± 0.03
5 nM	26	256	450	2 ± 0.08
10 nM	18	33	535	17 ± 0.7
50 nM	13	16	1312[b]	82 ± 3
100 nM	11	11	1282[b]	120 ± 3
200 nM	9	11.5	1358[b]	120 ± 3

[a]Errors represent counting uncertainties
[b]Rings stacked together in pairs to form doublets and/or coils

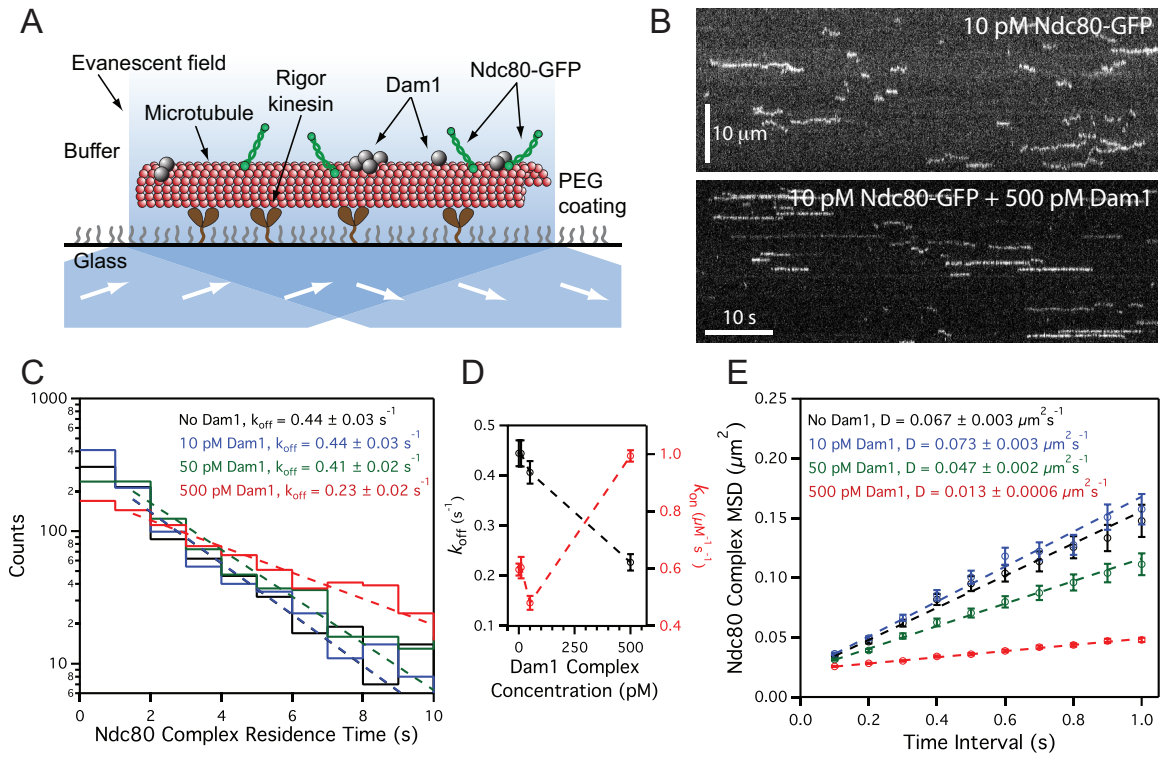

Figure 3.1 Dam1 complex enhances binding of individual Ndc80 complexes to microtubules
(*A*) Schematic of the TIRF assay developed to visualize the behavior of GFP-tagged Ndc80 complexes (green rods) in the presence of untagged Dam1 complexes (grey spheres) on microtubules. (*B*) Representative kymographs showing the binding and one-dimensional diffusion of 10 pM Ndc80 complexes on taxol-stabilized microtubules in the absence or presence of 500 pM Dam1 complex. Positions along the microtubule are shown on the vertical axis, while the passage of time is depicted along the horizontal axis. Concentrations are of free complexes in solution. (*C*) Residence time distributions of 10 pM Ndc80 complex on microtubules without Dam1 complex (black histogram, $n = 883$ events), with 10 pM Dam1 complex (blue histogram, $n = 966$), with 50 pM Dam1 complex (green histogram, $n = 928$), and with 500 pM Dam1 complex (red histogram, $n = 1003$). Dotted lines show exponential fits used to determine dissociation rate constants, k_{off}. (*D*) Dissociation rate constants (k_{off}, left axis, black markers) for the Ndc80 complex, calculated from the data in (*C*), are plotted against the concentration of Dam1 complex. Association rate constants (k_{on}, right axis, red markers) of the Ndc80 complex are also plotted (without Dam1 complex, $n = 1103$; with 10 pM Dam1 complex, $n = 1426$; with 50 pM Dam1 complex, $n = 1179$; with 500 pM Dam1 complex, $n = 1412$). (*E*) Mean-squared displacement (MSD) is plotted against time for 10 pM Ndc80 complex on microtubules without Dam1 complex (black markers, $n = 803$ events), with 10 pM Dam1 complex (blue markers, $n = 859$), with 50 pM Dam1 complex (green markers, $n = 883$), and with 500 pM Dam1 complex (red markers, $n = 968$). Dotted lines show the weighted linear fit used to determine diffusion constant, D. Markers are mean values ± s.e.m.

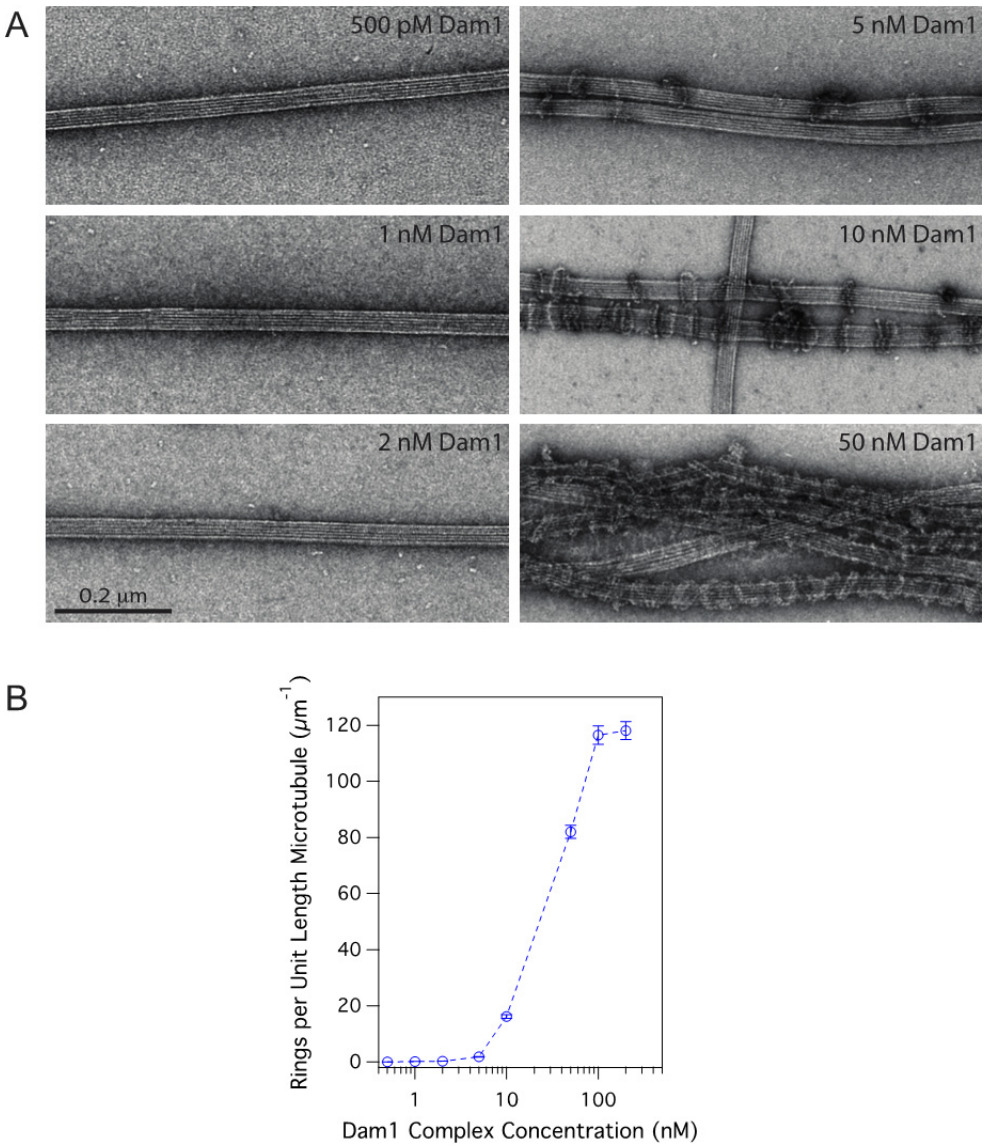

Figure 3.2 Assembly of oligomeric rings of the Dam1 complex around microtubules
(*A*) Negative-stain electron micrographs of oligomeric rings formed by the Dam1 complex around taxol-stabilized microtubules. (*B*) The number of rings observed per unit length (µm) of microtubule was quantified (statistics shown in Table 3.1) and plotted against the total concentration of Dam1 complex. Error bars represent counting uncertainties.

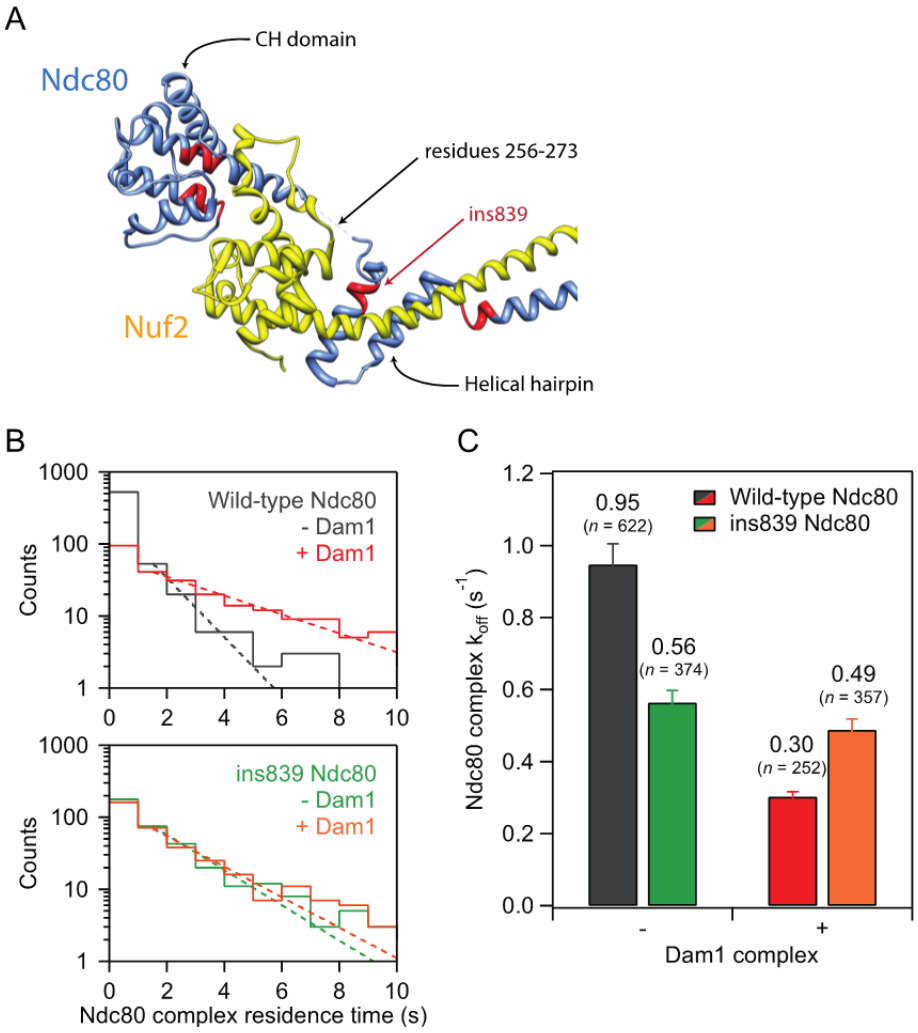

Figure 3.3 The ability of the Dam1 complex to enhance binding of Ndc80 complexes to microtubules is abrogated by a lethal insertion in the helical hairpin

(*A*) Four lethal insertion clusters (red) are mapped onto homologous regions of the human Ndc80 (blue) crystal structure (PDB 2VE7; CIFERRI *et al.* 2008), with the ins839 cluster labeled. The structure is illustrated with the UCSF Chimera package (PETTERSEN *et al.* 2004). Illustration reproduced from Figure 2.4A. (*B*) Residence time distributions of GFP-tagged Ndc80 complex on microtubules fit with single exponentials (dashed lines) were used to determine the dissociation rate constants, k_{off}. Top: wild-type Ndc80 complex in the absence (grey) or presence (red) of Dam1 complex. Bottom: ins839 Ndc80 complex in the absence (green) or presence (orange) of Dam1 complex. (*C*) The dataset in (*B*) is plotted as a bar graph. Wild-type Ndc80 complex data reproduced from Figure 2.4.

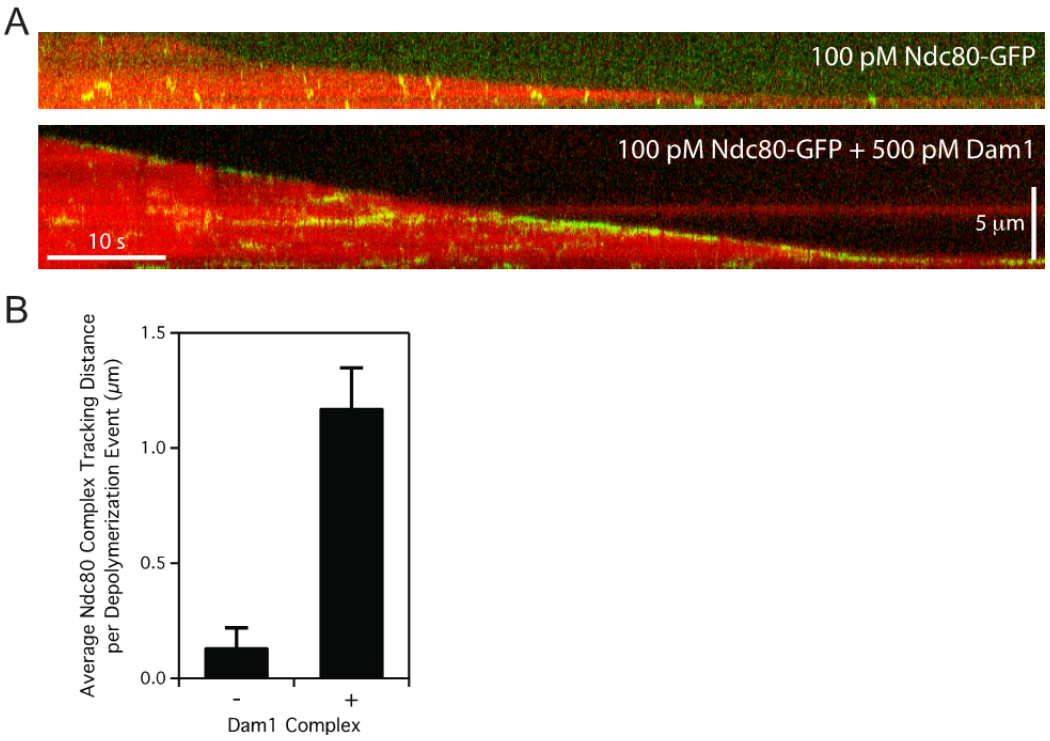

Figure 3.4 Ndc80 complex tracks with disassembling tips in the presence of Dam1 complex
(*A*) Representative two-color kymographs showing the tip-tracking ability of Ndc80 complex (100 pM) in the presence or absence of Dam1 complex (500 pM). Movement of GFP-tagged Ndc80 complex (green) is shown on disassembling microtubules (red). Concentrations are of free complexes in solution.
(*B*) Average tracking distance of Ndc80 complex per depolymerization event in the absence of Dam1 complex (n = 19) or in the presence of 500 pM Dam1 complex (n = 62). Bars are mean values ± s.e.m.

Chapter 4

Regulation of kinetochore-microtubule attachments by Aurora B

Introduction

Kinetochores not only serve as physical bridges between chromosomes and spindle microtubules, but also are regulatory hubs that ensure chromosome segregation fidelity during mitosis. For example, Aurora B kinase is responsible for resetting aberrant kinetochore-microtubule attachments to achieve biorientation (CHEESEMAN *et al.* 2002; HAUF *et al.* 2003; PINSKY *et al.* 2006; TANAKA *et al.* 2002). Many of the microtubule-binding components of the kinetochore, including the Ndc80 and Dam1 complexes, are targets of Aurora B (CHEESEMAN *et al.* 2002; CHEESEMAN *et al.* 2006; DELUCA *et al.* 2006; GESTAUT *et al.* 2008; PINSKY *et al.* 2006; SHANG *et al.* 2003). It is generally thought that phosphorylation of these targets triggers the release of incorrect attachments (BIGGINS and MURRAY 2001; CHEESEMAN *et al.* 2002; CIMINI *et al.* 2006; HAUF *et al.* 2003; PINSKY *et al.* 2006; TANAKA *et al.* 2002).

Previously, we demonstrated that phosphorylation by the yeast Aurora B homolog Ipl1 at one target site within the Dam1 complex, Ser 20 of Dam1, reduces its affinity for the microtubule lattice (GESTAUT *et al.* 2008). Two-hybrid assays and pull downs with *in vitro* translated proteins using phosphomimetic mutations at Ipl1 target sites in Dam1 also suggested that phosphorylation of the Dam1 complex modulates its interaction with the Ndc80 complex (SHANG *et al.* 2003). Moreover, Ipl1 target sites on Dam1 are dephosphorylated as cells enter metaphase in a cohesin-dependent manner, which could prevent kinetochore-microtubule attachment turnover as biorientation is established (KEATING *et al.* 2009). In this study, we show that Ipl1 regulates the interaction between the Ndc80 and Dam1 complexes. This provides

evidence for a mechanism by which Aurora B resets aberrant kinetochore-microtubule attachments by targeting multiple interfaces within the kinetochore.

Emerging evidence suggests that in higher eukaryotes, Aurora B activity does not always result in kinetochore-microtubule detachment. For example, early in mitosis when merotelic attachments are more prevalent, phosphorylation of the Ndc80 complex is relatively high, yet kinetochores do not appear to release from their K-fibers (CIMINI *et al.* 2003; DELUCA *et al.* 2011). Similarly, syntelic attachments formed in the presence of a reversible Aurora B inhibitor are not immediately released when the kinase is reactivated (LAMPSON *et al.* 2004). Instead, the K-fiber microtubules disassemble, carrying the kinetochores back to the centrosome, where the attachments are corrected by an unknown mechanism. These results suggest that Aurora B additionally acts to regulate microtubule dynamics as a part of its mechanism of error correction.

Additional findings suggest that Aurora B modulates microtubule dynamics through regulation of the Ndc80 complex. A component of the human Ndc80 complex, the Hec1 protein, has a disordered N-terminal tail that is targeted by Aurora B *in vivo* (GUIMARAES *et al.* 2008; MILLER *et al.* 2008). In PtK cells, preventing phosphorylation of these target sites not only results in hyper-stable kinetochore-microtubule attachments, but also damped kinetochore oscillations (DELUCA *et al.* 2011). The abnormal oscillations could be explained by direct or indirect contributions from the Ndc80 complex. The Ndc80 complex could itself directly control microtubule dynamics in response to Aurora B activity. An alternative (but not mutually exclusive) explanation is that phosphorylation of Hec1 alters the localization of other factors that modulate dynamics. These may include the microtubule stabilizer EB1 and the microtubule depolymerase MCAK, both of which are also targets of Aurora B (HUNTER *et al.* 2003; JIANG *et*

al. 2009; KNOWLTON *et al.* 2006; MANNA *et al.* 2008; TIRNAUER *et al.* 2002; ZHANG *et al.* 2007; ZIMNIAK *et al.* 2009).

Here, we show that the human Ndc80 complex directly stabilizes the tips of disassembling microtubules, slows the rate of disassembly, and promotes microtubule rescue (the transition from microtubule shortening to growth) *in vitro*. By contrast, Ndc80 complex with mutations mimicking Aurora B phosphorylation was impaired in its ability to influence microtubule dynamics, even while tracking with the tips of disassembling microtubules. This diminished ability of the phosphomimetic complex to affect dynamics is not solely a result of weakened microtubule binding, as an N-terminally truncated complex with similar affinity was still able to promote rescue. These results suggest that Aurora B modulates microtubule dynamics through regulation of the human Ndc80 complex, and this mechanism could be separable from effects on attachment stability.

Materials and methods

Protein expression and purification

Recombinant *S. cerevisiae* Ndc80 and Dam1 complexes were expressed and purified as described above (Chapter 3). Human Ndc80 complex was co-expressed from two di-cistronic plasmids encoding Spc25/Spc24-His_6 and Hec1/Nuf2 in *E. coli* BL21 cells (Rosetta; Novagen) and purified as previously described (POWERS *et al.* 2009).

Phosphorylation of the Dam1 complex

Dam1 complex was phosphorylated with purified GST-Ipl1 and GST-Sli15 as described (GESTAUT *et al.* 2008). The reaction (50 µl) contained 4 µM GFP- or mCherry-tagged S20A Dam1 complex, 0.5 µM GST-Ipl1, 0.5 µM GST-Sli15 (residues 554-698), 200 mM NaCl, 10 mM ATP, 25 mM $MgCl_2$ and 50 mM HEPES buffer, pH 7.2. Reactions were incubated at 30°C for 90 min. Control reactions lacked GST-Ipl1 and GST-Sli15. Control reactions lacking ATP were also performed and gave similar results as previously reported (GESTAUT *et al.* 2008). Ipl1 activity was not eliminated after the phosphorylation reaction. Therefore, to ensure that residual Ipl1 from the reaction did not affect our assays, we performed mock phosphorylation reactions using BSA in place of the Dam1 complex. The components of this mock reaction had no effect on the diffusion and dissociation rate constants of the Ndc80 complex either in the absence or presence of the Dam1 complex (Appendix B, Figure S5).

TIRF microscopy

TIRF microscopy with *S. cerevisiae* Dam1 complex and GFP-tagged Ndc80 complex was performed as described above (Chapter 3). GFP-tagged human Ndc80 complex was assayed in BRB80 (80 mM PIPES, 120 mM K^+, 1 mM $MgCl_2$, and 1 mM EGTA, pH 6.9) or BRB40

(40 mM PIPES, 60 mM K^+, 1 mM $MgCl_2$, and 1 mM EGTA, pH 6.9) with 8 mg ml^{-1} BSA, 10 μM taxol and an oxygen scavenger system.

Bulk microtubule binding assays

Microtubule binding assays were performed as described (GRACZYK and DAVIS 2011) with the following modifications. GFP-tagged human Ndc80 complex was incubated with taxol-stabilized microtubules in BRB80 with 10 μM taxol and 8% gel filtration buffer (50 mM HEPES, 200 mM NaCl, pH 7.6), and pelleted through a glycerol cushion onto a coverslip. Slides were imaged on a DeltaVision system (Applied Precision) equipped with an IX70 inverted microscope (Olympus), an U Plan Apo 100x objective (1.35 NA), and a CoolSnap HQ digital camera (Photometrics). For each slide, 10 z-sections (0.3 μm) were taken in 10 consecutive panels (512 x 512 pixels, binned 2 x 2) using filter sets to detect GFP and Alexa-568. To determine the amount of GFP-tagged Ndc80 complex for each slide, the average pixel intensity for the second z-section image in the GFP channel was averaged for the 10 panels. These values were corrected for background (a slide in which microtubules were incubated in the absence of Ndc80 complex) and lamp intensity (using the photosensor value). Standard curves were made by incubating increasing concentrations (up to ~60 nM) of wild-type or mutant Ndc80 complex with a saturating amount of microtubules (140 nM) in the appropriate buffers (BRB80 or BRB40), such that all Ndc80 complex added to the reaction was bound to microtubules. Microtubules were pelleted and imaged as described above. Slopes from the standard curves were used to convert fluorescence intensity values to concentrations for microtubule-bound Ndc80 complexes.

To generate binding curves, increasing concentrations of Ndc80 complex (0 to 15 nM) were assayed with microtubules (2.5 nM tubulin dimers). Microtubule binding for the 9D and

ΔN Ndc80 complexes was undetectable in BRB80, so binding assays were performed with 0 to 35 nM complex in BRB40. Binding curves were fitted to the Hill (HILL 1910) and McGhee and von Hippel (MCGHEE and VON HIPPEL 1974) models in Igor Pro (Wavemetrics) using iterative least-squares fitting. Errors on curve fit parameters (K_d, n_H, w, and i) represent the standard deviation estimated by Igor Pro.

Electron microscopy

For the disassembly assay, microtubules were assembled by incubating cleared tubulin (~6 μg/μl) in BRB80 containing 2 mM GTP, 5 mM $MgCl_2$, and 4% DMSO at 37°C for 30 min. After assembly, 1 volume of warm BRB80 (37°C) was added to make the stock microtubule mix. Disassembly was induced by diluting 1 μl of microtubule mix into 200 μl of a filtered BRB80 solution (0.22 μm filter, Millipore) containing 25 nM human Ndc80 complex, 25 nM *S. cerevisiae* Dam1 complex, or 10 μM taxol, and incubating for 2 minutes at room temperature.

Copper grids were carbon-coated and positively charged in a glow discharge device (EMS) at 25 mA for 2 minutes. Immediately after microtubule disassembly, a drop of the reaction mix (2 μl) was applied onto a freshly discharged grid and incubated for 20 seconds. Excess sample was blotted off, the grid was washed twice with BRB80, once with 0.075% uranyl formate, and stained with uranyl formate. Excess stain was blotted off and the grid was air-dried. Grids were viewed on a transmission electron microscope (Spirit T12, FEI) operating at 120kV and images were recorded on a 1k x 1k bottom-mount slow-scan CCD camera (Gatan) at a nominal magnification of 21,000x at the specimen level.

Additional Material and methods are described in Appendices B and C.

Results

Ipl1 phosphorylation regulates the interaction between Ndc80 and Dam1 complexes of budding yeast

Previous experiments have suggested that Ipl1 phosphorylation of the budding yeast Dam1 complex regulates its interaction with the Ndc80 complex (SHANG *et al.* 2003). Phosphorylation of Ser 20 on the Dam1 protein weakens the interaction of the Dam1 complex with microtubules (GESTAUT *et al.* 2008). To determine how phosphorylation at sites other than Ser 20 affects the interaction between the Dam1 and Ndc80 complexes, we used a modified Dam1 complex with a Ser 20 to Ala mutation (S20A). Working with Neil Umbreit, we found that Dam1 complex with the S20A substitution interacts with microtubules in a manner that is indistinguishable from the wild-type complex, except that the interaction is insensitive to Ipl1 phosphorylation (Appendix B, Figure S4A and B). The phosphorylated S20A Dam1 complex also tracks with disassembling microtubule tips and is less diffusive at high concentrations, as expected for oligomers (Appendix B, Figure S3). Phosphorylated S20A Dam1 complex also slows the disassembly of microtubules, as reported for wild-type Dam1 complex (FRANCK *et al.* 2007; GRISHCHUK *et al.* 2008a; WESTERMANN *et al.* 2006).

In the presence of unphosphorylated S20A Dam1 complex, diffusion of the Ndc80 complex on microtubules is slowed, dissociation rate constant is decreased and tip-tracking is enhanced as described for the wild-type Dam1 complex (Figure 4.1). However, Ipl1 phosphorylation of the S20A Dam1 complex abolished the ability of Dam1 complex to slow the diffusion and to decrease the dissociation rate constant of the Ndc80 complex (Figure 4.1B and C). Moreover, phosphorylated S20A Dam1 complex did not enhance the tip-tracking ability of the Ndc80 complex (Figure 4.1D). Control experiments were performed to

ensure that after the initial Ipl1 phosphorylation reaction with the S20A Dam1 complex, residual Ipl1 activity was negligible (Appendix B, Figure S5 and Materials and methods). Furthermore, working with Daniel Gestaut, we found that the ten proteins of the Dam1 complex do not dissociate from one another when the complex is phosphorylated by Ipl1 (Appendix B, Figure S4C). Since phosphorylation of the S20A Dam1 complex does not alter the behavior of the Dam1 complex alone but abolishes its ability to change the behavior of the Ndc80 complex, we conclude that Ipl1 phosphorylation of the Dam1 complex inhibits its interaction with the Ndc80 complex.

The human Ndc80 complex directly stabilizes disassembling microtubule tips and promotes microtubule rescue

Our results provide a model for how Aurora B kinase in budding yeast (Ipl1) can modulate corrective detachment by targeting the Dam1 complex. However, no homologs of the Dam1 complex have been identified in higher eukaryotes. Furthermore, observations in cultured mammalian cells suggest that Aurora B could also regulate microtubule dynamics to correct aberrant kinetochore-microtubule linkages (LAMPSON *et al.* 2004), possibly though Ndc80 (DELUCA *et al.* 2011). While the Ndc80 complex from yeast and worms has been extensively studied *in vitro* (CHEESEMAN *et al.* 2006; LAMPERT *et al.* 2010; POWERS *et al.* 2009; WEI *et al.* 2006; WEI *et al.* 2005), most work on the human complex has been limited to the use of truncated forms (ALUSHIN *et al.* 2010; CHEESEMAN *et al.* 2006; CIFERRI *et al.* 2008; TOOLEY *et al.* 2011; WEI *et al.* 2007; WILSON-KUBALEK *et al.* 2008). Using full-length recombinant human Ndc80 complex, I first characterized the affinity and cooperativity of microtubule binding using a bulk microtubule binding assay that measures the amount of GFP-tagged complex bound to microtubules over varying concentrations of complex (Figure 4.2A) (GESTAUT *et al.* 2008;

GRACZYK and DAVIS 2011). Based on a standard Hill model fit (HILL 1910), the human Ndc80 complex binds microtubules with a strong apparent affinity (K_d = 3.3 ± 0.2 nM) and has a Hill coefficient of 2.2 ± 0.2 (Figure 4.2B). The Hill model describes cooperativity arising from allosteric changes that enhance ligand binding to a protein. In the binding assay, cooperativity is likely based on interactions between Ndc80 complexes that occur while they are bound to microtubules. Therefore, we employed a model previously developed by McGhee and von Hippel that describes cooperativity between ligands binding to a polymer lattice (MCGHEE and VON HIPPEL 1974). Fitting the binding data with this model (Figure 4.2C) also showed a strong apparent affinity (K_d = 8.3 ± 1.5 nM) and cooperativity between Ndc80 complexes on the microtubule lattice (w = 3.4 ± 0.5). As compared to the Hill model fit, the McGhee and von Hippel model fit yielded a weaker apparent K_d for a single complex. Thus, interactions between complexes bound to the microtubule contribute to the K_d predicted by the Hill model. This finding is supported by the observation that at high concentrations, truncated human Ndc80 complex binds microtubules in clusters (ALUSHIN *et al.* 2010). Fits to both models revealed a lattice occupancy of ~2 Ndc80 complexes per tubulin dimer, consistent with cryo-electron microscopy reconstructions that showed a 4-nm spacing of the truncated complex on microtubules (ALUSHIN *et al.* 2010).

Using TIRF microscopy, Daniel Gestaut in our laboratory visualized GFP-tagged human Ndc80 complex on disassembling microtubules. The human Ndc80 complex can track with disassembling microtubule tips (Appendix C, Figure 2A), unlike the budding yeast Ndc80 complex, which requires the Dam1 complex or oligomerization on the surface of beads. The human Ndc80 complex also slowed the rate of microtubule disassembly (Appendix C, Figure 2C). In some cases, disassembly appeared to stall as the tip reached bright particles of

GFP-tagged Ndc80 complex, and only continued after the complex appeared to detach. This behavior resulted in a step-like appearance in kymographs (Appendix C, Figure 2B). Furthermore, Alexa-647-labeled tubulin decorated with Ndc80 complex was often seen bending away from the long axis of the microtubule (observed for 66 ± 10% of microtubules; Figure 4.3A). Because these curled extensions can be resolved by light microscopy (116-nm pixels), their curvature is gentler than the tight 20-nm curls seen at bare disassembling tips by cryo-electron microscopy *in vitro* (MANDELKOW *et al.* 1991). To further investigate tip structure in the presence of Ndc80 complex, I performed a similar disassembly assay and visualized the microtubule tips by negative-stain electron microscopy. Working with Breanna Vollmar (Gonen laboratory, Janelia Farm, HHMI), we observed open protofilament sheets emanating from the tips of microtubules stabilized by Ndc80 complex (Figure 4.3B). These sheets were not observed at the tips of microtubules stabilized by taxol or by the Dam1 complex (Figure 4.3C) (WESTERMANN *et al.* 2005). Microtubules exposed to the same conditions in the absence of any stabilizing factor completely disassembled into free tubulin. Although we were unable to distinguish between microtubule plus- and minus-ends in the electron micrographs, curled extensions were observed in the presence of Ndc80 complex at both microtubule ends in the TIRF assay (Appendix C, Figure S3A). Together, the TIRF and electron microscopy assays suggest that the Ndc80 complex slows disassembly by stabilizing protofilament extensions at microtubule tips.

To test how purified Ndc80 complex couples to dynamic microtubule tips under force, Neil Umbreit in our laboratory employed an optical trap-based bead motility assay (FRANCK *et al.* 2010). Beads decorated with human Ndc80 complex remained coupled to microtubule tips against 2 pN of tension (Appendix C, Figure 3A and B), similar to the forces sustained by

kinetochore-microtubule attachments *in vivo*, which are estimated to be 0.4 to 8 pN (NICKLAS 1988; PEARSON *et al.* 2001; POWERS *et al.* 2009). Against the applied force, beads tracked robustly with the tips of disassembling microtubules and slowed the rate of microtubule disassembly, consistent with results from the TIRF-based assays (Figure 4.4A and B). Strikingly, disassembling microtubule tips coupled to beads coated with the Ndc80 complex rescued ~70-fold more frequently than bare microtubules (Figure 4.4C; 135 ± 24 hr^{-1} compared to 2 ± 1 hr^{-1}). Therefore, the human Ndc80 complex is an effective tip-coupler that can directly slow microtubule disassembly and promote rescue.

By contrast, in our previous work with the budding yeast Ndc80 complex, we observed little effect on the rate of microtubule rescue (POWERS *et al.* 2009). Here we analyzed the dataset reported in Powers *et al*., specifically looking for rescue events. Microtubules rescued at a frequency of 9 ± 5 hr^{-1} while coupled to beads coated with budding yeast Ndc80 complex (n = 4 rescues, ~100-2700 complexes per bead, against ~1 pN of force). This is close to the rate of rescue for microtubules not coupled to beads (reported above). Therefore, the budding yeast Ndc80 complex, unlike the human complex, appears to have little ability to promote microtubule rescue.

Aurora B phosphomimetic mutations in the human Ndc80 complex inhibit its ability to influence microtubule dynamics

The Hec1 protein of the Ndc80 complex contains a calponin homology domain that is important for its microtubule binding activity (CIFERRI *et al.* 2008; WEI *et al.* 2007). In addition, Hec1 has a disordered N-terminal tail that contributes to the affinity of the complex for microtubules (GUIMARAES *et al.* 2008; MILLER *et al.* 2008; WEI *et al.* 2007). *In vivo*, the tail is a target for the Aurora B kinase, and mutations that mimic phosphorylation at these sites result in

unattached kinetochores (GUIMARAES *et al.* 2008; SUNDIN *et al.* 2011). Consistent with this observation, Aurora B phosphorylation of a truncated Ndc80 complex reduces its binding to microtubules *in vitro* (CIFERRI *et al.* 2008). On the other hand, mutations that block phosphorylation severely damp kinetochore oscillations *in vivo* (DELUCA *et al.* 2011). These findings suggest that phosphorylation in the Hec1 tail is required not only for regulation of kinetochore-microtubule attachments, but also for normal kinetochore-microtubule dynamics. Using the optical trap assay, Neil Umbreit tested the direct contribution of the tail to microtubule dynamics *in vitro*. In addition to the wild-type complex, Neil Umbreit and Daniel Gestaut purified Ndc80 complex with the nine putative Aurora B target sites in the Hec1 tail mutated to aspartic acid to mimic phosphorylation (9D), and Ndc80 complex with the Hec1 tail deleted (ΔN).

Beads coated with wild-type, 9D, and ΔN complexes were all able to slow the rate of microtubule disassembly in a concentration-dependent manner while tracking with disassembling tips against ~2 pN of applied force (Figure 4.4A and B). However, the 9D and ΔN complexes were impaired relative to the wild-type complex. The ability of these mutant complexes to track with and slow disassembly was recovered to wild-type levels by increasing the density of decoration on beads ~20-fold (Figure 4.4A and B; compare 0.5 and 1 nM wild-type to 10 and 20 nM mutant complexes, respectively). Therefore, increasing the number of mutant complexes on beads compensates for their decreased coupling performance. When assayed at comparable coupling performance, the wild-type and ΔN complexes promoted microtubule rescue, but the 9D complex did not (Figure 4.4C). Deletion of the Hec1 tail reduced the ability of the complex to promote rescue only modestly (~2-fold). In contrast, phosphomimetic mutations in the tail nearly abolished this activity. In addition, the ΔN

complex, but not the 9D complex, stabilized curled extensions at disassembling microtubule tips in the TIRF assay (Appendix C, Figure 3F). Thus, phosphomimetic mutations do not simply negate the activity of the tail, but actively interfere with the ability to modify microtubule tip structure and promote rescue.

The ΔN and 9D complexes performed similarly in tracking with and slowing microtubule disassembly, suggesting that their disparate effects on microtubule rescue and tip structure are not due simply to a difference in their microtubule-binding affinities. I quantified binding of GFP-tagged 9D and ΔN complexes directly by bulk microtubule binding assays. Unlike the wild-type complex, binding of the mutant complexes was undetectable in standard BRB80 (120 mM K^+) buffer conditions, so the assays were performed in BRB40 (60 mM K^+) buffer. Fits to both the Hill and the McGhee and von Hippel models (Figure 4.4D and E) show that the 9D and ΔN complexes are indistinguishable from one another in their apparent affinities, cooperativity constants, and lattice occupancies (McGhee and von Hippel fit for 9D and ΔN: K_d = 78 ± 20 and 73 ± 20 nM, w = 7 ± 2 and 7 ± 1, i = 2.4 ± 0.1 and 2.4 ± 0.1 per tubulin dimer, respectively). Therefore, phosphomimetic mutations reduce the affinity of the Ndc80 complex for microtubules and impair its ability to promote microtubule rescue. However, these two effects are not strictly coupled; deletion of the Hec1 tail equally reduces the affinity of the complex for microtubules, but is not as detrimental to its ability to modify microtubule tip structure and dynamics. These findings suggest that Aurora B phosphorylation has separable effects on attachment stability and microtubule dynamics at the kinetochore.

Discussion

A mechanism for Aurora B-mediated corrective detachment in budding yeast

The regulatory mechanism that ensures chromosome biorientation has been proposed to respond to the level of tensile force on the kinetochore (KELLY and FUNABIKI 2009). When kinetochores make attachments that generate little tension, such as monotelic or syntelic attachments, progression to anaphase is blocked. Key to this regulation, the conserved Aurora B kinase is responsible for the release of aberrant kinetochore-microtubule attachments (BIGGINS *et al.* 1999; HAUF *et al.* 2003; PINSKY *et al.* 2006; TANAKA *et al.* 2002). We showed previously that phosphorylation by the yeast Aurora B kinase Ipl1 at Ser 20 of Dam1 decreases the affinity of the Dam1 complex for the microtubule lattice (GESTAUT *et al.* 2008). We show here that Ipl1 phosphorylation of the Dam1 complex at sites other than Ser 20 weakens its interaction with the Ndc80 complex. Together these observations suggest that Ipl1 phosphorylation of the Dam1 complex promotes corrective detachment of kinetochores via two distinct mechanisms, decreasing the affinity of the Dam1 complex for both the Ndc80 complex and for microtubules. Regulation by Aurora B kinase is a conserved feature of kinetochore function in all eukaryotes. Therefore, we propose that regulation at both the kinetochore-microtubule interface and between components of the kinetochore itself will extend to mechanisms of corrective detachment in higher eukaryotes.

The human Ndc80 complex directly modulates microtubule dynamics

The Ndc80 complex is a conserved and essential microtubule-binding component of the kinetochore. Here, we characterized the binding of full-length human Ndc80 complex to microtubules *in vitro*. The Ndc80 complex bound cooperatively to microtubules with a strong affinity, and directly promoted microtubule rescue. Our *in vitro* results using unphosphorylated

wild-type Ndc80 complex explain observations made in cells. In the absence of Hec1 phosphorylation, we found that the Ndc80 complex antagonizes microtubule disassembly. This effect explains why blocking Hec1 phosphorylation *in vivo* causes hyper-stabilized K-fibers, and leads to damped sister kinetochore oscillations and severe defects in cell division (DELUCA *et al.* 2011). We believe our findings represent the first demonstration that a core component of the human kinetochore directly modifies microtubule rescue rate *in vitro*. This ability has been shown previously for a core kinetochore component only once, with the budding yeast Dam1 complex (FRANCK *et al.* 2007), which has no known homolog in higher eukaryotes. Notably, the budding yeast Ndc80 complex does not effectively promote microtubule rescue (POWERS *et al.* 2009), even though the composition and domain structure of the complex are highly conserved.

Our results also indicate a possible mechanism by which the Ndc80 complex promotes microtubule rescue. In the absence of stabilizing factors, protofilaments at disassembling microtubule tips form tight ~20-nm curls (MANDELKOW *et al.* 1991). When microtubules are stabilized by a non-hydrolyzable GTP analog, protofilaments are straighter at disassembling tips (MULLER-REICHERT *et al.* 1998). We found that the tips of disassembling microtubules in the presence of Ndc80 complex were gently curved (as seen by TIRF microscopy) and formed large protofilament sheets (as seen by electron microscopy). These observations suggest that the Ndc80 complex promotes microtubule rescue by stabilizing tip structures with straighter protofilaments. Alushin and coworkers proposed that the Hec1 calponin homology domain recognizes the interface between tubulin monomers (ALUSHIN *et al.* 2010), at a putative hinge region (WANG and NOGALES 2005). Our findings are consistent with this model. Ndc80 complex lacking the Hec1 tail was able to modify microtubule tip structure and promote rescue, indicating that other parts of the complex (outside of the tail) are primarily responsible for this

activity. We propose that binding of the Hec1 calponin homology domain at the hinge region between tubulin subunits induces a straighter protofilament conformation that facilitates microtubule rescue.

Aurora B regulates microtubule dynamics through the Ndc80 complex

Consistent with the role of Aurora B kinase in releasing aberrant kinetochore-microtubule attachments (LIU and LAMPSON 2009), PtK cells carrying a phosphomimetic mutant Ndc80 (9D) complex have unattached kinetochores (GUIMARAES *et al.* 2008; SUNDIN *et al.* 2011). We found that the human 9D complex bound to microtubules more weakly relative to the wild-type complex as determined by three independent *in vitro* assays: (1) Single molecules of the 9D complex dissociated more quickly (>10-fold) from the microtubule lattice (Appendix C, Figure 4A). (2) In our bulk assays, binding of the 9D complex was undetectable under conditions in which the wild-type complex bound strongly to microtubules. (3) At equal surface density on beads, the 9D complex was impaired in its ability to track with microtubule disassembly against force. In all three of these assays, the 9D complex behaved similarly to and not worse than Ndc80 complex that lacks the tail domain (ΔN). Therefore, mutations that mimic complete phosphorylation of the Hec1 tail prevent the tail from contributing to microtubule binding.

In vivo observations suggest that in higher eukaryotes, Aurora B does not simply trigger kinetochore-microtubule detachment but additionally regulates microtubule dynamics (DELUCA *et al.* 2006; DELUCA *et al.* 2011; LAMPSON *et al.* 2004) (Figure 4.5). In PtK cells, syntelic kinetochore-microtubule attachments are not lost immediately following Aurora B activation (LAMPSON *et al.* 2004). Instead, reactivation of Aurora B appears to induce disassembly of the kinetochore microtubules, and the kinetochores track with disassembly back to the centrosome,

where the attachments are corrected. Our results offer insight into these observations. At higher surface densities on beads (20 nM), the 9D complex tracked robustly with disassembling microtubule tips against force. Based on geometric constraints (POWERS *et al.* 2009), we estimate ~80 complexes can interact with the microtubule tip at this surface density. This is more than the number of Ndc80 complexes per microtubule *in vivo* (~20 per microtubule), but fewer than the number of complexes at a single mammalian kinetochore, which binds 20-25 microtubules through more than 400 attachments (LAWRIMORE *et al.* 2011; RIEDER 1982). Relative to the wild-type complex, the 9D and ΔN complexes are similarly impaired in their binding affinity and tracking performance. However, the ΔN complex promotes microtubule rescue, while the 9D complex does not. Thus, a phosphomimetic Hec1 tail interferes with the ability of the Ndc80 complex to modulate microtubule dynamics, possibly by blocking the ability of the calponin homology domain to stabilize a straighter protofilament conformation. Taken together, these *in vitro* observations explain how phosphorylation relieves microtubule stabilization at syntelic kinetochores to promote K-fiber disassembly, allowing the attached kinetochores to track back to the centrosome.

Here, we show that a conserved core microtubule-binding component of the human kinetochore directly influences microtubule dynamics. In addition, we find that phosphomimetic mutations of essential Aurora B phosphorylation sites in Hec1 not only weaken attachment, but also nearly abolish the ability of the Ndc80 complex to influence dynamics. These effects are separable, and might be independently tunable through phosphorylation of different subsets of target sites in the Hec1 tail. Together, our results indicate that microtubule dynamics can be regulated through Aurora B phosphorylation of the Ndc80 complex.

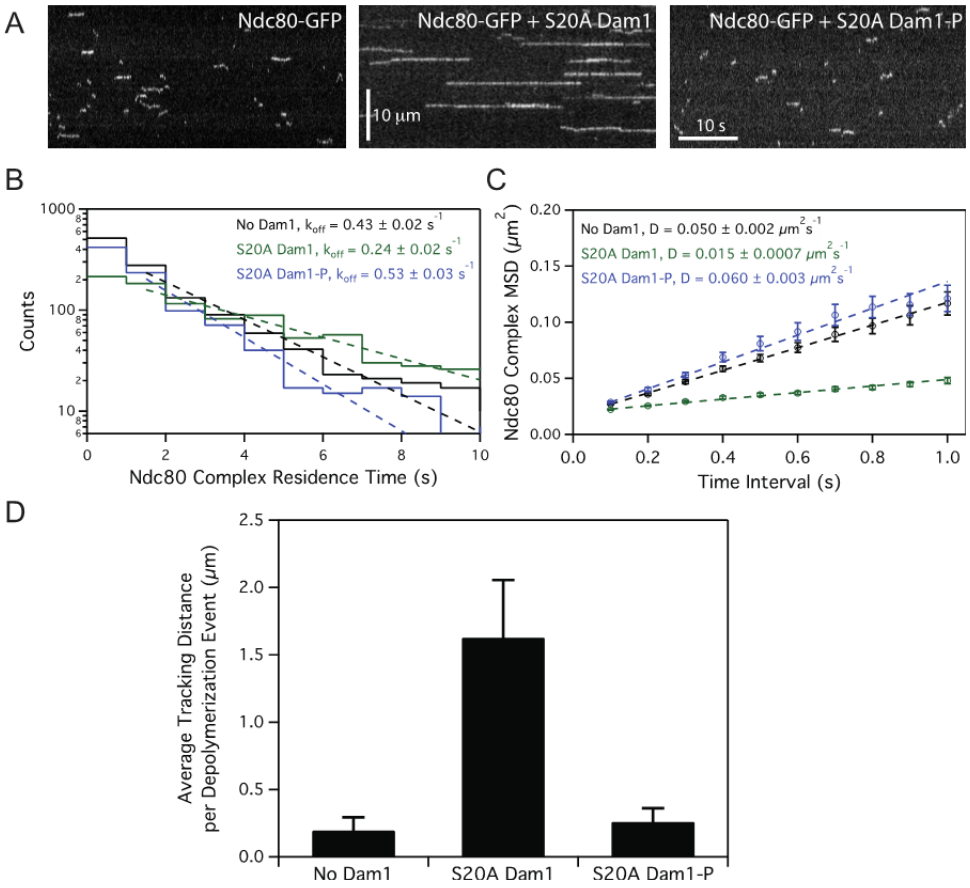

Figure 4.1 Ipl1 phosphorylation of the Dam1 complex regulates its interaction with the Ndc80 complex in budding yeast

(*A*) Representative kymographs showing changes in behavior of the Ndc80 complex (10 pM) with the addition of S20A Dam1 complex (500 pM) with or without Ipl1 phosphorylation. Concentrations are of free complexes in solution. (*B*) Residence time distributions of Ndc80 complex (10 pM) on microtubules without Dam1 complex (black histogram, n = 1266 events), with 500 pM S20A Dam1 complex (green histogram, n = 1081), and with 500 pM Ipl1 phosphorylated S20A Dam1 complex (blue histogram, n = 974). Dotted lines show the weighted exponential fits used to determine dissociation rate constants, k_{off}. (*C*) Mean-squared displacement (MSD) is plotted against time for Ndc80 complex (10 pM) on microtubules without Dam1 complex (black markers, n = 1102), with 500 pM S20A Dam1 complex (green markers, n = 1030), and with 500 pM Ipl1 phosphorylated S20A Dam1 complex (blue markers, n = 860). Markers are mean values ± s.e.m. Dotted lines show the weighted linear fit used to determine diffusion constant, D. (*D*) Average tracking distance of 100 pM Ndc80 complex per depolymerization event in the absence of Dam1 complex (n = 19), in the presence of 500 pM S20A Dam1 complex (n = 28), or in the presence of 500 pM Ipl1 phosphorylated S20A Dam1 complex (n = 39). Bars are mean values ± s.e.m.

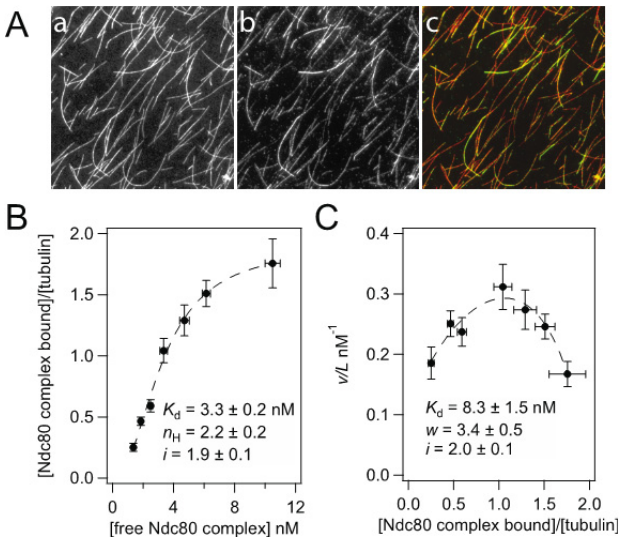

Figure 4.2 The human Ndc80 complex binds cooperatively to microtubules
(*A*) Representative image from the bulk microtubule binding assay with GFP-tagged human Ndc80 complex (2 nM) on taxol-stabilized Alexa-568-labeled microtubules (2.5 nM tubulin dimer). Panels show microtubules (**a**), Ndc80 complex (**b**), and merge (**c**). (*B*) Plot of binding density (v) versus free Ndc80 complex concentration (L). A fit to the Hill model (dashed line) was used to determine the apparent affinity (K_d), Hill coefficient (n_H), and lattice occupancy (i, the number of Ndc80 complexes bound per tubulin dimer). (*C*) Scatchard plot of the same data shown in (*B*), fit to the McGhee and von Hippel model (dashed line) to calculate the K_d, cooperativity parameter (w), and i. For (*B*) and (*C*), n = 8-10 replicates per data point, markers are mean ± s.e.m., and errors on model fit parameters (K_d, n_H, w, and i) represent s.d.

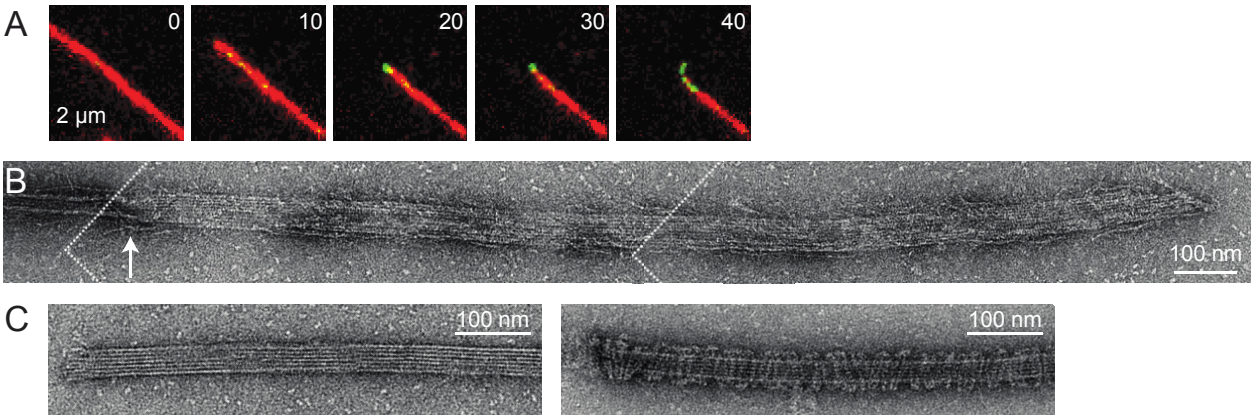

Figure 4.3 The human Ndc80 complex stabilizes protofilament extensions at disassembling microtubule tips

(*A*) Time-lapse images of a disassembling microtubule (red) in the presence of 500 pM GFP-tagged human Ndc80 complex (green) as a curled extension formed at the tip. Inset numbers show elapsed time, in seconds. Images provided by Daniel Gestaut. (*B*) Negative-stain electron micrograph of a disassembling microtubule tip stabilized by the Ndc80 complex. An arrow marks the transition from a closed microtubule to an open sheet. The figure was constructed from three images, whose boundaries are depicted by dotted white lines. (*C*) Negative-stain electron micrographs of a disassembling microtubule tip stabilized by taxol (left) or budding yeast Dam1 complex (right).

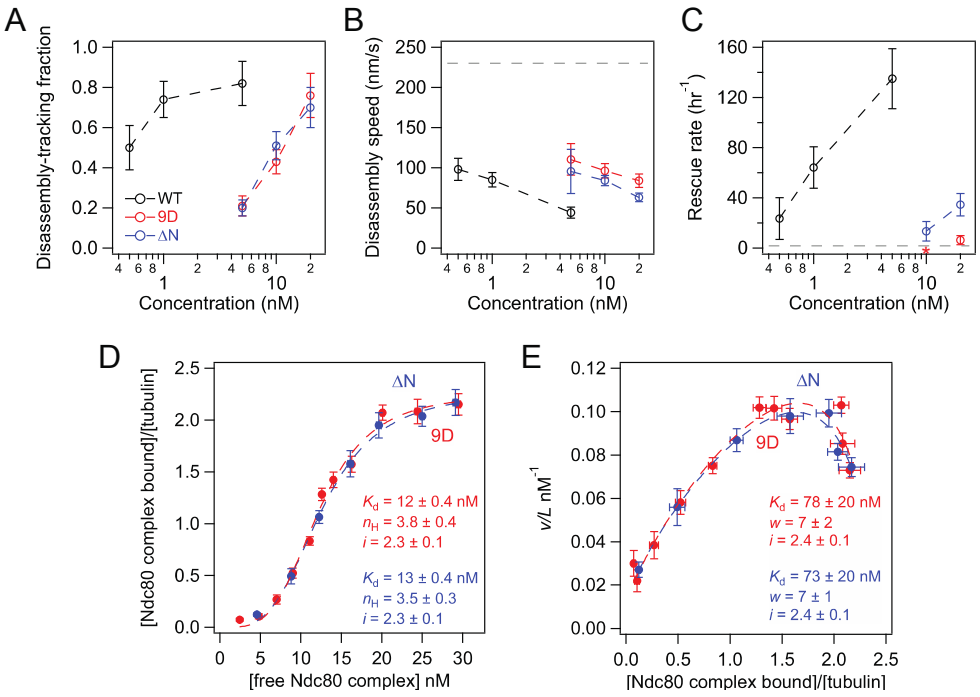

Figure 4.4 Phosphomimetic mutations in the human Ndc80 complex inhibit its ability to promote microtubule rescue

(*A*) The fraction of beads coated with wild-type or mutant Ndc80 complex capable of tracking against ~2 pN. From the disassembly-tracking events in (*A*), (*B*) mean microtubule disassembly speeds ± s.e.m. and (*C*) rescue rates were measured. Without load and in the absence of bead-bound Ndc80 complex, the disassembly rate was 230 ± 14 nm/s (dashed line in (*B*), $n = 26$) and the rescue rate was 2 ± 1 hr^{-1} (dashed line in (*C*), $n = 3$ events in 104 minutes of disassembly). Data in (*A*-*C*) collected by Neil Umbreit. Asterisks indicate that no rescues were observed. (*D* and *E*) Bulk microtubule binding assays of 9D (red traces, $n = 4$-7 replicates per data point) and ΔN (blue traces, $n = 6$-7 replicates per data point) Ndc80 complex on taxol-stabilized microtubules. Markers represent mean ± s.e.m. and assays were performed in BRB40 buffer. Dashed lines show fits of binding data to (*D*) Hill and (*E*) McGhee and von Hippel models. Errors on model fit parameters (K_d, n_H, w, and i) represent s.d.

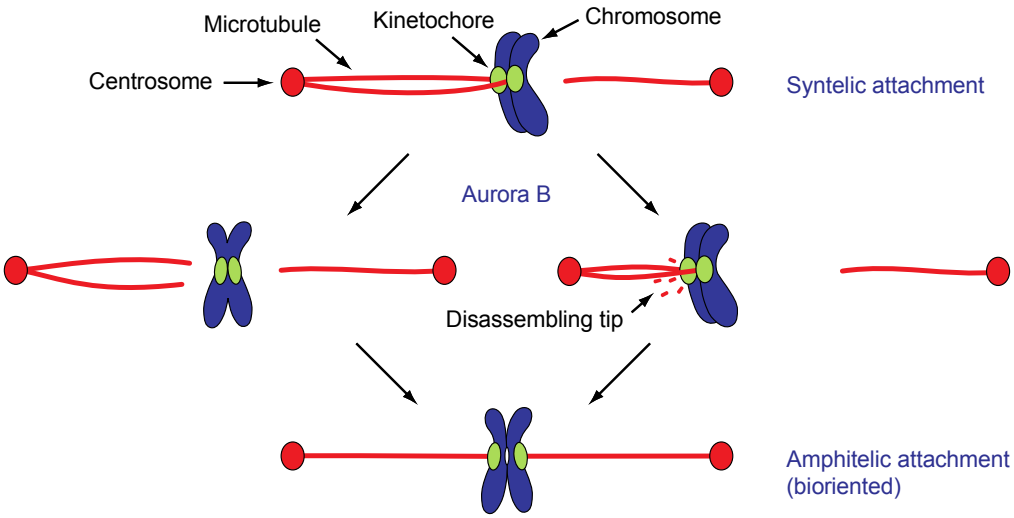

Figure 4.5 Models for Aurora B-mediated correction of syntelic kinetochore-microtubule attachments

Chapter 5
Conclusions and future directions

Dissecting the architecture of the Ndc80 complex at the budding yeast kinetochore

The Ndc80 complex is a conserved component of the kinetochore (MERALDI *et al.* 2006), and features an N-terminal calponin homology (CH) domain that is essential for kinetochore-microtubule coupling during mitosis (CIFERRI *et al.* 2008; WEI *et al.* 2007). However, the full extent of the role of the Ndc80 complex during cell division remains unknown. In this study, I employed an unbiased mutagenesis screen to identify essential domains in the budding yeast Ndc80 protein. I showed that one such domain, within a helical hairpin adjacent to the CH domain, influences microtubule binding by the complex *in vitro*. Furthermore, I defined a C-terminal segment of Ndc80 required for tetramerization of the Ndc80 complex *in vivo*. This tetramerization domain is smaller than one previously proposed based on experiments utilizing limited proteolysis (WEI *et al.* 2005). Future studies will be aimed at identifying the reciprocal domains in Nuf2, Spc24, and Spc25. Based on computational predictions, the tetramerization domain is likely not coiled-coil, and the nature of this structure has yet to be determined.

In addition to the helical hairpin and the tetramerization domain, the mutagenesis screen also identified essential domains in previously uncharacterized regions of Ndc80. Insertions in one of these domains were temperature sensitive. Here, I characterized one representative mutant from this domain, *ndc80-121*. At the non-permissive temperature, *ndc80-121* cells have unclustered kinetochores, fail to assemble a metaphase spindle, and arrest in a checkpoint-dependent manner. The *ndc80-121* mutations lie ~30 residues upstream of the predicted "loop" in Ndc80, while suppressor mutations mapped to the C-terminal end of Ndc80 and Nuf2, ~40 residues downstream of the loop. Combined with *in vitro* cross-linking experiments, these

results suggest that the Ndc80 complex folds at the loop, such that the *ndc80-121* mutation sites can contact the suppressor sites. Furthermore, this folded conformational is required to establish a metaphase spindle. This hypothesis is consistent with previous studies showing flexibility in the recombinant complex *in vitro* and a shortening in the distance between the N- and C-termini of the Ndc80 complex during the metaphase-to-anaphase transition *in vivo* (JOGLEKAR *et al.* 2009; WANG *et al.* 2008). However, the structural basis of this conformational change and its function during mitosis are still unknown. Therefore, future studies will address three main questions: (1) Is folding of the Ndc80 complex at the loop directly responsible for the change in distance between the two globular ends of the Ndc80 complex observed *in vivo*? (2) What is the structural organization of the loop region in Ndc80/Nuf2? (3) Do the *ndc80-121* mutation sites ($Ndc80^{Y465/I469}$) physically interact with the suppressor mutation sites ($Ndc80^{N564}$, $Nuf2^{L344}$)? These interactions could be within the same Ndc80 complex, or between adjacent Ndc80 complexes. The latter scenario is consistent with unclustering of kinetochore components in *ndc80-121* cells. If the *ndc80-121* mutation and suppressor sites do not physically interact, they could instead bind a separate kinetochore component that has yet to be identified. By addressing these questions, I hope to uncover the function of this new domain in Ndc80, and determine why it is required for spindle integrity. Future studies will also be aimed at characterizing the remaining temperature-sensitive mutants to discover new functions of Ndc80.

The Ndc80 complex as a coupler at the kinetochore-microtubule interface

Kinetochores attach to the plus-ends of spindle microtubules and harness microtubule dynamics to power chromosome movement (reviewed in INOUE and SALMON 1995). Remarkably, kinetochores can remain attached to microtubule tips even as tubulin dimers are added and removed from underneath its grasp. Two physical models describing this behavior

were proposed well before identification of the kinetochore components involved (reviewed in ASBURY *et al.* 2011). In the biased diffusion model, an array of individually weak binding elements can remain attached to a disassembling microtubule tip provided that its total binding energy is large enough and each element diffuses fast enough (HILL 1985). In the conformational wave model, curling protofilaments at the disassembling microtubule tip act via a power stroke to physically pull on kinetochore elements (KOSHLAND *et al.* 1988). The multivalent Ndc80 complex and the Dam1 complex ring were hypothesized to be the key kinetochore couplers, functioning through the biased diffusion and conformational wave models, respectively (JOGLEKAR *et al.* 2009; MIRANDA *et al.* 2005; POWERS *et al.* 2009; WAN *et al.* 2009; WESTERMANN *et al.* 2006). Indeed, the Ndc80 and Dam1 complexes can both couple cargo to assembling and disassembling microtubule tips under picoNewtons of external force *in vitro* (ASBURY *et al.* 2006; MCINTOSH *et al.* 2008; POWERS *et al.* 2009). However, it remains unclear how native kinetochores *in vivo*, which employ both Ndc80 and Dam1 complexes, utilize biased diffusion and conformational wave mechanisms to couple to microtubules. Future studies will test whether both biased diffusion and conformational wave models apply *in vivo*, or if one mechanism overrides the other. Alternatively, a hybrid mechanism combining aspects of both models could be employed. To begin testing these hypotheses, we first need to determine the oligomeric state of the Dam1 complex *in vivo*, since rings have only been observed *in vitro* and may not be necessary for tracking disassembling microtubule tips (GESTAUT *et al.* 2008). Furthermore, while we know that multiple copies of the Ndc80 complex are present at each kinetochore (JOGLEKAR *et al.* 2009; WAN *et al.* 2009), we do not know if this multivalency is required for kinetochore-microtubule coupling *in vivo*.

The Ndc80 complex is part of the conserved KMN network (CHEESEMAN *et al.* 2006; MERALDI *et al.* 2006). Since native kinetochore particles can couple to dynamic microtubule tips *in vitro* better than our Ndc80/Dam1 system (AKIYOSHI *et al.* 2010), we hypothesize that the other members of the KMN network may also be involved in strengthening microtubule attachments. This could occur through direct microtubule interactions (e.g., microtubule binding by the Spc105 component), or through indirect mechanisms (e.g., controlling the avidity of Ndc80 complexes, or influencing the microtubule-binding ability of the Ndc80 complex through conformational changes). Ultimately, we wish to develop a model describing kinetochore behavior *in vivo* through reconstitution of all the necessary components *in vitro*.

Comparisons between the Ndc80 complex of budding yeast and metazoans: implications for Aurora B regulation

The Ndc80 complex is an essential component of all eukaryotic kinetochores, and contains several conserved domain structures (MERALDI *et al.* 2006). The primary amino acid sequence, however, is poorly conserved; the budding yeast and human Ndc80 protein sequences are only 18% identical (ClustalW2, EMBL-EBI). One key distinction lies in the N-terminal tail, which is required for kinetochore function in metazoans, but is dispensable for growth in budding yeast (AKIYOSHI *et al.* 2009; GUIMARAES *et al.* 2008; KEMMLER *et al.* 2009; MILLER *et al.* 2008). One possible explanation for this discrepancy is the yeast-specific Dam1 complex. As discussed above, the budding yeast Ndc80 complex binds weakly to microtubules (POWERS *et al.* 2009), and the Dam1 complex acts as a processivity factor to strengthen kinetochore-microtubule attachments. By contrast, I found that the human Ndc80 complex binds microtubules with a stronger affinity and in a cooperative manner, more similar to the Dam1 complex (GESTAUT *et al.* 2008). Removing the N-terminal tail of the human Ndc80 complex significantly weakens its

affinity for microtubules. Additionally, the Dam1 complex could be responsible for controlling microtubule dynamics at the kinetochore (FRANCK *et al.* 2007), similar to the Ndc80 complex in humans (UMBREIT *et al.* 2012). Therefore, the budding yeast N-terminal tail could play a diminished role in kinetochore-microtubule coupling.

In both budding yeast and humans, the conserved Aurora B kinase is responsible for correcting syntelic kinetochore-microtubule attachments (reviewed in LIU and LAMPSON 2009). We show here that phosphomimetic mutations in the N-terminal tail of human Ndc80 inhibit its ability to promote microtubule rescue *in vitro*. This potentially explains observations made in cultured mammalian cells. Upon Aurora B activation, syntelic kinetochore pairs do not immediately detach from microtubules, but rather track with disassembling K-fibers back to the centrosome (LAMPSON *et al.* 2004). These erroneous attachments are then corrected, via an undefined mechanism. The involvement of Aurora B in breaking these syntelic attachments at the centrosome is also not known. In budding yeast, Aurora B destabilizes syntelic kinetochore-microtubule attachments directly (BIGGINS and MURRAY 2001; PINSKY *et al.* 2006; TANAKA *et al.* 2002). Aurora B phosphorylation of the yeast Dam1 complex not only weakens its binding to microtubules (GESTAUT *et al.* 2008), but also abolishes its interaction with the Ndc80 complex. Furthermore, phosphomimetic mutations in the N-terminal tail of budding yeast Ndc80 also weaken attachment strength *in vitro* (SARANGAPANI *et al.* 2013). Unlike with human Ndc80, these mutations in the yeast N-terminal tail do not appear to influence microtubule rescue (SARANGAPANI *et al.* 2013). Therefore, it remains unclear whether budding yeast Aurora B targets microtubule dynamics in addition to attachment strength during corrective detachment.

Future studies will be aimed at dissecting similar and divergent functions of Aurora B. For example, human and budding yeast Ndc80 have multiple Aurora B target sites (nine and

seven sites, respectively) in the N-terminal tail (AKIYOSHI *et al.* 2009; GUIMARAES *et al.* 2008; SUNDIN *et al.* 2011). This suggests that the ability of Aurora B to regulate microtubule attachment and/or dynamics can be tuned, perhaps by phosphorylation of a subset of available sites. Additionally, it is unclear why Aurora B targets other members of the KMN network (MASKELL *et al.* 2010; WELBURN *et al.* 2010; WESTERMANN *et al.* 2003), which may not function directly at the kinetochore-microtubule interface. By using our *in vitro* reconstitution system, we can dissect the effects of Aurora B phosphorylation at each site individually, and in combination.

BIBLIOGRAPHY

AKIYOSHI, B., C. R. NELSON, J. A. RANISH and S. BIGGINS, 2009 Analysis of Ipl1-mediated phosphorylation of the Ndc80 kinetochore protein in *Saccharomyces cerevisiae*. Genetics **183:** 1591-1595.

AKIYOSHI, B., K. K. SARANGAPANI, A. F. POWERS, C. R. NELSON, S. L. REICHOW *et al.*, 2010 Tension directly stabilizes reconstituted kinetochore-microtubule attachments. Nature **468:** 576-579.

ALUSHIN, G. M., V. H. RAMEY, S. PASQUALATO, D. A. BALL, N. GRIGORIEFF *et al.*, 2010 The Ndc80 kinetochore complex forms oligomeric arrays along microtubules. Nature **467:** 805-810.

ASBURY, C. L., D. R. GESTAUT, A. F. POWERS, A. D. FRANCK and T. N. DAVIS, 2006 The Dam1 kinetochore complex harnesses microtubule dynamics to produce force and movement. Proc Natl Acad Sci U S A **103:** 9873-9878.

ASBURY, C. L., J. F. TIEN and T. N. DAVIS, 2011 Kinetochores' gripping feat: conformational wave or biased diffusion? Trends Cell Biol **21:** 38-46.

BAKHOUM, S. F., S. L. THOMPSON, A. L. MANNING and D. A. COMPTON, 2009 Genome stability is ensured by temporal control of kinetochore-microtubule dynamics. Nat Cell Biol **11:** 27-35.

BENDER, A., and J. R. PRINGLE, 1991 Use of a screen for synthetic lethal and multicopy suppresser mutants to identify two new genes involved in morphogenesis in *Saccharomyces cerevisiae*. Mol Cell Biol **11:** 1295-1305.

BIANCONI, E., A. PIOVESAN, F. FACCHIN, A. BERAUDI, R. CASADEI *et al.*, 2013 An estimation of the number of cells in the human body. Ann Hum Biol **40:** 463-471.

BIGGINS, S., 2013 The composition, functions, and regulation of the budding yeast kinetochore. Genetics **194:** 817-846.

BIGGINS, S., and A. W. MURRAY, 2001 The budding yeast protein kinase Ipl1/Aurora allows the absence of tension to activate the spindle checkpoint. Genes Dev **15:** 3118-3129.

BIGGINS, S., F. F. SEVERIN, N. BHALLA, I. SASSOON, A. A. HYMAN *et al.*, 1999 The conserved protein kinase Ipl1 regulates microtubule binding to kinetochores in budding yeast. Genes Dev **13:** 532-544.

BLACKSHIELDS, G., F. SIEVERS, W. SHI, A. WILM and D. G. HIGGINS, 2010 Sequence embedding for fast construction of guide trees for multiple sequence alignment. Algorithms Mol Biol **5:** 21.

BROWN, M. T., L. GOETSCH and L. H. HARTWELL, 1993 MIF2 is required for mitotic spindle integrity during anaphase spindle elongation in *Saccharomyces cerevisiae*. J Cell Biol **123:** 387-403.

BURKE, D., D. DAWSON and T. STEARNS, 2000 *Methods in Yeast Genetics*. Cold Spring Harbor Laboratory Press, New York.

CALDAS, G. V., K. F. DELUCA and J. G. DELUCA, 2013 KNL1 facilitates phosphorylation of outer kinetochore proteins by promoting Aurora B kinase activity. J Cell Biol **203:** 957-969.

CAMPBELL, C. S., and A. DESAI, 2013 Tension sensing by Aurora B kinase is independent of survivin-based centromere localization. Nature **497:** 118-121.

CANE, S., A. A. YE, S. J. LUKS-MORGAN and T. J. MARESCA, 2013 Elevated polar ejection forces stabilize kinetochore-microtubule attachments. J Cell Biol **200:** 203-218.

CHEERAMBATHUR, D. K., R. GASSMANN, B. COOK, K. OEGEMA and A. DESAI, 2013 Crosstalk between microtubule attachment complexes ensures accurate chromosome segregation. Science **342:** 1239-1242.

CHEESEMAN, I. M., S. ANDERSON, M. JWA, E. M. GREEN, J. KANG *et al.*, 2002 Phospho-regulation of kinetochore-microtubule attachments by the Aurora kinase Ipl1p. Cell **111:** 163-172.

CHEESEMAN, I. M., C. BREW, M. WOLYNIAK, A. DESAI, S. ANDERSON *et al.*, 2001 Implication of a novel multiprotein Dam1p complex in outer kinetochore function. J Cell Biol **155:** 1137-1145.

CHEESEMAN, I. M., J. S. CHAPPIE, E. M. WILSON-KUBALEK and A. DESAI, 2006 The conserved KMN network constitutes the core microtubule-binding site of the kinetochore. Cell **127:** 983-997.

CIFERRI, C., J. DE LUCA, S. MONZANI, K. J. FERRARI, D. RISTIC *et al.*, 2005 Architecture of the human Ndc80-Hec1 complex, a critical constituent of the outer kinetochore. J Biol Chem **280:** 29088-29095.

CIFERRI, C., S. PASQUALATO, E. SCREPANTI, G. VARETTI, S. SANTAGUIDA *et al.*, 2008 Implications for kinetochore-microtubule attachment from the structure of an engineered Ndc80 complex. Cell **133:** 427-439.

CIMINI, D., and F. DEGRASSI, 2005 Aneuploidy: a matter of bad connections. Trends Cell Biol **15:** 442-451.

CIMINI, D., B. MOREE, J. C. CANMAN and E. D. SALMON, 2003 Merotelic kinetochore orientation occurs frequently during early mitosis in mammalian tissue cells and error correction is achieved by two different mechanisms. J Cell Sci **116:** 4213-4225.

CIMINI, D., X. WAN, C. B. HIREL and E. D. SALMON, 2006 Aurora kinase promotes turnover of kinetochore microtubules to reduce chromosome segregation errors. Curr Biol **16:** 1711-1718.

CRASTA, K., N. J. GANEM, R. DAGHER, A. B. LANTERMANN, E. V. IVANOVA *et al.*, 2012 DNA breaks and chromosome pulverization from errors in mitosis. Nature **482:** 53-58.

DAVIS, T. N., 1992 Mutational analysis of calmodulin in *Saccharomyces cerevisiae*. Cell Calcium **13:** 435-444.

DE ANTONI, A., C. G. PEARSON, D. CIMINI, J. C. CANMAN, V. SALA *et al.*, 2005 The Mad1/Mad2 complex as a template for Mad2 activation in the spindle assembly checkpoint. Curr Biol **15:** 214-225.

DE WULF, P., A. D. MCAINSH and P. K. SORGER, 2003 Hierarchical assembly of the budding yeast kinetochore from multiple subcomplexes. Genes Dev **17:** 2902-2921.

DELUCA, J. G., W. E. GALL, C. CIFERRI, D. CIMINI, A. MUSACCHIO *et al.*, 2006 Kinetochore microtubule dynamics and attachment stability are regulated by Hec1. Cell **127:** 969-982.

DELUCA, K. F., S. M. LENS and J. G. DELUCA, 2011 Temporal changes in Hec1 phosphorylation control kinetochore-microtubule attachment stability during mitosis. J Cell Sci **124:** 622-634.

EVANS, L., T. MITCHISON and M. KIRSCHNER, 1985 Influence of the centrosome on the structure of nucleated microtubules. J Cell Biol **100:** 1185-1191.

FITZGERALD-HAYES, M., L. CLARKE and J. CARBON, 1982 Nucleotide sequence comparisons and functional analysis of yeast centromere DNAs. Cell **29:** 235-244.

FRANCK, A. D., A. F. POWERS, D. R. GESTAUT, T. N. DAVIS and C. L. ASBURY, 2010 Direct physical study of kinetochore-microtubule interactions by reconstitution and interrogation with an optical force clamp. Methods **51:** 242-250.

FRANCK, A. D., A. F. POWERS, D. R. GESTAUT, T. GONEN, T. N. DAVIS *et al.*, 2007 Tension applied through the Dam1 complex promotes microtubule elongation providing a direct mechanism for length control in mitosis. Nat Cell Biol **9:** 832-837.

GANEM, N. J., and D. PELLMAN, 2012 Linking abnormal mitosis to the acquisition of DNA damage. J Cell Biol **199:** 871-881.

GESTAUT, D. R., J. COOPER, C. L. ASBURY, T. N. DAVIS and L. WORDEMAN, 2010 Reconstitution and functional analysis of kinetochore subcomplexes. Methods Cell Biol **95:** 641-656.

GESTAUT, D. R., B. GRACZYK, J. COOPER, P. O. WIDLUND, A. ZELTER *et al.*, 2008 Phosphoregulation and depolymerization-driven movement of the Dam1 complex do not require ring formation. Nat Cell Biol **10:** 407-414.

GIMONA, M., K. DJINOVIC-CARUGO, W. J. KRANEWITTER and S. J. WINDER, 2002 Functional plasticity of CH domains. FEBS Lett **513:** 98-106.

GORDON, D. J., B. RESIO and D. PELLMAN, 2012 Causes and consequences of aneuploidy in cancer. Nat Rev Genet **13:** 189-203.

GRACZYK, B., and T. N. DAVIS, 2011 An assay to measure the affinity of proteins for microtubules by quantitative fluorescent microscopy. Anal Biochem **410:** 313-315.

GREENLAND, K. B., H. DING, M. COSTANZO, C. BOONE and T. N. DAVIS, 2010 Identification of *Saccharomyces cerevisiae* spindle pole body remodeling factors. PLoS One **5:** e15426.

GREGAN, J., S. POLAKOVA, L. ZHANG, I. M. TOLIC-NORRELYKKE and D. CIMINI, 2011 Merotelic kinetochore attachment: causes and effects. Trends Cell Biol **21:** 374-381.

GRISHCHUK, E. L., A. K. EFREMOV, V. A. VOLKOV, I. S. SPIRIDONOV, N. GUDIMCHUK *et al.*, 2008a The Dam1 ring binds microtubules strongly enough to be a processive as well as energy-efficient coupler for chromosome motion. Proc Natl Acad Sci U S A **105:** 15423-15428.

GRISHCHUK, E. L., I. S. SPIRIDONOV, V. A. VOLKOV, A. EFREMOV, S. WESTERMANN *et al.*, 2008b Different assemblies of the DAM1 complex follow shortening microtubules by distinct mechanisms. Proc Natl Acad Sci U S A **105:** 6918-6923.

GUIMARAES, G. J., Y. DONG, B. F. MCEWEN and J. G. DELUCA, 2008 Kinetochore-microtubule attachment relies on the disordered N-terminal tail domain of Hec1. Curr Biol **18:** 1778-1784.

HACH, F., F. HORMOZDIARI, C. ALKAN, I. BIROL, E. E. EICHLER *et al.*, 2010 mrsFAST: a cache-oblivious algorithm for short-read mapping. Nat Methods **7:** 576-577.

HARDWICK, K. G., E. WEISS, F. C. LUCA, M. WINEY and A. W. MURRAY, 1996 Activation of the budding yeast spindle assembly checkpoint without mitotic spindle disruption. Science **273:** 953-956.

HAUF, S., 2013 The spindle assembly checkpoint: progress and persistent puzzles. Biochem Soc Trans **41:** 1755-1760.

HAUF, S., R. W. COLE, S. LATERRA, C. ZIMMER, G. SCHNAPP *et al.*, 2003 The small molecule Hesperadin reveals a role for Aurora B in correcting kinetochore-microtubule attachment and in maintaining the spindle assembly checkpoint. J Cell Biol **161:** 281-294.

HAYASHI, I., and M. IKURA, 2003 Crystal structure of the amino-terminal microtubule-binding domain of end-binding protein 1 (EB1). J Biol Chem **278:** 36430-36434.

HE, X., M. H. JONES, M. WINEY and S. SAZER, 1998 Mph1, a member of the Mps1-like family of dual specificity protein kinases, is required for the spindle checkpoint in *S. pombe*. J Cell Sci **111:** 1635-1647.

HE, X., D. R. RINES, C. W. ESPELIN and P. K. SORGER, 2001 Molecular analysis of kinetochore-microtubule attachment in budding yeast. Cell **106:** 195-206.

HENIKOFF, S., K. AHMAD and H. S. MALIK, 2001 The centromere paradox: stable inheritance with rapidly evolving DNA. Science **293:** 1098-1102.

HIETER, P., D. PRIDMORE, J. H. HEGEMANN, M. THOMAS, R. W. DAVIS *et al.*, 1985 Functional selection and analysis of yeast centromeric DNA. Cell **42:** 913-921.

HILL, A. V., 1910 The possible effects of the aggregation of molecules of haemoglobin on its dissociation curves. J Physiol **40:** iv-vii.

HILL, T. L., 1985 Theoretical problems related to the attachment of microtubules to kinetochores. Proc Natl Acad Sci U S A **82:** 4404-4408.

HORNUNG, P., M. MAIER, G. M. ALUSHIN, G. C. LANDER, E. NOGALES *et al.*, 2011 Molecular architecture and connectivity of the budding yeast Mtw1 kinetochore complex. J Mol Biol **405:** 548-559.

HOYT, M. A., L. TOTIS and B. T. ROBERTS, 1991 *S. cerevisiae* genes required for cell cycle arrest in response to loss of microtubule function. Cell **66:** 507-517.

HUNTER, A. W., M. CAPLOW, D. L. COY, W. O. HANCOCK, S. DIEZ *et al.*, 2003 The kinesin-related protein MCAK is a microtubule depolymerase that forms an ATP-hydrolyzing complex at microtubule ends. Mol Cell **11:** 445-457.

INOUE, S., and E. D. SALMON, 1995 Force generation by microtubule assembly/disassembly in mitosis and related movements. Mol Biol Cell **6:** 1619-1640.

JANKE, C., J. ORTIZ, J. LECHNER, A. SHEVCHENKO, M. M. MAGIERA *et al.*, 2001 The budding yeast proteins Spc24p and Spc25p interact with Ndc80p and Nuf2p at the kinetochore and are important for kinetochore clustering and checkpoint control. EMBO J **20:** 777-791.

JANKE, C., J. ORTIZ, T. U. TANAKA, J. LECHNER and E. SCHIEBEL, 2002 Four new subunits of the Dam1-Duo1 complex reveal novel functions in sister kinetochore biorientation. EMBO J **21:** 181-193.

JIANG, K., J. WANG, J. LIU, T. WARD, L. WORDEMAN *et al.*, 2009 TIP150 interacts with and targets MCAK at the microtubule plus ends. EMBO Rep **10:** 857-865.

JOGLEKAR, A. P., K. BLOOM and E. D. SALMON, 2009 In vivo protein architecture of the eukaryotic kinetochore with nanometer scale accuracy. Curr Biol **19:** 694-699.

JOKELAINEN, P. T., 1967 The ultrastructure and spatial organization of the metaphase kinetochore in mitotic rat cells. J Ultrastruct Res **19:** 19-44.

KEATING, P., N. RACHIDI, T. U. TANAKA and M. J. STARK, 2009 Ipl1-dependent phosphorylation of Dam1 is reduced by tension applied on kinetochores. J Cell Sci **122:** 4375-4382.

KELLY, A. E., and H. FUNABIKI, 2009 Correcting aberrant kinetochore microtubule attachments: an Aurora B-centric view. Curr Opin Cell Biol **21:** 51-58.

KELMAN, Z., 1997 PCNA: structure, functions and interactions. Oncogene **14:** 629-640.

KEMMLER, S., M. STACH, M. KNAPP, J. ORTIZ, J. PFANNSTIEL *et al.*, 2009 Mimicking Ndc80 phosphorylation triggers spindle assembly checkpoint signalling. EMBO J **28:** 1099-1110.

KING, J. M., T. S. HAYS and R. B. NICKLAS, 2000 Dynein is a transient kinetochore component whose binding is regulated by microtubule attachment, not tension. J Cell Biol **151:** 739-748.

KING, S. J., and T. A. SCHROER, 2000 Dynactin increases the processivity of the cytoplasmic dynein motor. Nat Cell Biol **2:** 20-24.

KIRSCHNER, M., and T. MITCHISON, 1986 Beyond self-assembly: from microtubules to morphogenesis. Cell **45:** 329-342.

KLINE-SMITH, S. L., S. SANDALL and A. DESAI, 2005 Kinetochore-spindle microtubule interactions during mitosis. Curr Opin Cell Biol **17:** 35-46.

KNOWLTON, A. L., W. LAN and P. T. STUKENBERG, 2006 Aurora B is enriched at merotelic attachment sites, where it regulates MCAK. Curr Biol **16:** 1705-1710.

KORENBAUM, E., and F. RIVERO, 2002 Calponin homology domains at a glance. J Cell Sci **115:** 3543-3545.

KOSHLAND, D. E., T. J. MITCHISON and M. W. KIRSCHNER, 1988 Polewards chromosome movement driven by microtubule depolymerization in vitro. Nature **331:** 499-504.

LAMPERT, F., P. HORNUNG and S. WESTERMANN, 2010 The Dam1 complex confers microtubule plus end-tracking activity to the Ndc80 kinetochore complex. J Cell Biol **189:** 641-649.

LAMPERT, F., C. MIECK, G. M. ALUSHIN, E. NOGALES and S. WESTERMANN, 2013 Molecular requirements for the formation of a kinetochore-microtubule interface by Dam1 and Ndc80 complexes. J Cell Biol **200:** 21-30.

LAMPSON, M. A., K. RENDUCHITALA, A. KHODJAKOV and T. M. KAPOOR, 2004 Correcting improper chromosome-spindle attachments during cell division. Nat Cell Biol **6:** 232-237.

LAWRIMORE, J., K. S. BLOOM and E. D. SALMON, 2011 Point centromeres contain more than a single centromere-specific Cse4 (CENP-A) nucleosome. J Cell Biol **195:** 573-582.

LEDBETTER, M. C., and K. R. PORTER, 1963 A "Microtubule" in Plant Cell Fine Structure. J Cell Biol **19:** 239-250.

LI, R., and A. W. MURRAY, 1991 Feedback control of mitosis in budding yeast. Cell **66:** 519-531.

LI, X., and R. B. NICKLAS, 1995 Mitotic forces control a cell-cycle checkpoint. Nature **373:** 630-632.

LIU, D., and M. A. LAMPSON, 2009 Regulation of kinetochore-microtubule attachments by Aurora B kinase. Biochem Soc Trans **37:** 976-980.

LIU, D., G. VADER, M. J. VROMANS, M. A. LAMPSON and S. M. LENS, 2009 Sensing chromosome bi-orientation by spatial separation of aurora B kinase from kinetochore substrates. Science **323:** 1350-1353.

LONDON, N., and S. BIGGINS, 2014 Mad1 kinetochore recruitment by Mps1-mediated phosphorylation of Bub1 signals the spindle checkpoint. Genes Dev **28:** 140-152.

LONDON, N., S. CETO, J. A. RANISH and S. BIGGINS, 2012 Phosphoregulation of Spc105 by Mps1 and PP1 regulates Bub1 localization to kinetochores. Curr Biol **22:** 900-906.

MADDOX, P., A. STRAIGHT, P. COUGHLIN, T. J. MITCHISON and E. D. SALMON, 2003 Direct observation of microtubule dynamics at kinetochores in Xenopus extract spindles: implications for spindle mechanics. J Cell Biol **162:** 377-382.

MAIOLICA, A., D. CITTARO, D. BORSOTTI, L. SENNELS, C. CIFERRI *et al.*, 2007 Structural analysis of multiprotein complexes by cross-linking, mass spectrometry, and database searching. Mol Cell Proteomics **6:** 2200-2211.

MALVEZZI, F., G. LITOS, A. SCHLEIFFER, A. HEUCK, K. MECHTLER *et al.*, 2013 A structural basis for kinetochore recruitment of the Ndc80 complex via two distinct centromere receptors. EMBO J **32:** 409-423.

MANDELKOW, E., E. MANDELKOW and R. MILLIGAN, 1991 Microtubule dynamics and microtubule caps: a time-resolved cryo-electron microscopy study. J Cell Biol **114:** 977-991.

MANNA, T., S. HONNAPPA, M. O. STEINMETZ and L. WILSON, 2008 Suppression of microtubule dynamic instability by the +TIP protein EB1 and its modulation by the CAP-Gly domain of p150glued. Biochemistry **47:** 779-786.

MARESCA, T. J., and E. D. SALMON, 2009 Intrakinetochore stretch is associated with changes in kinetochore phosphorylation and spindle assembly checkpoint activity. J Cell Biol **184:** 373-381.

MARTIN-LLUESMA, S., V. M. STUCKE and E. A. NIGG, 2002 Role of Hec1 in spindle checkpoint signaling and kinetochore recruitment of Mad1/Mad2. Science **297:** 2267-2270.

MASKELL, D. P., X. W. HU and M. R. SINGLETON, 2010 Molecular architecture and assembly of the yeast kinetochore MIND complex. J Cell Biol **190:** 823-834.

MAURE, J. F., S. KOMOTO, Y. OKU, A. MINO, S. PASQUALATO *et al.*, 2011 The Ndc80 loop region facilitates formation of kinetochore attachment to the dynamic microtubule plus end. Curr Biol **21:** 207-213.

MCDONNELL, A. V., T. JIANG, A. E. KEATING and B. BERGER, 2006 Paircoil2: improved prediction of coiled coils from sequence. Bioinformatics **22:** 356-358.

MCGHEE, J., and P. VON HIPPEL, 1974 Theoretical aspects of DNA-protein interactions: co-operative and non-co-operative binding of large ligands to a one-dimensional homogeneous lattice. J Mol Biol **86:** 469-489.

MCINTOSH, J. R., E. L. GRISHCHUK, M. K. MORPHEW, A. K. EFREMOV, K. ZHUDENKOV *et al.*, 2008 Fibrils connect microtubule tips with kinetochores: a mechanism to couple tubulin dynamics to chromosome motion. Cell **135:** 322-333.

MERALDI, P., A. D. MCAINSH, E. RHEINBAY and P. K. SORGER, 2006 Phylogenetic and structural analysis of centromeric DNA and kinetochore proteins. Genome Biol **7:** R23.

MILLER, S. A., M. L. JOHNSON and P. T. STUKENBERG, 2008 Kinetochore attachments require an interaction between unstructured tails on microtubules and Ndc80(Hec1). Curr Biol **18:** 1785-1791.

MILUTINOVICH, M., E. UNAL, C. WARD, R. V. SKIBBENS and D. KOSHLAND, 2007 A multi-step pathway for the establishment of sister chromatid cohesion. PLoS Genet **3:** e12.

MIRANDA, J. J., P. DE WULF, P. K. SORGER and S. C. HARRISON, 2005 The yeast DASH complex forms closed rings on microtubules. Nat Struct Mol Biol **12:** 138-143.

MIRANDA, J. J., D. S. KING and S. C. HARRISON, 2007 Protein arms in the kinetochore-microtubule interface of the yeast DASH complex. Mol Biol Cell **18:** 2503-2510.

MITCHISON, T., and M. KIRSCHNER, 1984 Dynamic instability of microtubule growth. Nature **312:** 237-242.

MULLER-REICHERT, T., D. CHRETIEN, F. SEVERIN and A. A. HYMAN, 1998 Structural changes at microtubule ends accompanying GTP hydrolysis: information from a slowly hydrolyzable analogue of GTP, guanylyl (alpha,beta)methylenediphosphonate. Proc Natl Acad Sci U S A **95:** 3661-3666.

MULLER, E. G., 1996 A glutathione reductase mutant of yeast accumulates high levels of oxidized glutathione and requires thioredoxin for growth. Mol Biol Cell **7:** 1805-1813.

MULLER, E. G. D., B. E. SNYDSMAN, I. NOVIK, D. W. HAILEY, D. R. GESTAUT *et al.*, 2005 The organization of the core proteins of the yeast spindle pole body. Mol Biol Cell **16:** 3341-3352.

NGUYEN, T., D. B. N. VINH, D. K. CRAWFORD and T. N. DAVIS, 1998 A genetic analysis of interactions with Spc110p reveals distinct functions of Spc97p and Spc98p, components of the yeast gamma-tubulin complex. Mol Biol Cell **9:** 2201-2216.

NICKLAS, R., 1988 The forces that move chromosomes in mitosis. Annu Rev Biophys Biophys Chem **17:** 431-449.

NICKLAS, R. B., and C. A. KOCH, 1969 Chromosome micromanipulation. 3. Spindle fiber tension and the reorientation of mal-oriented chromosomes. J Cell Biol **43:** 40-50.

NICKLAS, R. B., and S. C. WARD, 1994 Elements of error correction in mitosis: microtubule capture, release, and tension. J Cell Biol **126:** 1241-1253.

NISHINO, T., F. RAGO, T. HORI, K. TOMII, I. M. CHEESEMAN *et al.*, 2013 CENP-T provides a structural platform for outer kinetochore assembly. EMBO J **32:** 424-436.

ORTIZ, J., C. FUNK, A. SCHAFER and J. LECHNER, 2009 Stu1 inversely regulates kinetochore capture and spindle stability. Genes Dev **23:** 2778-2791.

OSBORNE, M. A., G. SCHLENSTEDT, T. JINKS and P. A. SILVER, 1994 Nuf2, a spindle pole body-associated protein required for nuclear division in yeast. J Cell Biol **125:** 853-866.

PAJUNEN, M., H. TURAKAINEN, E. POUSSU, J. PERANEN, M. VIHINEN *et al.*, 2007 High-precision mapping of protein protein interfaces: an integrated genetic strategy combining en masse mutagenesis and DNA-level parallel analysis on a yeast two-hybrid platform. Nucleic Acids Res **35:** e103.

PEARSON, C., P. MADDOX, E. SALMON and K. BLOOM, 2001 Budding yeast chromosome structure and dynamics during mitosis. J Cell Biol **152:** 1255-1266.

PERPELESCU, M., and T. FUKAGAWA, 2011 The ABCs of CENPs. Chromosoma **120:** 425-446.

PETERSON, J. B., and H. RIS, 1976 Electron-microscopic study of the spindle and chromosome movement in the yeast Saccharomyces cerevisiae. J Cell Sci **22:** 219-242.

PETROVIC, A., S. PASQUALATO, P. DUBE, V. KRENN, S. SANTAGUIDA *et al.*, 2010 The MIS12 complex is a protein interaction hub for outer kinetochore assembly. J Cell Biol **190:** 835-852.

PETTERSEN, E. F., T. D. GODDARD, C. C. HUANG, G. S. COUCH, D. M. GREENBLATT *et al.*, 2004 UCSF Chimera--a visualization system for exploratory research and analysis. J Comput Chem **25:** 1605-1612.

PETYUK, V., J. MCDERMOTT, M. COOK and B. SAUER, 2004 Functional mapping of Cre recombinase by pentapeptide insertional mutagenesis. J Biol Chem **279:** 37040-37048.

PINES, J., 2011 Cubism and the cell cycle: the many faces of the APC/C. Nat Rev Mol Cell Biol **12:** 427-438.

PINSKY, B. A., C. KUNG, K. M. SHOKAT and S. BIGGINS, 2006 The Ipl1-Aurora protein kinase activates the spindle checkpoint by creating unattached kinetochores. Nat Cell Biol **8:** 78-83.

PINSKY, B. A., S. Y. TATSUTANI, K. A. COLLINS and S. BIGGINS, 2003 An Mtw1 complex promotes kinetochore biorientation that is monitored by the Ipl1/Aurora protein kinase. Dev Cell **5:** 735-745.

POWERS, A. F., A. D. FRANCK, D. R. GESTAUT, J. COOPER, B. GRACYZK *et al.*, 2009 The Ndc80 kinetochore complex forms load-bearing attachments to dynamic microtubule tips via biased diffusion. Cell **136:** 865-875.

RICE, P., I. LONGDEN and A. BLEASBY, 2000 EMBOSS: the European Molecular Biology Open Software Suite. Trends Genet **16:** 276-277.

RICE, S., A. W. LIN, D. SAFER, C. L. HART, N. NABER *et al.*, 1999 A structural change in the kinesin motor protein that drives motility. Nature **402:** 778-784.

RIEDER, C. L., 1982 The formation, structure, and composition of the mammalian kinetochore and kinetochore fiber. Int Rev Cytol **79:** 1-58.

RIEDER, C. L., and S. P. ALEXANDER, 1990 Kinetochores are transported poleward along a single astral microtubule during chromosome attachment to the spindle in newt lung cells. J Cell Biol **110:** 81-95.

RIEDER, C. L., R. W. COLE, A. KHODJAKOV and G. SLUDER, 1995 The checkpoint delaying anaphase in response to chromosome monoorientation is mediated by an inhibitory signal produced by unattached kinetochores. J Cell Biol **130:** 941-948.

SARANGAPANI, K. K., B. AKIYOSHI, N. M. DUGGAN, S. BIGGINS and C. L. ASBURY, 2013 Phosphoregulation promotes release of kinetochores from dynamic microtubules via multiple mechanisms. Proc Natl Acad Sci U S A **110:** 7282-7287.

SCANNELL, D. R., O. A. ZILL, A. ROKAS, C. PAYEN, M. J. DUNHAM *et al.*, 2011 The Awesome Power of Yeast Evolutionary Genetics: New Genome Sequences and Strain Resources for the Saccharomyces sensu stricto Genus. G3 **1:** 11-25.

SCHMIDT, J. C., H. ARTHANARI, A. BOESZOERMENYI, N. M. DASHKEVICH, E. M. WILSON-KUBALEK *et al.*, 2012 The kinetochore-bound Ska1 complex tracks depolymerizing microtubules and binds to curved protofilaments. Dev Cell **23:** 968-980.

SHANG, C., T. R. HAZBUN, I. M. CHEESEMAN, J. ARANDA, S. FIELDS *et al.*, 2003 Kinetochore protein interactions and their regulation by the Aurora kinase Ipl1p. Mol Biol Cell **14:** 3342-3355.

SHEPPERD, L. A., J. C. MEADOWS, A. M. SOCHAJ, T. C. LANCASTER, J. ZOU *et al.*, 2012 Phosphodependent recruitment of Bub1 and Bub3 to Spc7/KNL1 by Mph1 kinase maintains the spindle checkpoint. Curr Biol **22:** 891-899.

SHIMOGAWA, M. M., B. GRACZYK, M. K. GARDNER, S. E. FRANCIS, E. A. WHITE *et al.*, 2006 Mps1 phosphorylation of Dam1 couples kinetochores to microtubule plus ends at metaphase. Curr Biol **16:** 1489-1501.

SHIMOGAWA, M. M., M. M. WARGACKI, E. G. MULLER and T. N. DAVIS, 2010 Laterally attached kinetochores recruit the checkpoint protein Bub1, but satisfy the spindle checkpoint. Cell Cycle **9:** 3619-3628.

SHIMOGAWA, M. M., P. O. WIDLUND, M. RIFFLE, M. ESS and T. N. DAVIS, 2009 Bir1 is required for the tension checkpoint. Mol Biol Cell **20:** 915-923.

SIKORSKI, R. S., and P. HIETER, 1989 A system of shuttle vectors and yeast host strains designed for efficient manipulation of DNA in *Saccharomyces cerevisiae*. Genetics **122:** 19-27.

SKIBBENS, R. V., C. L. RIEDER and E. D. SALMON, 1995 Kinetochore motility after severing between sister centromeres using laser microsurgery: evidence that kinetochore directional instability and position is regulated by tension. J Cell Sci **108 (Pt 7):** 2537-2548.

SKIBBENS, R. V., V. P. SKEEN and E. D. SALMON, 1993 Directional instability of kinetochore motility during chromosome congression and segregation in mitotic newt lung cells: a push-pull mechanism. J Cell Biol **122:** 859-875.

STERN, B. M., and A. W. MURRAY, 2001 Lack of tension at kinetochores activates the spindle checkpoint in budding yeast. Curr Biol **11:** 1462-1467.

SUDAKIN, V., G. K. CHAN and T. J. YEN, 2001 Checkpoint inhibition of the APC/C in HeLa cells is mediated by a complex of BUBR1, BUB3, CDC20, and MAD2. J Cell Biol **154:** 925-936.

SUNDIN, L. J., G. J. GUIMARAES and J. G. DELUCA, 2011 The NDC80 complex proteins Nuf2 and Hec1 make distinct contributions to kinetochore-microtubule attachment in mitosis. Mol Biol Cell **22:** 759-768.

TANAKA, K., E. KITAMURA, Y. KITAMURA and T. U. TANAKA, 2007 Molecular mechanisms of microtubule-dependent kinetochore transport toward spindle poles. J Cell Biol **178:** 269-281.

TANAKA, K., N. MUKAE, H. DEWAR, M. VAN BREUGEL, E. K. JAMES *et al.*, 2005 Molecular mechanisms of kinetochore capture by spindle microtubules. Nature **434:** 987-994.

TANAKA, T. U., N. RACHIDI, C. JANKE, G. PEREIRA, M. GALOVA *et al.*, 2002 Evidence that the Ipl1-Sli15 (Aurora kinase-INCENP) complex promotes chromosome bi-orientation by altering kinetochore-spindle pole connections. Cell **108:** 317-329.

TIRNAUER, J. S., S. GREGO, E. D. SALMON and T. J. MITCHISON, 2002 EB1-microtubule interactions in Xenopus egg extracts: role of EB1 in microtubule stabilization and mechanisms of targeting to microtubules. Mol Biol Cell **13:** 3614-3626.

TOOLEY, J. G., S. A. MILLER and P. T. STUKENBERG, 2011 The Ndc80 complex uses a tripartite attachment point to couple microtubule depolymerization to chromosome movement. Mol Biol Cell **22:** 1217-1226.

UCHIDA, K. S., K. TAKAGAKI, K. KUMADA, Y. HIRAYAMA, T. NODA *et al.*, 2009 Kinetochore stretching inactivates the spindle assembly checkpoint. J Cell Biol **184:** 383-390.

UMBREIT, N. T., D. R. GESTAUT, J. F. TIEN, B. S. VOLLMAR, T. GONEN *et al.*, 2012 The Ndc80 kinetochore complex directly modulates microtubule dynamics. Proc Natl Acad Sci U S A **109:** 16113-16118.

WAN, X., R. P. O'QUINN, H. L. PIERCE, A. P. JOGLEKAR, W. E. GALL *et al.*, 2009 Protein architecture of the human kinetochore microtubule attachment site. Cell **137:** 672-684.

WANG, H., and E. NOGALES, 2005 Nucleotide-dependent bending flexibility of tubulin regulates microtubule assembly. Nature **435:** 911-915.

WANG, H. W., S. LONG, C. CIFERRI, S. WESTERMANN, D. DRUBIN *et al.*, 2008 Architecture and flexibility of the yeast Ndc80 kinetochore complex. J Mol Biol **383:** 894-903.

WANG, H. W., V. H. RAMEY, S. WESTERMANN, A. E. LESCHZINER, J. P. WELBURN *et al.*, 2007 Architecture of the Dam1 kinetochore ring complex and implications for microtubule-driven assembly and force-coupling mechanisms. Nat Struct Mol Biol **14:** 721-726.

WARGACKI, M. M., J. C. TAY, E. G. MULLER, C. L. ASBURY and T. N. DAVIS, 2010 Kip3, the yeast kinesin-8, is required for clustering of kinetochores at metaphase. Cell Cycle **9:** 2581-2588.

WEAVER, B. A., A. D. SILK, C. MONTAGNA, P. VERDIER-PINARD and D. W. CLEVELAND, 2007 Aneuploidy acts both oncogenically and as a tumor suppressor. Cancer Cell **11:** 25-36.

WEI, R. R., J. AL-BASSAM and S. C. HARRISON, 2007 The Ndc80/HEC1 complex is a contact point for kinetochore-microtubule attachment. Nat Struct Mol Biol **14:** 54-59.

WEI, R. R., J. R. SCHNELL, N. A. LARSEN, P. K. SORGER, J. J. CHOU *et al.*, 2006 Structure of a central component of the yeast kinetochore: the Spc24p/Spc25p globular domain. Structure **14:** 1003-1009.

WEI, R. R., P. K. SORGER and S. C. HARRISON, 2005 Molecular organization of the Ndc80 complex, an essential kinetochore component. Proc Natl Acad Sci U S A **102:** 5363-5367.

WEISS, E., and M. WINEY, 1996 The *Saccharomyces cerevisiae* spindle pole body duplication gene MPS1 is part of a mitotic checkpoint. J Cell Biol **132:** 111-123.

WELBURN, J. P., M. VLEUGEL, D. LIU, J. R. YATES, 3RD, M. A. LAMPSON *et al.*, 2010 Aurora B phosphorylates spatially distinct targets to differentially regulate the kinetochore-microtubule interface. Mol Cell **38:** 383-392.

WESTERMANN, S., A. AVILA-SAKAR, H. WANG, H. NIEDERSTRASSER, J. WONG *et al.*, 2005 Formation of a dynamic kinetochore- microtubule interface through assembly of the Dam1 ring complex. Mol Cell **17:** 277-290.

WESTERMANN, S., I. M. CHEESEMAN, S. ANDERSON, J. R. YATES, 3RD, D. G. DRUBIN *et al.*, 2003 Architecture of the budding yeast kinetochore reveals a conserved molecular core. J Cell Biol **163:** 215-222.

WESTERMANN, S., H. W. WANG, A. AVILA-SAKAR, D. G. DRUBIN, E. NOGALES *et al.*, 2006 The Dam1 kinetochore ring complex moves processively on depolymerizing microtubule ends. Nature **440:** 565-569.

WIGGE, P. A., O. N. JENSEN, S. HOLMES, S. SOUES, M. MANN *et al.*, 1998 Analysis of the Saccharomyces spindle pole by matrix-assisted laser desorption/ionization (MALDI) mass spectrometry. J Cell Biol **141:** 967-977.

WIGGE, P. A., and J. V. KILMARTIN, 2001 The Ndc80p complex from Saccharomyces cerevisiae contains conserved centromere components and has a function in chromosome segregation. J Cell Biol **152:** 349-360.

WILSON-KUBALEK, E. M., I. M. CHEESEMAN, C. YOSHIOKA, A. DESAI and R. A. MILLIGAN, 2008 Orientation and structure of the Ndc80 complex on the microtubule lattice. J Cell Biol **182:** 1055-1061.

WINEY, M., C. L. MAMAY, E. T. O'TOOLE, D. N. MASTRONARDE, T. H. GIDDINGS JR. *et al.*, 1995 Three-dimensional ultrastructural analysis of the *Saccharomyces cerevisiae* mitotic spindle. J Cell Biol **129:** 1601-1615.

WOOLFSON, D. N., 2005 The design of coiled-coil structures and assemblies. Adv Protein Chem **70:** 79-112.

ZELTER, A., M. R. HOOPMANN, R. VERNON, D. BAKER, M. J. MACCOSS *et al.*, 2010 Isotope Signatures Allow Identification of Chemically Cross-Linked Peptides by Mass Spectrometry: A Novel Method to Determine Interresidue Distances in Protein Structures through Cross-Linking. J Proteome Res **9:** 3583-3589.

ZENG, X., J. A. KAHANA, P. A. SILVER, M. K. MORPHEW, J. R. MCINTOSH *et al.*, 1999 Slk19p is a centromere protein that functions to stabilize mitotic spindles. J Cell Biol **146:** 415-425.

ZHANG, X., W. LAN, S. C. EMS-MCCLUNG, P. T. STUKENBERG and C. E. WALCZAK, 2007 Aurora B phosphorylates multiple sites on mitotic centromere-associated kinesin to spatially and temporally regulate its function. Mol Biol Cell **18:** 3264-3276.

ZIMNIAK, T., K. STENGL, K. MECHTLER and S. WESTERMANN, 2009 Phosphoregulation of the budding yeast EB1 homologue Bim1p by Aurora/Ipl1p. J Cell Biol **186:** 379-391.

APPENDIX A

Coupling unbiased mutagenesis to high-throughput DNA sequencing uncovers functional domains in the Ndc80 kinetochore protein of *Saccharomyces cerevisiae*

TIEN, J. F., K. K. FONG, N. T. UMBREIT, C. PAYEN, A. ZELTER *et al.*, 2013 Coupling unbiased mutagenesis to high-throughput DNA sequencing uncovers functional domains in the Ndc80 kinetochore protein of *Saccharomyces cerevisiae*. Genetics **195:** 159-170.

Coupling Unbiased Mutagenesis to High-throughput DNA Sequencing Uncovers Functional Domains in the Ndc80 Kinetochore Protein of *Saccharomyces cerevisiae*

Jerry F. Tien,* Kimberly K. Fong,* Neil T. Umbreit,* Celia Payen,† Alex Zelter,* Charles L. Asbury,‡ Maitreya J. Dunham,† and Trisha N. Davis*,1

*Department of Biochemistry, †Department of Genome Sciences, and ‡Department of Physiology and Biophysics, University of Washington, Seattle, Washington 98195

ABSTRACT During mitosis, kinetochores physically link chromosomes to the dynamic ends of spindle microtubules. This linkage depends on the Ndc80 complex, a conserved and essential microtubule-binding component of the kinetochore. As a member of the complex, the Ndc80 protein forms microtubule attachments through a calponin homology domain. Ndc80 is also required for recruiting other components to the kinetochore and responding to mitotic regulatory signals. While the calponin homology domain has been the focus of biochemical and structural characterization, the function of the remainder of Ndc80 is poorly understood. Here, we utilized a new approach that couples high-throughput sequencing to a saturating linker-scanning mutagenesis screen in *Saccharomyces cerevisiae*. We identified domains in previously uncharacterized regions of Ndc80 that are essential for its function *in vivo*. We show that a helical hairpin adjacent to the calponin homology domain influences microtubule binding by the complex. Furthermore, a mutation in this hairpin abolishes the ability of the Dam1 complex to strengthen microtubule attachments made by the Ndc80 complex. Finally, we defined a C-terminal segment of Ndc80 required for tetramerization of the Ndc80 complex *in vivo*. This unbiased mutagenesis approach can be generally applied to genes in *S. cerevisiae* to identify functional properties and domains.

ACCURATE chromosome segregation depends on the attachment between kinetochores and the dynamic ends of spindle microtubules. This attachment requires the Ndc80 complex, an essential and conserved microtubule-binding component of the kinetochore. *In vivo*, inactivation or depletion of Ndc80 complex components leads to detached kinetochores and severe chromosome segregation defects (reviewed in Kline-Smith *et al.* 2005). Mirroring kinetochore-microtubule linkages *in vivo*, recent experiments show that attachments between purified Ndc80 complexes and microtubule tips can persist throughout rounds of microtubule growth and shortening, can withstand tensile forces, can modulate microtubule dynamics, and can respond to regulation by mitotic kinases (Guimaraes *et al.* 2008; Miller *et al.* 2008; Powers *et al.* 2009; Tien *et al.* 2010; DeLuca *et al.* 2011; Schmidt *et al.* 2012; Umbreit *et al.* 2012).

The Ndc80 complex (Figure 1) is a rod-shaped heterotetramer of Ndc80, Nuf2, Spc24, and Spc25 (Osborne *et al.* 1994; Janke *et al.* 2001; Wigge and Kilmartin 2001; Wei *et al.* 2005). The two ends of the complex have globular domains, formed by Ndc80/Nuf2 and Spc24/Spc25, respectively. All four components of the complex are predicted to participate in coiled-coil interactions that link these two globular ends. Structural studies of the complex at atomic resolution have been limited to the two globular domains, revealing a microtubule-binding calponin homology (CH) domain in Ndc80 (Wei *et al.* 2006, 2007; Ciferri *et al.* 2008).

These structural studies on the globular ends of the Ndc80 complex have provided high-resolution views of key protein–protein interfaces (Alushin *et al.* 2010; Malvezzi *et al.* 2013; Nishino *et al.* 2013). Together, they help explain how the Ndc80 complex plays a central role in kinetochore function by physically linking spindle microtubules

doi: 10.1534/genetics.113.152728
Manuscript received April 29, 2013; accepted for publication June 25, 2013
Supporting information is available online at http://www.genetics.org/lookup/suppl/doi:10.1534/genetics.113.152728/-/DC1.
[1]Corresponding author: Box 357350, Department of Biochemistry, University of Washington, Seattle, WA 98195. E-mail: tdavis@uw.edu

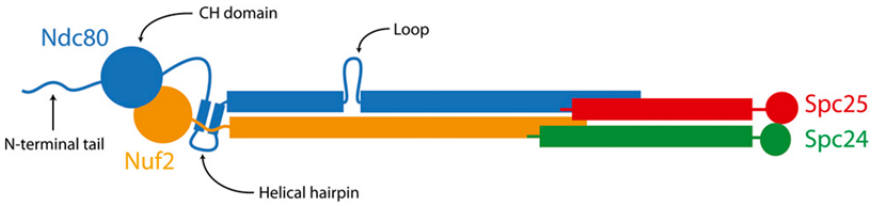

Figure 1 The Ndc80 complex contains Ndc80, Nuf2, Spc24, and Spc25.

to centromere-proximal kinetochore components. However, genetic and biochemical studies have suggested additional roles for the Ndc80 complex during mitosis. For example, mutations in *NDC80* result in mislocalization of kinetochore- and microtubule-associated proteins, such as the Dam1 complex and Stu2 in yeast (He *et al.* 2001; Janke *et al.* 2002). It is still unknown how the Ndc80 complex interacts with many of its proposed binding partners, and much of the complex is composed of long coiled-coil elements that have not been amenable to structural characterization. To identify the functionally important regions within Ndc80, we employed an unbiased linker-scanning mutagenesis screen. This screen utilizes short insertions at random positions within a protein to determine putative functional domains. Previous applications of linker-scanning mutagenesis have been successful in generating mutants to examine cohesin complex formation and Cre recombinase activity, and to map the Rab8A interaction interface on JFC1 (Petyuk *et al.* 2004; Milutinovich *et al.* 2007; Pajunen *et al.* 2007). Here, we comprehensively covered *NDC80* with 15-bp insertions at random positions, and the resulting mutant library was screened for viability in a red/white plasmid shuffle assay. High-throughput Illumina sequencing showed that lethal mutations fell into clusters, revealing several regions of Ndc80 that are essential for its function. These include the microtubule-binding domain, the helical hairpin, the tetramerization domain, and previously uncharacterized segments. Our approach, which couples unbiased mutagenesis to high-throughput sequencing, can be generally applied to reveal new functional domains of proteins in *Saccharomyces cerevisiae*.

Materials and Methods

Media

The compositions of YPD (yeast peptone dextrose rich) and SD (synthetic dextrose minimal) media were previously described (Burke *et al.* 2000). YPD-NAT medium is YPD with 25 μg/ml nourseothricin (clonNAT, Werner BioAgents). SD–lys medium was described previously (Nguyen *et al.* 1998). SD–ura low ade is SD medium containing 100 μg/ml tryptophan, 0.1% casamino acids, and 5 μg/ml adenine.

Plasmids

All plasmids used in this study are listed in Supporting Information, Table S1. QuikChange Lightning site-directed mutagenesis (Stratagene) was used to construct plasmids containing lethal mutations in *NDC80*.

Strains

All yeast strains used in this study were derived from W303 and are listed in Table S2. To make the strain used in the linker-scanning mutagenesis screen, JTY5-5C, the endogenous copy of *NDC80* was deleted by PCR amplifying a *NatMX* cassette from pKG9 using primers with homology to the flanking DNA of *NDC80*. The deletion cassette was then transformed into the diploid strain JTY1 and selected for on YPD-NAT to generate JTY4. The deletion was checked by PCR to ensure replacement of *NDC80* with the cassette. JTY4 was transformed with the "*ADE3* plasmid" (pJT12) containing *ADE3 LYS2 NDC80* and selected for on SD–lys. The transformants were sporulated and dissected to obtain JTY5-5C.

Linker-scanning mutagenesis

A "target plasmid" (pJT36) was constructed containing the wild-type *NDC80* gene (including 245 upstream and 299 downstream base pairs), the ampicillin resistance gene, and the *URA3* gene for selection. Importantly, this plasmid did not contain a *Not*I recognition sequence. Using the MuA transposase, an artificial transposon was inserted at a random location within the target plasmid (Finnzymes). Transposition efficiency was kept low so that, on average, each plasmid would contain only one transposon insertion. The transposon contains a kanamycin resistance gene flanked by the 8-bp *Not*I recognition sequence. Plasmids that contained a transposon were isolated by selection on kanamycin. These plasmids were then cut with *Not*I to remove the kanamycin cassette and then religated. The resulting "transposition library" contained plasmids that each have 15 bp inserted at a random location. Each 15-bp insertion contained 5 bp of duplicated target sequence and the *Not*I recognition sequence.

Red/white plasmid shuffle screen

To identify lethal insertions in *NDC80*, the transposition library was screened in *S. cerevisiae* using a red/white plasmid shuffle system (Davis 1992; Muller 1996). This screen was carried out in the strain JTY5-5C (*ade2–1oc ade3Δ–100 ura3-1 ndc80Δ::NatMX*), transformed with pJT12 (*NDC80 ADE3* in a 2-μm vector). In an *ade2–1oc ade3Δ–100* background, yeast containing this *ADE3* plasmid produce a red pigment when grown on low adenine plates (Bender and Pringle 1991). The transposition library was transformed into this strain and selected for growth on SD–ura low ade plates at 37°. Insertions that abolish the function of *NDC80* are lethal and render cells dependent on the *ADE3* plasmid

with the wild-type copy of *NDC80* for survival. Therefore, lethal mutations can be identified as those that yield solid red colonies. Insertions that do not disrupt the function of *NDC80* have no effect on cell viability, making the *ADE3* plasmid extraneous. These colonies have a sectored appearance—red in the center and white around the edges where the *ADE3* plasmid was lost. Nonsectored red colonies, containing lethal mutations, were isolated and their plasmid DNA was extracted for sequencing.

We determined that the false-positive rate of the red/white plasmid shuffle screen is <0.3%. This was accomplished by transforming JTY5-5C [pJT12] with a plasmid containing wild-type *NDC80* (pJT36) and counting the number of nonsectoring colonies. These false positives therefore represent colonies that were solid red despite the presence of a second wild-type copy of the gene. The representative lethal insertions selected for characterization (see below) were also retested in the red/white plasmid shuffle assay. JTY5-5C [pJT12] cells transformed with plasmids containing these insertions were confirmed to not sector.

Illumina sequencing

Illumina sequencing was used to determine the coverage of insertions in the transposition library and to identify the location of each lethal insertion obtained from the solid red colonies. Using the Expand Long Template PCR System (Roche), *NDC80* was amplified both from the transposition library and the pooled lethal mutants. In this PCR, primers were designed to specifically amplify the mutant alleles from the transposition library plasmids and not *NDC80* from the *ADE3* plasmid (Table S3). Single-end Illumina libraries were prepared from PCR products that were sheared to an average size of 500 bp by sonication. The sheared DNA ends were repaired using the End-It DNA repair kit (Epicentre), and A-tailed for ligation of adaptors (Table S3). The products were size selected (250–350 bp) and enriched by PCR using the primers presented in Table S3. Unique 6-bp indices on the PCR primers permitted multiplexed Illumina sequencing to distinguish between products from the transposition library and the pooled lethal mutants. One sequencing run of the transposition library and both sequencing runs of the lethal insertion subsets were alternatively prepared using the TruSeq DNA Sample Preparation v2 Kit. Briefly, PCR products were sheared to an average size of 500 bp using a Covaris E210. The sheared DNA ends were repaired and adenylated using the TruSeq protocol. Adapters AD002, AD018, and AD019 (Table S3) were ligated onto the transposition library sample and the two lethal insertion subset samples, respectively. The products were size selected (400–500 bp) and enriched by PCR using the TruSeq PCR Master Mix. All sequencing was performed on an Illumina Genome Analyzer II, to obtain 36-bp single reads. Sequencing results are provided in Table S4.

Custom programs (available upon request) were used to analyze the FASTQ files for each Illumina sequencing run. The 36-bp reads were queried for the *Not*I recognition sequence; for each hit, the position of the *Not*I sequence within the read was recorded. The sequences flanking each *Not*I insertion were then aligned to the *NDC80* gene using mrsFAST (Hach *et al.* 2010) to determine the position of the insertion in *NDC80*. Read coverage was obtained by aligning all reads (with and without *Not*I) to *NDC80* using mrsFAST. Each 15-bp insertion was also translated to determine the protein sequence of the five inserted amino acids. See Table 1 for examples of insertion positions, resulting sequences, and the translated insertion residues.

We selected representative mutations from each lethal insertion cluster for further analysis. Each mutation represents the insertion with one of the highest number of *Not*I reads in the cluster. For further characterization, we required that each insertion was lethal at both the screening temperature of 37° and additionally 24°. Based on these criteria, we selected ins506, ins656, ins839, ins940, ins1148, ins1687, and ins1957 (Table 1) for further analysis.

Coiled-coil prediction and sequence alignment of Ndc80

The probabilities of coiled-coil formation for wild-type and mutant Ndc80 were predicted using Paircoil2 (McDonnell *et al.* 2006). To perform sequence alignments, *NDC80* from *S. cerevisiae* and its orthologs in *Saccharomyces bayanus*, *S. kudriavzevii*, *S. mikatae* (Scannell *et al.* 2011), *Lachancea (Kluyveromyces) thermotolerans*, *Kluyveromyces lactis*, and *Debaryomyces hansenii* (http://genolevures.org) were translated using Transeq (Rice *et al.* 2000) and then aligned using Clustal-O (Blackshields *et al.* 2010). The similarity score was plotted for each position using Plotcon (Rice *et al.* 2000) with a window size of 21 bp.

Protein expression and purification

Recombinant *S. cerevisiae* Ndc80 and Dam1 complexes were expressed and purified as previously described (Miranda *et al.* 2005; Wei *et al.* 2005; Asbury *et al.* 2006; Powers *et al.* 2009).

Immunoprecipitation

JTY29-1C (*NUF2-TAP*) and JTY47-2B (*SPC24-TAP*) were transformed with plasmids encoding wild-type or mutant *GFP–NDC80* (Table S1) and selected for growth on SD–ura at 24°. Controls for the immunoprecipitation include JTY29-1C and JTY47-2B transformed with pRS316, as well as JTY29-1B (*NUF2*) and JTY47-2A (*SPC24*) transformed with a wild-type *GFP–NDC80* plasmid. Cells were grown to ~100 Klett units in 50 ml SD–ura at 24° and washed with dH_2O, and the pellets were frozen in liquid nitrogen. Pellets were resuspended in 500 μl lysis buffer (20 mM HEPES, pH 7.4, 300 mM NaCl, 100 μM GTP, 1 mM $MgCl_2$, 1 mM dithiothreitol, 4 μg/ml pepstatin, 4 μg/ml leupeptin, 4 μg/ml aprotinin, 4 μg/ml chymostatin, 1 mM phenylmethanesulfonyl fluoride, 1 mM sodium pyrophosphate, 1 mM sodium fluoride, 1 mM β-glycerophosphate, 5% glycerol) and vortexed with ice-cold glass beads in 1-min intervals until >60% of cells were lysed. Triton X-100 was added to 0.5% and lysates were cleared by centrifugation at 18,000 × *g*

Table 1 Representative lethal insertions in *NDC80*

Insertion position	Sequence[a]	Inserted residues	First mutation	*In vivo* expression[b]	Kinetochore localization[c]
506	TTCAAGTGGT**TGCGGCCGCAGTGGT**TATAT	LRPQW	Y170R	+	−
656	CACAAATTTC**TGCGGCCGCAATTTC**TTGGC	LRPQF	G220R	+	+
839	AAACTGTTAA**TGCGGCCGCAGTTAA**TTGAT	MRPQL	I280M	+	+
940	ATTCGTTCAC**TGCGGCCGCATTCAC**ATAAT	CGRIH	I314C	+	+
1148	AAGATGAAAT**TGCGGCCGCAGAAAT**CCGAG	LRPQK	S383L	+	+
1687	GAAAACTCAA**TGCGGCCGCACTCAA**ATTAA	CGRTQ	I563C	+	+
1957	TATTGATATA**TGCGGCCGCAATATA**ACAAG	CGRNI	T653C	+	−

[a] 15-bp insertions are in boldface text.
[b] Figure 3E.
[c] Figure 5, A and B.

for 20 min at 4°. An aliquot (50 μl) of 60 mg/ml Dynabeads (Invitrogen) conjugated with rabbit IgG (MP Biomedicals) was added to the clarified lysate and incubated for 30 min at 4°. Beads were then washed with 150 μl of wash buffer (20 mM HEPES, pH 7.4, 200 mM NaCl, 100 μM GTP, 1 mM $MgCl_2$, 5% glycerol) three times and resuspended in 50 μl of SDS–PAGE sample buffer.

Fluorescence microscopy

For live-cell imaging, JTY12-25A (*NUF2-mCherry NDC80*) was transformed with plasmids encoding wild-type or mutant *GFP–NDC80* (Table S1) and selected for growth on SD–ura at 24°. Cells were mounted for microscopy as previously described (Muller *et al.* 2005). Images of cells were taken at a single focal plane, binned 1 × 1, using a DeltaVision system (Applied Precision) equipped with an IX70 inverted microscope (Olympus), an U Plan Apo 100× objective (1.35 NA), and a CoolSnap HQ digital camera (Photometrics). Exposures were 0.4 sec for both GFP and mCherry. Images were processed as previously described (Shimogawa *et al.* 2010) using custom Matlab programs (available upon request) to isolate and quantify the fluorescence intensities of GFP and mCherry spots.

Total internal reflection fluorescence (TIRF) microscopy was performed as previously described (Tien *et al.* 2010), with the following modifications. A custom TIRF illumination system was constructed by modification of a commercial inverted microscope (Nikon Ti-U). Total internal reflection of 488 nm (Sapphire 488-100 CW, Coherent Inc.) and 561 nm (Sapphire 561-100 CW, Coherent Inc.) wavelength lasers was achieved using a through-the-objective arrangement with a 100× oil immersion 1.49 NA lens (Nikon CFI APO 100× Oil TIRF NA 1.49 WD 0.12 mm). Simultaneous imaging of GFP and Alexa Fluor 568 was captured by two cooled EM CCD cameras (iXon+ DU897, Andor Technology). Flow cell channels were constructed using double-sided sticky tape (Scotch), sandwiched between a glass slide (Gold Seal) and silanized coverslip (Corning). To bind taxol-stabilized microtubules, a modified "rigor" kinesin was flowed into the channel and bound nonspecifically to the coverslip. The flow cell channel was washed with 50 μl BB80 (80 mM Pipes, 120 mM K^+, 1 mM $MgCl_2$, 1 mM EGTA, 8 mg/ml BSA, pH 6.9) and 50 μl BB80T (BB80 with 10 μM taxol). Alexa Fluor 568-labeled microtubules diluted in BB80T were flowed in and allowed to bind for 5 min. The channel was washed once more with 50 μl BB80T. Proteins were then introduced, diluted in BB80T containing 0.1 mg/ml κ-casein, 200 μg/ml glucose oxidase, 35 μg/ml catalase, 25 mM glucose, and 5 mM dithiothreitol. GFP-tagged Ndc80 complex was assayed at 50 pM to resolve single molecules, and untagged Dam1 complex was added at 2.5 nM. Flow cell channels were sealed with nail polish and immediately imaged for 1500 frames at 10 frames per second. Software analysis of TIRF microscopy data was performed using custom software (available upon request) in Labview (National Instruments) and Igor Pro (WaveMetrics), as previously described (Tien *et al.* 2010).

Results

Construction of the linker-scanning transposition library

To discover new functional domains in the Ndc80 kinetochore protein (Figure 1), we performed a saturating screen that combined linker-scanning mutagenesis with a plasmid shuffle colorimetric assay and high-throughput sequencing. We first constructed a transposition library using an artificial transposition system (Figure 2A; *Materials and Methods*). This library contains a collection of plasmids, each with a single 15-bp insertion at a random location, corresponding to a five-amino-acid insertion in the translated protein product. Our *NDC80* transposition library was generated from ~11,000 transposition events on a 7.4-kb plasmid, which includes the 2.1-kb *NDC80* gene. Each 15-bp insertion contained the 8-bp *Not*I recognition sequence, which was used to identify the position of the insertion within the gene.

Insertion coverage of the *NDC80* gene was determined by Illumina sequencing (Figure 3, A–D, and Figure S1). From three independent sequencing runs, we determined that transpositions targeted 1074 unique positions on *NDC80*, corresponding to 52% coverage of the 2076-bp gene (see Table S4 for a summary of the sequencing study). Furthermore, insertions were spread evenly across *NDC80*, with an average of 10.8 insertions per 21-bp window across the entire gene

(Figure 3D, right plot). From the 1074 insertion positions identified in the library, the translated protein sequences were determined. The frame of each insertion and its surrounding wild-type *NDC80* sequence ultimately dictates the identity of the amino acids inserted into the protein (Figure S2A). By experimental design, the insertions did not introduce stop codons and were always 15 bp long to prevent frame shifts in the resulting coding sequence (Figure S2A). The transposition library contained insertions at 444 unique codons, resulting in 64% coverage of the 691-amino-acid Ndc80 protein. Of these insertions, 30% were in frame 1, 26% were in frame 2, and 44% were in frame 3 (Figure S2B). The transposition library was then screened in *S. cerevisiae* to identify mutations that disrupt the function of Ndc80.

Linker-scanning mutagenesis screen of Ndc80

A red/white plasmid shuffle system (Davis 1992; Muller 1996) was used to screen the transposition library for insertions detrimental to the function of *NDC80* in *S. cerevisiae* (Figure 2B). In this screen, colonies containing library plasmids with lethal mutations in *NDC80* do not sector and are solid red (see *Materials and Methods*). We screened 25,439 total colonies and isolated 959 red colonies (4%). These red colonies were pooled and the positions of the insertions were determined by Illumina sequencing (Table S4). Lethal insertions were found at 336 unique positions in 162 unique codons of *NDC80*, corresponding to 16% coverage of the gene and 23% of the protein. Unlike the transposition library, in which insertions were found evenly spread throughout the *NDC80* gene, plasmids isolated from the red colonies contained insertions that mapped to distinct clusters (Figure S1). This was most evident on a coverage density map, showing the number of lethal insertions in 21-bp windows across *NDC80* (Figure 3D). We defined a stretch of lethal insertions as a cluster if four or more insertions per 21-bp window were lethal (Figure 3D). In several windows within these clusters, every single insertion present in the transposition library was lethal. Surprisingly, lethal insertions were not enriched in any particular frame relative to the transposition library (Figure S2B). Furthermore, each of the three frames was well represented in all of the clusters identified (Figure S2C). These results suggest that the position of the insertion, rather than the identity of the residues, was most important in disrupting the function of Ndc80.

To verify that the clusters identified in our screen are not a result of random sampling, we divided the nonsectoring red colonies into two random pools. When sequenced independently (Table S4), both subsets had the same lethal insertion clusters as the original pool (Figure S3), indicating we have comprehensively screened the starting transposition library. Overall, our screen demonstrates that five-amino-acid insertions are tolerated throughout most of Ndc80 without disrupting its function. We did not identify lethal insertions in the putative "loop" (Figure 3A, blue bar), nor in a segment of Ndc80 that is disordered based on the human Ndc80 globular domain crystal structure (Figure 3A, black bar) (Ciferri *et al.* 2008). No lethal insertion clusters were found in the 113-amino acid N-terminal tail of Ndc80, which is dispensable in *S. cerevisiae* (Akiyoshi *et al.* 2009; Kemmler *et al.* 2009). Likewise, there were no lethal insertion clusters in the last ~30 amino acid residues of Ndc80, consistent with the viability of the *ndc80-1* temperature-sensitive allele, which contains a frameshift mutation that alters the last 18 amino acids of the protein (Wigge *et al.* 1998).

From the lethal insertion clusters identified in the linker-scanning mutagenesis screen, we selected representative mutations for further analysis. These lethal insertions are referred to as, for example, "ins506" to indicate that the first position of the insertion is nucleotide 506 of the mutant allele. A representative insertion from each cluster was independently verified to be lethal (see *Materials and Methods*). Insertions from the cluster around nucleotide 1400 of *NDC80* were found to be temperature sensitive; six insertions from this cluster, ranging from nucleotide 1380 to 1406, were lethal at 37° but not 24°. Therefore, this cluster was omitted from further analysis. Here, we selected a total of seven representative mutations from the remaining lethal insertion clusters for analysis (Table 1). We first tested if these mutations perturb protein expression or assembly of Ndc80 into a heterotetrameric complex. *In vivo*, all seven lethal insertion mutant alleles were expressed (Figure 3E). In these cells, the endogenous wild-type copy of *NDC80* was maintained for viability. A GFP tag on the mutant Ndc80 was used to distinguish it from the wild-type protein. In a recombinant expression system, six of the seven mutant Ndc80 proteins copurified as heterotetrameric complexes with Nuf2, Spc24, and Spc25 (Figure 3F). These results suggest that most of the insertions identified in this screen specifically disrupt the function of Ndc80 independent from protein production and folding.

Lethal insertions in the Ndc80 microtubule-binding domain

Two of the seven clusters of lethal insertions (represented by ins506 and ins656) are in the conserved microtubule-binding CH domain (Figure 3, A–D and Figure 4A). Based on homology to the human Ndc80 CH domain crystal structure (Ciferri *et al.* 2008), these lethal insertion clusters map to helices αC and αG, respectively. Even though these helices are adjacent in the crystal structure, the two mutations had drastically different effects. Ndc80 containing the ins506 mutation was expressed *in vivo* (Figure 3E), but failed to assemble into a recombinant complex. Consistent with our conclusion that the position of the insertion is likely most important in disrupting the function of Ndc80, we found that the ins511 mutation, which overlaps ins506 by 10 bp but is in a different frame, also impairs assembly of Ndc80 into a recombinant complex. By contrast, we successfully purified ins656 Ndc80 complex and further demonstrated that this complex binds microtubules *in vitro* (Figure 3F and Figure S4). Two additional clusters of lethal insertions (represented by ins839 and ins940) were found in a region of Ndc80 that folds into a helical hairpin (αH and αI) in the

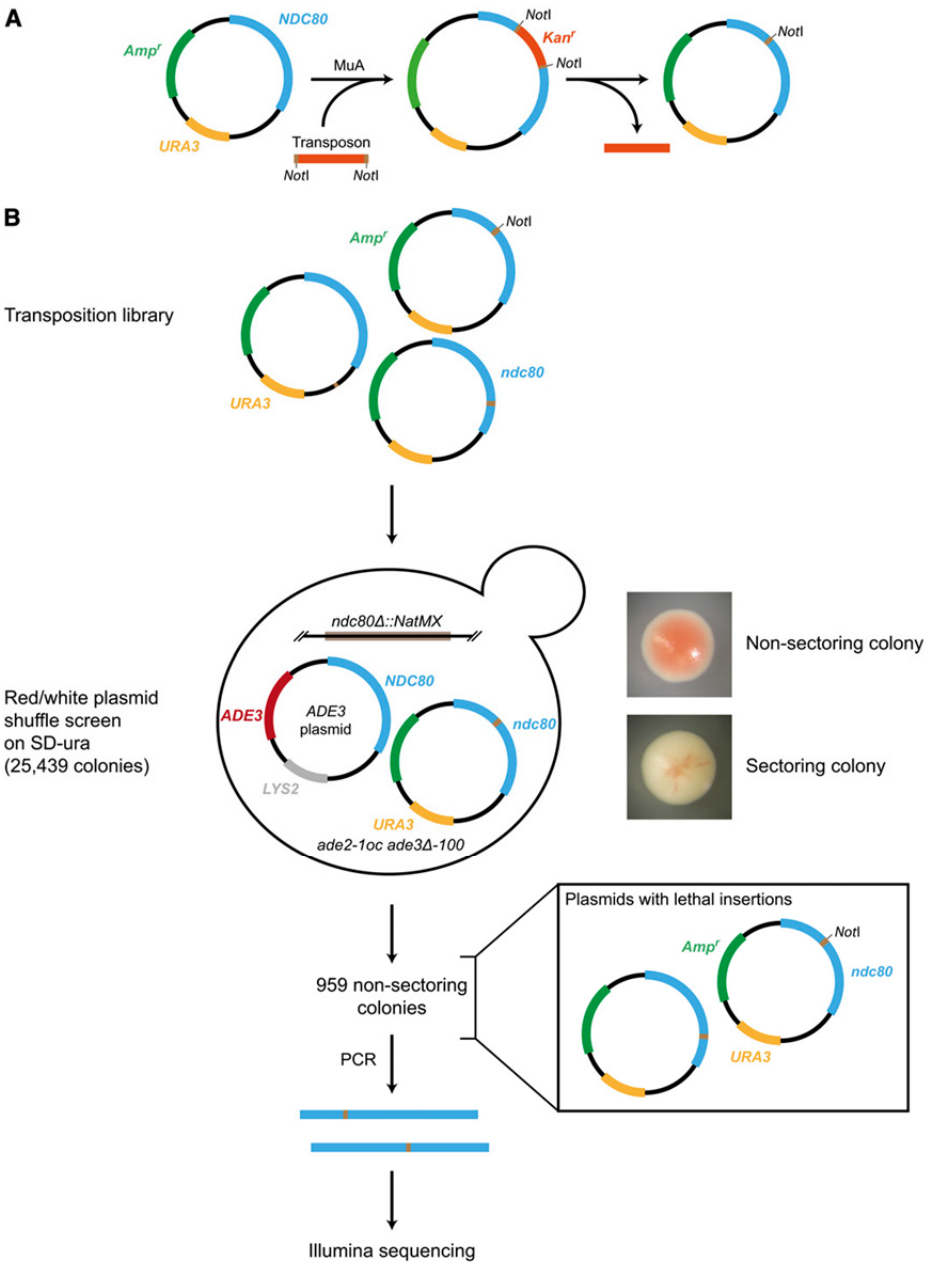

Figure 2 Workflow of the linker-scanning mutagenesis screen. (A) An Ndc80 transposition library, containing 15-bp insertions at random locations, was created using MuA transposition. (B) The transposition library was screened in *S. cerevisiae* using a red/white plasmid shuffle system. Lethal insertions that disrupt the function of Ndc80 appear as nonsectoring red colonies in the screen. From these red colonies, plasmids were isolated and the positions of the lethal insertions were determined by Illumina sequencing.

human crystal structure. The hairpin forms C-terminal to the Ndc80 CH domain and, together, they "sandwich" the globular domain of Nuf2 (Ciferri *et al.* 2008). Both of these mutant complexes bound to microtubules *in vitro* (Figure S4). Furthermore, the ins839 mutation altered the behavior of single molecules of the Ndc80 complex on microtubules, increasing their residence time and slowing their diffusion as compared to wild type (Figure 4, B and C). This observation suggests that although the hairpin is not part of the microtubule-binding interface, it indirectly affects the attachment between the Ndc80 complex and microtubules.

The ins839 Ndc80 complex is insensitive to the presence of the Dam1 complex on microtubules

Ndc80 is required for recruitment of the essential Dam1 complex to kinetochores *in vivo* (Janke *et al.* 2002). *In vitro*, the Ndc80 and Dam1 complexes interact directly, in a microtubule-dependent manner (Lampert *et al.* 2010; Tien *et al.* 2010). The Dam1 complex causes the Ndc80 complex to dissociate more slowly from microtubules and to diffuse more slowly on the lattice (Tien *et al.* 2010). The ins839 mutation in the hairpin of Ndc80 has a similar but less dramatic effect,

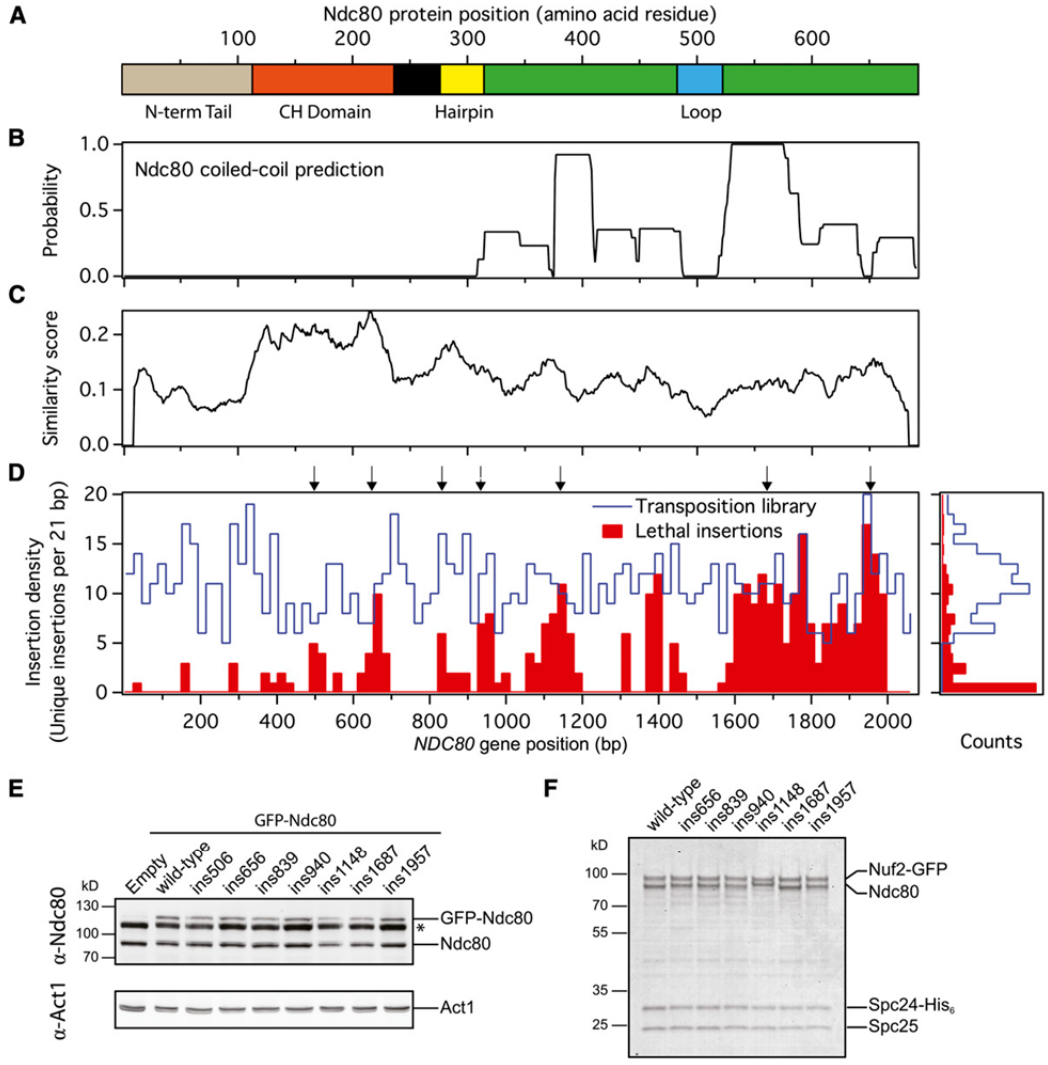

Figure 3 Lethal insertions were found in distinct clusters in *NDC80*. (A) Bar diagram showing the positions of notable structural features in Ndc80. (B) Probability of coiled-coil formation as predicted by Paircoil2 (McDonnell *et al.* 2006). (C) Similarity of Ndc80 protein sequences between select fungal species (see *Materials and Methods*). (D) Left: the insertion density for the transposition library (blue line) and from the red colonies (red bars) is shown along *NDC80*. Insertion density is plotted as the number of unique insertion sites within a 21-bp window. Arrows indicate the positions of the representative insertions characterized. Right: from the insertion density plot, the distributions of insertion densities for the transposition library (blue line) and from the red colonies (red bars) are shown. (E) Immunoblot of cell lysate showing that lethal insertion mutants (GFP tagged) are expressed *in vivo* over the endogenous Ndc80 (untagged). (*) Nonspecific band from the α-Ndc80 antibody. Act1 serves as a loading control. (F) Coomassie-stained gel of recombinant Ndc80 complex containing lethal insertions. Recombinant Ndc80 complexes were purified by affinity chromatography and gel filtration. Mutant Ndc80 complexes migrated similarly to the wild-type complex in the gel filtration column and were collected at the same elution volume. The band for Ndc80 containing the ins1148 mutation reproducibly migrates higher than the wild-type protein.

causing a twofold decrease in the diffusion and dissociation rate constants (Figure 4, B and C). Therefore, we asked whether the Dam1 complex can further alter the microtubule-binding properties of the Ndc80 complex with the ins839 mutation. Surprisingly, unlike wild-type Ndc80 complex and the other five lethal mutant complexes we purified, the ins839 Ndc80 complex was not influenced by the presence of the Dam1 complex (Figure 4, B and C, and Figure S4). Instead, the ins839 mutation makes the Ndc80 complex insensitive to the presence of the Dam1 complex. Whether this is a result of the mutation perturbing the microtubule-binding ability of the Ndc80 complex or disrupting an interaction with the Dam1 complex remains to be determined (see *Discussion*).

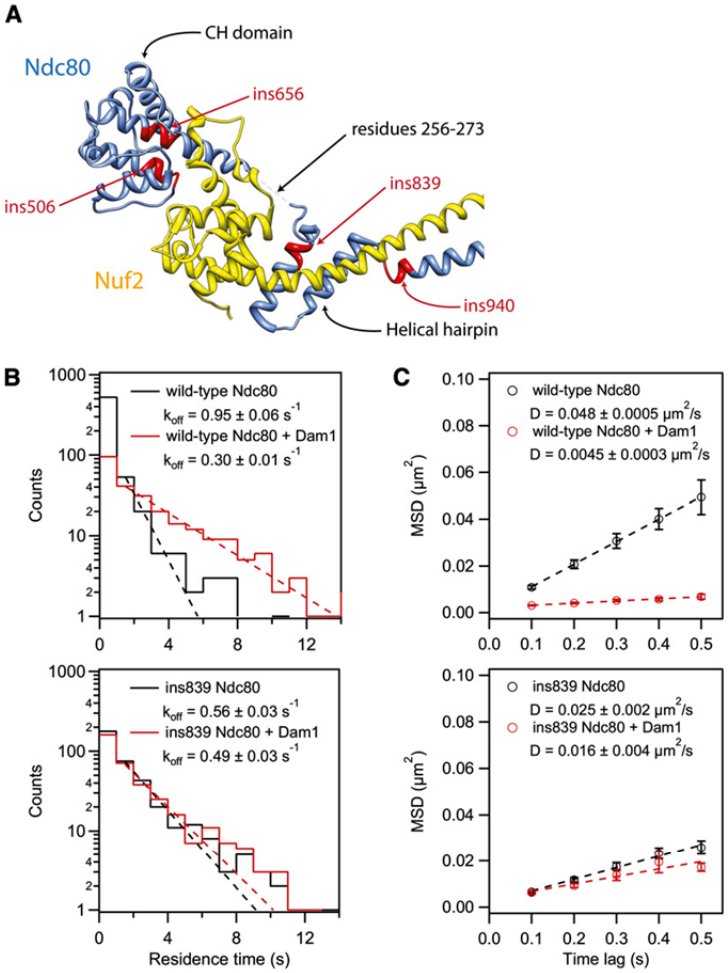

Figure 4 The ability of the Dam1 complex to enhance binding of Ndc80 complexes to microtubules is abrogated by a lethal insertion in the helical hairpin. (A) Four lethal insertion clusters (red) are mapped onto homologous regions of the human Ndc80 (blue) crystal structure (PDB 2VE7; Ciferri *et al.* 2008). Lethal insertion clusters are labeled based on their representative insertion. The structure is illustrated with the UCSF Chimera package (Pettersen *et al.* 2004). (B) Residence time distributions of GFP-tagged Ndc80 complex on microtubules fit with single exponentials (dashed lines) to determine the dissociation rate constants, k_{off}. Top: wild-type Ndc80 complex in the absence (black, n = 622) or presence (red, n = 252) of Dam1 complex. Bottom: ins839 Ndc80 complex in the absence (black, n = 374) or presence (red, n = 357) of Dam1 complex. (C) Plots of mean-squared displacement (MSD) ± SEM *vs.* time lag for the binding events in B. Linear fits to the data (dashed lines) were used to determine the diffusion constant, D.

The ins1957 mutation in Ndc80 disrupts tetramerization of the Ndc80 complex

Localization of Ndc80 to the kinetochore depends on its assembly into an intact complex with Nuf2, Spc24, and Spc25. This complex is anchored to the kinetochore via interactions between Spc24/Spc25 and other components, such as the Mtw1 complex (De Wulf *et al.* 2003; Maskell *et al.* 2010; Petrovic *et al.* 2010; Hornung *et al.* 2011). From cross-linking and limited proteolysis experiments, it was proposed that the C termini of Ndc80/Nuf2 contact Spc24/Spc25 to assemble the Ndc80 complex (Ciferri *et al.* 2005; Wei *et al.* 2005; Maiolica *et al.* 2007). However, the proteins and residues involved in this putative tetramerization domain and the structural basis for assembly of the complex remain poorly understood.

Our linker-scanning mutagenesis screen identified three previously uncharacterized regions in Ndc80 that are essential for its function (represented by ins1148, ins1687, and ins1957). These regions are C-terminal to the CH domain, and all three representative mutant Ndc80 complexes bound microtubules similar to the wild-type complex (Figure S4). The ins1687 and ins1957 mutations represent broad, neighboring clusters of lethal insertions that cover an area including the putative tetramerization domain. We screened these and our other representative mutations for defective kinetochore localization of Ndc80. Using fluorescence microscopy, we measured the amount of GFP-tagged mutant Ndc80 that colocalized with Nuf2–mCherry at kinetochores (Figure 5, A and B). The ins656, ins839, ins940, ins1148, and ins1687 mutant GFP–Ndc80 proteins colocalized with Nuf2–mCherry, indicating that these insertions do not disrupt formation of the Ndc80 complex or its association with the kinetochore *in vivo*. By contrast, ins1957 GFP–Ndc80 was absent from kinetochores. Given its position at the C terminus of Ndc80, we hypothesized that the ins1957 mutation disrupts tetramerization of the complex. However, the ins1957 mutant copurifies with Nuf2, Spc24, and Spc25 in a recombinant Ndc80 complex (Figure 3F), suggesting that the mutation does not completely abolish complex formation. To address this question *in vivo*, we performed immunoprecipitation experiments with TAP tags fused to the endogenous Nuf2

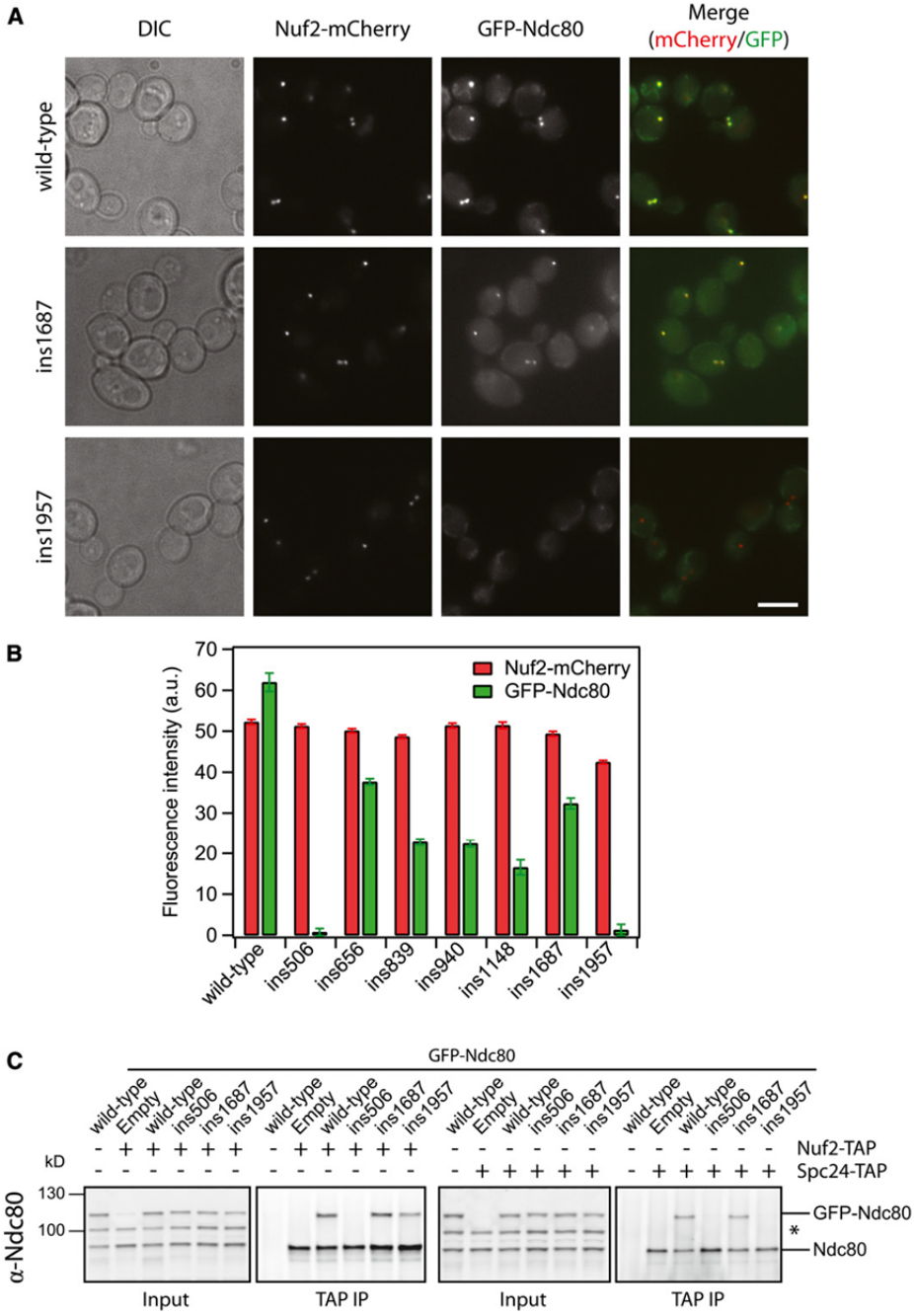

Figure 5 A C-terminal segment of Ndc80 controls tetramerization of the Ndc80 complex. (A) Sample images of GFP–Ndc80 lethal insertion mutants colocalized with Nuf2–mCherry at kinetochores *in vivo*. Endogenous Ndc80 is untagged. Scale bar, 5 μm. (B) The fluorescence intensity of GFP and mCherry are quantified and shown. Intensity is plotted as the mean of fluorescence signal—mean of background signal. Error bars represent SEM. The total numbers of mCherry spots quantified are: wild type (n = 686), ins506 (n = 788), ins656 (n = 760), ins839 (n = 913), ins940 (n = 643), ins1148 (n = 372), ins1687 (n = 576), and ins1957 (n = 389). (C) Immunoprecipitation (IP) of GFP–Ndc80 lethal insertion mutants, and untagged endogenous Ndc80, with Nuf2-TAP or Spc24–TAP. (*) Nonspecific band from the α-Ndc80 antibody. On the immunoblots, input is 0.5% of the clarified lysate and TAP IP is 10% of the total volume.

or Spc24 (Figure 5C). We found that ins1957 GFP–Ndc80 co-immunoprecipitated with Nuf2-TAP, but not Spc24–TAP. As a control, wild-type and ins1687 GFP–Ndc80 co-immunoprecipitated with both Nuf2–TAP and Spc24–TAP. Consistent with its inability to form a recombinant complex, ins506 GFP–Ndc80 did not interact with Nuf2–TAP or Spc24–TAP in the co-immunoprecipitation assay and was absent from kinetochores (Figure 5B and C). These results show that ins506 GFP–Ndc80 cannot pair with Nuf2 and consequently fails to assemble into an intact complex. By contrast, ins1957 GFP–Ndc80 can pair with Nuf2 *in vivo*, but is unable to compete with endogenous Ndc80 for association with Spc24/Spc25 at kinetochores. Therefore, the lethal insertion cluster represented by ins1957 is likely the tetramerization domain, which mediates the association of Ndc80/Nuf2 with Spc24/Spc25 into intact complexes at kinetochores.

Discussion

Linker-scanning mutagenesis specifically identifies regions essential for function

Here, we describe an approach to uncover new functional domains of essential proteins in *S. cerevisiae*. We accomplished this by combining linker-scanning mutagenesis, a plasmid shuffle assay, and high-throughput sequencing together in a comprehensive screen. We applied this screen to the conserved Ndc80 kinetochore protein, which contains a microtubule-binding globular domain and is predicted to contain long coiled-coil domains. While the short insertions resulting from transposon mutagenesis were generally well tolerated, several clusters of insertions were detrimental to Ndc80 function *in vivo*. These clusters of lethal insertions highlight important regions of the protein, many of which are not readily apparent by inspecting sequence conservation (Figure 3C and D).

New functions for the N terminus of Ndc80

Binding of Ndc80 to microtubules is accomplished by its N terminus, which contains an unstructured tail domain and a conserved CH domain that is commonly found on actin- and microtubule-binding proteins (Gimona *et al.* 2002; Korenbaum and Rivero 2002; Hayashi and Ikura 2003; Wei *et al.* 2007; Ciferri *et al.* 2008). In our linker-scanning mutagenesis screen, insertions were generally tolerated throughout the entire N terminus of Ndc80, with just two clusters of lethal insertions in the CH domain. A representative mutation from the first cluster (ins506) is expressed *in vivo*, but is absent from kinetochores and does not co-immunoprecipitate with Nuf2–TAP. This mutant impairs the formation of the Ndc80 complex, likely by disrupting the interaction between the Ndc80 and Nuf2 CH domains. This suggests that the CH domain plays a critical role in the dimerization of Ndc80 and Nuf2. The second cluster lies in an interior helix of the CH domain adjacent to the first cluster. A representative mutation from this cluster (ins656) surprisingly did not abolish microtubule binding by the recombinant complex or disrupt kinetochore localization *in vivo*. It is unlikely that this mutation is lethal because of subtle changes in the microtubule-binding ability of Ndc80, as several mutations that are known to impair microtubule binding by the human complex *in vitro* are tolerated in *S. cerevisiae* (Ciferri *et al.* 2008; Akiyoshi *et al.* 2009; Kemmler *et al.* 2009; Lampert *et al.* 2013; Umbreit *et al.* 2012). We propose that this mutation instead disrupts another essential function of the Ndc80 CH domain that is independent of microtubule binding.

Downstream of the CH domain, we mapped two clusters of lethal insertions to a putative helical hairpin motif. Together with the Ndc80 CH domain, this hairpin packs against the paired CH domain of Nuf2 in a crystal structure of the truncated human Ndc80 complex (Ciferri *et al.* 2008). One of these lethal insertions, ins839, slows the dissociation and diffusion rates of Ndc80 complexes on microtubules *in vitro*. These effects cannot be due to cooperative interactions between Ndc80 complexes on microtubules, as our experiments were performed at the single-molecule level. Moreover, given its position in the crystal structure, the hairpin is unlikely to contact microtubules directly. Therefore, we propose that the hairpin contributes indirectly to microtubule binding, perhaps through structural stabilization or organization of the microtubule-binding interface.

One key role of Ndc80 *in vivo* is to recruit the Dam1 complex to kinetochores (Janke *et al.* 2002), but the nature of this interaction remains unclear. *In vitro*, the wild-type Ndc80 complex interacts directly with the Dam1 complex in a microtubule-dependent manner (Lampert *et al.* 2010; Tien *et al.* 2010). We found previously that the addition of Dam1 complex decreases the dissociation and diffusion rates of single Ndc80 complexes on microtubules. Here we show that the ins839 mutation parallels these effects on the Ndc80 complex and that the addition of Dam1 complex does not further change the behavior of the ins839 Ndc80 complex on microtubules. Notably, while the dissociation and diffusion rates of single ins839 Ndc80 complexes on microtubules are lower than that of the wild-type complex, they are higher than that of the wild-type complex when assayed in the presence of Dam1 complex. This observation raises the interesting possibility that the Dam1 complex does not simply contribute an additional microtubule-binding domain when it interacts with the Ndc80 complex, but changes how the Ndc80 complex binds to the microtubule lattice. The ins839 mutation could partially mimic this effect, which explains why the mutant Ndc80 complex is not further influenced by the Dam1 complex.

An alternative explanation for our observations is that the ins839 mutation disrupts the interaction interface between Ndc80 and the Dam1 complex. Recent studies have proposed that the Dam1 complex binds directly to Ndc80 within the Ndc80 complex, but did not agree on the location of this interaction interface (Maure *et al.* 2011; Lampert *et al.* 2013). One of these proposed regions, a stretch of Ndc80 between the CH domain and the hairpin (residues 256–273; Figure 4A), lies in close proximity to the ins839 mutation. When this region was deleted, the Dam1 complex did not enhance the cosedimentation of the mutant complex with microtubules *in vitro* (Lampert *et al.* 2013). The authors concluded that residues 256–273 represent an interaction interface between Ndc80 and the Dam1 complex. However, like the ins839 mutation, a deletion of this region alters the microtubule-binding behavior of the Ndc80 complex alone (Lampert *et al.* 2013). Therefore, it remains unclear whether these mutations directly disrupt the Dam1 binding interface, or if microtubule attachments made by the mutant complexes are simply unable to be strengthened by the Dam1 complex. Future studies will be aimed at determining whether this region of Ndc80 is in direct contact with the Dam1 complex.

Identification of novel domains in Ndc80 and defining the tetramerization domain

Our linker-scanning mutagenesis screen successfully identified three previously uncharacterized segments of Ndc80 as

regions essential for its function *in vivo*. These three lethal insertion clusters lie in the last ~300 amino acid residues of Ndc80, predicted to form the "rod-shaped" part of the complex as seen by electron microscopy (Wei *et al.* 2005; Wang *et al.* 2008). The first cluster is centered on residue K380 of Ndc80, and coincides with a change in predicted coiled-coil character that may represent a transition point where the coiled-coil begins. Consistent with this prediction, limited proteolysis experiments identified K380 as a cleavage site that is likely unprotected by coiled-coil (Wei *et al.* 2005). The representative insertion from this cluster, ins1148, is predicted to abolish the formation of coiled coil after the insertion (Figure S5). Nevertheless it forms a stable tetramer both *in vivo* and *in vitro*, suggesting the coiled coil in this region is not driving the interaction between Ndc80 and Nuf2, Spc24, or Spc25. Similarly the cluster represented by ins1687 abolishes the probability of coiled-coil formation after this insertion, but again has no effect on tetramer formation and represents a domain with an, as yet, unknown function.

The cluster represented by ins1957 is in a region predicted to overlap with the N termini of Spc24/Spc25 by crosslinking experiments (Maiolica *et al.* 2007). While this general region is proposed to mediate tetramerization of the complex (Ciferri *et al.* 2005; Wei *et al.* 2005; Maiolica *et al.* 2007), it is not clear which complex components are directly involved and which segments of these components are required. We found that the ins1957 mutation disrupts formation of the Ndc80 complex *in vivo* and that the mutant Ndc80 was consequently defective at incorporating into kinetochores. These results suggest that the lethal insertion cluster represented by the ins1957 mutation defines a region in Ndc80 important for tetramerization of the Ndc80 complex.

Using the linker-scanning mutagenesis screen, we have identified lethal insertions in known structural elements of Ndc80 and, additionally, defined new functional domains in the protein. Future experiments will examine individual domains with the goal of defining binding interfaces with known partners, searching for novel protein interactions, and uncovering new roles for Ndc80. This approach is generally applicable to other genes in *S. cerevisiae* and is particularly useful in revealing functional properties and domains in proteins that are not yet amenable to structural characterization.

Acknowledgments

We thank members of the Davis Lab and the Seattle Mitosis group for helpful discussions. We also thank I. Onn, D. Koshland, C. Lee, and J. Shendure for technical assistance and A. Desai for the α-Ndc80 antibody. This work was supported by a National Sciences and Engineering Research Council of Canada scholarship (to J.F.T.), National Institutes of Health Grants T32 GM008268 (to N.T.U.) and T32 GM007270 (to K.K.F.), Searle Scholar Award Grant 06-L-111 (to C.L.A.), Packard Fellowship for Science and Engineering Grant 2006-30521 (to C.L.A), National Center for Research Resources Grant S10 RR26406 (to C.L.A.), and National Institute of General Medical Sciences Grants R01 GM40506 (to T.N.D.) and R01 GM079373 (to C.L.A.). M.J.D. is funded by the National Institute of General Medical Sciences Grant P41 GM103533 to T.N.D. M.J.D. is a Rita Allen Scholar.

Literature Cited

Akiyoshi, B., C. R. Nelson, J. A. Ranish, and S. Biggins, 2009 Analysis of Ipl1-mediated phosphorylation of the Ndc80 kinetochore protein in *Saccharomyces cerevisiae*. Genetics 183: 1591–1595.

Alushin, G. M., V. H. Ramey, S. Pasqualato, D. A. Ball, N. Grigorieff *et al.*, 2010 The Ndc80 kinetochore complex forms oligomeric arrays along microtubules. Nature 467: 805–810.

Asbury, C. L., D. R. Gestaut, A. F. Powers, A. D. Franck, and T. N. Davis, 2006 The Dam1 kinetochore complex harnesses microtubule dynamics to produce force and movement. Proc. Natl. Acad. Sci. USA 103: 9873–9878.

Bender, A., and J. R. Pringle, 1991 Use of a screen for synthetic lethal and multicopy suppresser mutants to identify two new genes involved in morphogenesis in *Saccharomyces cerevisiae*. Mol. Cell. Biol. 11: 1295–1305.

Blackshields, G., F. Sievers, W. Shi, A. Wilm, and D. G. Higgins, 2010 Sequence embedding for fast construction of guide trees for multiple sequence alignment. Algorithms Mol. Biol. 5: 21.

Burke, D., D. Dawson, and T. Stearns, 2000 *Methods in Yeast Genetics*. Cold Spring Harbor Laboratory Press, Cold Spring Harbor, NY.

Ciferri, C., J. De Luca, S. Monzani, K. J. Ferrari, D. Ristic *et al.*, 2005 Architecture of the human ndc80-hec1 complex, a critical constituent of the outer kinetochore. J. Biol. Chem. 280: 29088–29095.

Ciferri, C., S. Pasqualato, E. Screpanti, G. Varetti, S. Santaguida *et al.*, 2008 Implications for kinetochore-microtubule attachment from the structure of an engineered Ndc80 complex. Cell 133: 427–439.

Davis, T. N., 1992 Mutational analysis of calmodulin in *Saccharomyces cerevisiae*. Cell Calcium 13: 435–444.

DeLuca, K. F., S. M. Lens, and J. G. DeLuca, 2011 Temporal changes in Hec1 phosphorylation control kinetochore-microtubule attachment stability during mitosis. J. Cell Sci. 124: 622–634.

De Wulf, P., A. D. McAinsh, and P. K. Sorger, 2003 Hierarchical assembly of the budding yeast kinetochore from multiple subcomplexes. Genes Dev. 17: 2902–2921.

Gimona, M., K. Djinovic-Carugo, W. J. Kranewitter, and S. J. Winder, 2002 Functional plasticity of CH domains. FEBS Lett. 513: 98–106.

Guimaraes, G. J., Y. Dong, B. F. McEwen, and J. G. Deluca, 2008 Kinetochore-microtubule attachment relies on the disordered N-terminal tail domain of Hec1. Curr. Biol. 18: 1778–1784.

Hach, F., F. Hormozdiari, C. Alkan, I. Birol, E. E. Eichler *et al.*, 2010 mrsFAST: a cache-oblivious algorithm for short-read mapping. Nat. Methods 7: 576–577.

Hayashi, I., and M. Ikura, 2003 Crystal structure of the amino-terminal microtubule-binding domain of end-binding protein 1 (EB1). J. Biol. Chem. 278: 36430–36434.

He, X., D. R. Rines, C. W. Espelin, and P. K. Sorger, 2001 Molecular analysis of kinetochore-microtubule attachment in budding yeast. Cell 106: 195–206.

Hornung, P., M. Maier, G. M. Alushin, G. C. Lander, E. Nogales *et al.*, 2011 Molecular architecture and connectivity of the budding yeast Mtw1 kinetochore complex. J. Mol. Biol. 405: 548–559.

Janke, C., J. Ortiz, J. Lechner, A. Shevchenko, M. M. Magiera *et al.*, 2001 The budding yeast proteins Spc24p and Spc25p interact with Ndc80p and Nuf2p at the kinetochore and are important for kinetochore clustering and checkpoint control. EMBO J. 20: 777–791.

Janke, C., J. Ortiz, T. U. Tanaka, J. Lechner, and E. Schiebel, 2002 Four new subunits of the Dam1–Duo1 complex reveal novel functions in sister kinetochore biorientation. EMBO J. 21: 181–193.

Kemmler, S., M. Stach, M. Knapp, J. Ortiz, J. Pfannstiel *et al.*, 2009 Mimicking Ndc80 phosphorylation triggers spindle assembly checkpoint signalling. EMBO J. 28: 1099–1110.

Kline-Smith, S. L., S. Sandall, and A. Desai, 2005 Kinetochore-spindle microtubule interactions during mitosis. Curr. Opin. Cell Biol. 17: 35–46.

Korenbaum, E., and F. Rivero, 2002 Calponin homology domains at a glance. J. Cell Sci. 115: 3543–3545.

Lampert, F., P. Hornung, and S. Westermann, 2010 The Dam1 complex confers microtubule plus end-tracking activity to the Ndc80 kinetochore complex. J. Cell Biol. 189: 641–649.

Lampert, F., C. Mieck, G. M. Alushin, E. Nogales, and S. Westermann, 2013 Molecular requirements for the formation of a kinetochore-microtubule interface by Dam1 and Ndc80 complexes. J. Cell Biol. 200: 21–30.

Maiolica, A., D. Cittaro, D. Borsotti, L. Sennels, C. Ciferri *et al.*, 2007 Structural analysis of multiprotein complexes by cross-linking, mass spectrometry, and database searching. Mol. Cell. Proteomics 6: 2200–2211.

Malvezzi, F., G. Litos, A. Schleiffer, A. Heuck, K. Mechtler *et al.*, 2013 A structural basis for kinetochore recruitment of the Ndc80 complex via two distinct centromere receptors. EMBO J. 32: 409–423.

Maskell, D. P., X. W. Hu, and M. R. Singleton, 2010 Molecular architecture and assembly of the yeast kinetochore MIND complex. J. Cell Biol. 190: 823–834.

Maure, J. F., S. Komoto, Y. Oku, A. Mino, S. Pasqualato *et al.*, 2011 The Ndc80 loop region facilitates formation of kinetochore attachment to the dynamic microtubule plus end. Curr. Biol. 21: 207–213.

McDonnell, A. V., T. Jiang, A. E. Keating, and B. Berger, 2006 Paircoil2: improved prediction of coiled coils from sequence. Bioinformatics 22: 356–358.

Miller, S. A., M. L. Johnson, and P. T. Stukenberg, 2008 Kinetochore attachments require an interaction between unstructured tails on microtubules and Ndc80(Hec1). Curr. Biol. 18: 1785–1791.

Milutinovich, M., E. Unal, C. Ward, R. V. Skibbens, and D. Koshland, 2007 A multi-step pathway for the establishment of sister chromatid cohesion. PLoS Genet. 3: e12.

Miranda, J. J., P. De Wulf, P. K. Sorger, and S. C. Harrison, 2005 The yeast DASH complex forms closed rings on microtubules. Nat. Struct. Mol. Biol. 12: 138–143.

Muller, E. G., 1996 A glutathione reductase mutant of yeast accumulates high levels of oxidized glutathione and requires thioredoxin for growth. Mol. Biol. Cell 7: 1805–1813.

Muller, E. G. D., B. E. Snydsman, I. Novik, D. W. Hailey, D. R. Gestaut *et al.*, 2005 The organization of the core proteins of the yeast spindle pole body. Mol. Biol. Cell 16: 3341–3352.

Nguyen, T., D. B. N. Vinh, D. K. Crawford, and T. N. Davis, 1998 A genetic analysis of interactions with Spc110p reveals distinct functions of Spc97p and Spc98p, components of the yeast gamma-tubulin complex. Mol. Biol. Cell 9: 2201–2216.

Nishino, T., F. Rago, T. Hori, K. Tomii, I. M. Cheeseman *et al.*, 2013 CENP-T provides a structural platform for outer kinetochore assembly. EMBO J. 32: 424–436.

Osborne, M. A., G. Schlenstedt, T. Jinks, and P. A. Silver, 1994 Nuf2, a spindle pole body-associated protein required for nuclear division in yeast. J. Cell Biol. 125: 853–866.

Pajunen, M., H. Turakainen, E. Poussu, J. Peranen, M. Vihinen *et al.*, 2007 High-precision mapping of protein protein interfaces: an integrated genetic strategy combining en masse mutagenesis and DNA-level parallel analysis on a yeast two-hybrid platform. Nucleic Acids Res. 35: e103.

Petrovic, A., S. Pasqualato, P. Dube, V. Krenn, S. Santaguida *et al.*, 2010 The MIS12 complex is a protein interaction hub for outer kinetochore assembly. J. Cell Biol. 190: 835–852.

Pettersen, E. F., T. D. Goddard, C. C. Huang, G. S. Couch, D. M. Greenblatt *et al.*, 2004 UCSF Chimera: a visualization system for exploratory research and analysis. J. Comput. Chem. 25: 1605–1612.

Petyuk, V., J. McDermott, M. Cook, and B. Sauer, 2004 Functional mapping of Cre recombinase by pentapeptide insertional mutagenesis. J. Biol. Chem. 279: 37040–37048.

Powers, A. F., A. D. Franck, D. R. Gestaut, J. Cooper, B. Gracyzk *et al.*, 2009 The Ndc80 kinetochore complex forms load-bearing attachments to dynamic microtubule tips via biased diffusion. Cell 136: 865–875.

Rice, P., I. Longden, and A. Bleasby, 2000 EMBOSS: the European Molecular Biology Open Software Suite. Trends Genet. 16: 276–277.

Scannell, D. R., O. A. Zill, A. Rokas, C. Payen, M. J. Dunham *et al.*, 2011 The awesome power of yeast evolutionary genetics: new genome sequences and strain resources for the Saccharomyces sensu stricto genus. G3: Genes, Genomes, Genetics 1: 11–25.

Schmidt, J. C., H. Arthanari, A. Boeszoermenyi, N. M. Dashkevich, E. M. Wilson-Kubalek *et al.*, 2012 The kinetochore-bound Ska1 complex tracks depolymerizing microtubules and binds to curved protofilaments. Dev. Cell 23: 968–980.

Shimogawa, M. M., M. M. Wargacki, E. G. Muller, and T. N. Davis, 2010 Laterally attached kinetochores recruit the checkpoint protein Bub1, but satisfy the spindle checkpoint. Cell Cycle 9: 3619–3628.

Tien, J. F., N. T. Umbreit, D. R. Gestaut, A. D. Franck, J. Cooper *et al.*, 2010 Cooperation of the Dam1 and Ndc80 kinetochore complexes enhances microtubule coupling and is regulated by aurora B. J. Cell Biol. 189: 713–723.

Umbreit, N. T., D. R. Gestaut, J. F. Tien, B. S. Vollmar, T. Gonen *et al.*, 2012 The Ndc80 kinetochore complex directly modulates microtubule dynamics. Proc. Natl. Acad. Sci. USA 109: 16113–16118.

Wang, H. W., S. Long, C. Ciferri, S. Westermann, D. Drubin *et al.*, 2008 Architecture and flexibility of the yeast Ndc80 kinetochore complex. J. Mol. Biol. 383: 894–903.

Wei, R. R., P. K. Sorger, and S. C. Harrison, 2005 Molecular organization of the Ndc80 complex, an essential kinetochore component. Proc. Natl. Acad. Sci. USA 102: 5363–5367.

Wei, R. R., J. R. Schnell, N. A. Larsen, P. K. Sorger, J. J. Chou *et al.*, 2006 Structure of a central component of the yeast kinetochore: the Spc24p/Spc25p globular domain. Structure 14: 1003–1009.

Wei, R. R., J. Al-Bassam, and S. C. Harrison, 2007 The Ndc80/HEC1 complex is a contact point for kinetochore-microtubule attachment. Nat. Struct. Mol. Biol. 14: 54–59.

Wigge, P. A., and J. V. Kilmartin, 2001 The Ndc80p complex from *Saccharomyces cerevisiae* contains conserved centromere components and has a function in chromosome segregation. J. Cell Biol. 152: 349–360.

Wigge, P. A., O. N. Jensen, S. Holmes, S. Soues, M. Mann *et al.*, 1998 Analysis of the *Saccharomyces* spindle pole by matrix-assisted laser desorption/ionization (MALDI) mass spectrometry. J. Cell Biol. 141: 967–977.

Communicating editor: O. Cohen-Fix

GENETICS

Supporting Information
http://www.genetics.org/lookup/suppl/doi:10.1534/genetics.113.152728/-/DC1

Coupling Unbiased Mutagenesis to High-throughput DNA Sequencing Uncovers Functional Domains in the Ndc80 Kinetochore Protein of *Saccharomyces cerevisiae*

Jerry F. Tien, Kimberly K. Fong, Neil T. Umbreit, Celia Payen, Alex Zelter, Charles L. Asbury, Maitreya J. Dunham, and Trisha N. Davis

DOI: 10.1534/genetics.113.152728

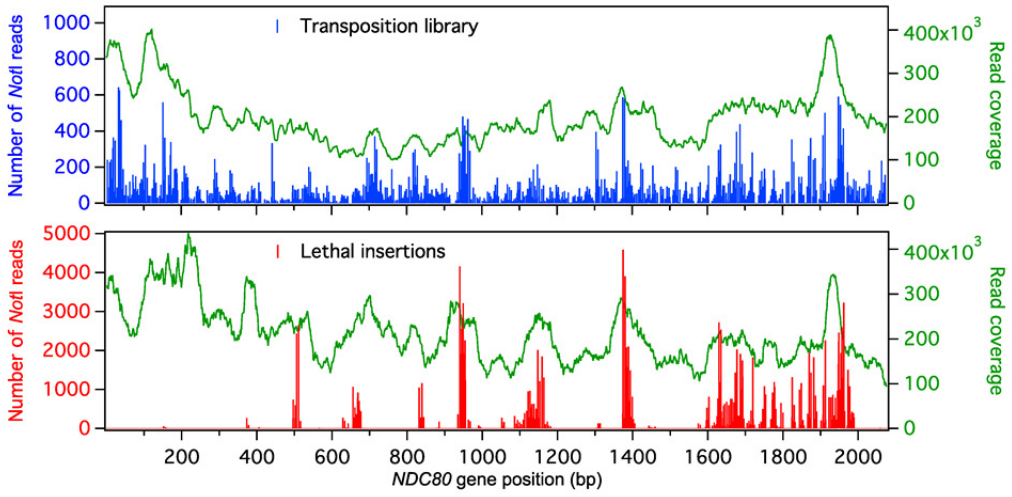

Figure S1 Positions of 15-bp insertions in the transposition library (blue lines) and from the non-sectoring red colonies (red lines) were determined by Illumina sequencing. Insertions were identified using the unique *Not*I recognition sequence and shown along the *NDC80* gene. The read coverage from the sequencing is shown in green.

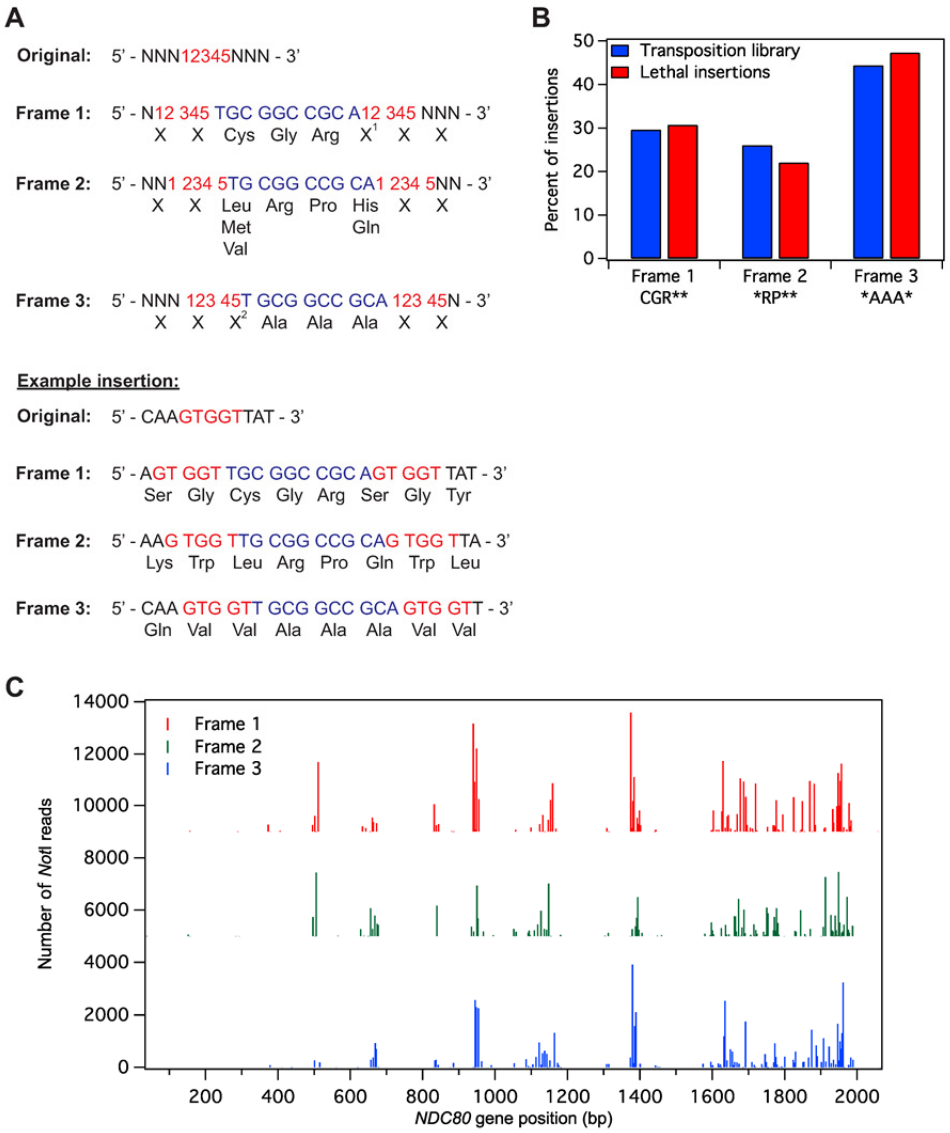

Figure S2 The reading frame targeted by transposition dictates the residues inserted. (A) The translation of the insertion depends on both the frame of insertion and the target sequence (adapted from Finnzymes Manual F-701). In the transposition library, each 15-bp insertion includes 5 bp of duplicated target sequence (red) and 10 additional nucleotides (blue). X is any amino acid; X^1 is Ile, Met, Thr, Asn, Lys, Ser, or Arg; X^2 is any amino acid except Gln, Glu, Lys, Met, and Trp. An example insertion is also shown. (B) The proportion of lethal insertions in each frame (red) is similar to that of the initial transposition library (blue). (C) The positions of lethal insertions (from Figure S1) are separated based on the frame of insertion. Traces are offset vertically for visual clarity.

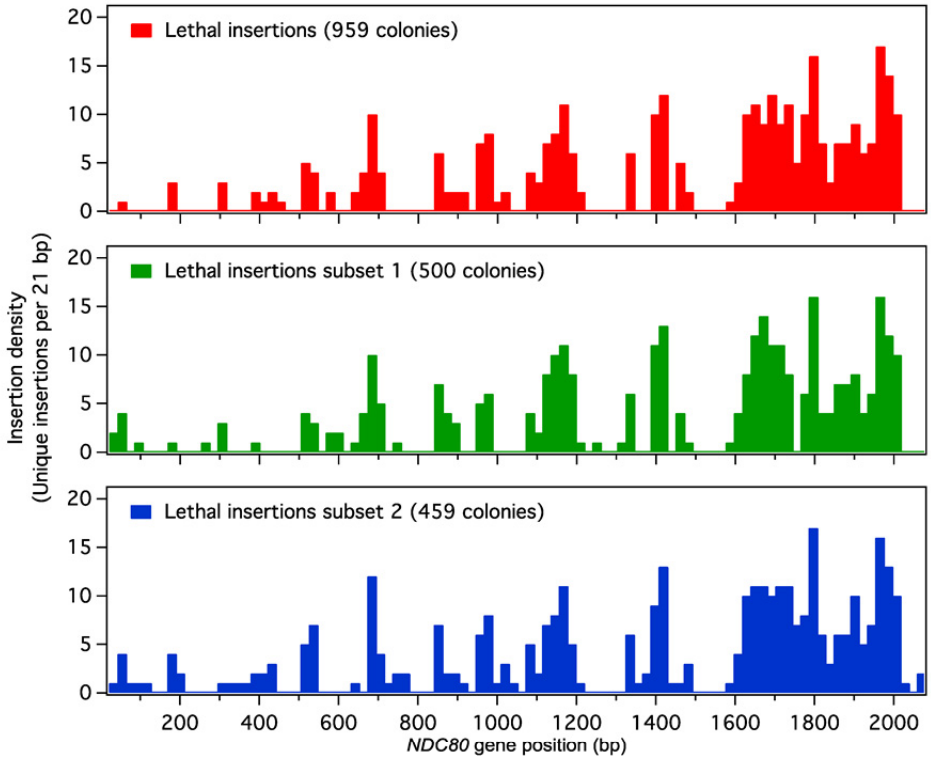

Figure S3 Validation of the lethal insertion clusters. Two subsets (green and blue bars) sequenced independently have the same lethal insertion clusters as the original 959 non-sectoring red colonies (red bars, from Figure 3D).

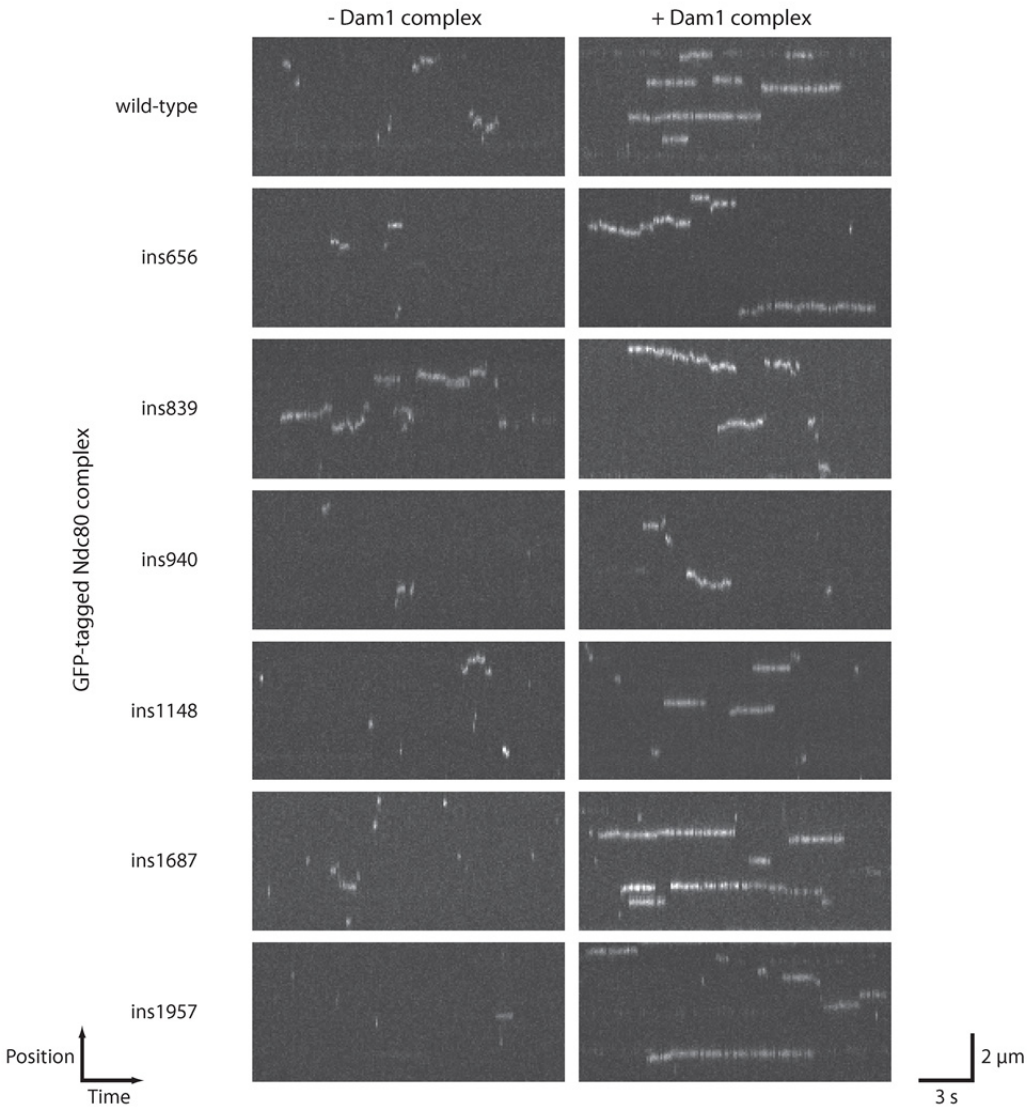

Figure S4 Lethal insertion mutants affect the ability of the Dam1 complex to enhance binding of the Ndc80 complex to microtubules. Using TIRF microscopy, single molecules of GFP-tagged Ndc80 complexes were visualized on taxol-stabilized microtubules. Representative kymographs show the binding and one-dimensional diffusion of 50 pM GFP-tagged Ndc80 complexes on microtubules in the presence or absence of 2.5 nM untagged Dam1 complex.

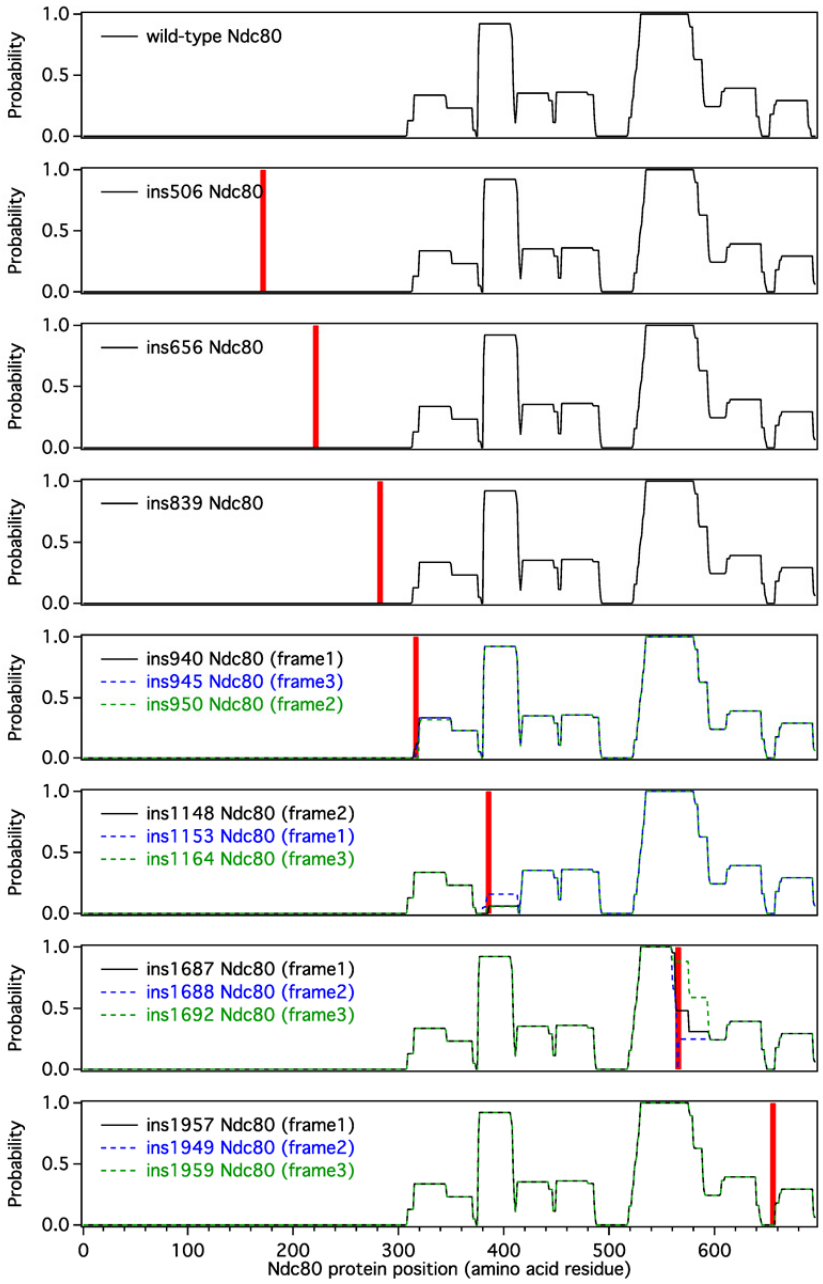

Figure S5 The effect of lethal insertions in Ndc80 on predicted coiled-coil formation. The probabilities of coiled-coil formation, as predicted by Paircoil2 (McDonnell *et al.* 2006), for Ndc80 containing the representative lethal insertions studied (black lines). Vertical red lines denote the positions of the representative insertions. The probabilities of coiled-coil formation for additional lethal insertions are also shown (blue and green dotted lines).

Table S1 Plasmids used in this study

Plasmid	Relevant markers	Reference
pRS316	*CEN6 ARSH4 URA3 Amp*^{r} f1 origin	SIKORSKI and HIETER 1989
pKG9	*NatMX*	GREENLAND *et al.* 2010
pJT12	*NDC80 ADE3 LYS2* in 2 µm vector	This study
pJT36	*NDC80* in pRS316	This study
pJT153	*GFP-NDC80* in pRS316	This study
pJT185	*ins506 GFP-ndc80* in pRS316	This study
pJT187	*ins656 GFP-ndc80* in pRS316	This study
pJT188	*ins839 GFP-ndc80* in pRS316	This study
pJT189	*ins940 GFP-ndc80* in pRS316	This study
pJT190	*ins1148 GFP-ndc80* in pRS316	This study
pJT154	*ins1687 GFP-ndc80* in pRS316	This study
pJT155	*ins1957 GFP-ndc80* in pRS316	This study
His_6-Spc24/Spc25 expression plasmid	*His_6-SPC24/SPC25* dicistron, *Kan*^{r}	WEI *et al.* 2005
Ndc80/Nuf2-GFP expression plasmid	*NDC80/NUF2-GFP* dicistron, *Amp*^{r}	POWERS *et al.* 2009
pJT138	*ins506 ndc80/NUF2-GFP* dicistron, *Amp*^{r}	This study
pJT139	*ins511 ndc80/NUF2-GFP* dicistron, *Amp*^{r}	This study
pJT140	*ins656 ndc80/NUF2-GFP* dicistron, *Amp*^{r}	This study
pJT141	*ins839 ndc80/NUF2-GFP* dicistron, *Amp*^{r}	This study
pJT142	*ins940 ndc80/NUF2-GFP* dicistron, *Amp*^{r}	This study
pJT143	*ins1148 ndc80/NUF2-GFP* dicistron, *Amp*^{r}	This study
pJT145	*ins1687 ndc80/NUF2-GFP* dicistron, *Amp*^{r}	This study
pJT146	*ins1957 ndc80/NUF2-GFP* dicistron, *Amp*^{r}	This study
Dam1 complex expression plasmid	*DAD4/DAD3/DAD2/SPC19/ASK1* and *DAD1/DUO1/SPC34-His_6/DAM1/HSK3* polycistrons, *Amp*^{r}	MIRANDA *et al.* 2005

Table S2 Yeast strains used in this study

Strain	Genotype	Reference
W303	*ade2-1oc can1-100 his3-11,15 leu2-3,112 trp1-1 ura3-1*	
JTY1	MAT**a**/α *ade2-1oc/ade2-1oc ade3Δ-100/ade3Δ-100 can1-100/can1-100 cyh2^r/CYH2^s his3-11,15/his3-11,15 leu2-3,112/leu2-3,112 lys2Δ::HIS3/lys2Δ::HIS3 trp1-1/trp1-1 ura3-1/ura3-1*	This study
JTY4	MAT**a**/α *ade2-1oc/ade2-1oc ade3Δ-100/ade3Δ-100 can1-100/can1-100 cyh2^r/CYH2^s his3-11,15/his3-11,15 leu2-3,112/leu2-3,112 lys2Δ::HIS3/lys2Δ::HIS3 trp1-1/trp1-1 ura3-1/ura3-1 NDC80/ndc80Δ::NatMX*	This study
JTY5-5C	MAT**a** *ade2-1oc ade3Δ-100 can1-100 cyh2^r his3-11,15 leu2-3,112 lys2Δ::HIS3 trp1-1 ura3-1 ndc80Δ::NatMX* [pJT12]	This study
JTY12-25A	MAT**a** *ade2-1oc ade3Δ-100 can1-100 cyh2^r his3-11,15 leu2-3,112 trp1-1 ura3-1 NDC80 NUF2-mCherry::hphMX*	This study
JTY29-1B	MATα *ade2-1oc ade3Δ-100 can1-100 cyh2^r his3-11,15 leu2-3,112 trp1-1 ura3-1 NUF2*	This study
JTY29-1C	MATα *ade2-1oc ade3Δ-100 can1-100 CYH2^s his3-11,15 leu2-3,112 trp1-1 ura3-1 NUF2-TAP::KanMX*	This study
JTY47-2A	MAT**a** *ade2-1oc ade3Δ-100 can1-100 CYH2^s his3-11,15 leu2-3,112 trp1-1 ura3-1 SPC24*	This study
JTY47-2B	MATα *ade2-1oc ade3Δ-100 can1-100 cyh2^r his3-11,15 leu2-3,112 trp1-1 ura3-1 SPC24-TAP::KanMX*	This study

Table S3 Oligonucleotides used for Illumina sequencing

Primer	Sequence
NDC80 forward PCR primer	TAAAGGGAACAAAAGCTGGG
NDC80 reverse PCR primer	ACGGCCAGTGAATTGTAA
Multiplex adapter 1	5' P-GATCGGAAGAGCACACGTCT
Multiplex adapter 2	ACACTCTTTCCCTACACGACGCTCTTCCGATCT
Multiplex forward PCR primer + index 1	AATGATACGGCGACCACCGCGATCTCGTGATACACTCTTTCCCTACACGACGCTCTTCCGATC
Multiplex forward PCR primer + index 2	AATGATACGGCGACCACCGCGATCTACATCGACACTCTTTCCCTACACGACGCTCTTCCGATC
Multiplex reverse PCR primer	CAAGCAGAAGACGGCATACGAGATACACTCTTTCCCTACACGACGCTCTTCCGATCT
Multiplex index sequencing primer	AGATCGGAAGAGCGTCGTGTAGGGAAAGAGTGT
Multiplex read1 sequencing primer	ACACTCTTTCCCTACACGACGCTCTTCCGATCT
TruSeq Indexed Adapter AD002	GATCGGAAGAGCACACGTCTGAACTCCAGTCACCGATGTATCTCGTATGCCGTCTTCTGCTTG
TruSeq Indexed Adapter AD018	GATCGGAAGAGCACACGTCTGAACTCCAGTCACGTCCGCATCTCGTATGCCGTCTTCTGCTTG
TruSeq Indexed Adapter AD019	GATCGGAAGAGCACACGTCTGAACTCCAGTCACGTGAAAATCTCGTATGCCGTCTTCTGCTTG

Table S4 Illumina sequencing results

	Transposition library	Lethal insertions	Lethal insertion subsets	
			Subset 1	Subset 2
Number of sequencing runs	3	1	1	1
Number of 36-bp reads mapped to Chromosome IX	14,000,357	13,710,514	10,075,540	13,424,377
Number of Chromosome IX reads containing *Not*I	96,569	166,135	290,126	319,434
Number of Chromosome IX reads with *Not*I in *NDC80* + promoter/terminator	93,826	N/A	N/A	N/A
Number of Chromosome IX reads with *Not*I in *NDC80*	70,215	165,414	289,470	318,637
Number of unique *Not*I sites in *NDC80*	1,074	336	320	351
Coverage of *NDC80* gene (%)	52	16	15	17
Number of unique codons containing insertions	444	162	149	165
Coverage of Ndc80 protein (%)	64	23	22	24

N/A, not applicable

Literature Cited

GREENLAND, K. B., H. DING, M. COSTANZO, C. BOONE and T. N. DAVIS, 2010 Identification of Saccharomyces cerevisiae spindle pole body remodeling factors. PLoS One **5:** e15426.

MCDONNELL, A. V., T. JIANG, A. E. KEATING and B. BERGER, 2006 Paircoil2: improved prediction of coiled coils from sequence. Bioinformatics **22:** 356-358.

MIRANDA, J. J., P. DE WULF, P. K. SORGER and S. C. HARRISON, 2005 The yeast DASH complex forms closed rings on microtubules. Nat Struct Mol Biol **12:** 138-143.

POWERS, A. F., A. D. FRANCK, D. R. GESTAUT, J. COOPER, B. GRACYZK *et al.*, 2009 The Ndc80 kinetochore complex forms load-bearing attachments to dynamic microtubule tips via biased diffusion. Cell **136:** 865-875.

SIKORSKI, R. S., and P. HIETER, 1989 A system of shuttle vectors and yeast host strains designed for efficient manipulation of DNA in Saccharomyces cerevisiae. Genetics **122:** 19-27.

WEI, R. R., P. K. SORGER and S. C. HARRISON, 2005 Molecular organization of the Ndc80 complex, an essential kinetochore component. Proc Natl Acad Sci U S A **102:** 5363-5367.

APPENDIX B

Cooperation of the Dam1 and Ndc80 kinetochore complexes enhances microtubule coupling and is regulated by Aurora B

TIEN, J. F., N. T. UMBREIT, D. R. GESTAUT, A. D. FRANCK, J. COOPER *et al.*, 2010 Cooperation of the Dam1 and Ndc80 kinetochore complexes enhances microtubule coupling and is regulated by aurora B. J Cell Biol **189:** 713-723.

Published May 17, 2010

Cooperation of the Dam1 and Ndc80 kinetochore complexes enhances microtubule coupling and is regulated by aurora B

Jerry F. Tien,[1] Neil T. Umbreit,[1] Daniel R. Gestaut,[1] Andrew D. Franck,[2] Jeremy Cooper,[2] Linda Wordeman,[2] Tamir Gonen,[1,3] Charles L. Asbury,[2] and Trisha N. Davis[1]

[1]Department of Biochemistry, [2]Department of Physiology and Biophysics, and [3]Howard Hughes Medical Institute, University of Washington, Seattle, WA 98195

The coupling of kinetochores to dynamic spindle microtubules is crucial for chromosome positioning and segregation, error correction, and cell cycle progression. How these fundamental attachments are made and persist under tensile forces from the spindle remain important questions. As microtubule-binding elements, the budding yeast Ndc80 and Dam1 kinetochore complexes are essential and not redundant, but their distinct contributions are unknown. In this study, we show that the Dam1 complex is a processivity factor for the Ndc80 complex, enhancing the ability of the Ndc80 complex to form load-bearing attachments to and track with dynamic microtubule tips in vitro. Moreover, the interaction between the Ndc80 and Dam1 complexes is abolished when the Dam1 complex is phosphorylated by the yeast aurora B kinase Ipl1. This provides evidence for a mechanism by which aurora B resets aberrant kinetochore–microtubule attachments. We propose that the action of the Dam1 complex as a processivity factor in kinetochore–microtubule attachment is regulated by conserved signals for error correction.

Introduction

During mitosis, kinetochores attach to assembling and disassembling microtubule tips while withstanding tensile forces from the mitotic spindle (Skibbens et al., 1993, 1995; Maddox et al., 2003). Kinetochores are able to harness energy from these disassembling microtubule tips to drive movement of chromosomes (for a review see Inoué and Salmon, 1995). Understanding how the kinetochore establishes microtubule attachments under force requires understanding the organization of the kinetochore components and how they bear and transmit load. Recent studies investigated the spatial organization of kinetochore components in vivo and how their arrangement changes throughout mitosis (Joglekar et al., 2009; Wan et al., 2009). Through systematic reconstitution of kinetochore components, we are pursuing a complementary approach with the ultimate goal of mapping the transmission of force across the kinetochore from the dynamic microtubule to the centromere. In this study, we focus on the kinetochore–microtubule interface.

The kinetochores of all eukaryotes contain multiple microtubule-binding elements. The KMN network (KNL-1, Mis12 complex, and Ndc80 complex) and the Ska1 complex both bind microtubules in higher eukaryotic cells (Cheeseman et al., 2006; Gaitanos et al., 2009; Welburn et al., 2009). Yeast also contain the KMN network and the Dam1 complex, possibly the functional homologue of the Ska1 complex (Hanisch et al., 2006; Gaitanos et al., 2009; Raaijmakers et al., 2009; Welburn et al., 2009). Cooperation of the three components of the conserved KMN network was shown by cosedimentation with taxol-stabilized microtubules (Cheeseman et al., 2006), but how or whether any of the microtubule-binding components cooperate to achieve attachment to dynamic microtubules is unknown. We show for the first time that cooperation between two

J.F. Tien, N.T. Umbreit, D.R. Gestaut, and A.D. Franck contributed equally to this paper.

Correspondence to Trisha N. Davis: tdavis@u.washington.edu

Abbreviations used in this paper: GB, growth buffer; TEV, tobacco etch virus; TIRF, total internal reflection fluorescence.

Supplemental Material can be found at:
http://jcb.rupress.org/content/suppl/2010/05/17/jcb.200910142.DC1.html

The Rockefeller University Press $30.00
J. Cell Biol. Vol. 189 No. 4 713–723
www.jcb.org/cgi/doi/10.1083/jcb.200910142

Published May 17, 2010

kinetochore subcomplexes enhances processive, load-bearing coupling to dynamic microtubule tips.

In the budding yeast kinetochore, all four proteins of the Ndc80 complex and all 10 proteins of the Dam1 complex are essential (Tanaka and Desai, 2008). In vitro, both complexes independently form diffusive attachments to the microtubule lattice and track with disassembling microtubule tips, although the Ndc80 complex requires artificial oligomerization to tip track (Westermann et al., 2006; Gestaut et al., 2008; Powers et al., 2009). The Dam1 complex also tracks robustly with polymerizing microtubules in vitro (Asbury et al., 2006; see Lampert et al. in this issue). When attached to beads, each complex forms load-bearing attachments to dynamic microtubule tips (Asbury et al., 2006; Franck et al., 2007; Grishchuk et al., 2008a,b; Powers et al., 2009). Despite these similarities, the Ndc80 and Dam1 complexes are not redundant. The Ndc80 complex is required in vivo for attachment to microtubules (Kline-Smith et al., 2005), and the Dam1 complex is required for attaching to the tips of microtubules and for establishing biorientation (Tanaka et al., 2005; Shimogawa et al., 2006). Moreover, the Ndc80 complex is required for the assembly of Dam1 complex onto the kinetochore (Janke et al., 2002), and an interaction between the two complexes has been suggested by localization and two-hybrid studies (Shang et al., 2003; Joglekar et al., 2009). Studying the combination of Ndc80 and Dam1 complexes in vitro will allow us to dissect their distinct roles in kinetochore–microtubule binding.

Kinetochores not only serve as physical bridges between chromosomes and spindle microtubules but are also regulatory hubs that ensure chromosome segregation fidelity during mitosis. For example, aurora B kinase is responsible for resetting aberrant kinetochore–microtubule attachments to achieve biorientation (Cheeseman et al., 2002; Tanaka et al., 2002; Hauf et al., 2003; Pinsky et al., 2006). Many of the microtubule-binding components of the kinetochore, including the Ndc80 and Dam1 complexes, are targets of aurora B (Cheeseman et al., 2002, 2006; Shang et al., 2003; DeLuca et al., 2006; Pinsky et al., 2006; Gestaut et al., 2008). In mammalian cells, aurora B phosphorylation of the N-terminal tail of the Ndc80 protein (Hec1 in humans) abolishes kinetochore–microtubule attachment (DeLuca et al., 2006; Guimaraes et al., 2008). Although the budding yeast Ndc80 protein also has an N-terminal tail, it is not essential (Akiyoshi et al., 2009; Kemmler et al., 2009). Previously, we demonstrated that phosphorylation by the yeast aurora B homologue Ipl1 at one target site within the Dam1 complex, Ser20 of Dam1, reduces its affinity for the microtubule lattice (Gestaut et al., 2008). Two-hybrid assays and pull-downs with in vitro–translated proteins using phosphomimetic mutations at Ipl1 target sites in Dam1 also suggested that phosphorylation of the Dam1 complex modulates its interaction with the Ndc80 complex (Shang et al., 2003). Moreover, Ipl1 target sites on Dam1 are dephosphorylated as cells enter metaphase in a cohesin-dependent manner, which could prevent kinetochore–microtubule attachment turnover as biorientation is established (Keating et al., 2009).

In this study, we show that the Dam1 complex is a phospho-regulated processivity factor for the Ndc80 complex in kinetochore–microtubule coupling. Using techniques for tracking and manipulating single molecules in vitro, we demonstrate directly an interaction between the Ndc80 and Dam1 complexes on microtubules. Through this interaction, the Dam1 complex enhances the ability of the Ndc80 complex to maintain attachment to dynamic microtubule tips even in the presence of external load. Finally, this interaction is regulated by Ipl1, further defining the mechanism for aurora B–mediated corrective detachment in vivo.

Results

The Dam1 and Ndc80 complexes interact on microtubules

We expressed recombinant *Saccharomyces cerevisiae* Ndc80 and Dam1 complexes in *Escherichia coli* and purified each complex by affinity chromatography and gel filtration (Wei et al., 2005; Gestaut et al., 2008; Powers et al., 2009). By velocity sedimentation analysis, we found weak interaction between the Ndc80 and Dam1 complexes free in solution (Fig. S1). Using total internal reflection fluorescence (TIRF) microscopy, we quantified the interaction of GFP-tagged Ndc80 complexes with microtubules in the presence and absence of Dam1 complex (Fig. 1). In the absence of Dam1 complex, individual Ndc80 complexes formed transient and diffusive attachments to microtubules, as reported previously (Powers et al., 2009). We measured a dissociation rate constant (k_{off}) of 0.44 ± 0.03 s^{-1}, an association rate constant (k_{on}) of 0.60 ± 0.02 $\mu M^{-1} \times s^{-1}$, and a diffusion constant of 0.067 ± 0.003 $\mu m^2 \times s^{-1}$ (Fig. 1, C–E), which are values comparable with our previous study (Powers et al., 2009). We also simultaneously visualized GFP-tagged Ndc80 complexes and mCherry-tagged Dam1 complexes on microtubules. At concentrations affording single molecule resolution of each complex, interaction events were rare. When the two complexes did associate with each other, they appeared to diffuse more slowly (Fig. S2). However, interaction events between individual Ndc80 and Dam1 complexes were too infrequent to affect population behavior. To increase the frequency of interactions, we raised the concentration of Dam1 complex while maintaining low concentrations (10 pM) of the Ndc80 complex. Overall, Ndc80 complex transitioned gradually to a more persistent and more slowly diffusing behavior as the concentration of Dam1 complex was increased (Fig. 1, C–E). At 500 pM Dam1 complex, the Ndc80 complex dissociated twofold more slowly from the microtubule (k_{off} = 0.23 ± 0.02 s^{-1}) and associated 1.6-fold faster onto the microtubule (k_{on} = 0.99 ± 0.02 $\mu M^{-1} \times s^{-1}$) as compared with the Ndc80 complex alone. This corresponds to a threefold decrease in the apparent equilibrium dissociation constant, $K_d = k_{off} \times k_{on}^{-1}$ (0.74 ± 0.06 to 0.23 ± 0.02 µM). At 500 pM Dam1 complex, the Ndc80 complex also diffused fivefold more slowly (0.013 ± 0.0006 $\mu m^2 \times s^{-1}$) as compared with Ndc80 complex alone. The Dam1 complex was unlikely to be acting as a simple barrier to diffusional motility, as the diffusive behavior of the Ndc80 complex was unchanged in the presence of phosphorylated Dam1 complex at the same lattice density (see Ipl1 phosphorylation regulates...). The brightness distribution of the GFP signal remained unchanged

Published May 17, 2010

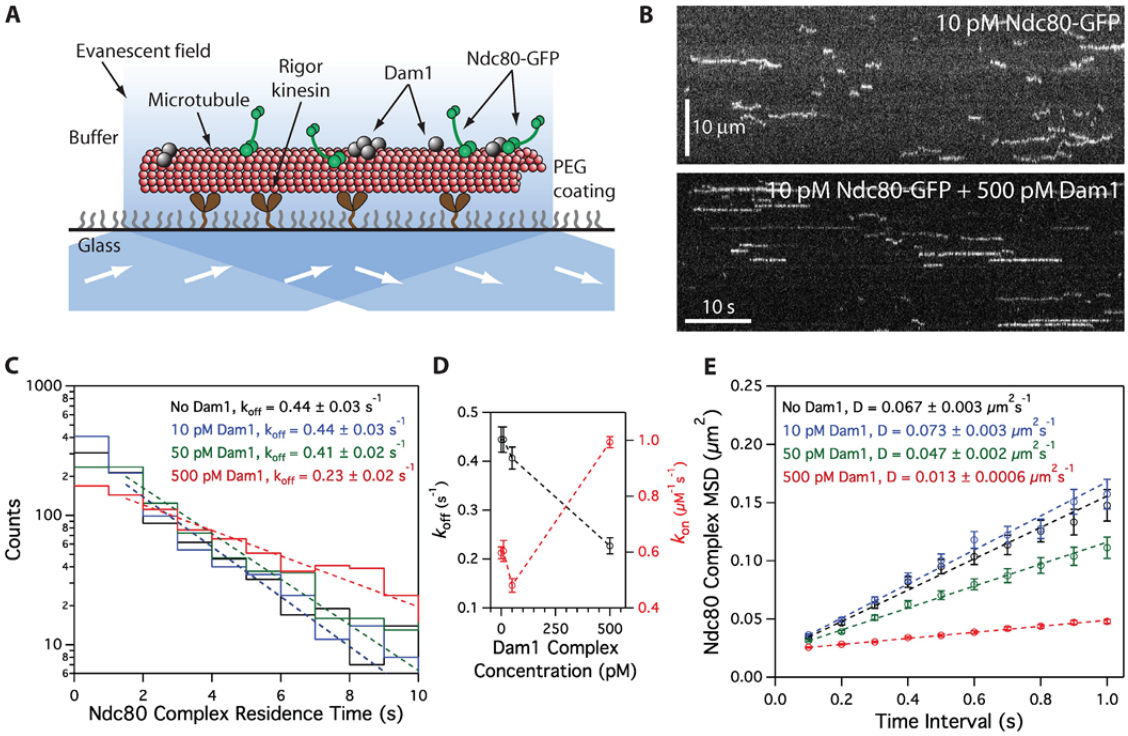

Figure 1. **Dam1 complex enhances binding of individual Ndc80 complexes to microtubules.** (A) Schematic of the TIRF assay developed to visualize the behavior of GFP-tagged Ndc80 complexes (green rods) in the presence of untagged Dam1 complexes (gray spheres) on microtubules. (B) Representative kymographs showing the binding and one-dimensional diffusion of 10 pM Ndc80 complexes on taxol-stabilized microtubules in the absence or presence of 500 pM Dam1 complex. Positions along the microtubule are shown on the vertical axis, whereas the passage of time is depicted along the horizontal axis. Concentrations are of free complexes in solution. (C) Residence time distributions of 10 pM Ndc80 complex on microtubules without Dam1 complex (black histogram; n = 883 events), with 10 pM Dam1 complex (blue histogram; n = 966), 50 pM Dam1 complex (green histogram; n = 928), and 500 pM Dam1 complex (red histogram; n = 1,003). Dotted lines show the weighted exponential fits used to determine dissociation rate constants, k_{off}. (D) Dissociation rate constants (k_{off}; left axis, black markers) for the Ndc80 complex, calculated from the data in C, are plotted against the concentration of Dam1 complex. Association rate constants (k_{on}; right axis, red markers) of the Ndc80 complex are also plotted (without Dam1 complex, n = 1,103; with 10 pM Dam1 complex, n = 1,426; with 50 pM Dam1 complex, n = 1,179; with 500 pM Dam1 complex, n = 1,412). (E) Mean-squared displacement (MSD) is plotted against time for 10 pM Ndc80 complex on microtubules without Dam1 complex (black markers; n = 803 events), with 10 pM Dam1 complex (blue markers; n = 859), 50 pM Dam1 complex (green markers; n = 883), and 500 pM Dam1 complex (red markers; n = 968). Dotted lines show the weighted linear fits used to determine diffusion constants, D. Markers indicate SEM.

across concentrations of the Dam1 complex, demonstrating that oligomerization of the Ndc80 complex did not contribute to its modified behavior in the presence of the Dam1 complex (Fig. 2). Even at 500 pM Dam1 complex, not all Ndc80 complexes bound persistently and diffused slowly. This indicates that not all Ndc80 complexes were associated with Dam1 complexes, so our calculated values describe a mixed population and likely underestimate Dam1 complex–mediated enhancement of Ndc80 complex–microtubule interactions.

In the presence of the Dam1 complex, diffusion of the Ndc80 complex is slowed far below the reported rate for a single Dam1 complex (Gestaut et al., 2008). Therefore, we hypothesized that at the concentrations required to observe significant changes in the population behavior of the Ndc80 complex, the Dam1 complex forms slowly diffusing oligomers. To test this, we measured the diffusion rate of GFP-tagged Dam1 complex on microtubules (Fig. S3, A and B). At 2 pM, single GFP-tagged Dam1 complexes diffused rapidly, at 0.060 ± 0.003 $\mu m^2 \times s^{-1}$, which is similar to the rates reported previously (Westermann et al., 2006; Gestaut et al., 2008). However, at 20 and 50 pM Dam1 complex, we observed slowly diffusing spots that exhibited fluorescence brighter than individual Dam1 complexes. To maintain single molecule resolution for quantifying the diffusion of Dam1 complex at higher concentrations, we mixed untagged Dam1 complex with a small amount of GFP-tagged Dam1 complex. At 500 pM, Dam1 complex diffused at least 60-fold more slowly than at 2 pM (Fig. S3 B). These observations indicate that oligomerization of the Dam1 complex slows its diffusion rate, as reported previously (Grishchuk et al., 2008a). Moreover, they imply that the enhanced binding of Ndc80 complex to microtubules that we have quantified here (Fig. 1, C–E) occurs via interaction with Dam1 complexes that are primarily in an oligomeric state.

In vitro, the Dam1 complex forms rings of 16–25 complexes that encircle microtubules (Miranda et al., 2007; Wang et al., 2007). To investigate whether rings are important for

Published May 17, 2010

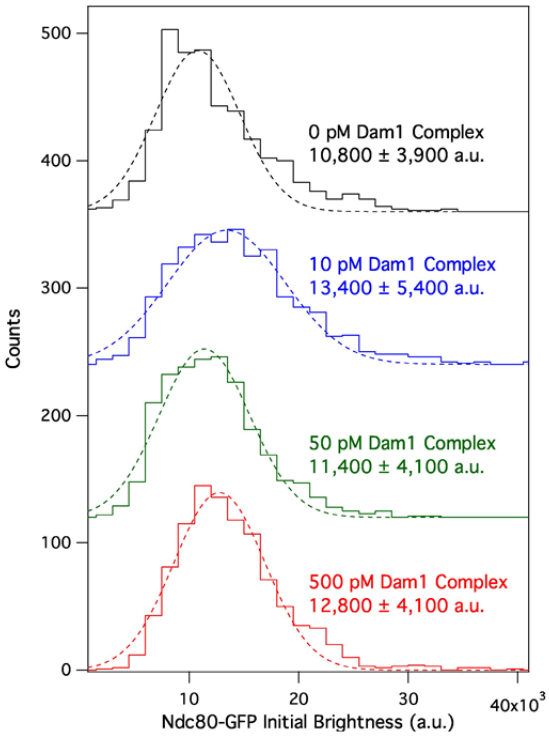

Figure 2. **Dam1 complex does not affect the oligomerization state of the Ndc80 complex on microtubules.** Mean initial brightness distributions of 10 pM GFP-tagged Ndc80 complex–binding events on microtubules without Dam1 complex (black histogram; n = 883 events), with 10 pM Dam1 complex (blue histogram; n = 966), 50 pM Dam1 complex (green histogram; n = 928), and 500 pM Dam1 complex (red histogram; n = 1,003). Dotted lines show Gaussian fits used to determine mean values ± SD. These values are similar to the mean brightness from rare single-bleach steps of GFP-tagged Ndc80 complex (9,300 ± 3,200 au; n = 11). For clarity, green, blue, and black histograms are offset vertically by 120, 240, and 360 counts, respectively.

interaction with the Ndc80 complex, we used negative-stain EM to quantify ring formation on taxol-stabilized microtubules (at 36 nM tubulin) across a range of Dam1 concentrations (Fig. 3). At 500 pM Dam1 complex, the highest concentration used in our TIRF assays, rings were absent. Instead, we observed small particles scattered around or attached to the filaments. The dimensions of these particles were consistent with Dam1 complex dimers (Wang et al., 2007). Rings first appear on microtubules at 1 nM Dam1 complex, substantially increase in density between 5 and 10 nM, and saturate at 100 nM (Table I). These findings are consistent with a strong and cooperative binding of the Dam1 complex to microtubules, as reported previously (Gestaut et al., 2008).

Although 500 pM Dam1 complex did not assemble into rings on microtubules at 36 nM tubulin, reducing the amount of tubulin could promote ring formation by increasing the density of Dam1 complex bound to microtubules. To explore the magnitude of this effect, we imaged 500 pM Dam1 complex on microtubules at fivefold lower tubulin (7 nM). Rings were again absent (n = 8 microtubules; 101 µm total). Further reductions in tubulin concentration were impractical because the microtubules became too sparse on the EM grids. Because the effective concentration of tubulin polymer in our TIRF assays was lower still (~1 nM), it remains possible that Dam1 complex rings contributed to the observed alterations in behavior of the Ndc80 complex. However, we note that two observations suggest that ring formation is not required for the initial interaction between the Ndc80 and Dam1 complexes. First, the Dam1 and Ndc80 complexes interact during velocity sedimentation, where the Dam1 complex is primarily in dimeric form (Fig. S1). Second, interactions between individual Ndc80 and Dam1 complexes can be observed directly in TIRF assays (albeit rarely; Fig. S2).

The Dam1 complex enhances attachment of the Ndc80 complex to dynamic microtubule tips

The Ndc80 complex has been shown to track efficiently with disassembling microtubule tips in vitro, but only when it is bound to beads or to antibodies (Powers et al., 2009). In contrast, the Dam1 complex tracks robustly with disassembling tips without artificial oligomerization (Westermann et al., 2006; Gestaut et al., 2008). Therefore, we tested whether the Dam1 complex enhances tip tracking by the Ndc80 complex. We grew microtubules from nonhydrolyzable GMPCPP seeds in the presence of free fluorescent-labeled tubulin and GTP. We visualized the behavior of GFP-tagged Ndc80 complex as microtubules disassembled after the free tubulin was removed. By itself, the Ndc80 complex localized only briefly to microtubule tips during disassembly (Fig. 4 A). Most binding events were transient and diffusive, which is similar to those seen on taxol-stabilized microtubules (Powers et al., 2009). In contrast, the addition of Dam1 complex, which accumulates at the disassembling microtubule tip (Fig. S3 C), substantially increased the tip tracking behavior of the Ndc80 complex (Fig. 4 A). Ndc80 complexes bound preferentially at the microtubule tip were more persistently attached and moved with the disassembling tip.

For quantification, we defined tip tracking as the colocalization of GFP-tagged Ndc80 complex with disassembling microtubule tips. In the presence of Dam1 complex, Ndc80 complex tracked with 78% (62/80) of disassembling microtubule tips over a mean distance of 1.2 ± 0.2 µm compared with only 27% (19/71) of tips over a mean distance of 0.13 ± 0.09 µm in the absence of Dam1 complex (Fig. 4 B). In the presence of the Dam1 complex, tip tracking events by the Ndc80 complex often continued until the tips reached the microtubule seeds. Therefore, we likely underestimate the effect of the Dam1 complex to enhance the ability of the Ndc80 complex to track disassembling tips.

We then used an optical trapping-based force clamp (Asbury et al., 2006; Franck et al., 2007, 2010; Powers et al., 2009) to test whether the Dam1 complex enhances the tip-tracking ability of Ndc80 complex while under load. We attached beads decorated with Ndc80 complex to the tips of assembling microtubules in the presence and absence of free Dam1 complex. We applied constant tensile force until the attachment broke, the microtubule switched to disassembly, or, in a few cases, the

Published May 17, 2010

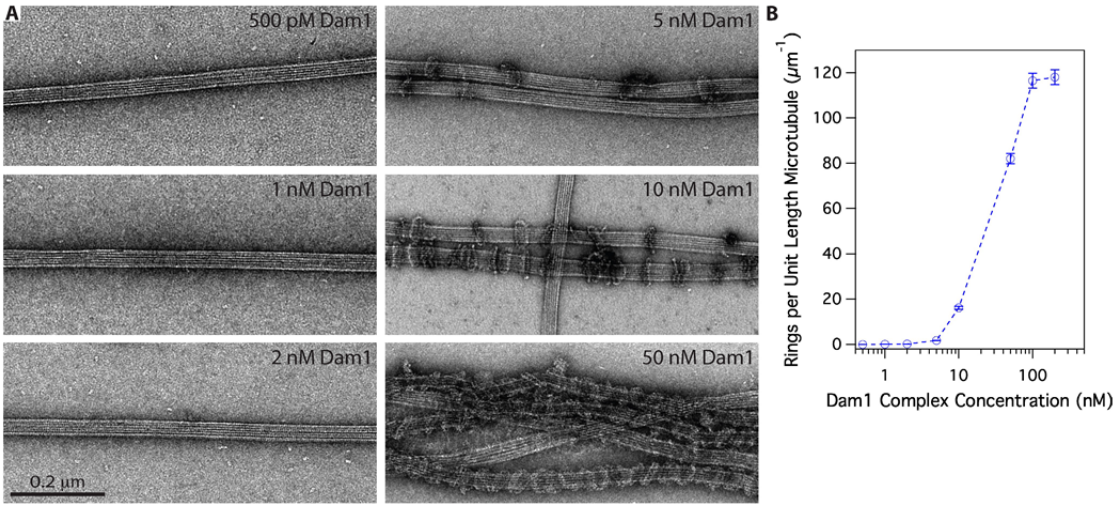

Figure 3. **Assembly of oligomeric rings of the Dam1 complex around microtubules.** (A) Negative-stain electron micrographs of oligomeric rings formed by the Dam1 complex around taxol-stabilized microtubules. (B) The number of rings observed per unit length (micrometers) of microtubule was quantified (statistics shown in Table I) and plotted against the total concentration of Dam1 complex. Error bars represent counting uncertainties.

event was terminated by other causes (e.g., the bead became stuck to the coverslip). In the absence of Dam1 complex, bead-bound Ndc80 complex formed persistent load-bearing attachments to assembling and disassembling microtubule tips (Fig. 5) as reported previously (Powers et al., 2009). While bearing 1.8 ± 0.4 pN (mean ± SD) of continuous load, travel distances during assembly were broadly distributed with a mean of 350 nm (n = 115). Detachment from assembling tips occurred at a rate of 0.026 ± 0.003 s^{-1} (Fig. 5 B). To mimic the likely arrangement in vivo, we added free Dam1 complex lacking an affinity tag so that it interacted with the beads only via its interaction with Ndc80 complex (i.e., direct Dam1 complex–bead interactions were prevented; see Materials and methods). In the presence of the Dam1 complex, the mean travel distance increased threefold to 1,100 nm (n = 42; P = 3×10^{-8} by Kolmogorov-Smirnov test), and the detachment rate decreased fivefold to 0.005 ± 0.0008 s^{-1} (Fig. 5 B). Accordingly, plots of survival probability versus distance show that the couplers remained more persistently attached when Dam1 complex was present (Fig. 5 C).

We also developed a force ramp assay to test the coupling performance of bead-bound Ndc80 complex across a broader range of forces on both assembling and disassembling microtubule tips (Franck et al., 2010). After an initial preload period at ∼1 pN constant force, we gradually increased the force on a tip-attached bead at a constant rate (0.25 pN × s^{-1}) until the bead detached from the microtubule tip, the load limit of the trap (10–12 pN) was reached, or, in the case of disassembling filaments, the microtubule switched from shortening to growth (Fig. 6). The maximum force achieved before any one of these termination points was recorded for each event. Without Dam1 complex present, all events recorded during microtubule assembly ended in detachment. Most events during disassembly also ended in detachment (93/96), but a few ended with a shortening to growth transition (2/96) or when the trap load limit was reached (1/96). The resulting maximum forces were distributed narrowly, with means of 2.7 ± 0.1 pN (n = 101) during assembly and 2.7 ± 0.1 pN (n = 96) during disassembly (Fig. 6, E and F). The addition of Dam1 complex

Table I. **EM of ring formation on microtubules at different Dam1 complex concentrations**

Dam1 complex concentration	No. of microtubules	Total microtubule length	No. of rings	Ring density
nM		*µm*		*µm*$^{-1}$[a]
0.5	27	259	0	0
1	16	280	20	0.1 ± 0.02
2	26	308	76	0.2 ± 0.03
5	26	256	450	2 ± 0.08
10	18	33	535	17 ± 0.7
50	13	16	1,312[b]	82 ± 3
100	11	11	1,282[b]	120 ± 3
200	9	11.5	1,358[b]	120 ± 3

[a]Errors represent counting uncertainties.

[b]Rings stacked together in pairs to form doublets and/or coils.

Published May 17, 2010

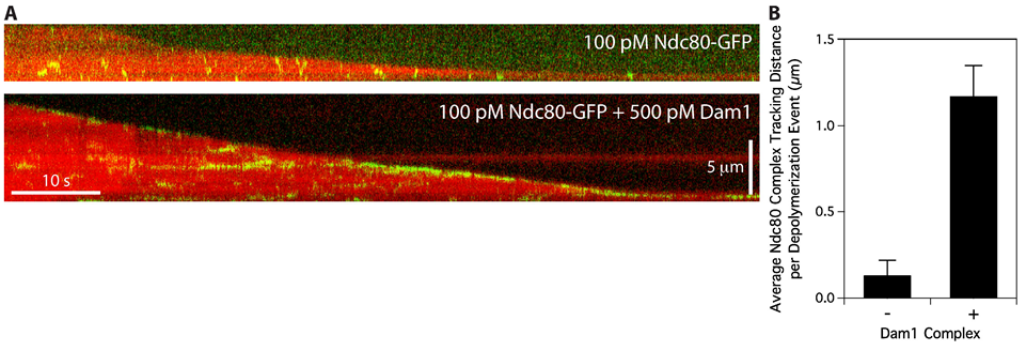

Figure 4. **Ndc80 complex tracks with disassembling tips in the presence of Dam1 complex.** (A) Representative two-color kymographs showing the tip tracking ability of 100 pM Ndc80 complex in the presence or absence of 500 pM Dam1 complex. Movement of GFP-tagged Ndc80 complex (green) is shown on disassembling microtubules (red). Concentrations are of free complexes in solution. (B) Mean tracking distance of Ndc80 complex per depolymerization event in the absence of Dam1 complex (n = 19) or in the presence of 500 pM Dam1 complex (n = 62). Error bars indicate SEM.

resulted in a clear improvement in the load-bearing capacity of the Ndc80 complex–coated beads. Most events recorded during assembly ended in detachment (112/131), but some persisted until the trap load limit was reached (19/131). Of the events recorded during disassembly, only about half ended in detachment (43/92). The remainder terminated when the microtubule switched to assembly (43/92), or, in a few cases, when the load limit was reached (6/92). The high frequency of shortening to growth transitions indicates that tension applied through linkages composed of both Ndc80 and Dam1 complexes promotes microtubule rescue, a phenomenon we saw previously using bead-bound Dam1 complex alone (Franck et al., 2007). The resulting maximum forces were distributed broadly with means of 5.2 ± 0.2 pN during assembly (n = 131) and 4.4 ± 0.2 pN during disassembly (n = 92), values that are twofold higher than in the absence of Dam1 complex (assembly, $P < 1 \times 10^{-8}$; disassembly, $P = 1 \times 10^{-8}$). These observations, together with the force clamp results, show that interactions between Dam1 and Ndc80 complexes enhance coupling to both assembling and disassembling microtubule tips under load. This enhancement persists across a range of loads (up to 10 pN), and it occurs under conditions in which the entire load is ultimately transmitted to the cargo through the Ndc80 complex.

Ipl1 phosphorylation regulates the interaction between Ndc80 and Dam1 complexes

We asked whether Ipl1 phosphorylation of the Dam1 complex regulates its interaction with the Ndc80 complex on microtubules. Phosphorylation of Ser20 on the Dam1 protein weakens the interaction of the Dam1 complex with microtubules (Gestaut et al., 2008). To determine how phosphorylation at sites other than Ser20 affects the interaction between the Dam1 and Ndc80 complexes, we used a modified Dam1 complex with a Ser20 to Ala mutation (S20A). With the S20A substitution, the Dam1 complex interacts with microtubules in a manner that is indistinguishable from the wild-type complex except that the interaction is insensitive to Ipl1 phosphorylation (Fig. S4, A and B). The phosphorylated S20A Dam1 complex also tracks with disassembling microtubule tips and is less diffusive at high concentrations, as expected for oligomers (Fig. S3). Phosphorylated S20A Dam1 complex also slows the disassembly of microtubules, as reported for wild-type Dam1 complex (Westermann et al., 2006; Franck et al., 2007; Grishchuk et al., 2008a).

In the presence of unphosphorylated S20A Dam1 complex, diffusion of the Ndc80 complex on microtubules is slowed, dissociation rate constant is decreased, and tip tracking is enhanced, as described for the wild-type Dam1 complex (Fig. 7). However, Ipl1 phosphorylation of the S20A Dam1 complex abolished the ability of Dam1 complex to slow the diffusion and decrease the dissociation rate constant of the Ndc80 complex (Fig. 7, B and C). Moreover, phosphorylated S20A Dam1 complex did not enhance the tip-tracking ability of the Ndc80 complex (Fig. 7 D). Control experiments were performed to ensure that after the initial Ipl1 phosphorylation reaction with the S20A Dam1 complex, residual Ipl1 activity was negligible (see Materials and methods; Fig. S5). Furthermore, the 10 proteins of the Dam1 complex do not dissociate from one another when the complex is phosphorylated by Ipl1 (Fig. S4 C). Because phosphorylation of the S20A Dam1 complex does not alter the behavior of the Dam1 complex alone but abolishes its ability to change the behavior of the Ndc80 complex, we conclude that Ipl1 phosphorylation of the Dam1 complex inhibits its interaction with the Ndc80 complex.

Discussion

The Dam1 complex acts as a processivity factor for the Ndc80 complex

Many molecular machines require factors that enhance their processivity. For example, the proliferating cell nuclear antigen sliding clamp is required for efficient DNA replication by DNA polymerase-ε (Kelman, 1997). Likewise, dynactin is required for long-distance movement of cytoplasmic dynein along microtubules (King and Schroer, 2000). Kinetochores are processive and form persistent attachments to dynamic microtubule tips over the times and distances required for chromosome biorientation and segregation. However, the contribution of individual

Published May 17, 2010

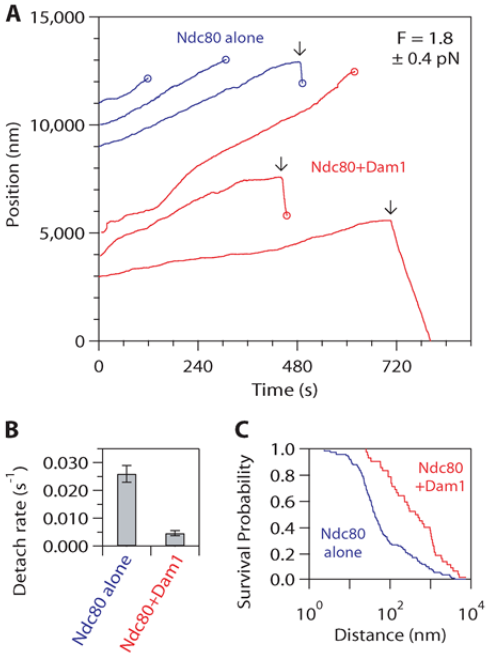

Figure 5. **Dam1 complex enhances the coupling of bead-bound Ndc80 complex to assembling microtubule tips under fixed load.** (A) Representative records of bead position versus time for microtubule tip attachments by bead-bound Ndc80 complex in the absence (blue traces) or presence (red traces) of free Dam1 complex during continuous application of tensile load. Increasing position represents assembly-coupled movement in the direction of applied force. Arrows mark transitions from assembly to disassembly. Decreasing position represents disassembly-driven movement against the applied force. Circles indicate detachment. For clarity, each record is offset vertically by an arbitrary amount. (B) Rates of bead detachment from assembling microtubule tips are estimated by counting the number of detachment events and dividing by total observation time. Error bars represent uncertainty based on Poisson statistics. (C) Survival probability versus distance for attachments composed of bead-bound Ndc80 complex in the absence (blue) or presence (red) of free Dam1 complex. The survival probability is the number of events that persisted beyond a given distance divided by the total number of events.

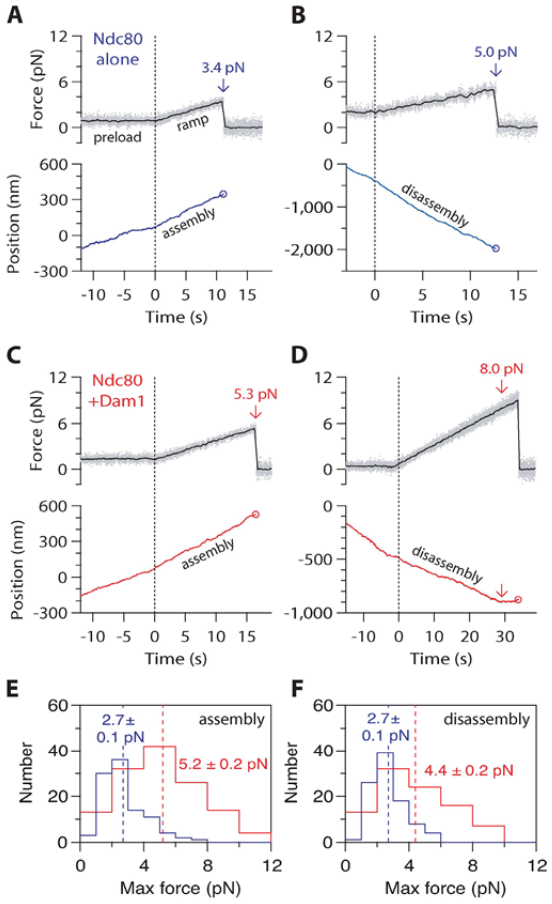

Figure 6. **Dam1 complex enhances the coupling of bead-bound Ndc80 complex to assembling and disassembling microtubule tips across a range of loads.** (A–D) Representative records showing tensile force (top) and bead position (bottom) versus time for bead-bound Ndc80 complexes attached to assembling and disassembling microtubule tips in the absence (A and B) or presence (C and D) of free Dam1 complex. The instrument was programmed to automatically increase the force at a constant rate (0.25 pN × s^{-1}) after ~500 nm of movement occurred. Arrows mark maximum forces, recorded either at rupture or when the microtubule switched from disassembly to assembly. Circles mark ruptures. (E) Distributions of maximum force for bead-bound Ndc80 complexes attached to assembling tips in the absence (blue histogram; n = 101) or presence (red histogram; n = 131) of free Dam1 complex. (F) Distributions of maximum force for bead-bound Ndc80 complexes attached to disassembling tips in the absence (blue histogram; n = 96), or presence (red histogram; n = 92) of free Dam1 complex. Dotted vertical lines indicate the mean for each distribution. Uncertainties represent standard errors.

components to the processivity of kinetochore–microtubule attachments is poorly understood. In this study, we show that the Dam1 complex enables the Ndc80 complex to track with disassembling microtubule tips over distances in excess of the length of the entire yeast spindle. We also show that the Dam1 complex strengthens the attachment of the Ndc80 complex to dynamic microtubule tips. In vivo, assembly of the Dam1 complex onto the kinetochore requires the Ndc80 complex (Janke et al., 2002). In our optical trap experiments, bead-bound Ndc80 complex was assayed with the Dam1 complex free in solution to mimic this arrangement in vitro. The increased ability of bead-bound Ndc80 complexes to bear load in the presence of free Dam1 complex indicates that tensile force can be transmitted through an Ndc80 complex–based linkage in a physiologically relevant arrangement.

We propose that the Dam1 complex acts as a processivity factor for the Ndc80 complex and that the two complexes cooperate to form load-bearing kinetochore–microtubule attachments. In vivo, the Ndc80 complex forms lateral attachments to spindle microtubules before kinetochore association of Dam1 complex and biorientation (Tanaka et al., 2005; Shimogawa et al., 2006). Our results are consistent with a model in which the Ndc80 complex initially mediates kinetochore attachment to microtubules. The Dam1 complex is later loaded onto the kinetochore to maintain attachment to dynamic microtubule tips. Association of the Dam1 complex is particularly important for these attachments to withstand the tensile forces required for biorientation.

Published May 17, 2010

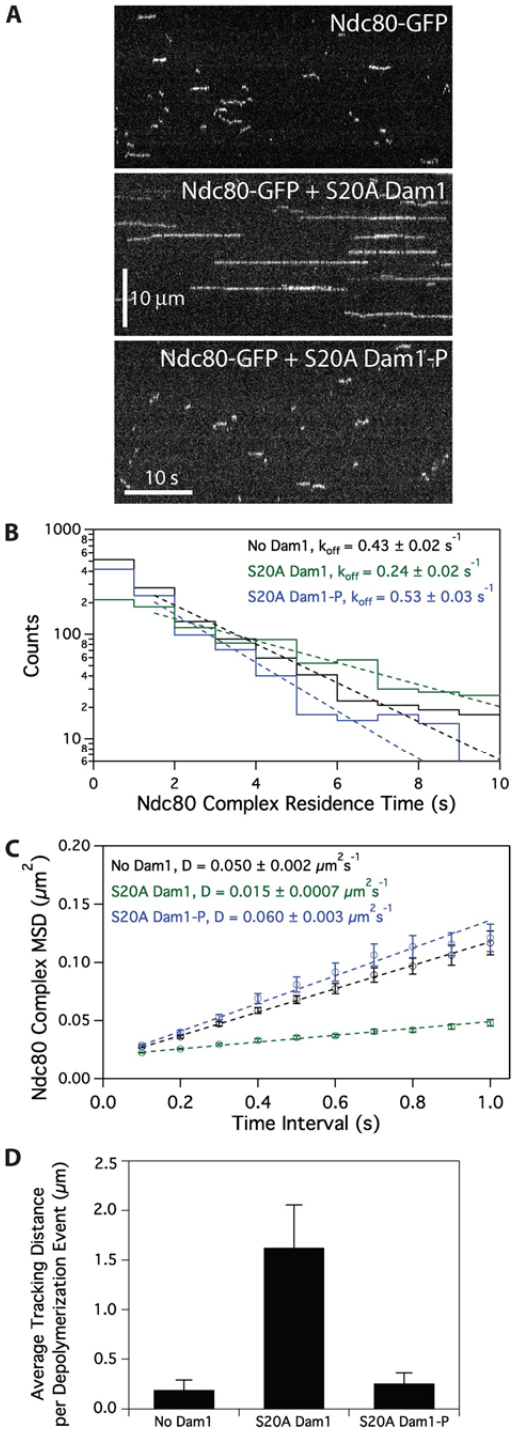

Figure 7. **Ipl1 phosphorylation of the Dam1 complex regulates its interaction with the Ndc80 complex.** (A) Representative kymographs showing changes in behavior of 10 pM Ndc80 complex with the addition of 500 pM S20A Dam1 complex with or without Ipl1 phosphorylation. Concentrations are of free complexes in solution. (B) Residence time distributions of 10 pM Ndc80 complex on microtubules without Dam1 complex (black histogram, n = 1,266 events), with 500 pM S20A Dam1 complex (green histogram, n = 1,081), and 500 pM Ipl1-phosphorylated S20A Dam1 complex (blue histogram, n = 974). Dotted lines show the weighted exponential fits used to determine dissociation rate constants, k_{off}. (C) Mean-squared displacement (MSD) is plotted against time for 10 pM Ndc80 complex on microtubules without Dam1 complex (black markers, n = 1,102), with 500 pM S20A Dam1 complex (green markers, n = 1,030), and with 500 pM Ipl1-phosphorylated S20A Dam1 complex (blue markers, n = 860). Dotted lines show the weighted linear fits used to determine diffusion constants, D. (D) Mean tracking distance of 100 pM Ndc80 complex per depolymerization event in the absence of Dam1 complex (n = 19), in the presence of 500 pM S20A Dam1 complex (n = 28), or in the presence of 500 pM Ipl1-phosphorylated S20A Dam1 complex (n = 39). Error bars indicate SEM.

The existence of a distinct and separable processivity factor also provides a point of regulation for corrective detachment.

A mechanism for aurora B–mediated corrective detachment

The regulatory mechanism that ensures chromosome biorientation has been proposed to respond to the level of tensile force on the kinetochore (Kelly and Funabiki, 2009). When kinetochores make attachments that generate little tension, such as monotelic or syntelic attachments, progression to anaphase is blocked. Key to this regulation, the conserved aurora B kinase is responsible for the release of aberrant kinetochore–microtubule attachments (Biggins et al., 1999; Tanaka et al., 2002; Hauf et al., 2003; Pinsky et al., 2006). We showed previously that phosphorylation by the yeast aurora B kinase Ipl1 at Ser20 of Dam1 decreases the affinity of the Dam1 complex for the microtubule lattice (Gestaut et al., 2008). We show in this study that Ipl1 phosphorylation of the Dam1 complex at sites other than Ser20 weakens its interaction with the Ndc80 complex. Collectively, these observations suggest that Ipl1 phosphorylation of the Dam1 complex promotes corrective detachment of kinetochores via two distinct mechanisms, decreasing the affinity of the Dam1 complex for both the Ndc80 complex and for microtubules. Regulation by aurora B kinase is a conserved feature of kinetochore function in all eukaryotes. Therefore, we propose that regulation at both the kinetochore–microtubule interface and between components of the kinetochore itself will extend to mechanisms of corrective detachment in higher eukaryotes.

Materials and methods

Protein expression and purification

The *S. cerevisiae* Ndc80 and Dam1 complexes were expressed from polycistronic vectors in *E. coli* as described previously (Wei et al., 2005; Gestaut et al., 2008, 2010; Powers et al., 2009). For TIRF microscopy, the Ndc80 complex Nuf2 subunit was tagged with GFP, and the Dam1 complex Dad1 subunit was tagged with GFP or mCherry. Complexes were purified by affinity chromatography and gel filtration as previously described (Asbury et al., 2006; Franck et al., 2007; Gestaut et al., 2008; Powers et al., 2009).

For optical trap bead assays, a tobacco etch virus (TEV) cleavage site was inserted adjacent to the His_6 affinity tag within the GFP-tagged Dam1 complex. The complex was purified by affinity chromatography and gel filtration as previously described (Gestaut et al., 2008). The cleavage reaction was performed in 50 mM phosphate buffer and 350 mM NaCl, pH 6.9, with 1 mM DTT, 0.5 mM EDTA, and recombinant TEV protease for

Published May 17, 2010

2 h at 4°C. TEV-cleaved Dam1 complex was isolated by gel filtration, and cleavage was verified by immunoblot analysis.

Phosphorylation of the Dam1 complex

Dam1 complex was phosphorylated with purified GST-Ipl1 and GST-Sli15 as described previously (Gestaut et al., 2008). The 50 µl reaction contained 4 µM GFP- or mCherry-tagged S20A Dam1 complex, 0.5 µM GST-Ipl1, 0.5 µM GST-Sli15 (residues 554–698), 200 mM NaCl, 10 mM ATP, 25 mM $MgCl_2$, and 50 mM Hepes buffer, pH 7.2. Reactions were incubated at 30°C for 90 min. Control reactions lacked GST-Ipl1 and GST-Sli15. Control reactions lacking ATP were also performed and gave similar results as previously reported (Gestaut et al., 2008). Ipl1 activity was not eliminated after the phosphorylation reaction. Therefore, to ensure that residual Ipl1 from the reaction did not affect our assays, we performed mock phosphorylation reactions using BSA in place of the Dam1 complex. The components of this mock reaction had no effect on the diffusion and dissociation rate constants of the Ndc80 complex either in the absence or presence of the Dam1 complex (Fig. S5).

TIRF microscopy

A custom TIRF illumination system was constructed for simultaneous excitation of Alexa Fluor 647 and GFP (Gestaut et al., 2008, 2010; Powers et al., 2009). Total internal reflection of a far-red laser (FTEC-635-0-25-PFQ; Blue Sky Research) and a blue laser (Sapphire 488–75; Coherent) was achieved using a through the objective arrangement with a 100× 1.4 NA Plan Apochromat lens (CFI; Nikon). Images from the far-red and green channels were projected side by side onto a cooled EM charge-coupled device camera (iXon 887-BI; Andor Technology).

A custom flow cell construction method was used (Gestaut et al., 2008, 2010; Powers et al., 2009). Glass slides (Gold Seal) were drilled with two holes along the short axis. Double-sided sticky tape (Scotch) was placed on either side of the holes to produce the walls of the flow channel. Silanized coverslips (Corning) were pressed firmly onto the tape, and the ends of the channel were sealed with vacuum grease. To draw fluid through the channel, a peristaltic pump was used via a custom adaptor attached above one of the holes on the glass slide with adhesive transfer tape (3M).

Flow cells were washed with three 100 µl vol dH_2O. To bind taxol-stabilized microtubules, we flowed in a modified "rigor" kinesin (G234A) lacking motor activity (Rice et al., 1999) diluted in BRB80 containing 8 mg × ml^{-1} BSA (BB80). Flow cells were washed with two 50 µl vol BB80, the second of which contained 10 µM taxol (BB80T). Alexa Fluor 647–labeled microtubules were diluted in BB80T and incubated in flow cells for 5 min. Flow cells were washed with two 50 µl vol BB80T. Proteins were then introduced, diluted in BB80T containing 0.02–0.1 mg × ml^{-1} κ-casein, 200 µg × ml^{-1} glucose oxidase, 35 µg × ml^{-1} catalase, 25 mM glucose, and 5 mM DTT. When assayed in combination, Ndc80 and Dam1 complexes were premixed before their introduction into flow cells. After flowing in the protein mixture, 2,000-frame videos were taken at 10 frames per second with iXon software (Andor Technology). All assays were performed at 26°C.

For disassembling microtubule assays, "rigor" kinesin was bound to flow cells and washed with 50 µl BB80 followed by 50 µl BB80 containing 0.1 mg ml^{-1} κ-casein and 1 mM GTP (growth buffer [GB]). Alexa Fluor 647–labeled GMPCPP microtubule seeds were bound and washed with two 50 µl vol GB. Microtubules were grown by incubating for ∼15 min in GB containing 2 mg × ml^{-1} tubulin (1:100; Alexa Fluor 647 labeled), 200 µg × ml^{-1} glucose oxidase, 35 µg ml^{-1} catalase, 25 mM glucose, and 5 mM DTT. Microtubule depolymerization was induced by buffer exchange removing free tubulin and simultaneously introducing proteins diluted in BB80 containing 0.1 mg × ml^{-1} κ-casein, 200 µg × ml^{-1} glucose oxidase, 35 µg × ml^{-1} catalase, 25 mM glucose, and 5 mM DTT. Videos were started concomitantly with induction of depolymerization and taken at 10 frames per second for 2,000 frames.

TIRF microscopy data analysis

Software analysis of TIRF microscopy data was performed using Labview (National Instruments) as previously described (Gestaut et al., 2008, 2010; Powers et al., 2009). The software generated the position and brightness of individual GFP-tagged complexes on microtubules over time. Custom Igor Pro (WaveMetrics) programs were used to generate histograms of Ndc80 complex residence times on microtubules. A weighted single exponential fit was applied to determine the mean residence time, τ, and to calculate the dissociation rate constant, $k_{off} = \tau^{-1}$. Association rate constants, k_{on}, were estimated as the number of observed Ndc80 complex–binding events per tubulin dimer per second divided by the free concentration of Ndc80 complex. Standard diffusion plots of mean-squared displacement versus time were generated in Igor Pro. A weighted linear fit was used to calculate the one-dimensional diffusion constant, D, of GFP-tagged complexes on microtubules.

To quantify Ndc80 complex tip tracking, brightness profiles along disassembling tips were created in Labview. Fluorescent signals at the tips were averaged across seven frames (0.7 s), and we required a minimum intensity threshold of 20% above background to score a tip-tracking event. For each individual frame, the instantaneous depolymerization rate was calculated as the change in tip position over 50 frames (5 s). A microtubule disassembly event was defined to start at the first appearance of GFP-tagged Ndc80 complex at the tip and to end when the rate of depolymerization dropped <0.03 µm × s^{-1}. Microtubule tips without tracking as defined by this criterion were omitted from further analysis. The total tracking distance for each individual tip was determined, and the mean tracking distance per depolymerization event was calculated.

To quantify binding to microtubules, we created brightness profiles of 500 pM mCherry-tagged Dam1 complex using our TIRF assay. After a 5-min incubation with taxol-stabilized microtubules, an image was recorded (six or seven images per condition). For each microtubule in the image, the integrated intensity of mCherry was measured in ImageJ (National Institutes of Health), and the brightness per unit length was calculated. Brightness per unit length values were averaged across all microtubules within one image and reported as means from multiple images.

EM

Taxol-stabilized microtubules were made by polymerizing cleared tubulin in a total volume of 40 µl BRB80 containing 1.75 mM GTP, 1 mM $MgCl_2$, and 3.5% DMSO at 37°C for 30 min. Various concentrations of Dam1 complex were mixed with taxol-stabilized microtubules to a final concentration of 36 nM tubulin in BRB80 containing 10 µM taxol and incubated for 15 min. Samples were prepared for analysis by EM as follows: carbon-coated copper grids were positively charged in a glow discharge device (Electron Microscopy Sciences) for 2 min. A 2-µl drop of sample was applied onto a freshly discharged grid and incubated for 20 s. Excess solution was blotted off, and the grid was washed twice with water and once with 0.075% uranyl formate before staining with uranyl formate. The stain was blotted off, and the grid was air dried. The preparations were viewed on a transmission electron microscope (Spirit T12; FEI) operating at 120 kV, and images were recorded on a 1,000 × 1,000 bottom-mount slow-scan charge-coupled device camera (Gatan) at a nominal magnification of either 15,000 or 52,000× at the specimen level. For each preparation, the total number of Dam1 complex rings on microtubules was counted and divided by the total length of microtubules to generate a mean number of Dam1 complex rings per microtubule micron. In control experiments performed in the presence of blocking proteins (8 mg × ml^{-1} BSA and 0.02 mg × ml^{-1} κ-casein), rings were still absent at 500 pM Dam1 complex.

Optical trap instrumentation and bead preparation

Our optical trap has been described previously (Franck et al., 2007, 2010; Powers et al., 2009). The instrument is built around an inverted microscope (TE2000; Nikon) equipped for video-enhanced differential interference contrast imaging. Custom-mounted optics direct the infrared trapping laser (J20-BL10–106Q; Spectra Physics) through a 100× 1.4 NA oil infrared Plan Apochromat objective lens (CFI; Nikon), through a high NA oil immersion condenser, and onto a position-sensitive detector. During force clamp experiments, a computer feedback–controlled piezo specimen stage (P-517.3CL; Physik Instrumente) was programmed (Labview) to maintain a fixed offset between the tip-attached bead and the trap center by moving to accommodate changes in microtubule length, thereby keeping the tensile force constant. During force ramp experiments, the bead trap separation was increased at a fixed rate, 0.25 pN × s^{-1}, up to a preset maximum of 10–12 pN (just below the escape force of the trap). For both force ramp and force clamp experiments, the stage position was updated and stored to disk at 50 Hz. Bead trap separation was sampled at 40 kHz but decimated to 200 Hz for storage.

Beads were prepared as previously described (Powers et al., 2009). Ndc80 complex was linked to 0.44-µm-diameter streptavidin-coated beads (Spherotech) with biotinylated His_5 antibody (QIAGEN). Ndc80 complex was diluted to 13–15 nM in BB80 with 1 mM DTT and incubated with 6 pM beads at 4°C for ∼90 min. In some experiments, recombinant His_6-tagged GFP was used as a blocking agent. In this case, Ndc80 complex was diluted to 30 nM in BB80 with 1 mM DTT and incubated with 12 pM beads at 4°C for ∼90 min. These beads were mixed 1:1 with 6 µM GFP and incubated for an additional 30 min before use. The amount of complex per bead and the final bead concentration was the same in both protocols. Both protocols yielded a molar ratio of Ndc80 complexes to

Published May 17, 2010

beads of 2,200–2,500. Based on simple geometric considerations (Powers et al., 2009), we estimate that <100 Ndc80 complexes could simultaneously interact with the filament. The Ndc80 complex/bead ratio was chosen to create tip attachments of moderate strength, so the full force range of the optical trap could be used to assess the contribution of Dam1 complex to the Ndc80 complex–based attachments. Results obtained with and without the GFP block were statistically indistinguishable (Ndc80 complex during assembly, P = 0.3010; Ndc80 complex during disassembly, P = 0.5518; Ndc80 complex + Dam1 complex during assembly, P = 0.1663; Ndc80 complex + Dam1 complex during disassembly, P = 0.8597), so they were pooled and analyzed together.

Optical trap bead assays, data collection, and analysis

Flow chambers were constructed and functionalized as previously described (Powers et al., 2009; Franck et al., 2010). In brief, two lengths of double-sided sticky tape (Scotch) were placed across the width of a microscope slide (Gold Seal) to form an inverted chamber of 2–3-mm width. A cleaned coverslip (Corning) longer than the slide width was pressed firmly onto the tape to form the chamber bottom, the overhanging edges acting as reservoirs for pipetting and aspirating solutions through the chamber. The chamber was functionalized by introducing 1 vol 1 mg × ml^{-1} biotinylated BSA (Vector Laboratories) and incubating for >10 min at room temperature. The chamber was washed with ∼20 vol BRB80 followed by ∼20 vol 0.33 mg × ml^{-1} avidin DN (Vector Laboratories). After a second wash with ∼20 vol BRB80, stable biotinylated microtubule seeds were introduced and washed with a growth and blocking buffer, BRB80 containing 1 mM GTP, 2 mg × ml^{-1} κ-casein, and 2% pluronic F-187. Subsequently, we introduced Ndc80 complex–coated beads that were diluted eightfold into GB, BB80 containing 1 mM GTP, 1.4 mg × ml^{-1} tubulin, 1 mM DTT, 250 µg × ml^{-1} glucose oxidase, 30 µg × ml^{-1} catalase, and 4.5 µg × ml^{-1} glucose. In assays with Dam1 complex, His_6-cleaved GFP-tagged Dam1 complex was used at a final concentration of 9–15 nM and added to the bead mixture just before introduction into the flow chamber. Microtubule disassembly events either occurred by a spontaneous switch from assembly to disassembly or were induced by laser scission (Franck et al., 2010). All trap assays were performed at 26°C.

Records of bead position versus time were analyzed using custom software written in Igor Pro. Periods of microtubule assembly and disassembly were visually identified in the records. Detachments were scored when the force on a bead under load suddenly dropped to zero and the stage exhibited open-loop ("run away") movement. The maximum force was taken as the mean of the final 10 data points before event termination (detachment or microtubule assembly/disassembly state switching). The survival probability was calculated by dividing the number of events that persisted beyond a given distance by the total number of events.

A bead–microtubule-binding assay was used to verify that His_6-cleaved GFP-tagged Dam1 complex did not bind directly to the GFP-blocked beads. Taxol-stabilized microtubules were introduced into a flow chamber and given 1 min to adhere nonspecifically to the coverslip. After a wash and 10-min incubation with surface block (BRB80 with 2 mg × ml^{-1} κ-casein and 10 µM taxol), free beads were introduced. After waiting 10 min to allow beads to bind, the number of microtubule-attached beads was counted across many fields of view (each 822 $µm^2$). Beads decorated with Ndc80 complex bound microtubules at a density of 7,800 beads × mm^{-2} (1,355 beads in 210 fields of view), whereas beads blocked with GFP in the presence of free Dam1 complex bound at only 24 beads × mm^{-2} (five beads in 250 fields of view) under identical conditions.

Online supplemental material

Fig. S1 shows a weak interaction between the Ndc80 and Dam1 complexes in solution by velocity sedimentation. Fig. S2 shows kymographs of single-molecule Ndc80 and Dam1 complexes interacting on taxol-stabilized microtubules. Fig. S3 shows that the Dam1 complex oligomerizes on microtubules and tracks with disassembling microtubule tips. This behavior is unaffected by the S20A mutation and subsequent phosphorylation by Ipl1. Fig. S4 further shows that phosphorylation of S20A Dam1 complex does not affect its microtubule binding. In addition, phosphorylation does not cause disassembly of the wild-type Dam1 complex. Fig. S5 shows that the behavior of the Ndc80 complex on microtubules is unaffected by residual components of the Dam1 complex phosphorylation reaction. Online supplemental material is available at http://www.jcb.org/cgi/content/full/jcb.200910142/DC1.

We thank V. MacKay and B. Kennedy for help with velocity sedimentation experiments. We also thank A. Powers, M. Shimogawa, B. Graczyk, and M. Wargacki for helpful scientific discussion.

We thank the Murdock Charitable Trust and the Washington Research Foundation for generous support of our electron cryomicroscopy facility. This work was supported by a National Sciences and Engineering Research Council of Canada scholarship (to J.F. Tien), a National Institutes of Health traineeship (grant T32 GM008268 to N.T. Umbreit), a National Science Foundation Integrative Graduate Education and Research traineeship (grant DGE-0504573 to A.D. Franck), a Searle Scholar award (grant 06-L-111 to C.L. Asbury), a Packard Fellowship for Science and Engineering (grant 2006-30521 to C.L. Asbury), and by the National Institute of General Medical Sciences (grants R01GM40506 and R01GM79373 to T.N. Davis and C.L. Asbury, respectively). T. Gonen is a Howard Hughes Medical Institute early career scientist.

Submitted: 26 October 2009
Accepted: 2 April 2010

References

Akiyoshi, B., C.R. Nelson, J.A. Ranish, and S. Biggins. 2009. Analysis of Ipl1-mediated phosphorylation of the Ndc80 kinetochore protein in *Saccharomyces cerevisiae*. *Genetics.* 183:1591–1595. doi:10.1534/genetics.109.109041

Asbury, C.L., D.R. Gestaut, A.F. Powers, A.D. Franck, and T.N. Davis. 2006. The Dam1 kinetochore complex harnesses microtubule dynamics to produce force and movement. *Proc. Natl. Acad. Sci. USA.* 103:9873–9878. doi:10.1073/pnas.0602249103

Biggins, S., F.F. Severin, N. Bhalla, I. Sassoon, A.A. Hyman, and A.W. Murray. 1999. The conserved protein kinase Ipl1 regulates microtubule binding to kinetochores in budding yeast. *Genes Dev.* 13:532–544. doi:10.1101/gad.13.5.532

Cheeseman, I.M., S. Anderson, M. Jwa, E.M. Green, J. Kang, J.R. Yates III, C.S. Chan, D.G. Drubin, and G. Barnes. 2002. Phospho-regulation of kinetochore-microtubule attachments by the Aurora kinase Ipl1p. *Cell.* 111:163–172. doi:10.1016/S0092-8674(02)00973-X

Cheeseman, I.M., J.S. Chappie, E.M. Wilson-Kubalek, and A. Desai. 2006. The conserved KMN network constitutes the core microtubule-binding site of the kinetochore. *Cell.* 127:983–997. doi:10.1016/j.cell.2006.09.039

DeLuca, J.G., W.E. Gall, C. Ciferri, D. Cimini, A. Musacchio, and E.D. Salmon. 2006. Kinetochore microtubule dynamics and attachment stability are regulated by Hec1. *Cell.* 127:969–982. doi:10.1016/j.cell.2006.09.047

Franck, A.D., A.F. Powers, D.R. Gestaut, T. Gonen, T.N. Davis, and C.L. Asbury. 2007. Tension applied through the Dam1 complex promotes microtubule elongation providing a direct mechanism for length control in mitosis. *Nat. Cell Biol.* 9:832–837. doi:10.1038/ncb1609

Franck, A.D., A.F. Powers, D.R. Gestaut, T.N. Davis, and C.L. Asbury. 2010. Direct physical study of kinetochore-microtubule interactions by reconstitution and interrogation with an optical force clamp. *Methods.* doi:10.1016/j.ymeth.2010.01.020.

Gaitanos, T.N., A. Santamaria, A.A. Jeyaprakash, B. Wang, E. Conti, and E.A. Nigg. 2009. Stable kinetochore-microtubule interactions depend on the Ska complex and its new component Ska3/C13Orf3. *EMBO J.* 28:1442–1452. doi:10.1038/emboj.2009.96

Gestaut, D.R., B. Graczyk, J. Cooper, P.O. Widlund, A. Zelter, L. Wordeman, C.L. Asbury, and T.N. Davis. 2008. Phosphoregulation and depolymerization-driven movement of the Dam1 complex do not require ring formation. *Nat. Cell Biol.* 10:407–414. doi:10.1038/ncb1702

Gestaut, D.R., J. Cooper, C.L. Asbury, T.N. Davis, and L. Wordeman. 2010. Reconstitution and functional analysis of kinetochore subcomplexes. *Methods Cell Biol.* In press.

Grishchuk, E.L., A.K. Efremov, V.A. Volkov, I.S. Spiridonov, N. Gudimchuk, S. Westermann, D. Drubin, G. Barnes, J.R. McIntosh, and F.I. Ataullakhanov. 2008a. The Dam1 ring binds microtubules strongly enough to be a processive as well as energy-efficient coupler for chromosome motion. *Proc. Natl. Acad. Sci. USA.* 105:15423–15428. doi:10.1073/pnas.0807859105

Grishchuk, E.L., I.S. Spiridonov, V.A. Volkov, A. Efremov, S. Westermann, D. Drubin, G. Barnes, F.I. Ataullakhanov, and J.R. McIntosh. 2008b. Different assemblies of the DAM1 complex follow shortening microtubules by distinct mechanisms. *Proc. Natl. Acad. Sci. USA.* 105:6918–6923. doi:10.1073/pnas.0801811105

Guimaraes, G.J., Y. Dong, B.F. McEwen, and J.G. Deluca. 2008. Kinetochore-microtubule attachment relies on the disordered N-terminal tail domain of Hec1. *Curr. Biol.* 18:1778–1784. doi:10.1016/j.cub.2008.08.012

Hanisch, A., H.H. Silljé, and E.A. Nigg. 2006. Timely anaphase onset requires a novel spindle and kinetochore complex comprising Ska1 and Ska2. *EMBO J.* 25:5504–5515. doi:10.1038/sj.emboj.7601426

Published May 17, 2010

Hauf, S., R.W. Cole, S. LaTerra, C. Zimmer, G. Schnapp, R. Walter, A. Heckel, J. van Meel, C.L. Rieder, and J.M. Peters. 2003. The small molecule Hesperadin reveals a role for Aurora B in correcting kinetochore–microtubule attachment and in maintaining the spindle assembly checkpoint. *J. Cell Biol.* 161:281–294. doi:10.1083/jcb.200208092

Inoué, S., and E.D. Salmon. 1995. Force generation by microtubule assembly/disassembly in mitosis and related movements. *Mol. Biol. Cell.* 6:1619–1640.

Janke, C., J. Ortíz, T.U. Tanaka, J. Lechner, and E. Schiebel. 2002. Four new subunits of the Dam1-Duo1 complex reveal novel functions in sister kinetochore biorientation. *EMBO J.* 21:181–193. doi:10.1093/emboj/21.1.181

Joglekar, A.P., K. Bloom, and E.D. Salmon. 2009. In vivo protein architecture of the eukaryotic kinetochore with nanometer scale accuracy. *Curr. Biol.* 19:694–699. doi:10.1016/j.cub.2009.02.056

Keating, P., N. Rachidi, T.U. Tanaka, and M.J. Stark. 2009. Ipl1-dependent phosphorylation of Dam1 is reduced by tension applied on kinetochores. *J. Cell Sci.* 122:4375–4382. doi:10.1242/jcs.055566

Kelly, A.E., and H. Funabiki. 2009. Correcting aberrant kinetochore microtubule attachments: an Aurora B-centric view. *Curr. Opin. Cell Biol.* 21:51–58. doi:10.1016/j.ceb.2009.01.004

Kelman, Z. 1997. PCNA: structure, functions and interactions. *Oncogene.* 14:629–640. doi:10.1038/sj.onc.1200886

Kemmler, S., M. Stach, M. Knapp, J. Ortiz, J. Pfannstiel, T. Ruppert, and J. Lechner. 2009. Mimicking Ndc80 phosphorylation triggers spindle assembly checkpoint signalling. *EMBO J.* 28:1099–1110. doi:10.1038/emboj.2009.62

King, S.J., and T.A. Schroer. 2000. Dynactin increases the processivity of the cytoplasmic dynein motor. *Nat. Cell Biol.* 2:20–24. doi:10.1038/71338

Kline-Smith, S.L., S. Sandall, and A. Desai. 2005. Kinetochore-spindle microtubule interactions during mitosis. *Curr. Opin. Cell Biol.* 17:35–46. doi:10.1016/j.ceb.2004.12.009

Lampert, F., P. Hornung, and S. Westermann. 2010. The Dam1 complex confers microtubule plus end–tracking activity to the Ndc80 kinetochore complex. *J. Cell Biol.* 189:641–649.

Maddox, P., A. Straight, P. Coughlin, T.J. Mitchison, and E.D. Salmon. 2003. Direct observation of microtubule dynamics at kinetochores in *Xenopus* extract spindles: implications for spindle mechanics. *J. Cell Biol.* 162:377–382. doi:10.1083/jcb.200301088

Miranda, J.J., D.S. King, and S.C. Harrison. 2007. Protein arms in the kinetochore-microtubule interface of the yeast DASH complex. *Mol. Biol. Cell.* 18:2503–2510. doi:10.1091/mbc.E07-02-0135

Pinsky, B.A., C. Kung, K.M. Shokat, and S. Biggins. 2006. The Ipl1-Aurora protein kinase activates the spindle checkpoint by creating unattached kinetochores. *Nat. Cell Biol.* 8:78–83. doi:10.1038/ncb1341

Powers, A.F., A.D. Franck, D.R. Gestaut, J. Cooper, B. Gracyzk, R.R. Wei, L. Wordeman, T.N. Davis, and C.L. Asbury. 2009. The Ndc80 kinetochore complex forms load-bearing attachments to dynamic microtubule tips via biased diffusion. *Cell.* 136:865–875. doi:10.1016/j.cell.2008.12.045

Raaijmakers, J.A., M.E. Tanenbaum, A.F. Maia, and R.H. Medema. 2009. RAMA1 is a novel kinetochore protein involved in kinetochore-microtubule attachment. *J. Cell Sci.* 122:2436–2445. doi:10.1242/jcs.051912

Rice, S., A.W. Lin, D. Safer, C.L. Hart, N. Naber, B.O. Carragher, S.M. Cain, E. Pechatnikova, E.M. Wilson-Kubalek, M. Whittaker, et al. 1999. A structural change in the kinesin motor protein that drives motility. *Nature.* 402:778–784. doi:10.1038/45483

Shang, C., T.R. Hazbun, I.M. Cheeseman, J. Aranda, S. Fields, D.G. Drubin, and G. Barnes. 2003. Kinetochore protein interactions and their regulation by the Aurora kinase Ipl1p. *Mol. Biol. Cell.* 14:3342–3355. doi:10.1091/mbc.E02-11-0765

Shimogawa, M.M., B. Graczyk, M.K. Gardner, S.E. Francis, E.A. White, M. Ess, J.N. Molk, C. Ruse, S. Niessen, J.R. Yates III, et al. 2006. Mps1 phosphorylation of Dam1 couples kinetochores to microtubule plus ends at metaphase. *Curr. Biol.* 16:1489–1501. doi:10.1016/j.cub.2006.06.063

Skibbens, R.V., V.P. Skeen, and E.D. Salmon. 1993. Directional instability of kinetochore motility during chromosome congression and segregation in mitotic newt lung cells: a push-pull mechanism. *J. Cell Biol.* 122:859–875. doi:10.1083/jcb.122.4.859

Skibbens, R.V., C.L. Rieder, and E.D. Salmon. 1995. Kinetochore motility after severing between sister centromeres using laser microsurgery: evidence that kinetochore directional instability and position is regulated by tension. *J. Cell Sci.* 108:2537–2548.

Tanaka, T.U., and A. Desai. 2008. Kinetochore-microtubule interactions: the means to the end. *Curr. Opin. Cell Biol.* 20:53–63.

Tanaka, T.U., N. Rachidi, C. Janke, G. Pereira, M. Galova, E. Schiebel, M.J. Stark, and K. Nasmyth. 2002. Evidence that the Ipl1-Sli15 (Aurora kinase-INCENP) complex promotes chromosome bi-orientation by altering kinetochore-spindle pole connections. *Cell.* 108:317–329. doi:10.1016/S0092-8674(02)00633-5

Tanaka, K., N. Mukae, H. Dewar, M. van Breugel, E.K. James, A.R. Prescott, C. Antony, and T.U. Tanaka. 2005. Molecular mechanisms of kinetochore capture by spindle microtubules. *Nature.* 434:987–994. doi:10.1038/nature03483

Wan, X., R.P. O'Quinn, H.L. Pierce, A.P. Joglekar, W.E. Gall, J.G. DeLuca, C.W. Carroll, S.T. Liu, T.J. Yen, B.F. McEwen, et al. 2009. Protein architecture of the human kinetochore microtubule attachment site. *Cell.* 137:672–684. doi:10.1016/j.cell.2009.03.035

Wang, H.W., V.H. Ramey, S. Westermann, A.E. Leschziner, J.P. Welburn, Y. Nakajima, D.G. Drubin, G. Barnes, and E. Nogales. 2007. Architecture of the Dam1 kinetochore ring complex and implications for microtubule-driven assembly and force-coupling mechanisms. *Nat. Struct. Mol. Biol.* 14:721–726. doi:10.1038/nsmb1274

Wei, R.R., P.K. Sorger, and S.C. Harrison. 2005. Molecular organization of the Ndc80 complex, an essential kinetochore component. *Proc. Natl. Acad. Sci. USA.* 102:5363–5367. doi:10.1073/pnas.0501168102

Welburn, J.P., E.L. Grishchuk, C.B. Backer, E.M. Wilson-Kubalek, J.R. Yates III, and I.M. Cheeseman. 2009. The human kinetochore Ska1 complex facilitates microtubule depolymerization-coupled motility. *Dev. Cell.* 16:374–385. doi:10.1016/j.devcel.2009.01.011

Westermann, S., H.W. Wang, A. Avila-Sakar, D.G. Drubin, E. Nogales, and G. Barnes. 2006. The Dam1 kinetochore ring complex moves processively on depolymerizing microtubule ends. *Nature.* 440:565–569. doi:10.1038/nature04409

Tien et al., http://www.jcb.org/cgi/content/full/jcb.200910142/DC1

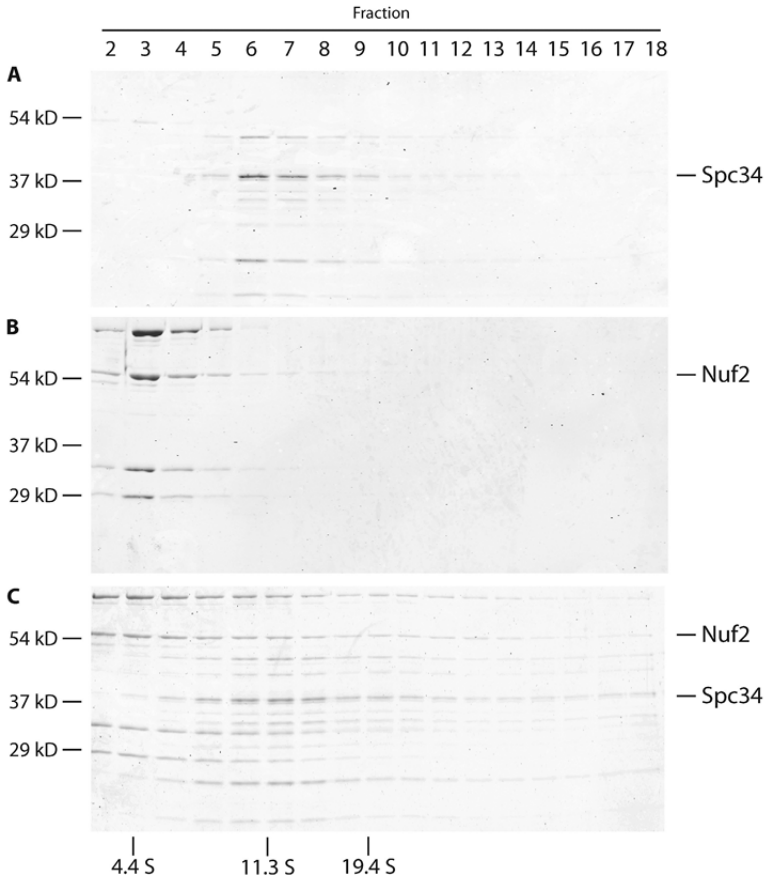

Figure S1. **Ndc80 and Dam1 complexes interact weakly free in solution.** The interaction between Ndc80 and Dam1 complexes free in solution was assayed by velocity sedimentation. 240 µl samples were layered onto 4.75 ml linear sucrose gradients (8–32%). Gradients were centrifuged at 189,000 *g* at 4°C for 6 h, and 265 µl fractions were collected. Fraction 1 is the top of the gradient. BSA (4.4S), catalase (11.3S), and thyroglobulin (19.4S) were used as standards. When assayed alone and together, Ndc80 complex and Dam1 complex had a sedimentation coefficient of 4.4S and 11.3S, respectively. Based on a Stokes radius of 9.9 nm, as determined by gel filtration, the molecular mass of the Dam1 complex was calculated to be ~470 kD (Siegel and Monty, 1966). Therefore, at the concentration in this assay, the 204-kD Dam1 complex exists primarily as a dimer free in solution. The positions of the Dam1 complex component Spc34 and the Ndc80 complex component Nuf2 are indicated on the right. (A–C) 2 µM Dam1 complex (A), 1 µM Ndc80 complex (B), and 2 µM Dam1 complex and 1 µM Ndc80 complex in combination (C) are shown.

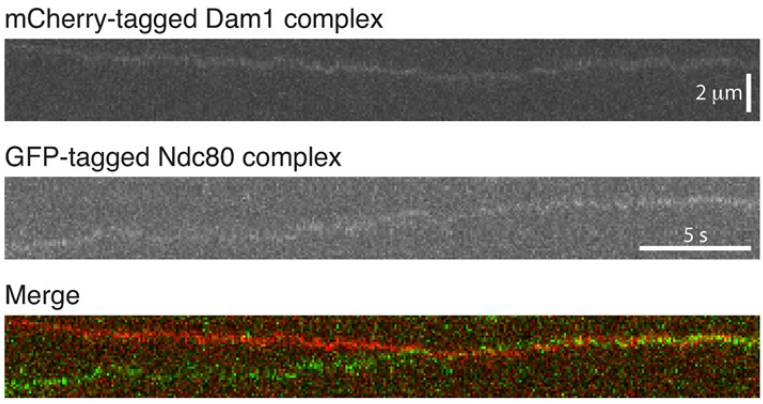

Figure S2. **The Ndc80 and Dam1 complexes interact on microtubules.** Representative kymograph showing the diffusion of 10 pM GFP-tagged Ndc80 complex and 2 pM mCherry-tagged Dam1 complex on microtubules. Both complexes are diffusive alone but appear to diffuse more slowly when they interact on microtubules.

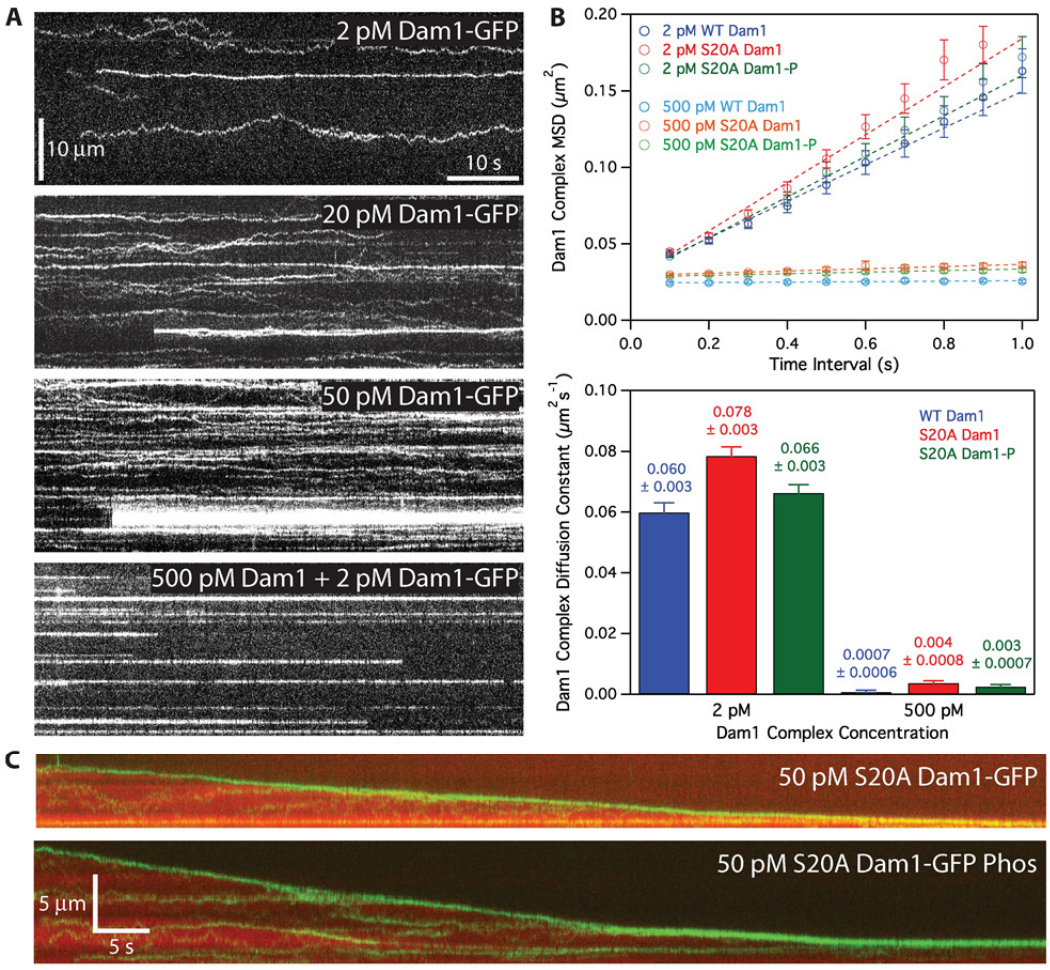

Figure S3. **The Dam1 complex oligomerizes on microtubules and tracks with disassembling tips.** (A) Representative kymographs showing changes in Dam1 complex behavior as it oligomerizes on microtubules. At 2 pM GFP-tagged Dam1 complex, single monomers were discernable. At 20 and 50 pM, slowly diffusing oligomers were seen as lines. At 500 pM Dam1 complex, the behaviors of individual oligomers were traced by visualizing a small proportion of labeled complex. Concentrations are of free complexes in solution. (B) Oligomerization of Dam1 complex slows its diffusion on taxol-stabilized microtubules, and oligomerization of S20A Dam1 complex is not abolished by Ipl1 phosphorylation. (top) Mean-squared displacement (MSD) is plotted against time for 2 pM wild-type (WT) Dam1 complex (blue markers; n = 188), 2 pM S20A Dam1 complex (red markers; n = 327), 2 pM Ipl1-phosphorylated S20A Dam1 complex (green markers; n = 346), 500 pM wild-type Dam1 complex (light blue markers; n = 129), 500 pM S20A Dam1 complex (orange markers; n = 188), and 500 pM Ipl1-phosphorylated S20A Dam1 complex (light green markers; n = 231). At 500 pM Dam1 complex, the behaviors of individual oligomers were traced by visualizing a small proportion of labeled complex. Markers are mean values ± SEM. Dotted lines show the weighted linear fits used to determine diffusion constants, D. (bottom) Diffusion constants derived from mean-squared displacement versus time plots are summarized as a bar graph. Wild-type Dam1 complex (blue bars), S20A Dam1 complex (red bars), and Ipl1-phosphorylated S20A Dam1 complex (green bars) are shown. Error bars indicate SEM. (C) Representative two-color kymographs demonstrating the tip-tracking ability of Ipl1-phosphorylated S20A Dam1 complex. Movement of 50 pM GFP-tagged unphosphorylated and phosphorylated S20A Dam1 complex (green) is shown on disassembling microtubules (red).

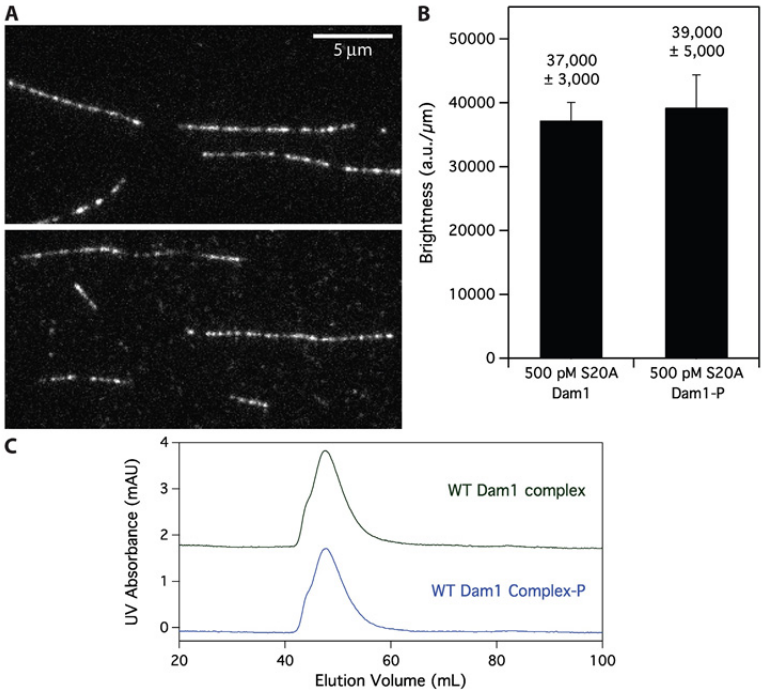

Figure S4. **Phosphorylation does not affect microtubule binding of S20A Dam1 complex and does not cause disassembly of wild-type Dam1 complex.** (A) Representative images of mCherry-tagged S20A Dam1 complex on microtubules. (top) 500 pM S20A Dam1 complex. (bottom) 500 pM Ipl1-phosphorylated S20A Dam1 complex. (B) Image means of mCherry brightness per unit length microtubules for unphosphorylated (n = 6 images, representing 68 microtubules, totaling 790 µm) and phosphorylated (n = 7 images, representing 51 microtubules, totaling 754 µm) S20A Dam1 complex. Error bars indicate SEM. (C) Unphosphorylated and Ipl1-phosphorylated wild-type (WT) Dam1 complexes each migrate as a single peak during gel filtration and elute at a volume consistent with previously reported values (Gestaut et al., 2008). The elution profile for unphosphorylated Dam1 complex is offset vertically by 2 mAU.

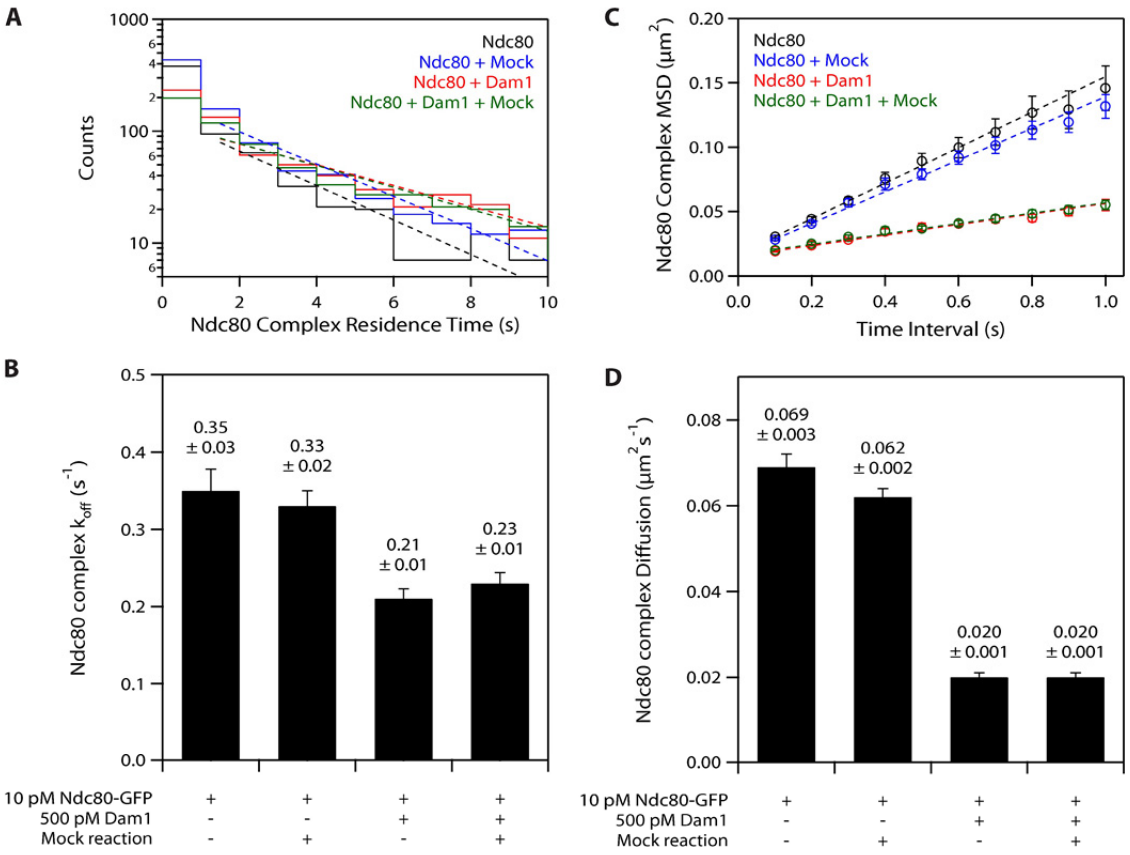

Figure S5. **Residual components of Ipl1 phosphorylation reactions have no effect on the behavior of the Ndc80 complex on microtubules.** Mock Ipl1 phosphorylation reactions were performed with BSA in place of Dam1 complex and added to TIRF assays at concentrations as in Fig. 6 (63 pM Ipl1, 63 pM Sli15, and 1.3 μM ATP). (A) Residence time distributions of 10 pM GFP-tagged Ndc80 complex on microtubules alone (black histogram; $n = 692$), with mock reaction (blue histogram; $n = 869$), 500 pM Dam1 complex (red histogram; $n = 752$), and 500 pM Dam1 complex and mock reaction (green histogram; $n = 699$). Dotted lines show the weighted exponential fits used to determine dissociation rate constants, k_{off}. (B) Dissociation rate constants derived from histograms are summarized as a bar graph. (C) Mean-squared displacement (MSD) is plotted against time for 10 pM GFP-tagged Ndc80 complex on microtubules alone (black markers; $n = 472$), with mock reaction (blue markers; $n = 670$), 500 pM Dam1 complex (red markers; $n = 636$), and 500 pM Dam1 complex and mock reaction (green markers; $n = 586$). Dotted lines show the weighted linear fits used to determine diffusion constants, D. (D) Diffusion rate constants derived from mean-squared displacement versus time plots are summarized as a bar graph. Error bars indicate SEM.

References

Gestaut, D.R., B. Graczyk, J. Cooper, P.O. Widlund, A. Zelter, L. Wordeman, C.L. Asbury, and T.N. Davis. 2008. Phosphoregulation and depolymerization-driven movement of the Dam1 complex do not require ring formation. *Nat. Cell Biol.* 10:407–414. doi:10.1038/ncb1702

Siegel, L.M., and K.J. Monty. 1966. Determination of molecular weights and frictional ratios of proteins in impure systems by use of gel filtration and density gradient centrifugation. Application to crude preparations of sulfite and hydroxylamine reductases. *Biochim. Biophys. Acta.* 112:346–362. doi:10.1016/0926-6585(66)90333-5

APPENDIX C

The Ndc80 kinetochore complex directly modulates microtubule dynamics

UMBREIT, N. T., D. R. GESTAUT, J. F. TIEN, B. S. VOLLMAR, T. GONEN *et al.*, 2012 The Ndc80 kinetochore complex directly modulates microtubule dynamics. Proc Natl Acad Sci U S A **109:** 16113-16118.

The Ndc80 kinetochore complex directly modulates microtubule dynamics

Neil T. Umbreit[a,1], Daniel R. Gestaut[a,1,2], Jerry F. Tien[a,1], Breanna S. Vollmar[a,3], Tamir Gonen[a,b,3], Charles L. Asbury[c], and Trisha N. Davis[a,4]

[a]Department of Biochemistry, [c]Department of Physiology and Biophysics, and [b]Howard Hughes Medical Institute, University of Washington, Seattle, WA 98195

Edited by John Carbon, University of California, Santa Barbara, CA, and approved August 2, 2012 (received for review June 5, 2012)

The conserved Ndc80 complex is an essential microtubule-binding component of the kinetochore. Recent findings suggest that the Ndc80 complex influences microtubule dynamics at kinetochores in vivo. However, it was unclear if the Ndc80 complex mediates these effects directly, or by affecting other factors localized at the kinetochore. Using a reconstituted system in vitro, we show that the human Ndc80 complex directly stabilizes the tips of disassembling microtubules and promotes rescue (the transition from microtubule shortening to growth). In vivo, an N-terminal domain in the Ndc80 complex is phosphorylated by the Aurora B kinase. Mutations that mimic phosphorylation of the Ndc80 complex prevent stable kinetochore-microtubule attachment, and mutations that block phosphorylation damp kinetochore oscillations. We find that the Ndc80 complex with Aurora B phosphomimetic mutations is defective at promoting microtubule rescue, even when robustly coupled to disassembling microtubule tips. This impaired ability to affect dynamics is not simply because of weakened microtubule binding, as an N-terminally truncated complex with similar binding affinity is able to promote rescue. Taken together, these results suggest that in addition to regulating attachment stability, Aurora B controls microtubule dynamics through phosphorylation of the Ndc80 complex.

mitosis | Hec1 | single molecule | optical trap | total internal reflection fluorescence microscopy

During mitosis, replicated chromosomes are segregated by the mitotic spindle, a bipolar array of dynamic microtubules. Each chromatid is linked to a bundle of microtubules (a "K-fiber") by a kinetochore. To ensure accurate chromosome segregation, regulatory mechanisms detect and correct errors in attachments between kinetochores and spindle microtubules. The conserved Aurora B kinase plays a crucial role in the resolution of aberrant kinetochore-microtubule attachments (1). Aurora B has many identified targets at the kinetochore, and it is generally thought that phosphorylation of these targets triggers the release of incorrect attachments (2–7). However, emerging evidence suggests that Aurora B activity does not always result in kinetochore-microtubule detachment. For example, early in mitosis when merotelic attachments are more prevalent, phosphorylation of the Ndc80 complex (the key microtubule-binding component of the kinetochore) is relatively high, yet kinetochores do not appear to release from their K-fibers (8, 9). Similarly, syntelic attachments formed in the presence of a reversible Aurora B inhibitor are not immediately released when the kinase is reactivated (10). Instead, the K-fiber microtubules disassemble, carrying the kinetochores back to the centrosome, where the attachments are corrected by an unknown mechanism. These results suggest that Aurora B additionally acts to regulate microtubule dynamics as a part of its mechanism of error correction.

Additional findings suggest that Aurora B modulates microtubule dynamics through regulation of the Ndc80 complex. A component of the Ndc80 complex, the Hec1 protein, has a disordered N-terminal tail that is targeted by Aurora B in vivo (11, 12). In PtK cells, preventing phosphorylation of these target sites not only results in hyperstable kinetochore-microtubule attachments, but also damped kinetochore oscillations (8). The abnormal oscillations could be explained by direct or indirect contributions from the Ndc80 complex. The Ndc80 complex could itself directly control microtubule dynamics in response to Aurora B activity. An alternative (but not mutually exclusive) explanation is that phosphorylation of Hec1 alters the localization of other factors that modulate dynamics. These factors may include the microtubule stabilizer EB1 and the microtubule depolymerase MCAK, both of which are also targets of Aurora B (13–19).

Here, we show that the human Ndc80 complex directly stabilizes the tips of disassembling microtubules, slows the rate of disassembly, and promotes microtubule rescue (the transition from microtubule shortening to growth) in vitro. In contrast, the Ndc80 complex with mutations mimicking Aurora B phosphorylation was impaired in its ability to influence microtubule dynamics, even when tracking with the tips of disassembling microtubules. This diminished ability of the phosphomimetic complex to affect dynamics is not solely a result of weakened microtubule binding, as an N-terminally truncated complex with similar affinity was still able to promote rescue. These results suggest that Aurora B modulates microtubule dynamics through regulation of the Ndc80 complex, and this mechanism could be separable from effects on attachment stability.

Results

Characterization of Full-Length Human Ndc80 Complex. The conserved Ndc80 complex is an essential microtubule-binding component of the kinetochore (20). Although the Ndc80 complex from yeast and worms has been extensively studied in vitro (21–26), most work on the human complex has been limited to the use of truncated forms (26–31). We expressed and purified full-length human Ndc80 complex from *Escherichia coli* for in vitro characterization (Fig. S1). As seen by negative-stain EM, this recombinant Ndc80 complex bound to taxol-stabilized microtubules (Fig. 1*A*). Using total internal reflection fluorescence (TIRF) microscopy, we visualized single molecules of GFP-tagged Ndc80 complex on taxol-stabilized microtubules (Fig. 1*B* and Fig. S2) and measured their dissociation and diffusion rate constants ($k_{off} = 0.21 \pm 0.01\ s^{-1}$, $D = 0.018 \pm 0.001\ \mu m^2 \cdot s^{-1}$) (Fig. 1 *C* and *D*). The affinity and cooperativity of microtubule binding were

Author contributions: N.T.U., D.R.G., J.F.T., T.G., C.L.A., and T.N.D. designed research; N.T.U., D.R.G., J.F.T., B.S.V., and T.G. performed research; B.S.V. and T.G. contributed new reagents/analytic tools; N.T.U., D.R.G., J.F.T., C.L.A., and T.N.D. analyzed data; and N.T.U., D.R.G., and J.F.T. wrote the paper.

The authors declare no conflict of interest.

This article is a PNAS Direct Submission.

See Commentary on page 15972.

[1]N.T.U., D.R.G., and J.F.T. contributed equally to this work.

[2]Present address: Department of Biology, Stanford University, Stanford, CA 94305.

[3]Present address: Janelia Farm Research Campus, Howard Hughes Medical Institute, Ashburn, VA 20147.

[4]To whom correspondence should be addressed. E-mail: tdavis@u.washington.edu.

This article contains supporting information online at www.pnas.org/lookup/suppl/doi:10.1073/pnas.1209615109/-/DCSupplemental.

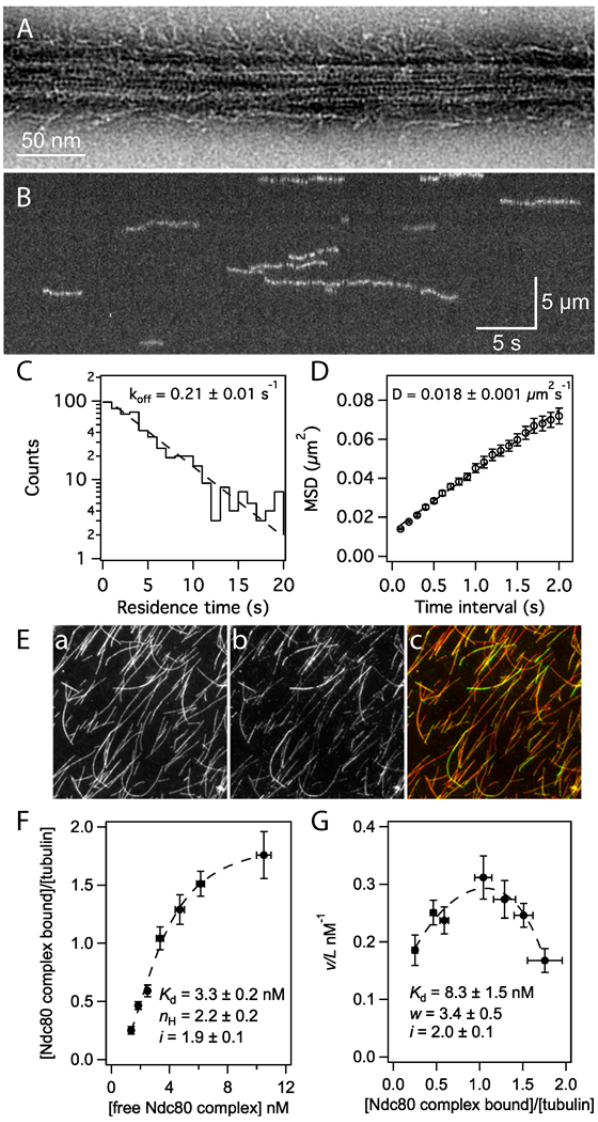

Fig. 1. The human Ndc80 complex binds to and diffuses along the microtubule lattice. (*A*) Negative-stain electron micrograph of the Ndc80 complex on a taxol-stabilized microtubule. (*B*) A representative kymograph showing the binding and diffusion of Ndc80 complex (5 pM complex in solution) on taxol-stabilized microtubules. Position along the microtubule is depicted on the vertical axis over time on the horizontal axis. (*C*) Residence time distributions of GFP-tagged Ndc80 complex on microtubules fit with a single exponential (dashed line) to calculate the off-rate constant, k_{off}. (*D*) Mean-squared displacement (MSD) ± SEM vs. time lag. A linear fit to the data (dashed line) was used to determine the diffusion constant, *D*. (*C* and *D*) n = 584. (*E*) Representative image from the bulk microtubule binding assay with GFP-tagged Ndc80 complex (2 nM) on taxol-stabilized Alexa-568-labeled microtubules (2.5 nM tubulin dimer). Panels show microtubules (a), Ndc80 complex (b), and merge (c). Panel dimensions are 66 by 66 μm. (*F*) Plot of binding density (v) versus free Ndc80 complex concentration (L). A fit to the Hill model (dashed line) was used to determine the apparent affinity (K_d), Hill coefficient (n_H), and lattice occupancy (i, the number of Ndc80 complexes bound per tubulin dimer). (*G*) Scatchard plot of the same data shown in *F*, fit to the McGhee and von Hippel model (dashed line) to calculate the K_d, cooperativity parameter (w), and i. For *F* and *G*, n = 8–10 replicates per data point, markers are mean ± SEM, and errors on model fit parameters (K_d, n_H, w, and i) represent SD.

measured using a bulk microtubule binding assay that measures the amount of GFP-tagged complex bound to microtubules over varying concentrations of complex (Fig. 1*E*) (32, 33). Based on a standard Hill model fit (34), the Ndc80 complex binds microtubules with a strong apparent affinity (K_d = 3.3 ± 0.2 nM) and has a Hill coefficient of 2.2 ± 0.2 (Fig. 1*F*). The Hill model describes cooperativity arising from allosteric changes that enhance ligand binding to a protein. In our binding assay, cooperativity is likely based on interactions between Ndc80 complexes that occur when they are bound to microtubules. Therefore, we used a model previously developed by McGhee and von Hippel that describes cooperativity between ligands binding to a polymer lattice (35). Fitting the binding data with this model (Fig. 1*G*) also showed a strong apparent affinity (K_d = 8.3 ± 1.5 nM) and cooperativity between Ndc80 complexes on the microtubule lattice (w = 3.4 ± 0.5). Compared with the Hill model fit, the McGhee and von Hippel model fit yielded a weaker apparent K_d for a single complex. Thus, interactions between complexes bound to the microtubule contribute to the K_d predicted by the Hill model. This finding is supported by the observation that at high concentrations, truncated Ndc80 complex binds microtubules in clusters (28). Fits to both models revealed a lattice occupancy of approximately two Ndc80 complexes per tubulin dimer, consistent with cryo-EM reconstructions that showed a 4-nm spacing of the truncated complex on microtubules (28).

Ndc80 Complex Directly Stabilizes Disassembling Microtubule Tips and Promotes Microtubule Rescue. In vivo, kinetochores transmit forces generated by the mitotic spindle to drive chromosome movement (36). This process depends on the ability of microtubule-binding components of the kinetochore to form stable attachments to dynamic microtubule tips. Using TIRF microscopy, we visualized the GFP-tagged Ndc80 complex on disassembling microtubules. In these assays, microtubule disassembly was induced by the removal of free tubulin. The human Ndc80 complex can track with disassembling microtubule tips (Fig. 2*A*), unlike the budding yeast Ndc80 complex, which requires the Dam1 complex or oligomerization on the surface of beads (23, 24). The human Ndc80 complex also slowed the rate of microtubule disassembly (Fig. 2*C*). As the concentration of the complex was increased from 0 to 500 pM, microtubule disassembly was slowed from 280 ± 20 nm/s to 100 ± 10 nm/s.

At 500 pM, bright particles of GFP-tagged Ndc80 complex were observed on microtubules (Fig. 2*B*), consistent with its cooperative binding behavior in our bulk assays. In some cases, disassembly appeared to stall as the tip reached these particles, and only continued after the Ndc80 complex appeared to detach. This behavior resulted in a step-like appearance in kymographs (Fig. 2*B*). Furthermore, Alexa-647–labeled tubulin decorated with Ndc80 complex was often seen bending away from the long axis of the microtubule (observed for 66 ± 10% of microtubules) (Fig. 2*D*, Fig. S3 *A* and *B*, and Movie S1). Because these curled extensions can be resolved by light microscopy (116-nm pixels), their curvature is gentler than the tight 20-nm curls seen at bare disassembling tips by cryo-EM in vitro (37). To further investigate tip structure in the presence of Ndc80 complex, we performed a similar disassembly assay and visualized the microtubule tips by negative-stain EM. We observed open protofilament sheets emanating from the tips of microtubules stabilized by Ndc80 complex (Fig. 2*E*). These sheets were not observed at the tips of microtubules stabilized by taxol or by the Dam1 complex (Fig. S3*C*) (38). Microtubules exposed to the same conditions in the absence of any stabilizing factor completely disassembled into free tubulin. Although we were unable to distinguish between microtubule plus- and minus-ends in the electron micrographs, curled extensions were observed in the presence of Ndc80 complex at both microtubule ends in the TIRF assay (Fig. S3*A*). Together, the TIRF and

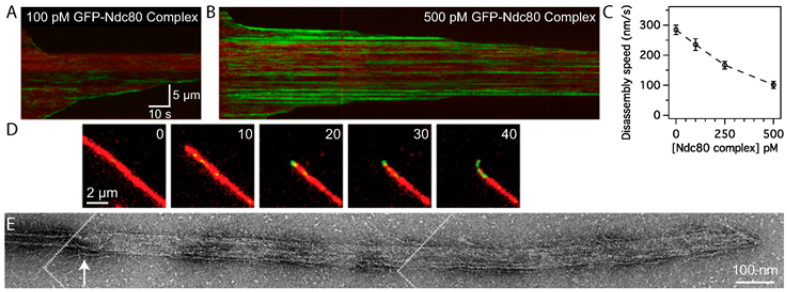

Fig. 2. The Ndc80 complex slows microtubule disassembly and stabilizes protofilament extensions. Kymographs of disassembling microtubules (red) in the presence of (*A*) 100 pM or (*B*) 500 pM GFP-tagged Ndc80 complex (green). Brightness and contrast were adjusted equally in *A* and *B*. (*C*) Mean disassembly speeds ± SEM for microtubules in the presence of increasing concentrations of Ndc80 complex (without Ndc80 complex, $n = 80$; 100 pM Ndc80 complex, $n = 31$; 250 pM, $n = 29$; 500 pM, $n = 34$). (*D*) Time-lapse images of a disassembling microtubule (red) in the presence of 500 pM GFP-tagged Ndc80 complex (green) as a curled extension formed at the tip. *Inset* numbers show elapsed time, in seconds. See Fig. S3*B* for a gallery of images showing curled extensions. (*E*) Negative-stain electron micrograph of a disassembling microtubule tip (see *SI Materials and Methods*) stabilized by the Ndc80 complex. An arrow marks the transition from a closed microtubule to an open sheet. The figure was constructed from three images, the boundaries of which are depicted by dotted white lines.

EM assays suggest that the Ndc80 complex slows disassembly by stabilizing protofilament extensions at microtubule tips.

To test how purified Ndc80 complex couples to dynamic microtubule tips under force, we used an optical trap-based bead motility assay (39). By incubating 11 pM beads with 5 nM Ndc80 complex (~450 complexes per bead), we estimate that up to ~20 complexes can interact with the microtubule tip based on geometric constraints (23). This number closely approximates the number of Ndc80 complexes per kinetochore microtubule in vivo (40). These beads remained coupled to microtubule tips against 2 pN of tension (Fig. 3 *A* and *B*), similar to the forces sustained by kinetochore-microtubule attachments in vivo, which are estimated to be 0.4–8 pN (23, 41, 42). Against the applied force, beads tracked robustly with the tips of disassembling microtubules over an average distance of 970 ± 190 nm ($n = 44$). Consistent with results from our TIRF-based assays, microtubule disassembly was slowed from 230 ± 14 nm/s (for microtubule tips not coupled to beads and in the absence of force) to 44 ± 7 nm/s by beads coated with Ndc80 complex under 2 pN of force (Fig. 3*C*). For episodes of disassembly-driven movement against the applied force, about half (53 ± 8%) ended in bead detachment, but a large proportion (40 ± 7%) underwent a microtubule rescue (the remaining events, 7 ± 3%, terminated for other reasons, such as the bead reaching the microtubule seed or nonspecifically adhering to the cover-slip). Strikingly, disassembling microtubule tips coupled to beads coated with the Ndc80 complex rescued ~70-fold more frequently than bare microtubules (Fig. 3*D*) (135 ± 24 h^{-1} compared with 2 ± 1 h^{-1}). Therefore, the Ndc80 complex is an effective tip-coupler that can directly slow microtubule disassembly and promote rescue.

In contrast, in our previous work with the budding yeast Ndc80 complex, we observed little effect on the rate of microtubule rescue (23). Here we analyzed the dataset reported in Powers et al. (23), specifically looking for rescue events. Microtubules rescued at a frequency of 9 ± 5 h^{-1} while coupled to beads coated with budding yeast Ndc80 complex ($n = 4$ rescues, ~100–2,700 complexes per bead, against ~1 pN of force). This number is close to the rate of rescue for microtubules not coupled to beads (reported above). Therefore, the budding yeast Ndc80 complex, unlike the human complex, appears to have little ability to promote microtubule rescue.

Phosphomimetic Mutations in the Ndc80 Complex Inhibit Its Ability to Influence Microtubule Dynamics. The Hec1 protein of the Ndc80 complex contains a calponin homology domain that is important for its microtubule binding activity (29, 30). In addition, Hec1 has a disordered N-terminal tail that contributes to the affinity of the complex for microtubules (11, 12, 30). In vivo, the tail is a target for the Aurora B kinase, and mutations that mimic phosphorylation at these sites result in unattached kinetochores (11, 43). Consistent with this observation, Aurora B phosphorylation of a truncated Ndc80 complex reduces its binding to microtubules in vitro (29). On the other hand, mutations that block phosphorylation severely damp kinetochore oscillations in vivo (8). These findings suggest that phosphorylation in the Hec1 tail is required not only for regulation of kinetochore-microtubule attachments, but also for normal kinetochore-microtubule dynamics. Using the optical trap assay, we tested the direct contribution of the tail to microtubule dynamics in vitro. In addition to the wild-type complex, we purified Ndc80 complex with the nine putative Aurora B target sites in the Hec1 tail mutated to aspartic acid to mimic phosphorylation (9D), and Ndc80 complex with the Hec1 tail deleted (ΔN). As a control, we also purified Ndc80 complex with alanine mutations at the Aurora B target sites (9A). Because this construct behaved like the wild-type complex in our TIRF assays (Figs. S3*B* and S4), it was not further characterized in the optical trap assay.

Beads coated with wild-type, 9D, and ΔN complexes were all able to slow the rate of microtubule disassembly in a concentration-dependent manner when tracking with disassembling tips against ~2 pN of applied force (Fig. 3 *B* and *C*). However, the 9D and ΔN complexes were impaired relative to the wild-type complex; when incubated with 5 nM of Ndc80 complex, 82 ± 11% of wild-type beads tracked with disassembling microtubule tips, but only 21 ± 5% of the 9D beads and 20 ± 4% of the ΔN beads tracked with disassembly (Fig. 3*B*). Furthermore, 5 nM wild-type beads slowed disassembly to 44 ± 7 nm/s, but 5 nM 9D and 5 nM ΔN beads slowed disassembly to 110 ± 20 and 96 ± 27 nm/s, respectively (Fig. 3*C*). The ability of the mutant complexes to track with and slow disassembly was recovered to wild-type levels by increasing the density of decoration on beads ~20-fold (Fig. 3 *B* and *C*: compare 0.5 and 1 nM wild-type to 10 and 20 nM mutant complexes, respectively). For example, beads coated with 20 nM 9D or 20 nM ΔN complex tracked with microtubules similarly to 1 nM wild-type beads (9D: 76 ± 11%; ΔN: 70 ± 10%; wild-type: 74 ± 9%). Therefore, increasing the number of mutant complexes on beads compensates for their decreased coupling performance.

When assayed at comparable coupling performance, the wild-type and ΔN complexes promoted microtubule rescue, but the 9D complex did not (Fig. 3 *D* and *E*). Deletion of the Hec1 tail reduced the ability of the complex to promote rescue only modestly (~twofold). In contrast, phosphomimetic mutations in the tail nearly abolished this activity. Using beads coated with 20 nM 9D complex, we observed only three rescue events in 29 min

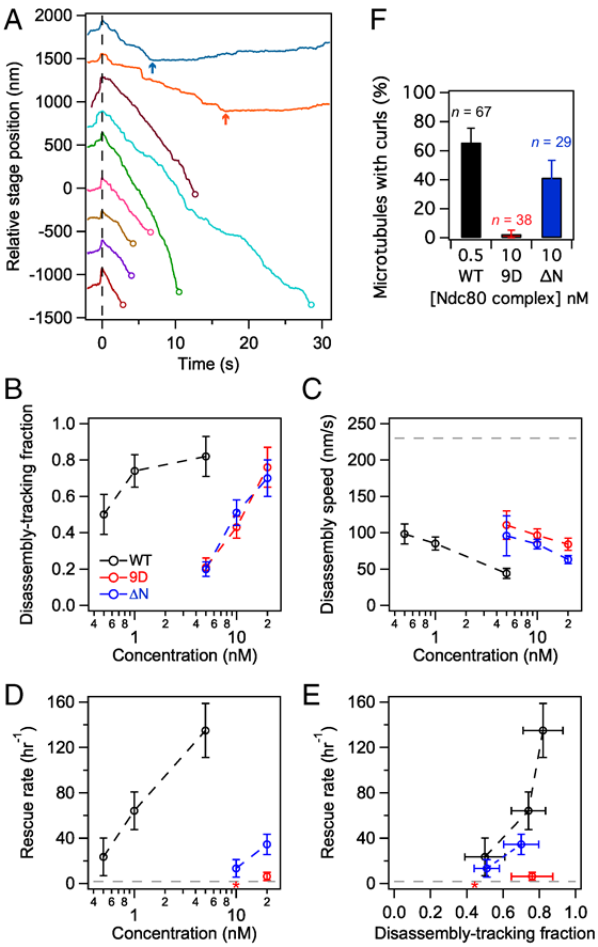

Fig. 3. Phosphomimetic mutations in the Ndc80 complex inhibit its ability to promote microtubule rescue. (*A*) Example traces of position vs. time for beads decorated with Ndc80 complex as they tracked microtubule disassembly against ~2 pN of applied force. Time t = 0 s (dashed vertical line) marks the onset of tracking, when the disassembling microtubule tip began to drive movement of the bead against the force of the trap. Disassembly-driven movement ended when the bead detached (open circles) or when the microtubule rescued (arrows). Traces are offset vertically for visual clarity. (*B*) The fraction of beads coated with wild-type or mutant Ndc80 complex capable of tracking against ~2 pN. From the disassembly-tracking events in *B*, (*C*) mean microtubule disassembly speeds ± SEM and (*D*) rescue rates were measured. Without load and in the absence of bead-bound Ndc80 complex, the disassembly rate was 230 ± 14 nm/s (dashed line in *C*, n = 26) and the rescue rate was 2 ± 1 h^{-1} (dashed line in *D*, n = 3 events in 104 min of disassembly). (*E*) Rescue rate is plotted against the fraction of beads that tracked disassembly against force. (*F*) Percentage of microtubules for which a curl (Fig. 2*D* and Fig. S3*B*) was observed at either tip during disassembly in the TIRF microscopy assay. The n for each data point in *B*–*D* is listed in Table S1. Asterisks indicate that no rescues were observed. Unless otherwise noted, all error bars represent uncertainties from counting statistics.

of microtubule disassembly, which is an average rescue frequency similar to that for bare microtubules (6 ± 4 vs. 2 ± 1 h^{-1}). In addition, the ΔN complex but not the 9D complex stabilized curled extensions at disassembling microtubule tips in the TIRF assay (Fig. 3*F*). Thus, phosphomimetic mutations do not simply negate the activity of the tail, but actively interfere with the ability to modify microtubule tip structure and promote rescue.

The ΔN and 9D complexes performed similarly in tracking with and slowing microtubule disassembly, suggesting that their disparate effects on microtubule rescue and tip structure are not simply the result of a difference in their microtubule-binding affinities. We quantified binding of GFP-tagged 9D and ΔN complexes directly by single-molecule TIRF microscopy and bulk microtubule binding assays. Unlike the wild-type complex, binding of the mutant complexes was undetectable in standard BRB80 (120 mM K^+) buffer conditions, so the assays were performed in BRB40 (60 mM K^+) buffer. Single molecules of 9D and ΔN complex exhibited similar dissociation and diffusion rate constants (Fig. 4 *A* and *B*) (k_{off} = 0.85 ± 0.07 and 0.90 ± 0.05 s^{-1}, and D = 0.060 ± 0.003 and 0.050 ± 0.002 $\mu m^2 \cdot s^{-1}$, respectively). In contrast, wild-type Ndc80 complexes dissociated from microtubules ~15-times more slowly (k_{off} = 0.062 ± 0.005 s^{-1}) and diffused on the lattice ~four-times more slowly (D = 0.015 ± 0.001 $\mu m^2 \cdot s^{-1}$). It has been previously suggested that the Hec1 tail contributes to microtubule binding by the Ndc80 complex or mediates cooperativity between complexes on microtubules (11, 12, 28). Our results establish that the tail contributes directly to microtubule binding, because deletion of the tail causes individual Ndc80 complexes (in the absence of cooperative binding) to dissociate more quickly from microtubules.

In the bulk binding assay, fits to both the Hill and the McGhee and von Hippel models (Fig. 4 *C* and *D*) show that the 9D and ΔN complexes are indistinguishable from one another in their apparent affinities, cooperativity constants, and lattice occupancies (McGhee and von Hippel fit for 9D and ΔN: K_d = 78 ± 20 and 73 ± 20 nM, w = 7 ± 2 and 7 ± 1, i = 2.4 ± 0.1 and 2.4 ± 0.1 per tubulin dimer, respectively). Therefore, phosphomimetic mutations reduce the affinity of the Ndc80 complex for microtubules and impair its ability to promote microtubule rescue. However, these two effects are not strictly coupled; deletion of the Hec1 tail equally reduces the affinity of the complex for microtubules, but is not as detrimental to its ability to modify microtubule tip structure and dynamics. These findings suggest that Aurora B phosphorylation has separable effects on attachment stability and microtubule dynamics at the kinetochore.

Discussion

Ndc80 Complex Directly Modulates Microtubule Dynamics. The Ndc80 complex is a conserved and essential microtubule-binding component of the kinetochore. Here, we characterized the binding of full-length human Ndc80 complex to microtubules in vitro. The Ndc80 complex bound cooperatively to microtubules with a strong affinity, and directly promoted microtubule rescue. Our in vitro results using unphosphorylated wild-type Ndc80 complex explain observations made in cells. In the absence of Hec1 phosphorylation, we found that the Ndc80 complex antagonizes microtubule disassembly. This effect explains why blocking Hec1 phosphorylation in vivo causes hyper-stabilized K-fibers, and leads to damped sister kinetochore oscillations and severe defects in cell division (8). We believe our findings are unique in representing a demonstration that a core component of the human kinetochore directly modifies microtubule rescue rate in vitro. This ability has been shown previously for a core kinetochore component only once, with the budding yeast Dam1 complex (44), which has no known homolog in higher eukaryotes. Notably, the budding yeast Ndc80 complex does not effectively promote microtubule rescue (23), even though the composition and domain structure of the complex are highly conserved.

Our results also indicate a possible mechanism by which the Ndc80 complex promotes microtubule rescue. In the absence of stabilizing factors, protofilaments at disassembling microtubule tips form tight ~20-nm curls (37). When microtubules are stabilized by a nonhydrolyzable GTP analog, protofilaments are straighter at disassembling tips (45). We found that the tips of disassembling microtubules in the presence of Ndc80 complex were gently

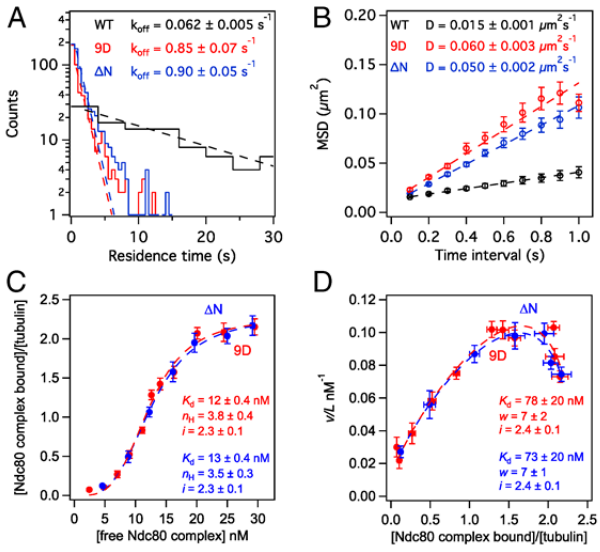

Fig. 4. The 9D and ΔN Ndc80 complexes exhibit similar binding behavior on microtubules. (*A*) Histograms of the residence time for single molecules (5 pM complex in solution) of wild-type (black trace, n = 131), 9D (red trace, n = 497), and ΔN (blue trace, n = 705) Ndc80 complex on taxol-stabilized microtubules. Each histogram was fit by a single exponential (dashed lines) to determine the off-rate constant, k_{off}. (*B*) Plots of MSD vs. time lag for binding events in *A*. The diffusion constant, D, was measured from linear fits to the data (dashed lines). (*C* and *D*) Bulk binding assays of 9D (red traces, n = 4–7 replicates per data point) and ΔN (blue traces, n = 6–7 replicates per data point) Ndc80 complex on taxol-stabilized microtubules. Dashed lines show fits of binding data to (*C*) Hill and (*D*) McGhee and von Hippel models. Errors on model fit parameters (K_d, n_H, w, and i) represent SD. All markers represent mean ± SEM and all assays were performed in BRB40 buffer (see *SI Materials and Methods*).

curved (as seen by TIRF microscopy) and formed large protofilament sheets (as seen by EM). These observations suggest that the Ndc80 complex promotes microtubule rescue by stabilizing tip structures with straighter protofilaments. Alushin et al. proposed that the Hec1 calponin homology domain recognizes the interface between tubulin monomers (28) at a putative hinge region (46). Our findings are consistent with this model. Ndc80 complex lacking the Hec1 tail was able to modify microtubule tip structure and promote rescue, indicating that other parts of the complex (outside of the tail) are primarily responsible for this activity. We propose that binding of the Hec1 calponin homology domain at the hinge region between tubulin subunits induces a straighter protofilament conformation that facilitates microtubule rescue.

Aurora B Regulates Microtubule Dynamics Through the Ndc80 Complex. The Aurora B kinase has an established role in releasing aberrant kinetochore-microtubule attachments (1). Consistent with this model, PtK cells carrying a phosphomimetic mutant Ndc80 (9D) complex have unattached kinetochores (11, 43). We found that the human 9D complex bound to microtubules more weakly relative to the wild-type complex, as determined by three independent in vitro assays. (*i*) Single molecules of the 9D complex dissociated more quickly (>10-fold) from the microtubule lattice. (*ii*) In our bulk assays, binding of the 9D complex was undetectable under conditions in which the wild-type complex bound strongly to microtubules. (*iii*) At equal surface density on beads, the 9D complex was impaired in its ability to track with microtubule disassembly against force. In all three of these assays, the 9D complex behaved similarly to and not worse than Ndc80 complex that lacks the tail domain (ΔN). Therefore, mutations that mimic complete phosphorylation of the Hec1 tail prevent the tail from contributing to microtubule binding.

In vivo observations suggest that in higher eukaryotes, Aurora B does not simply trigger kinetochore-microtubule detachment but additionally regulates microtubule dynamics (8, 10, 47). In PtK cells, syntelic kinetochore-microtubule attachments are not lost immediately following Aurora B activation (10). Instead, reactivation of Aurora B appears to induce disassembly of the kinetochore microtubules, and the kinetochores track with disassembly back to the centrosome, where the attachments are corrected. Our results offer insight into these observations. At higher surface densities on beads (20 nM), the 9D complex tracked robustly with disassembling microtubule tips against force. Based on geometric constraints (23), we estimate ~80 complexes can interact with the microtubule tip at this surface density. This number is more than the number of Ndc80 complexes per microtubule in vivo (~20 per microtubule), but fewer than the number of complexes at a single mammalian kinetochore, which binds 20–25 microtubules through more than 400 attachments (40, 48). Relative to the wild-type complex, the 9D and ΔN complexes are similarly impaired in their binding affinity and tracking performance. However, the ΔN complex promotes microtubule rescue, but the 9D complex does not. Thus, a phosphomimetic Hec1 tail interferes with the ability of the Ndc80 complex to modulate microtubule dynamics, possibly by blocking the ability of the calponin homology domain to stabilize a straighter protofilament conformation. Taken together, these in vitro observations explain how phosphorylation relieves microtubule stabilization at syntelic kinetochores to promote K-fiber disassembly, allowing the attached kinetochores to track back to the centrosome.

Here, we show that a conserved core microtubule-binding component of the human kinetochore directly influences microtubule dynamics. In addition, we find that phosphomimetic mutations of essential Aurora B phosphorylation sites in Hec1 not only weaken attachment, but also nearly abolish the ability of the Ndc80 complex to influence dynamics. These effects are separable, and might be independently tunable through phosphorylation of different subsets of target sites in the Hec1 tail. Taken together, our results indicate that microtubule dynamics can be regulated through Aurora B phosphorylation of the Ndc80 complex.

Materials and Methods

Protein Expression and Purification. The Ndc80 complex was coexpressed from two di-cistronic plasmids encoding Spc25/Spc24-His_6 and Hec1/Nuf2 (see *SI Materials and Methods*) in *E. coli* BL21 cells (Rosetta; Novagen). Protein expression and purification were carried out as previously described (23).

TIRF Microscopy. TIRF microscopy was performed on a custom illumination system (49) (see *SI Materials and Methods*). Taxol-stabilized Alexa-647-labeled microtubules were bound to the cover-slip with "rigor" kinesin (50). GFP-tagged Ndc80 complex was assayed in BRB80 (80 mM Pipes, 120 mM K^+, 1 mM $MgCl_2$, and 1 mM EGTA, pH 6.9) or BRB40 (40 mM Pipes, 60 mM K^+, 1 mM $MgCl_2$, and 1 mM EGTA, pH 6.9) with 8 mg·mL^{-1} BSA, 10 μM taxol, and an oxygen scavenger system. For dynamic microtubule assays, GMPCPP-stabilized microtubule seeds were bound to the cover-slip using "rigor" kinesin, and Alexa-647-labeled extensions were grown in BRB80 containing 8 mg·mL^{-1} BSA and 1 mM GTP. Microtubule disassembly was triggered by buffer exchange to remove free tubulin and simultaneously introduce GFP-tagged Ndc80 complex in BRB80 with 8 mg·mL^{-1} BSA, 1 mM GTP, and an oxygen scavenger system. See *SI Materials and Methods* for additional details.

Microtubule Binding Assays. Microtubule binding assays were performed as previously described (32), with the following modifications: GFP-tagged Ndc80 complex was incubated with taxol-stabilized microtubules in BRB80 with 10 μM taxol and 8% (vol/vol) gel filtration buffer (50 mM Hepes, 200 mM NaCl, pH 7.6), and pelleted through a glycerol cushion onto a cover-slip. The amount of microtubule-bound Ndc80 complex was quantified by fluorescence microscopy. Increasing concentrations of the complex (0–15 nM) were assayed with microtubules (2.5 nM tubulin dimers) to generate a binding curve. Microtubule binding for the 9D and ΔN Ndc80 complexes was undetectable in

BRB80, so binding assays were performed with 0–35 nM complex in BRB40. Binding curves were fitted to the Hill (34) and McGhee and von Hippel (35) models in Igor Pro (Wavemetrics) using iterative least-squares fitting. Errors on curve fit parameters (K_d, n_H, w, and i) represent the SD estimated by Igor Pro. See *SI Materials and Methods* for details of the assay.

Electron Microscopy. Ndc80 complex (50 nM) was incubated with taxol-stabilized microtubules (37 nM tubulin dimers) in BRB80 with 10 μM taxol. For disassembly assays, microtubules were assembled in the absence of taxol and disassembly was induced by dilution into BRB80 containing 25 nM Ndc80 complex. Samples were applied onto carbon-coated copper grids and stained with uranyl formate. Grids were viewed on a transmission electron microscope (Spirit T12; FEI). Additional details are provided in *SI Materials and Methods*.

Optical Trap Bead Motility Assays. Anti-His_5 antibody-coated polystyrene beads (11 pM) were functionalized by incubation with His_6-tagged wild-type (0.5–5 nM) or mutant (5–20 nM) Ndc80 complex. Beads were attached to the tips of disassembling microtubule extensions, which were grown from GMPCPP-stabilized microtubule seeds bound to the cover-slip. An optical trap was used to apply a constant force of ∼2 pN opposite the direction of microtubule disassembly. Assays were performed in BRB80 containing 1.4 $mg{\cdot}mL^{-1}$ tubulin, 8 $mg{\cdot}mL^{-1}$ BSA, 1 mM DTT, 250 $\mu g{\cdot}mL^{-1}$ glucose oxidase, 30 $\mu g{\cdot}mL^{-1}$ catalase, and 4.5 $\mu g{\cdot}mL^{-1}$ glucose. Records of bead position over time were generated and analyzed using custom software (Labview and Igor Pro, respectively). These data were used to determine the fraction of beads that tracked with disassembly, and the rates of microtubule disassembly and rescue. Additional details are included in *SI Materials and Methods*.

ACKNOWLEDGMENTS. We thank A. Franck, A. Powers, B. Graczyk, and E. Mazanka for helpful discussions. We also thank the Murdock Charitable Trust and the Washington Research Foundation for support of our electron cryomicroscopy facility. This work was supported by National Institutes of Health Grant T32 GM008268 (to N.T.U.); a Natural Sciences and Engineering Research Council of Canada scholarship (to J.F.T.); Searle Scholar Award Grant 06-L-111 (to C.L.A.); Packard Fellowship for Science and Engineering Grant 2006-30521 (to C.L.A.); National Institute of General Medical Sciences Grants R01 GM40506 (to T.N.D.) and R01 GM079373 (to C.L.A.); Public Health Service National Research Science Award 2T32 GM007270 from the National Institute of General Medical Sciences (to B.S.V.); and the Howard Hughes Medical Institute (T.G.).

1. Liu D, Lampson MA (2009) Regulation of kinetochore-microtubule attachments by Aurora B kinase. *Biochem Soc Trans* 37:976–980.
2. Biggins S, Murray AW (2001) The budding yeast protein kinase Ipl1/Aurora allows the absence of tension to activate the spindle checkpoint. *Genes Dev* 15:3118–3129.
3. Cheeseman IM, et al. (2002) Phospho-regulation of kinetochore-microtubule attachments by the Aurora kinase Ipl1p. *Cell* 111:163–172.
4. Hauf S, et al. (2003) The small molecule Hesperadin reveals a role for Aurora B in correcting kinetochore-microtubule attachment and in maintaining the spindle assembly checkpoint. *J Cell Biol* 161:281–294.
5. Pinsky BA, Kung C, Shokat KM, Biggins S (2006) The Ipl1-Aurora protein kinase activates the spindle checkpoint by creating unattached kinetochores. *Nat Cell Biol* 8:78–83.
6. Tanaka TU, et al. (2002) Evidence that the Ipl1-Sli15 (Aurora kinase-INCENP) complex promotes chromosome bi-orientation by altering kinetochore-spindle pole connections. *Cell* 108:317–329.
7. Cimini D, Wan X, Hirel CB, Salmon ED (2006) Aurora kinase promotes turnover of kinetochore microtubules to reduce chromosome segregation errors. *Curr Biol* 16: 1711–1718.
8. DeLuca KF, Lens SM, DeLuca JG (2011) Temporal changes in Hec1 phosphorylation control kinetochore-microtubule attachment stability during mitosis. *J Cell Sci* 124: 622–634.
9. Cimini D, Moree B, Canman JC, Salmon ED (2003) Merotelic kinetochore orientation occurs frequently during early mitosis in mammalian tissue cells and error correction is achieved by two different mechanisms. *J Cell Sci* 116:4213–4225.
10. Lampson MA, Renduchitala K, Khodjakov A, Kapoor TM (2004) Correcting improper chromosome-spindle attachments during cell division. *Nat Cell Biol* 6:232–237.
11. Guimaraes GJ, Dong Y, McEwen BF, Deluca JG (2008) Kinetochore-microtubule attachment relies on the disordered N-terminal tail domain of Hec1. *Curr Biol* 18:1778–1784.
12. Miller SA, Johnson ML, Stukenberg PT (2008) Kinetochore attachments require an interaction between unstructured tails on microtubules and Ndc80(Hec1). *Curr Biol* 18:1785–1791.
13. Hunter AW, et al. (2003) The kinesin-related protein MCAK is a microtubule depolymerase that forms an ATP-hydrolyzing complex at microtubule ends. *Mol Cell* 11: 445–457.
14. Jiang K, et al. (2009) TIP150 interacts with and targets MCAK at the microtubule plus ends. *EMBO Rep* 10:857–865.
15. Knowlton AL, Lan W, Stukenberg PT (2006) Aurora B is enriched at merotelic attachment sites, where it regulates MCAK. *Curr Biol* 16:1705–1710.
16. Manna T, Honnappa S, Steinmetz MO, Wilson L (2008) Suppression of microtubule dynamic instability by the +TIP protein EB1 and its modulation by the CAP-Gly domain of p150glued. *Biochemistry* 47:779–786.
17. Tirnauer JS, Grego S, Salmon ED, Mitchison TJ (2002) EB1-microtubule interactions in *Xenopus* egg extracts: Role of EB1 in microtubule stabilization and mechanisms of targeting to microtubules. *Mol Biol Cell* 13:3614–3626.
18. Zhang X, Lan W, Ems-McClung SC, Stukenberg PT, Walczak CE (2007) Aurora B phosphorylates multiple sites on mitotic centromere-associated kinesin to spatially and temporally regulate its function. *Mol Biol Cell* 18:3264–3276.
19. Zimniak T, Stengl K, Mechtler K, Westermann S (2009) Phosphoregulation of the budding yeast EB1 homologue Bim1p by Aurora/Ipl1p. *J Cell Biol* 186:379–391.
20. Kline-Smith SL, Sandall S, Desai A (2005) Kinetochore-spindle microtubule interactions during mitosis. *Curr Opin Cell Biol* 17:35–46.
21. Wei RR, et al. (2006) Structure of a central component of the yeast kinetochore: The Spc24p/Spc25p globular domain. *Structure* 14:1003–1009.
22. Wei RR, Sorger PK, Harrison SC (2005) Molecular organization of the Ndc80 complex, an essential kinetochore component. *Proc Natl Acad Sci USA* 102:5363–5367.
23. Powers AF, et al. (2009) The Ndc80 kinetochore complex forms load-bearing attachments to dynamic microtubule tips via biased diffusion. *Cell* 136:865–875.
24. Tien JF, et al. (2010) Cooperation of the Dam1 and Ndc80 kinetochore complexes enhances microtubule coupling and is regulated by aurora B. *J Cell Biol* 189:713–723.
25. Lampert F, Hornung P, Westermann S (2010) The Dam1 complex confers microtubule plus end-tracking activity to the Ndc80 kinetochore complex. *J Cell Biol* 189:641–649.
26. Cheeseman IM, Chappie JS, Wilson-Kubalek EM, Desai A (2006) The conserved KMN network constitutes the core microtubule-binding site of the kinetochore. *Cell* 127: 983–997.
27. Tooley JG, Miller SA, Stukenberg PT (2011) The Ndc80 complex uses a tripartite attachment point to couple microtubule depolymerization to chromosome movement. *Mol Biol Cell* 22:1217–1226.
28. Alushin GM, et al. (2010) The Ndc80 kinetochore complex forms oligomeric arrays along microtubules. *Nature* 467:805–810.
29. Ciferri C, et al. (2008) Implications for kinetochore-microtubule attachment from the structure of an engineered Ndc80 complex. *Cell* 133:427–439.
30. Wei RR, Al-Bassam J, Harrison SC (2007) The Ndc80/HEC1 complex is a contact point for kinetochore-microtubule attachment. *Nat Struct Mol Biol* 14:54–59.
31. Wilson-Kubalek EM, Cheeseman IM, Yoshioka C, Desai A, Milligan RA (2008) Orientation and structure of the Ndc80 complex on the microtubule lattice. *J Cell Biol* 182: 1055–1061.
32. Graczyk B, Davis TN (2011) An assay to measure the affinity of proteins for microtubules by quantitative fluorescent microscopy. *Anal Biochem* 410:313–315.
33. Gestaut DR, et al. (2008) Phosphoregulation and depolymerization-driven movement of the Dam1 complex do not require ring formation. *Nat Cell Biol* 10:407–414.
34. Hill AV (1910) The possible effects of the aggregation of molecules of haemoglobin on its dissociation curves. *J Physiol* 40:iv–vii.
35. McGhee JD, von Hippel PH (1974) Theoretical aspects of DNA-protein interactions: Co-operative and non-co-operative binding of large ligands to a one-dimensional homogeneous lattice. *J Mol Biol* 86:469–489.
36. Koshland DE, Mitchison TJ, Kirschner MW (1988) Polewards chromosome movement driven by microtubule depolymerization in vitro. *Nature* 331:499–504.
37. Mandelkow EM, Mandelkow E, Milligan RA (1991) Microtubule dynamics and microtubule caps: A time-resolved cryo-electron microscopy study. *J Cell Biol* 114:977–991.
38. Westermann S, et al. (2005) Formation of a dynamic kinetochore- microtubule interface through assembly of the Dam1 ring complex. *Mol Cell* 17:277–290.
39. Franck AD, Powers AF, Gestaut DR, Davis TN, Asbury CL (2010) Direct physical study of kinetochore-microtubule interactions by reconstitution and interrogation with an optical force clamp. *Methods* 51:242–250.
40. Lawrimore J, Bloom KS, Salmon ED (2011) Point centromeres contain more than a single centromere-specific Cse4 (CENP-A) nucleosome. *J Cell Biol* 195:573–582.
41. Nicklas RB (1988) The forces that move chromosomes in mitosis. *Annu Rev Biophys Biophys Chem* 17:431–449.
42. Pearson CG, Maddox PS, Salmon ED, Bloom K (2001) Budding yeast chromosome structure and dynamics during mitosis. *J Cell Biol* 152:1255–1266.
43. Sundin LJ, Guimaraes GJ, Deluca JG (2011) The NDC80 complex proteins Nuf2 and Hec1 make distinct contributions to kinetochore-microtubule attachment in mitosis. *Mol Biol Cell* 22:759–768.
44. Franck AD, et al. (2007) Tension applied through the Dam1 complex promotes microtubule elongation providing a direct mechanism for length control in mitosis. *Nat Cell Biol* 9:832–837.
45. Müller-Reichert T, Chrétien D, Severin F, Hyman AA (1998) Structural changes at microtubule ends accompanying GTP hydrolysis: Information from a slowly hydrolyzable analogue of GTP, guanylyl (alpha,beta)methylenediphosphonate. *Proc Natl Acad Sci USA* 95:3661–3666.
46. Wang HW, Nogales E (2005) Nucleotide-dependent bending flexibility of tubulin regulates microtubule assembly. *Nature* 435:911–915.
47. DeLuca JG, et al. (2006) Kinetochore microtubule dynamics and attachment stability are regulated by Hec1. *Cell* 127:969–982.
48. Rieder CL (1982) The formation, structure, and composition of the mammalian kinetochore and kinetochore fiber. *Int Rev Cytol* 79:1–58.
49. Gestaut DR, Cooper J, Asbury CL, Davis TN, Wordeman L (2010) Reconstitution and functional analysis of kinetochore subcomplexes. *Methods Cell Biol* 95:641–656.
50. Rice S, et al. (1999) A structural change in the kinesin motor protein that drives motility. *Nature* 402:778–784.

Supporting Information

Umbreit et al. 10.1073/pnas.1209615109

SI Materials and Methods

Cloning. The human Ndc80 complex was coexpressed in *Escherichia coli* from two di-cistronic plasmids: one encoded Spc25 and His_6-tagged Spc24 in the pCDF backbone, and the other encoded Hec1 and Nuf2 in the pST39 backbone. To generate the Spc25/Spc24-His_6 plasmid, cDNA clones of Spc25 and Spc24 were purchased from ATCC and cloned into pST39 (1) using XbaI/ApaI and EcoRI/HindIII, respectively. A C-terminal His_6-tag was added to Spc24 for affinity purification and binding to polystyrene beads. The di-cistron of Spc25/Spc24-His_6 was transferred from the pST39 backbone into the pCDF backbone (Merck KGaA) using AscI (added by PCR amplification). To generate the Hec1/Nuf2 plasmid, cDNA clones of Hec1 (purchased from ATCC) and Nuf2 (kindly provided by Jennifer DeLuca, Colorado State University, Fort Collins, CO) were inserted into pST39 using EcoRV/KpnI and BspEI/MluI, respectively. For GFP-tagged Ndc80 complex expression, three fragments were generated and ligated together to clone GFP onto the C terminus of human Nuf2. First, the C terminus of Nuf2 was removed from the Hec1/Nuf2 pST39 plasmid using SphI and MluI. Second, a Nuf2 fragment was created by PCR to introduce a PacI site in place of the stop codon, and cut with SphI/PacI. Third, a GFP fragment was similarly created by PCR, to introduce sites for and cut with PacI and MluI. Simultaneous ligation of all three fragments generated pST39 containing a di-cistron of Hec1 and Nuf2-GFP. Ndc80 complex mutants were generated by site-directed mutagenesis using QuikChange Lightning kits (Stratagene) according to the manufacturer's protocol.

Total Internal Reflection Fluorescence Microscopy. Total internal reflection fluorescence (TIRF) microscopy was performed as previously described (2–5). A far-red laser (FTEC-635-0-25-PFQ; Blue Sky Research) and blue laser (Sapphire 488-75; Coherent) were used for simultaneous excitation of Alexa-647 and GFP. The illumination light reaching the sample was collimated and collected through the objective lens (CFI Planapochromat, 100×, 1.49 numerical aperture; Nikon). Emission channels from GFP and Alexa-647 were projected side-by-side onto a CCD camera (iXon 887-BI; Andor Technology), and images were collected at 10 frames per second with iXon software (Andor Technology).

Flow cells for TIRF microscopy were constructed and prepared as previously described (3). Flow cells were washed with H_2O and subsequently incubated for 5 min with "rigor" kinesin (6) diluted in BRB80 (80 mM Pipes, 120 mM K^+, 1 mM $MgCl_2$, and 1 mM EGTA, pH 6.9) with 8 mg·mL^{-1} BSA. Taxol-stabilized microtubules (1% Alexa-647–labeled tubulin) were bound for ∼1 min and washed with BRB80 containing 8 mg·mL^{-1} BSA and 10 μM taxol. Flow cells were washed again with BRB80 or BRB40 (40 mM Pipes, 60 mM K^+, 1 mM $MgCl_2$, and 1 mM EGTA, pH 6.9) containing 8 mg·mL^{-1} BSA, 10 μM taxol, and an oxygen scavenger system (200 μg·mL^{-1} glucose oxidase, 35 μg·mL^{-1} catalase, 25 mM glucose and 5 mM DTT). GFP-tagged Ndc80 complex was introduced in BRB80 or BRB40 with 8 mg·mL^{-1} BSA, 10 μM taxol and an oxygen scavenger system. Single-molecule conditions were confirmed by measuring photobleach steps (at various excitation laser powers) for wild-type Ndc80 complexes on taxol-stabilized microtubules (Fig. S2). Laser powers were measured before entry into the microscope body.

In the dynamic microtubule TIRF experiments, GMPCPP-stabilized seeds (2% Alexa-647–labeled) were bound to the cover-slip with "rigor" kinesin and washed with growth buffer (BRB80 with 8 mg·mL^{-1} BSA and 1 mM GTP). Dynamic extensions were polymerized off the seeds by the addition of growth buffer supplemented with 2 mg·mL^{-1} tubulin (1% Alexa-647–labeled) and an oxygen scavenger system. Disassembly was induced by buffer exchange with BRB80 containing 8 mg·mL^{-1} BSA, an oxygen scavenger system, and the reported concentration of GFP-labeled Ndc80 complex. All dynamic microtubule assays were done at 30 °C.

Software analysis was performed using Labview (National Instruments), as previously described (2–5). Kymographs were generated for both the Alexa-647 and GFP channels. The position and brightness over time was recorded for individual GFP-tagged complexes on microtubules. Custom programs (available upon request) written in Igor Pro (Wavemetrics) were used to generate residence time histograms and standard diffusion rate plots (mean-squared displacement vs. time lag). The dissociation rate constant (k_{off}) was calculated from a single exponential fit to the histogram of residence time. Diffusion rate constants were calculated from linear fits to diffusion plots. For dynamic microtubule assays, disassembly rates were measured as the average distance disassembled over time, as determined from Alexa-647 channel kymographs. Disassembly rates were measured only for the longer extension of each microtubule, and extensions shorter than 4 μm were discarded from analysis because of unreliability in measurements for short events. Microtubule tips were scored visually for the formation of extensions that curled away from the long axis of the microtubule during disassembly (Fig. S3 *A* and *B*). Only microtubules for which the tip was in focus throughout disassembly were scored.

Microtubule Binding Assays. The bulk binding assay was performed as previously described (3, 7). GFP-tagged Ndc80 complex was incubated with Alexa-568-labeled taxol-stabilized microtubules (2.5 nM tubulin dimers) for 10 min at room temperature. The incubation was done in BRB80 or BRB40 with 10 μM taxol and 8% gel filtration buffer (50 mM Hepes, 200 mM NaCl, pH 7.6). The reaction was fixed by addition of three volumes of 2% glutaraldehyde in BRB80 or BRB40 and incubated for 2 min at room temperature. The assay is not sensitive to the amount of glutaraldehyde used or the duration of the fix (7). A 750-μL glycerol cushion (15% wt/vol in PBS) was layered on top of a polylysine-treated glass cover-slip sitting on a custom spacer (Ellard Instrumentation) in a TLS-55 centrifuge tube (Beckman). A 250-μL portion of the fixed reaction mixture was layered onto the glycerol cushion and the microtubules were pelleted onto the cover-slip at 135,000 × *g* for 10 min at 25 °C. The supernatant and glycerol cushion were removed by aspiration and the cover-slip was placed onto a drop of Citifluor (Ted Pella), microtubule-side down, on a glass slide. The slide was sealed with nail polish to prevent evaporation.

Slides were imaged on a DeltaVision microscopy system (Applied Precision) containing an Olympus IX70 microscope, a 100× oil objective (1.35 numerical aperture), and a CoolSnap HQ digital camera (Roper Scientific). For each slide, 10 *z*-sections (0.3 μm) were taken in 10 consecutive panels (512 × 512 pixels, binned 2 × 2) using filter sets to detect GFP and Alexa-568. To determine the amount of GFP-tagged Ndc80 complex for each slide, the average pixel intensity for the second *z*-section image in the GFP channel was averaged for the 10 panels. These values were corrected for background (a slide in which microtubules were incubated in the absence of Ndc80 complex) and lamp intensity (using the photosensor value). Standard curves were made by incubating increasing concentrations (up to ∼60 nM) of wild-type or mutant

Ndc80 complex with a saturating amount of microtubules (140 nM) in the appropriate buffers (BRB80 or BRB40), such that all Ndc80 complex added to the reaction was bound to microtubules. Microtubules were pelleted and imaged as described above. Slopes from the standard curves were used to convert fluorescence intensity values to concentrations for microtubule-bound Ndc80 complexes.

Electron Microscopy. Taxol-stabilized microtubules (37 nM tubulin dimers) were incubated with wild-type Ndc80 complex (50 nM) in BRB80 containing 10 μM taxol for ∼10 min. Copper grids were carbon-coated and positively charged in a glow discharge device (EMS) at 25 mA for 2 min. A drop of the reaction mix (2 μL) was applied onto a freshly discharged grid and incubated for 20 s. Excess sample was blotted off, the grid was washed twice with BRB80, once with 0.075% uranyl formate, and stained with uranyl formate. Excess stain was blotted off and the grid was air-dried. Grids were viewed on a transmission electron microscope (Spirit T12, FEI) operating at 120 kV and images were recorded on a 1 k × 1 k bottom-mount slow-scan CCD camera (Gatan) at a nominal magnification of 21,000× at the specimen level.

For the disassembly assay, microtubules were assembled by incubating cleared tubulin (∼6 μg/μL) in BRB80 containing 2 mM GTP, 5 mM $MgCl_2$, and 4% DMSO at 37 °C for 30 min. After assembly, 1 volume of warm BRB80 (37 °C) was added to make the stock microtubule mix. Disassembly was induced by diluting 1 μL of microtubule mix into 200 μL of a filtered BRB80 solution (0.22-μm filter; Millipore) containing 25 nM human Ndc80 complex, 25 nM budding yeast Dam1 complex (8), or 10 μM taxol, and incubating for 2 min at room temperature. Samples were then prepared for analysis and imaged by electron microscopy, as described above.

Optical Trap Bead Motility Assays. Ndc80 complexes were linked to the surface of polystyrene beads, as previously described (4, 5, 9). Streptavidin-coated beads (Spherotech) were functionalized with biotinylated anti-His_5 antibodies (Qiagen). His_6-tagged wild-type or mutant Ndc80 complex was incubated at the appropriate concentration (0.5, 1, 5, 10, or 20 nM) with 11 pM beads, rotating for 30 min at 4 °C. Beads were spun down at 16,100 × *g* in a desktop centrifuge for 5 min at 4 °C, and resuspended in 200 μL assay buffer (BRB80 containing 8 mg·mL^{-1} BSA and 1 mM DTT) to wash away unbound Ndc80 complex. The beads were spun again at 16,100 × *g* for 5 min at 4 °C, and resuspended with assay buffer to the original incubation volume.

Flow chambers were constructed and functionalized as previously described (9). First, one flow chamber volume of 1 mg·mL^{-1} biotinylated BSA (Vector Laboratories) was introduced and allowed to bind to the glass surface for ∼10 min at room temperature. The chamber was then washed twice with ∼20 volumes BRB80. Next, ∼10 volumes 0.33 mg·mL^{-1} avidin DN (Vector Laboratories) was introduced, incubated for ∼2 min, and washed out with ∼20 volumes BRB80. GMPCPP-stabilized biotinylated microtubule seeds were introduced in BRB80, and allowed to bind to the functionalized glass surface for ∼2 min. The chamber was then washed with ∼20 volumes blocking buffer (BRB80 containing 1 mM GTP, 8 mg·mL^{-1} BSA, and 1 mg·mL^{-1} κ-casein), followed by a second wash with growth buffer (BRB80 containing 1 mM GTP and 8 mg·mL^{-1} BSA). Lastly, Ndc80 complex-coated beads were introduced at an eightfold dilution from the incubation mix (see above) in a solution of growth buffer containing 1.4 mg·mL^{-1} tubulin, 8 mg·mL^{-1} BSA, 1 mM DTT, 250 μg·mL^{-1} glucose oxidase, 30 μg·mL^{-1} catalase, and 4.5 μg·mL^{-1} glucose. The edges of the flow chamber were sealed with nail polish to prevent evaporation. Microtubule disassembly events occurred either by a spontaneous switch from assembly to disassembly or by laser scission, as described previously (9). All optical trap assays were performed at 26 °C.

Records of bead position vs. time were analyzed using custom software written in Igor Pro (available upon request). To be considered in the analysis, beads were required to have undergone tracking in the direction of disassembly against the applied force for at least 25 nm. Detachments were scored during the experiment and verified in analysis when the force on a bead under load suddenly dropped to zero, and the bead position trace exhibited "run-away" movement. Microtubule rescues were scored visually during the experiment and verified in analysis by identifying the time at which microtubule disassembly halted. Beads were observed for an additional ∼30 s to verify that the bead subsequently underwent motion in the direction of microtubule growth at an assembly-limited rate (∼10 nm/s) (Fig. 3*A*, top two traces). Intrinsic disassembly and rescue rates for bare microtubules in the absence of force were measured from traces of tip position versus time, as determined from differential interference contrast recordings (10). We also determined that microtubule rescue was not a result of the disassembling tip reaching the GMPCPP-stabilized microtubule seed; the microtubule lattice was laser-ablated approximately at the point where rescue occurred, and the microtubule was verified to undergo disassembly back to the stabilized seed. The rescue rate for microtubules was calculated by dividing the number of observed microtubule rescues by the total time of disassembly-driven motility recorded for each assay condition. Disassembly rates were estimated for each event by the slope of a linear fit to the bead position versus time trace, taken over the second half of the entire duration of the disassembly event. Events that lasted less than 2 s were not included in disassembly rate analysis because of unreliability in the linear fits over short time intervals.

1. Tan S (2001) A modular polycistronic expression system for overexpressing protein complexes in *Escherichia coli*. *Protein Expr Purif* 21:224–234.
2. Gestaut DR, Cooper J, Asbury CL, Davis TN, Wordeman L (2010) Reconstitution and functional analysis of kinetochore subcomplexes. *Methods Cell Biol* 95:641–656.
3. Gestaut DR, et al. (2008) Phosphoregulation and depolymerization-driven movement of the Dam1 complex do not require ring formation. *Nat Cell Biol* 10:407–414.
4. Powers AF, et al. (2009) The Ndc80 kinetochore complex forms load-bearing attachments to dynamic microtubule tips via biased diffusion. *Cell* 136:865–875.
5. Tien JF, et al. (2010) Cooperation of the Dam1 and Ndc80 kinetochore complexes enhances microtubule coupling and is regulated by aurora B. *J Cell Biol* 189:713–723.
6. Rice S, et al. (1999) A structural change in the kinesin motor protein that drives motility. *Nature* 402:778–784.
7. Graczyk B, Davis TN (2011) An assay to measure the affinity of proteins for microtubules by quantitative fluorescent microscopy. *Anal Biochem* 410:313–315.
8. Franck AD, et al. (2007) Tension applied through the Dam1 complex promotes microtubule elongation providing a direct mechanism for length control in mitosis. *Nat Cell Biol* 9:832–837.
9. Franck AD, Powers AF, Gestaut DR, Davis TN, Asbury CL (2010) Direct physical study of kinetochore-microtubule interactions by reconstitution and interrogation with an optical force clamp. *Methods* 51:242–250.
10. Walker RA, et al. (1988) Dynamic instability of individual microtubules analyzed by video light microscopy: Rate constants and transition frequencies. *J Cell Biol* 107: 1437–1448.

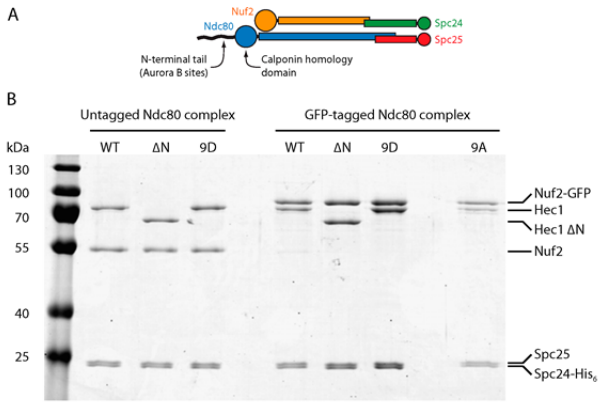

Fig. S1. The human Ndc80 complex was expressed in and purified from *E. coli* using affinity and size-exclusion chromatography. (*A*) Schematic of the heterotetrameric Ndc80 complex. (*B*) A Coomassie-stained gel shows the purified, recombinant wild-type and mutant versions of the Ndc80 complex used in this study. Molecular weight size markers are labeled on the left, and Ndc80 complex proteins, identified by size, are labeled on the right.

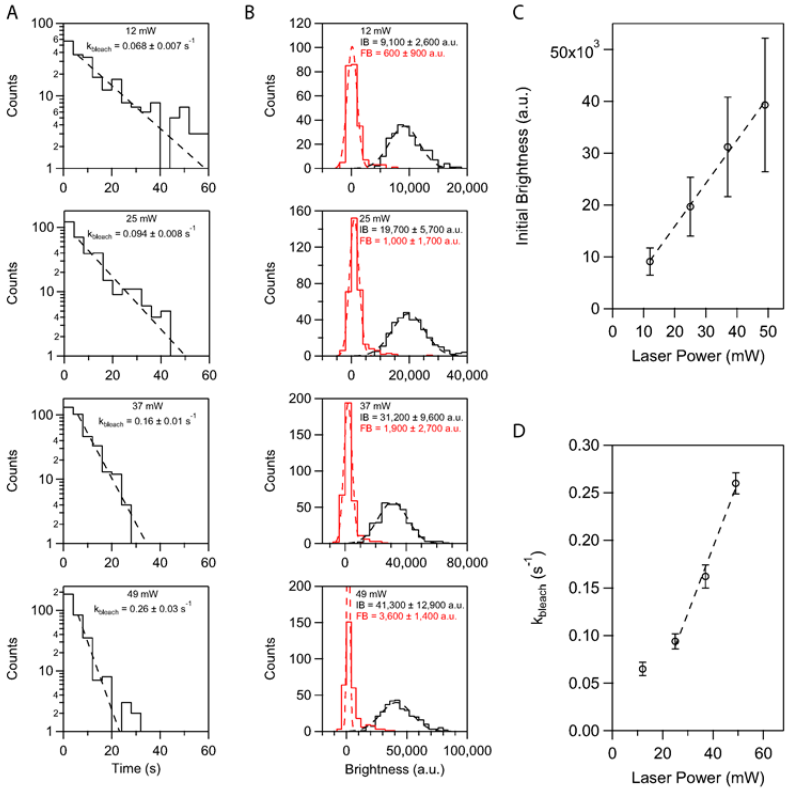

Fig. S2. The Ndc80 complex binds microtubules primarily as a monomer in the single-molecule TIRF assay. To determine if the GFP-tagged Ndc80 complex binds microtubules as a monomer in our single-molecule conditions (5–10 pM complex in solution), we imaged individual particles in BRB40 buffer under conditions that enhanced photobleaching. For example, a monomer would photobleach to near-background levels in a single step, whereas a dimer would photobleach in two steps of half the initial particle brightness. (*A*) Histograms of residence time with exponential fits (dashed lines) used to calculate the apparent bleach rate constant, k_{bleach} (a combination of GFP photobleaching rate and off-rate constants), at various excitation laser intensities. (*B*) Histograms and corresponding Gaussian fits of initial brightness (IB, black traces) and final brightness after photobleaching or detachment (FB, red traces). Note that the single bleach step (~95% of IB) for each condition is consistent with a monomeric species. (*C*) Plot of initial brightness vs. laser power with a linear fit (dashed line). (*D*) Plot of k_{bleach} vs. laser power. Above 12 mW, k_{bleach} increases linearly with laser power (dashed line), indicating that photobleaching (rather than detachment) contributes primarily to k_{bleach} under these conditions. For the datasets in *A*–*D*: n = 228 at 12 mW, n = 337 at 25 mW, n = 347 at 37 mW, and n = 327 at 49 mW.

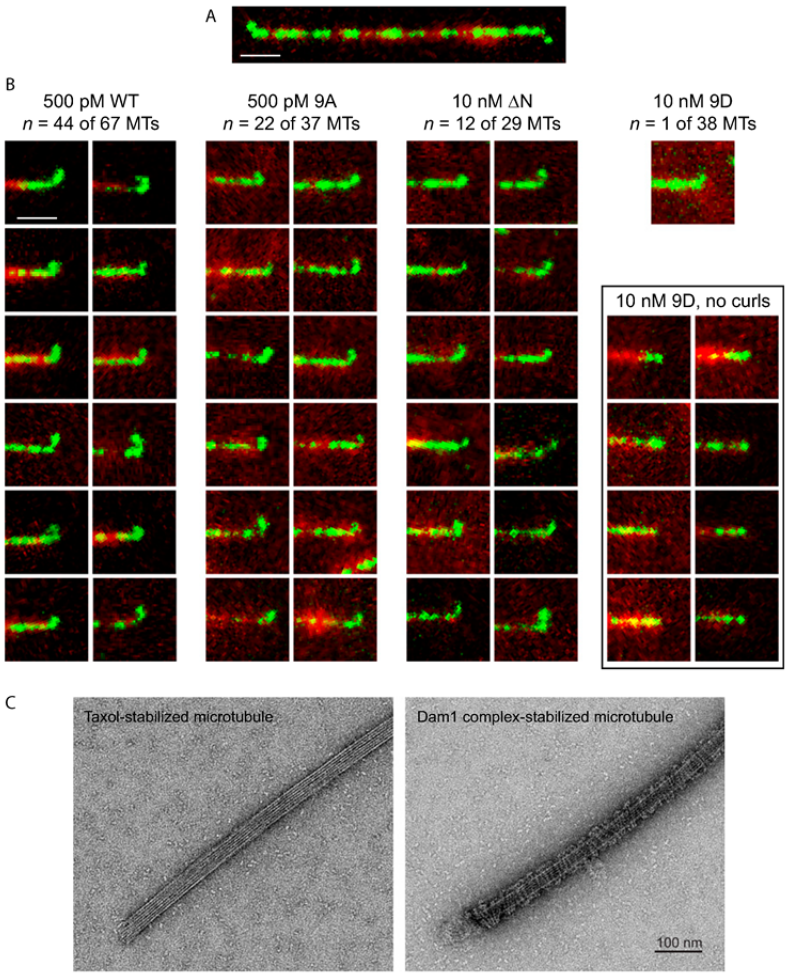

Fig. S3. Curls form at disassembling microtubule tips in the presence of Ndc80 complex. (*A*) In the presence of 500 pM GFP-tagged wild-type Ndc80 complex (green), curled extensions were observed at both ends of disassembling Alexa-647-labeled microtubules (red). (Scale bar, 2 μm.) (*B*) Gallery of curled extensions at the tips of disassembling microtubules in the presence of wild-type, 9A, ΔN, and 9D Ndc80 complex. The number (*n*) of microtubules (MTs) that formed curled extensions during disassembly is noted for each condition. (Scale bar, 2 μm.) (*C*) Negative-stain electron micrographs of disassembling microtubule tips (see *SI Materials and Methods*) stabilized by taxol or budding yeast Dam1 complex.

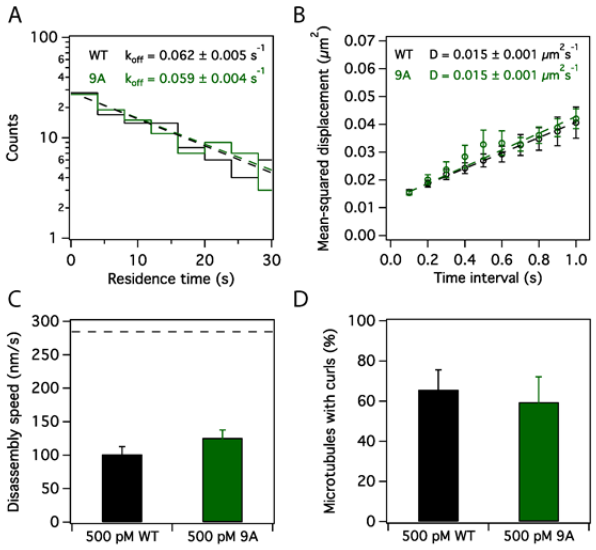

Fig. S4. Wild-type and 9A Ndc80 complexes exhibit similar binding behavior on microtubules. By TIRF microscopy, single molecules (5 pM complex in solution) of GFP-tagged wild-type (black traces, from Fig. 4 *A* and *B*) and 9A (green traces, n = 124) Ndc80 complexes have similar (*A*) residence time distributions and (*B*) diffusion rates on taxol-stabilized microtubules. A single exponential fit to the residence time distribution (*A*, dashed line) was used to calculate the off-rate constant, k_{off}. A linear fit to the mean-squared displacement versus time-lag plot (*B*, dashed line) was used to determine the diffusion constant, D. Markers represent the mean ± SEM (*C*) Microtubule disassembly speeds were measured in the presence of 500 pM wild-type (black bar, from Fig. 2*C*) or 500 pM 9A (green bar, n = 35) Ndc80 complex. Error bars represent SEM. Dashed horizontal line represents the intrinsic disassembly rate, 284 ± 15 nm/s, value reproduced from Fig. 2*C*. (*D*) Percentage of microtubules for which a curl was observed at the microtubule tip during disassembly in the presence of 500 pM wild-type (black bar, from Fig. 3*F*) or 500 pM 9A (green bar, n = 37) Ndc80 complex. Error bars represent counting uncertainties.

Table S1. Number of replicates for optical trap assays

Ndc80 complex	WT				9D			ΔN	
Concentration (nM)	0.5	1	5	5	10	20	5	10	20
n (Disassembly-tracking fraction)	40	84	74	98	134	58	122	111	74
n (Disassembly speed)	21	47	54	8	46	53	11	39	40
n (Number of rescues)	2	15	32	ND	0	3	ND	3	15
Rescue rate observation time (minutes of disassembly)	5	14	14	ND	16	29	ND	13	26

ND, not determined.

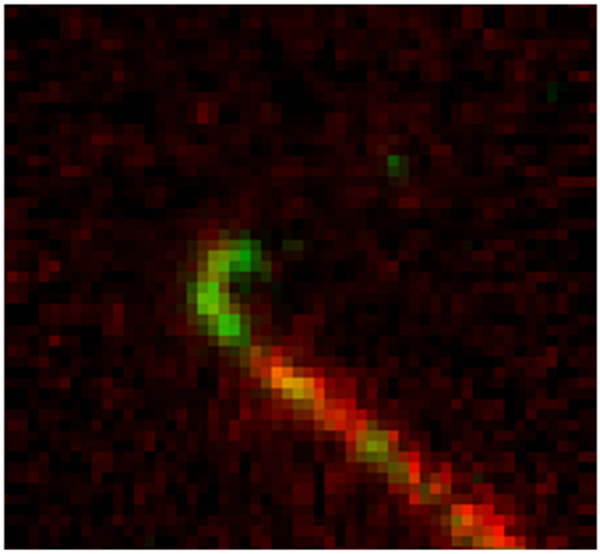

Movie S1. Ndc80 complex stabilizes curled extensions at disassembling microtubule tips. Movie shows 500 pM GFP-tagged Ndc80 complex (green) on a disassembling Alexa-647-labeled microtubule (red). GFP and Alexa-647 channels were visually aligned, and the brightness and contrast were adjusted for clarity using custom Labview software. Movie dimensions are 6.5 by 5.9 μm, and playback is at 9× speed.

Movie S1